Advanced Ultrasonic NDE of Composite Airframe Components: Physics, Modelling and Technology

Martin Mienczakowski, BEng. (Hons)

Thesis submitted to the University of Nottingham
for the degree of Doctor of Philosophy

December 2010

Abstract

In recent years the use of composites in engineering has greatly increased due to the advantages which may be obtained. These are weight savings, increased strength, the ability to construct complex geometries and the use of mixed materials. Of particular interest in this work are carbon fibre reinforced plastics (CFRP) which are increasingly used in the aerospace industry. Historically, NDE methods for CFRPs have concentrated on through thickness measurements of ultrasonic attenuation or velocity to determine the presence of defects. Whilst this method is relatively fast and easy to employ there are significant disadvantages in terms of defect characterisation and the location of defects in three dimensions. The advent of full waveform capture and increased computing power allowing processing of large volumes of data, has made 3-D characterisation possible for the first time.

The overall aim of this work is to develop new signal processing techniques with which to interpret ultrasonic signals from composite materials. The primary consideration is the propagation of normal incidence compression waves through the multi-layered composite structure, and the interaction of the waves with the various types of defect which may be present. The principal interest is the detection and classification of porosity. A multi-layered model of ultrasonic propagation in a composite is combined with a model which calculates the scattering response due to porosity. The model is used to simulate the ultrasonic signals that are obtained from NDE procedures applied to composite. The simulations are then used as the basis on which to develop novel signal processing schemes for the detection, location and characterisation of porosity and other types of defect. The response obtained from differing defect conditions is isolated and investigated using both time domain and frequency domain techniques.

Comparisons are drawn between the responses obtained from modelling and from experimental samples. Consideration of the various methods which are sensitive to porosity leads to a system which can be applied to full waveform data to provide 3-D profiles of porosity and other defects.

The work described in this thesis is covered by UK Patent Application Number 0818383.2.

Acknowledgements

This work formed part of a targeted research program of the Research Centre for Non-Destructive Evaluation (RCNDE), UK, funded through the Engineering and Physical Sciences Research Council (EPSRC), UK, and contributing industries, and hence I gratefully acknowledge support from Airbus UK.

I am grateful to Dr. Richard Freemantle (Wavelength NDT, UK) and Mr. Andrew Bond-Thorely (Airbus, UK) for constructive discussion throughout the duration of this project.

I would like to thank the members of the Applied Ultrasonics Laboratory at the University of Nottingham for providing a stimulating and interesting environment in which to work. In particular I would like to thank Dr. Andrew Holmes and Dr. Valerie Pinfield who have provided me with extensive guidance on the functionality of the scattering model ECAH, Dr. Albert Phang for his help during the course of this work on many matters and Dr. Marion Unwin for setting me off on the road to doing a PhD many years ago.

I am grateful to my companion PhD student Mr. Robert Smith (QinetiQ, UK), with whom I have shared much of this experience.

I wish to acknowledge the excellent guidance that has been provided to me by my supervisor Professor Richard Challis, not just in this work but for many years previously.

I would like to thank the people in my personal life who have supported me throughout this work by providing light relief. In particular thanks to all those people who sent me messages of support in the later stages of this work, without you this would never have been finished.

Finally I would like to thank my parents who have supported me in this endeavour, I'm only too glad I could keep my promise.

Table of Contents

List of Figures

List of Tables

Glossary of terms

E	Young's modulus
K	Bulk modulus
G	Shear modulus
υ	*Po*isson's ratio
C_{ij}	Matrix elastic constants
φ_v	void volume fraction
φ_f	fibre volume fraction

Subscripts/superscripts

X_0	void free values
X_f	fibre
X_R	resin
X_1	in direction of fibres
X_2	transverse with respect to direction of fibres
X^C	whole composite
X_L	longitudinal wave
X_S	shear wave
X_v	pertaining to porosity

Chapter 1

Introduction

1.1 Introduction

In recent years the use of composites in engineering has greatly increased due to the advantages which may be obtained. These are weight savings, increased strength, the ability to construct complex geometries and the use of mixed materials. The fields in which composites are being used are many and varied, from medical to motorsport. With the expansion of composite usage there is an increased need for better material characterisation and defect detection. Of particular interest in this work are carbon fibre reinforced plastics (CFRP) which are increasingly used in the aerospace industry; indeed in the latest aircraft 50% of the structure is CFRP (Kollgaard and LaRiviere (2007)). Both Boeing and Airbus have plans to expand the use of composite within their latest aircraft for many aircraft structures within the fuselage and wings. Similarly engine manufacturers such as Rolls-Royce and General Electric are revisiting the idea of using composite fan blades. Historically, NDE methods for CFRPs have concentrated on through thickness measurements of ultrasonic attenuation or velocity to determine the presence of defects. Whilst this method is relatively fast and easy to employ there are significant disadvantages in terms of defect characterisation and location of the defects in three dimensions. The advent of full waveform capture and increased computing power allowing processing of large volumes of data, has made 3-D characterisation possible for the first time. The ability to locate and characterise defects in this manner would allow better acceptance / rejection criteria to be devised, by providing more comprehensive information to material engineers. The detection of

porosity is particularly important; if it were possible to determine the size and the location of the pores, components which might have been rejected based upon through thickness measurements might be useable or repairable rather than being scrapped. The work described in this thesis is covered by UK Patent Application Number 0818383.2.

1.2 Composite Structures

Although the detailed material specification for CFRPs can vary greatly between manufacturers and intended applications, there are some common restrictions. Typically the structure will consist of layers of carbon fibres which may be orientated in different directions contained within an epoxy resin matrix as shown in figure 1.1.

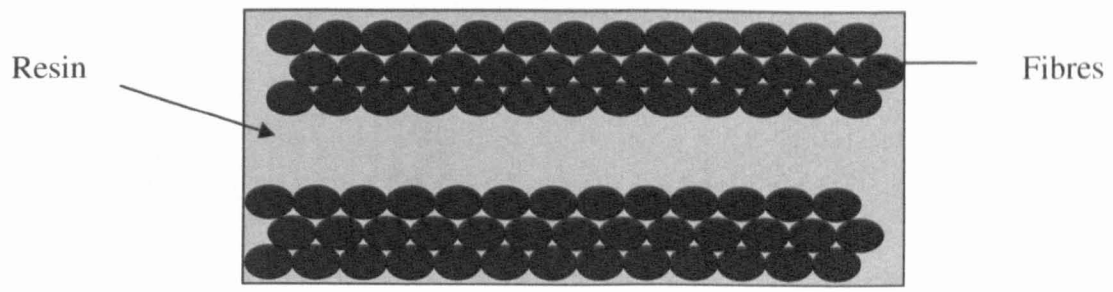

Figure 1.1 Typical carbon fibre composite, showing fibre layers and resin layers.

The fibre volume fraction employed is generally in the region of 65%. The types of fibres used and their arangement within the epoxy matrix can vary widely depending upon the application. The orientation of the fibres or "fibre lay-up" greatly affects the strength of the resultant structure, and hence the fibre plies are normally orientated in several directions for example 0, 45, 90 or -45° as shown in figure 1.2.

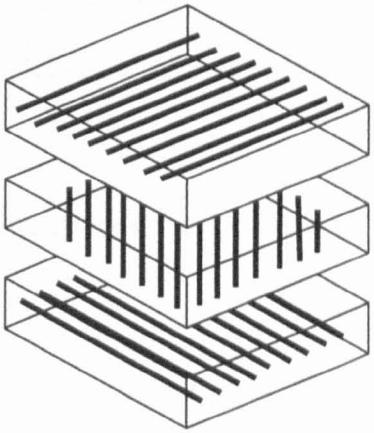

Figure 1.2 Typical orientation of fibres in a CFRP.

The plies themselves may contain fibres in one orientation or alternatively fibres which are woven and are in two directions, generally perpendicular to each other. Both types of fibre plies are employed depending upon the structure under construction. The typical structure of these types of fibres are shown in figure 1.3.

Figure 1.3 Structure of woven (left) and unidirectional fibre plies (right).

The thickness of the plies can also vary with application and it is usually expressed as a number of plies per millimetre which can range from 8 plies per mm for thin structures to 4 or fewer for larger structures.

Components are generally constructed by one of two methods: Using preformed composite which is a mixture of fibres and resin; the preform is then treated with heat

and pressure to form it to the shape desired. Alternatively dry fibres are placed in a mould and the resin infused under controlled temperature and pressure.

1.3 Defects Present in Composite Structures

There are many types of defect which may form during the manufacturing process. The causes of these defects are numerous and include, but are not limited to, incorrect application of temperature and pressure, sub-standard constituent materials, incorrect fibre layup and non-ideal control of atmospheric conditions - for example humidity. The most common manufacturing defects are typically:

- An incompletely cured epoxy matrix
- Introduction of foreign bodies
- Ply or fibre misalignment
- Fibre waviness
- Thermal cracking of plies
- Delamination
- Porosity

The detection of these defects during the manufacturing process is necessary because their presence can have a significant effect on the material properties, and they may worsen as a result of service fatigue. The primary aim for non destructive evaluation (NDE) in this area is to classify defects into three categories: first, defects which are present but which are not critical to component performance; second, defects which may have a significant impact and result in damage and reduced strength, but which

may, through characterisation and careful management, not render the component unusable; third, defects which are critical to the strength of the component to such an extent that the component should be scrapped, often at high cost.

Fibre volume fraction and void content may be controlled by careful application of temperature and pressure; however, if there is a deviation away from specified process conditions there is the possibility of fibre volume variation or the generation of porosity. This is especially the case when there are problems in the fabrication and storage of the preformed composite or, alternatively, when complex geometries are constructed. There is a tendency for porosity to form in clusters depending on the flow conditions in resin transfer moulding, and/or the geometry of the component. The detection of the presence of porosity is of critical importance since it has a significant effect on the structural integrity of the resultant composite (see for example Judd and Wright (1978), Uhl et al (1988) and de Almeida and Neto (1994)). A maximum allowable void volume fraction of 5% throughout the composite structure was specified by Hagemaier and Fassbender (1979). This figure, interpreted as an average through the depth of the composite is widely used as the basis for acceptance criteria in the aerospace industry. However, an average concentration of 5% could correspond to a much higher localised concentration that is structurally significant but never the less difficult to detect with conventional ultrasonic techniques. If such defects could be detected and characterised then more advanced criteria for sentencing tested components and lighter design would be possible. It is on this basis that this thesis aims to detect and characterise areas of porosity which are structurally significant but of insufficient volume to result in an abnormality in the A-scan response as would a major void.

Further damage may be introduced to the structure during service, most of the types of damage which are observed being related to impact damage and component fatigue. The defects which arise are typically:

- Impact damage
- Delamination
- Fibre splitting and fracture
- Transverse cracking

These kinds of defects can reduce the material strength of the components and so the detection and monitoring of the presence of these defects in-service is necessary in order to assess the safety implications and allow repair or replacement of the component.

1.4 NDE Methods for Defect Detection

There are numerous methods of defect detection which are employed in composite NDE, the principle methods being:

- Radiography
- Shearography
- Low frequency vibration
- Acoustic Emission
- Thermography
- Microwave

- Ultrasonics

Radiography is widely used for the non-destructive evaluation of materials, however, composites are relatively transparent to x-rays and hence low energy x-rays are generally used for composite inspection (Fassbender et al (1983)). To further aid detection of defects, tracer fibres or penetrant may be used to enhance the image, see for example Cotterell et al (1962). Although such faults as impact damage, fibre waviness and delaminations may be observed by this method, the observation of resin layer variations and porosity is difficult from conventional radiography. Porosity may be observed by use of computed tomography; however, this method places limits on the sample size and many exposures must be taken to build a complete picture of a component. For components that have large differences in their dimensions artefacts can be introduced into the image; there is also a need for access to all sides of the component. For these reasons computed tomography is unsuitable for many aerospace applications (Bossi et al (1995)).

Shearography involves stressing the component by either application of a vacuum or thermal stress (Newman (1990)). The component is then illuminated by a laser to produce two speckle patterns on the surface. By examining the interference between these two patterns delaminations may be observed (Tiziani (1978)). The method works best for large flat structures and can generally reveal defects just below the surface of the component (Shang et al (1990)).

Low frequency vibration is the name given to a variety of NDE methods such as tap testing, mechanical impedance, membrane resonance and velocimetric methods. The

methods work in the region of 10-20kHz and have found use due to their portability, low cost and speed with which an inspection may be employed. However, their use is generally limited to large scale planar defects and is insensitive to more subtle responses from defects such as porosity or fibre lay up (Adams and Cawley (1988)).

Acoustic emission is generally used as an in-service method for the detection of defects such as cracks as they occur. Transducers are mounted to the component in convenient locations and recordings are made whilst the component is stressed (Scruby (1987)). Although the technique can be used to locate defect growth, this process is generally irreversible.

Thermography involves the inducement of a thermal wave within the component which decays exponentially from the surface (see for example Milne et al (1985)). The wave reflects from defects within the composite structure, however these defects must be planar to the wave direction, and the detection of angled defects or defects at depth is difficult (Hobbs et al (1994)).

Microwaves are well suited to large scale composite inspection, their use to detect impact damage and disbonds in sandwich composites has been demonstrated in laboratory conditions. However, microwave inspection of composites is a relatively immature technology and as yet no commercial NDE equipment exists.

Ultrasonics is used in many areas of inspection and provides many advantages when compared to the other methods available. The small wavelength employed allows the imaging of relatively small defects; the waves may also be angled to allow imaging of

angled defects and are sensitive to the internal structure of CFRPs. The ability to record the full waveform received from a component allows the formation of 3-D images of the internal structure. A thorough examination of the use of ultrasonics in composite inspection is given in chapter 2.

Although all of these methods are used for defect detection, the method of choice in most cases is ultrasound on the basis that is sensitive to many of the defects which may be present in composite structures, and it does not require exclusion zones as for radiography or microwave methods; also it is relatively fast and the propagation of ultrasonic waves is relatively well understood. The focus of this thesis is the detection of porosity using ultrasound.

1.5 Aims and Context of this Thesis

The overall aim of this work is to develop new signal processing techniques with which to interpret ultrasonic signals from composite materials. The primary consideration is the propagation of normal incidence compression waves through the multi-layered composite structure, and the interaction of the waves with the various types of defect which may be present. The principal interest is the detection and classification of porosity. Where there is more than one type of defect present in an area, it is assumed that this is easily detected and the component is rejected. The focus of this thesis is the detection of low level defects which would not have otherwise resulted in automatic rejection. A multi-layered model of ultrasonic propagation in a composite is combined with a model which calculates the scattering response due to porosity. The model is used to simulate the ultrasonic signals that might arrive from NDE procedures applied

to composite. The simulations are then used as the basis on which to develop novel signal processing schemes for the detection, location and characterisation of porosity and other types of defect. The response obtained from differing defect conditions is isolated and investigated using both time domain and frequency domain techniques. Comparisons are drawn between the responses obtained from modelling and from experimental samples. A series of techniques is developed aimed at detecting porosity and thick resin layers and, importantly, differentiating between the two. The techniques described are in a sequence (Chapters 5, 6, 7 and 8) of increasing complexity. The reason for this is that the simpler methods detect both types of flaw well, but may not differentiate between them reliably, necessitating new methods of increasing complexity. Consideration of the various methods which are sensitive to porosity leads to a system which can be applied to full waveform data to provide three-dimensional profiles (3-D) of porosity and other defects.

Chapter 2 provides a background to the methods which have historically been employed to detect changes in fibre volume fraction and the presence of porosity within CFRPs. Chapter 3 examines algorithms which have been used to model the attenuation due to scattering from voids, and alterations which may be made to the models to create a model suitable for modelling the scattering due to porosity.

Chapter 4 details updates which have been made to a multi-layered model of ultrasonic propagation which had previously been used to model the response from adhesive layers in bonded automotive structures. The software is updated to allow the simulation of structures containing many layers, such as those which may be found in aerospace

components. A simple mixture rule is examined to allow modelling of the propagation of ultrasound through mixtures of fibres and resin.

Chapter 5 describes the construction of an algorithm for the time domain analysis of the ultrasonic signal received from a composite structure using envelope analysis. The method employs filters to suppress the ply resonance components and the effects of visco-elastic losses. It is shown that in the time domain the presence of a thick resin layer can produces a response similar to porosity.

Chapter 6 examines the responses obtained from porosity and thick resin layers in the frequency domain. This analysis leads to methods which are based upon short time gate time-frequency analysis. Through a detailed analysis it is found that it is possible to separately identify regions of excess resin and porosity in 3-D images.

Chapter 7 investigates how the resonances from within the ply and resin layers contribute to the frequency spectrum from a long time gate. A method is proposed which uses filtering to remove the ply resonance to leave the responses due to porosity or thick resin only. An equation is proposed which describes the individual contributions to the frequency spectrum and is applicable to both short and long time gates.

In Chapter 8 a method is derived which decomposes the spectrum to provide an indication of the contribution from normal ply and resin layer resonances, porosity and thick resin layers. This method is tested with the experimental data previously obtained

to confirm that it is possible using this method to produce 3-D images of porosity and thick resin layers.

Chapter 9 gives a discussion of the main conclusions of this work, and suggestions for further work which may be required to further validate and apply this method in industrial situations.

Chapter 2

Ultrasonic Examination of Composites: Current Theory, Practice and Limitations

2.1 Introduction

This Chapter presents a review of the current ultrasonic methods employed to detect the presence of fibre volume fraction changes and porosity within carbon fibre reinforced panels (CFRPs). The limitations of these methods are examined and the need for an improved procedure for the detection of porosity within CFRPs is explained. An overview of the current world scientific literature and the areas where work has previously been done to advance knowledge is presented.

2.2 Ultrasonic Methods

We have seen that there are many methods with which to analyse composite for the detection of a broad range of defects, however, these methods have not been found adequate for the detection of porosity and fibre volume fraction. Ultrasonic methods have traditionally been used for the detection of porosity. Variation in fibre volume fraction has not generally been considered a significant effect and as such has not received a great deal of attention in the literature.

2.2.1 Fibre Volume Fraction

An investigation into the effects of fibre volume fraction reveals several works which concentrate on theoretical models. One such work is that of Martin (1977), and the aim of this paper was to provide a comprehensive modelling formulation for the calculation of ultrasonic velocity in differing wave modes through composite structures. The principal focus was to investigate the effect of porosity although there was a provision for differing fibre volume fractions. In this study, the CFRP is modelled as a mixture – averaging the effects of material elasticity over the composite from estimated bulk and shear moduli, taking into account the effects of void and fibre content. The equations used which consider void content are those derived by Hashin (1962).

$$K = K_0\left(1 - \frac{3(1-v_c)}{2(1-2v_0)}P\right) \tag{2.1}$$

$$G = G_0\left(1 - \frac{15(1-v_0)}{7-5v_0}P\right) \tag{2.2}$$

$$P = 1 - \frac{\rho}{\rho_0} \tag{2.3}$$

Where P is the volume fraction of void content, K is the bulk modulus, G is the shear modulus, and v is Poisson's ratio. The zero subscripts indicate void free values and the c subscript indicate the composite value. The effective elastic (Young's) modulus (E) can then be calculated from:

$$E = \frac{9KG}{3K+G} \tag{2.4}$$

The results of these equations were then combined with results from Greszczuk (1971) which concern the effect of fibre volume fraction.

$$E_1 = E_f + E(1-\phi_f) \tag{2.5}$$

$$E_2 = E'\beta + E^*(1-\beta) \tag{2.6}$$

$$G_1 = G'\beta + G^*(1-\beta) \tag{2.7}$$

Where:

$$E' = \frac{E^* + 2\beta(E_f - E^*)}{1 + [2\beta(1-2\beta)/E^* E_f] \times [(E_f - E^*)^2 - (\nu E_f - \nu_f E^*)^2]} \tag{2.8}$$

$$E^* = \frac{E}{1-\nu^2} \tag{2.9}$$

$$G' = \frac{G^* G_f}{G_f + 2\beta(G^* - G_f)} \tag{2.10}$$

$$G^* = \frac{G}{1-[2\nu^2/(1-\nu)]} \tag{2.11}$$

$$\beta = \left(\frac{\phi_f}{\pi}\right)^{1/2} \tag{2.12}$$

Where E_1 is the composite modulus of elasticity in the fibre direction, E_2 is the composite modulus of elasticity in the transverse direction, G_1 is the composite shear modulus, ϕ_f is the fibre volume fraction and ν is the Poisson's ratio. Whilst this model is an approximation it is quoted by the author as "being consistent with the accuracy of the initial assumptions which are made when solving the micromechanics problems in composites and applying the results to practical composites". The principal

assumptions of the combined formulation are that both constituent materials obey Hooke's Law; the fibres are circular, uniform in shape and arranged in a prescribed array; there are no voids or other irregularities; both materials are homogeneous, isotropic and are firmly bonded together. These values can then be used to calculate ultrasonic velocity within the CFRP containing fibres and voids via material parameters obtained by Zimmer and Cost (1970). Using these elastic constants the ultrasonic compressive wave velocity (V_L) and the ultrasonic shear wave velocities (V_{T1} along the fibres and V_{T2} normal to the fibres) can be calculated thus:

$$C_{11}^{(c)} = \frac{E_1 E_2}{2E_1(1-\nu_2) - 4E_2\nu_1^2} + \frac{E_2}{2(1+\nu_2)} \tag{2.13}$$

$$C_{12}^{(c)} = \frac{E_1 E_2}{2E_1(1-\nu_2) - 4E_2\nu_1^2} - \frac{E_2}{2(1+\nu_2)} \tag{2.14}$$

$$C_{44}^{(c)} = G_1 \tag{2.15}$$

$$V_L = (C_{11}^{(c)} / \rho_c)^{1/2} \tag{2.16}$$

$$V_{T1} = (C_{44}^{(c)} / \rho_c)^{1/2} \tag{2.17}$$

$$V_{T2} = \left[(C_{11}^{(c)} - C_{12}^{(c)})/2\rho_c\right]^{1/2} \tag{2.18}$$

Where the subscript 1 denotes the fibre direction and the subscript 2 is transverse with respect to direction of fibres in the plane of the composite. The composite density ρ_c is calculated using the simple mixture rule:

$$\rho_c = \rho_f \phi_f + \rho(1-\phi_f) \tag{2.19}$$

Where:

$$\rho = \rho_o \frac{1-\phi_f - P_c}{1-\phi_f} \tag{2.20}$$

The void content for the composite ϕ_c is calculated from the void content ϕ_v:

$$\phi_c = \phi_v(1-\phi_f) \tag{2.21}$$

This model has the limitation that the entire composite structure is modelled as a homogenous mixture. The manufacturing process often leaves rich or void areas of fibres, resin and porosity. The model does provide an approximation to the effects of fibre volume fraction. The model works by considering the effects on bulk and shear modulus of void content, fibre reinforcement and the epoxy resin itself; it then considers two cases, isotropic and anisotropic fibres.

Using the model, simulations were conducted by Martin (1977) to find the effect of increasing fibre volume fraction on ultrasonic velocity. The results of the simulations are presented in figure 2.1, where V_L is the compression wave velocity normal to the fibre direction and V_{T1} and V_{T2} represent shear wave velocities normal and perpendicular to the direction of the fibres.

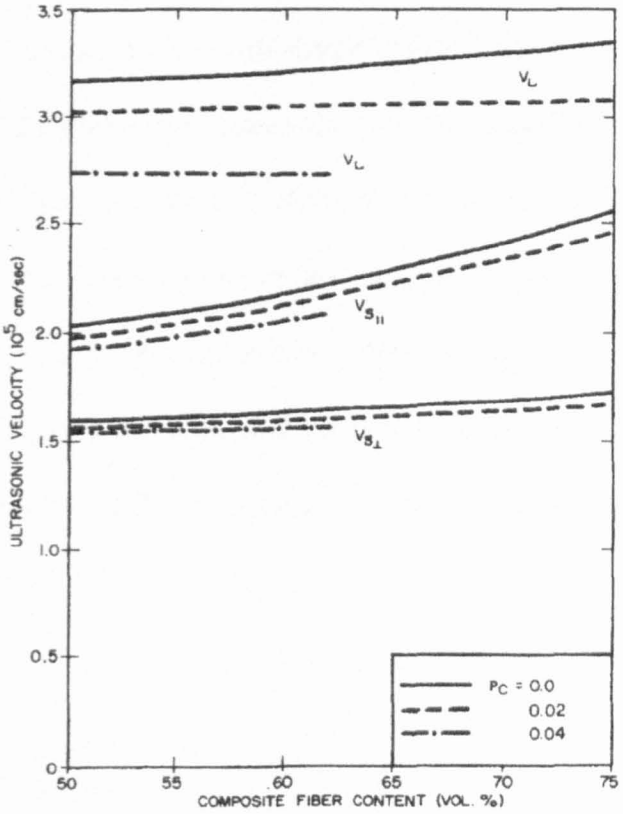

Figure 2.1 Ultrasonic velocity in a CFRP as a function of fibre content for several values of void content. (Reproduced from Martin (1977)).

Figure 2.1 shows the variation in ultrasonic velocity for the three principal wave modes V_L (compression waves), V_{SII} (shear waves along the fibre direction) and $V_{S\perp}$ (shear waves normal to the fibre direction). For both compression and shear waves an increase in ultrasonic velocity with increasing fibre volume fraction is predicted, a 1% decrease in ultrasonic velocity is shown for a drop in fibre volume fraction from 0.6 to 0.5. This compares well with experimentally measured values provided by Stone and Clarke (1975). Reynolds and Wilkinson (1978) also predicted an increase in ultrasonic velocity with increasing fibre volume fraction as part of a study to quantify the effects of porosity in CFRPs. The model used built upon that previously used by Martin; it has the same basic structure but uses a better method of computing the effective elastic

constants of the material using numerical integration as provided by Boucher (1976). Boucher provided evidence of the equivalence between this scheme and experimental data, and found good agreement between the two. This model requires several assumptions: Firstly, the concentration of the inclusions (porosity) must be relatively small, secondly the wavelength of the ultrasonic waves used must be larger than the dimensions of the inclusions but smaller than the specimen under investigation. Providing that these assumptions are met then the bulk and shear moduli (K^* and G^*) for an isotropic solid matrix (suffix 1) containing voids of concentration Δc (suffix 2) but no fibres are given by:

$$\frac{K^*-K_1}{K_2-K_1}=\Delta c\frac{K_1+(4/3)G_1}{K_2+(4/3)G_2} \tag{2.22}$$

$$\frac{G^*-G_1}{G_2-G_1}=\Delta c\frac{G_1+G_s}{G_2+G_s} \tag{2.23}$$

Where:

$$G_s=\frac{G_1(9K_1+8G_1)}{6(K_1+2G_1)} \tag{2.24}$$

The compressive wave velocity is then given by:

$$V^2=\frac{K^*+(4/3)G^*}{\rho} \tag{2.25}$$

The values for the bulk and shear moduli can then be obtained by stepwise numerical integration of the coupled equations 2.21 and 2.22, with a step size of $\Delta c/(1-c)$ substituting the results for K^* and G^* for K_1 and G_1 with each step. This takes into account the contribution from porosity in a CFRP. The effect of fibre volume fraction itself is not considered in these equations, but fortunately an analogous work considering the effect of fibre volume fraction exists (Hashin 1965). Hashin derived expressions for the plane strain bulk modulus k^* and the transverse shear modulus m^* for an isotropic matrix (suffix 1) containing a uniaxial array of fibres (suffix 2). From these expressions it is possible to calculate the effective moduli of the composite for small fibre volume concentrations Δc using the scheme provided by Boucher:

$$\frac{k^*-k_1}{k_2-k_1} = \Delta c \frac{k_1+m_1}{k_2+m_1} \tag{2.26}$$

$$\frac{m^*-m_1}{m_2-m_1} = \Delta c \frac{2m_1(k_1+m_1)}{(m_1+m_2)k_1+2m_1m_2} \tag{2.27}$$

Integrating numerically as previously with a step size of Δc/(1-c), the compressive wave velocity V_L can be obtained from:

$$V_L^2 = \frac{k^*+m^*}{\rho} \tag{2.28}$$

Using these equations Reynolds and Wilkinson were able to calculate values for ultrasonic velocity within CFRPs containing porosity up to 25% and fibre volume fractions of 40-70%. The ultrasonic waves were simulated in three different modes,

longitudinal waves normal to the direction of the fibres (V_L) and shear waves polarised parallel to and perpendicular to the fibre orientation (V_{T1} and V_{T2}).

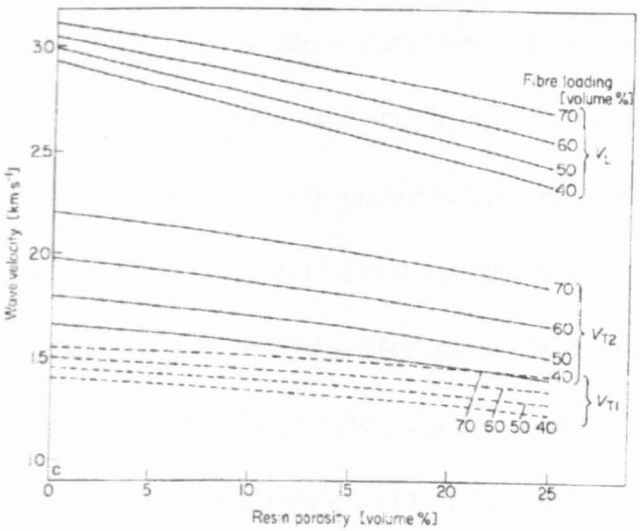

Figure 2.2 Variation in ultrasonic velocity with resin porosity and fibre volume fraction. (Reproduced from Reynolds and Wilkinson (1978)).

Figure 2.2 shows the effect of increasing porosity concentration on the ultrasonic wave velocity for the three principal wave modes V_L (compression waves), V_{T1} (shear waves perpendicular to the fibre direction) and V_{T2} (shear waves along the fibre direction). Figure 2.2 also shows the effect of increasing fibre volume fraction and predicts that as the fibre volume fraction increases the ultrasonic velocity within the CFRP also increases.

Kline (1986) used the expressions derived by Hashin to estimate the effective fibre volume fraction from an ultrasonic A-scan signal using estimates of ultrasonic velocity. Comparisons were made between experimentally determined fibre volume fraction and measurements taken by microscopy and determined using image analysis techniques. Kline found good agreement between ultrasonic and optical techniques with typically

2% or less measured difference. Kline found that for increasing levels of fibre volume fraction there was an increase in the ultrasonic velocity, as would be expected.

Kline (1990) determined the effective elastic constants of a composite laminate by making ultrasonic velocity measurements at multiple angles of incidence and interpreting the raw data using a wave propagation model. He found that by using a fixed transducer and varying the position of the receiving transducer multiple measurements of ultrasonic velocity and hence local material properties could be obtained. Stijnman (1994) also investigated the angular dependence of the velocity and amplitude of compression and shear waves in composite materials. The study focussed on a variety of glass and Kevlar fibre composites and did not include carbon fibre reinforced material. He found that by varying the angle of incidence of the interrogating waves the elastic properties of the composite could be estimated. An important outcome of this work was that the measured ultrasonic velocities could be very sensitive to incidence angle. This implied that experimental measurements should be as accurate and precise as possible, and that the formulation of propagation models should match the physics of the structure as closely as possible.

Williams et al (1980) measured the variation in compression and shear wave velocity and attenuation with respect to frequency in graphite-epoxy composite. The composite contained unidirectional fibres in an epoxy matrix; measurements were taken for a variety of transducers at directions perpendicular to the fibres and along the direction of the fibres. The frequency ranges investigated were 0.5-3 MHz for compression waves and 0.25-14 MHz for shear waves. The authors found that there was no variation in ultrasonic velocity for compression waves across the frequency band, although the

velocity did vary with the angle of interrogation. The attenuation of compression waves was found to vary as frequency squared as shown in figure 2.3.

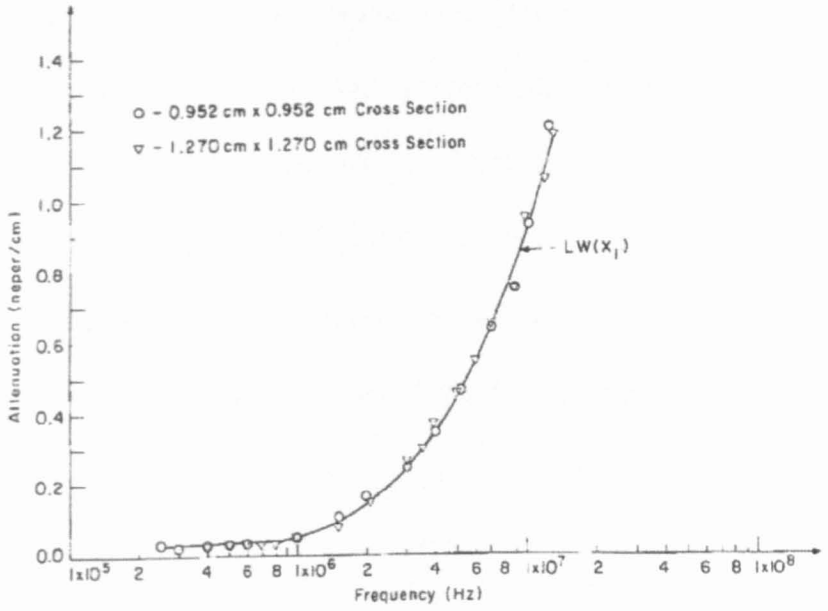

Figure 2.3 Variation in ultrasonic attenuation with frequency for normal incidence compression waves. (Reproduced from Williams et al (1980)).

The attenuation was also found to be dependent on the angle of the fibres relative to the angle of incidence of the interrogating waves. Similar results were observed for shear waves. The velocity and attenuation were found to be independent of the amplitude of the interrogating waves and hence the authors concluded that the combined composite could be described as a linear visco-elastic material.

Pelletier et al (1993) carried out a similar analysis on a composite formed of an alumina matrix reinforced with silicon carbide whiskers, showing that ultrasonic velocity increased as the whisker fraction volume increased.

Much of the scientific literature concerning the effects of fibre volume fraction considers the effect on shear and lamb waves and not compression waves which are the

basis of most NDE procedures and therefore the focus of this work. The effect of fibre volume fraction on ultrasonic compression waves was also studied by Kim and Park (1987). The effect on attenuation and wave velocity was considered for waves parallel and normal to fibre direction for a variety of fibre volume fractions in unidirectional CFRPs. The measurements were conducted in the frequency range of 1.84 to 11.9 MHz using the pulse-echo method; it was found that as fibre volume fraction increased ultrasonic attenuation decreased, and this effect was more noticeable when the direction of propagation was normal to the direction of the fibres, figure 2.4.

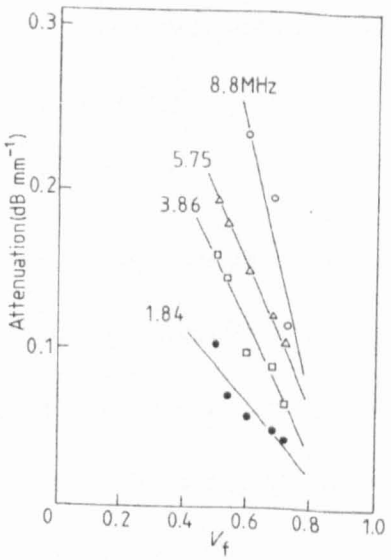

Figure 2.4 Attenuation of compression waves propagating along the fibre direction as a function of fibre volume fraction at various frequencies. (Reproduced from Kim and Park (1987)).

Similarly, for shear waves a decrease in ultrasonic attenuation was also noted, figure 2.5.

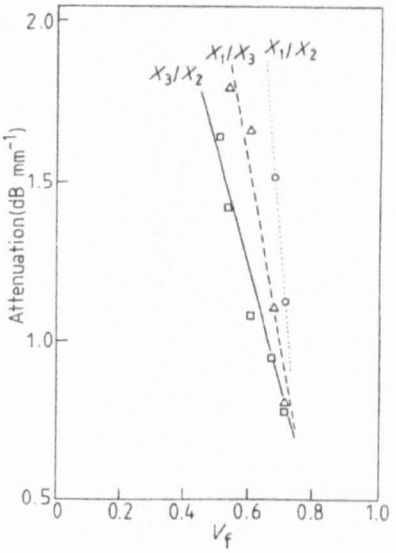

Figure 2.5 Attenuation of shear waves propagating in various modes at 1.84 MHz. (Reproduced from Kim and Park (1987)).

These effects were attributed to the fact that the majority of losses within the composite which caused attenuation were due to viscoelastic losses in the epoxy matrix rather than scattering caused by the fibres themselves. Hence as the fibre volume fraction increases the epoxy content reduces and so do the losses which cause attenuation. They make this conclusion since the losses in a fibrous composite may be written as:

$$\alpha = a - bV_f \tag{2.29}$$

Where $a = \alpha_s + \alpha_m$, $b = \alpha_m$, and α_m is the attenuation function related to wave mode and α_s is the attenuation function related to fibre volume fraction, frequency and wave mode. Since it had been previously shown by Bose and Mal (1973) that attenuation increased with fibre volume fraction it was shown that the coefficient a of the equation increased with increasing fibre volume fraction and that coefficient b was constant, being independent of fibre volume fraction for a given frequency and wave mode. Kim

and Park therefore concluded that coefficient *b* was dominant and that the losses were caused by viscoelastic losses in the matrix rather than scattering losses from the fibres. They also presented a consideration of the effects of fibre volume fraction with respect to ultrasonic velocity, showing that as fibre volume fraction increased, so too did ultrasonic wave velocity, although no explanation for this effect was offered. In addition it was found that the attenuation was higher at increasing frequencies for a given fibre volume fraction, and this was attributed to scattering losses as well as viscoelastic losses in the matrix. It was also noted that the attenuation decreased at a higher rate for higher frequencies as fibre volume fraction was increased.

A similar study was conducted using Lamb waves to assess the fibre volume fraction within a CFRP by Seale et al (1998). The velocity of Lamb waves was measured for composite samples with varying fibre volume fractions, and a model of Lamb wave propagation in CFRPs was presented which was similar to formulations presented by both Martin (1976) and Reynolds and Wilkinson (1978) – considering the composite as a model of mixtures to calculate effective elastic moduli and Poisson ratio. The model was based on estimates of the in-plane elastic properties of the CFRP. Experimentally it was found that as the fibre volume fraction was increased the Lamb wave velocity also increased, when and comparison with modelled values resulted in a good correlation.

Finally, a study was conducted using induced acoustic emission from within fibre reinforced plastics by Choi and Takahashi (1990). Obviously this work is of less interest in the context of this project, but it is of note that it was found that, as fibre volume fraction increased, a decrease in attenuation of the induced acoustic emission signals was observed.

2.2.2 Porosity

Martin (1977) also used his equations to model the effect on ultrasonic velocity of increasing levels of porosity. The formulation employed was valid for small concentrations of voids. He simulated the presence of 0 to 5% porosity for three fibre volume fractions, and the results were presented for the three principal wave modes as shown in figure 2.6.

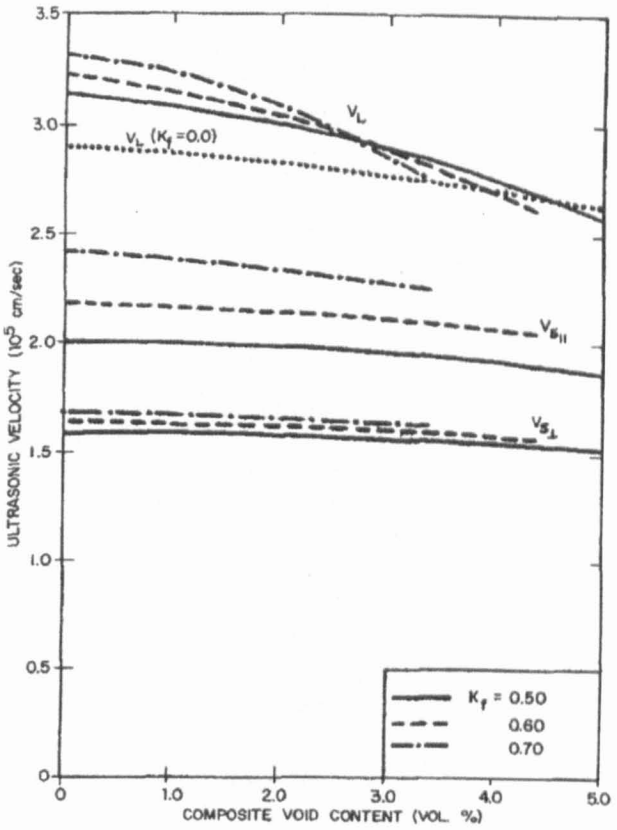

Figure 2.6 Variation in ultrasonic velocity with increasing levels of porosity. (Reproduced from Martin (1977)).

Figure 2.6 shows the variation in ultrasonic velocity with increasing porosity for three different wave modes V_L (compression waves), V_{SII} (shear waves perpendicular to the fibre direction) and V_S (shear waves along the fibre direction); as the void content

increases a decrease in ultrasonic velocity is predicted. For a fibre volume fraction of 0.6 the compression wave velocity decreases with the addition of 4% porosity by 20%. Although this seems like a large variation it should be noted that the use of a water couplant, as is common in the aerospace industry, may affect the measured velocity due to variations in couplant velocity caused by temperature change.

Reynolds and Wilkinson (1978) were able to simulate the effect of higher concentrations of voids and made similar observations to those of Martin, figure 2.7.

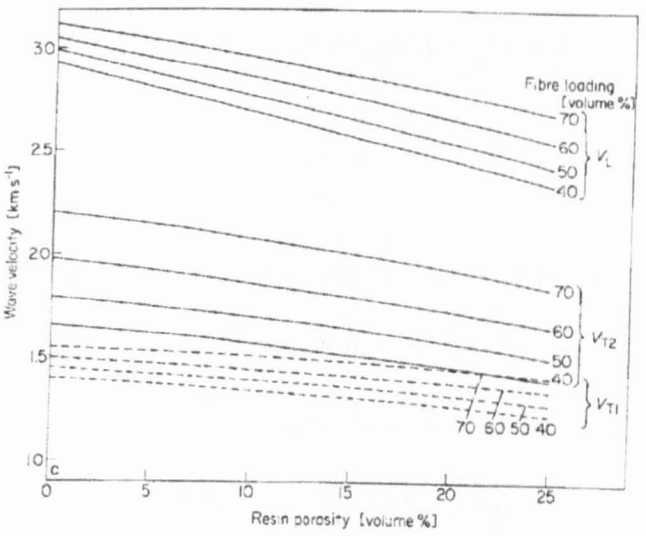

Figure 2.7 Variation in ultrasonic velocity with resin porosity and fibre volume fraction. (Reproduced from Reynolds and Wilkinson (1978)).

The figure shows the effect of increasing levels of porosity on the ultrasonic wave velocity for three different wave mode V_L (compression waves), V_{T1} (shear waves perpendicular to the fibre direction) and V_{T2} (shear waves along the fibre direction). Observation of the compression wave mode shows that the presence of 25% porosity by volume causes a decrease in ultrasonic velocity of 20%. This result seems to be in

disagreement with those shown previously by Martin (1977); however, Reynolds and Wilkinson measured porosity in the resin before addition to the mixture and Martin measured the resultant porosity in the entire structure. The results are in fact in good agreement.

Jeong and Hsu (1995) investigated the frequency dependence of the ultrasonic velocity in the presence of voids. The authors created a theoretical framework for calculation of the dispersion based upon a local form of Kramers-Kronig relations (see for example O'Donnell et al 1978) and made comparisons with experimental evidence. They found that the ultrasonic velocity decreased with increasing levels of porosity and the velocity dispersion increased. It was found that this effect was strongest in unidirectional composite.

Much of the literature concerning the detection of porosity within CFRPs has involved measurement of the ultrasonic attenuation brought about by porosity. The first such work in this area was conducted by Stone and Clarke (1975). Experimental samples were made with varying levels of porosity, by varying the pressure used during the cure cycle. Acid digestion was used to determine the porosity content of the panels and this was found to be in the range of 0.4 to 4%. The ultrasonic attenuation of the system was calculated using three pairs of transducers with centre frequencies of 2.5, 5 and 7 MHz using through transmission. The attenuation coefficient was calculated in $dBmm^{-1}$ and plotted against percentage porosity. A theoretical fit to the data was not presented, although attempts were made to fit to the data empirically. The best fit was found when a bilinear form was used as follows:

$$\alpha = a_1(f)V_v + b_1(f) \qquad V_v < 1.5\% \text{ porosity} \qquad \textbf{(2.30)}$$

$$\alpha = a_2(f)V_v + b_2(f) \qquad V_v > 1.5\% \text{ porosity} \qquad \textbf{(2.31)}$$

Where a_1, a_2, b_1 and b_2 are constant for a given frequency and V_v is the volume fraction of the porosity. The authors justified these two different equations based upon the assumption that the size and morphology of the voids varied with the volume fraction of porosity. For values of $V_v < 1.5\%$, the voids were found to be spherical and of diameters from 5 to 20 microns. For $V_v > 1.5\%$ the voids were found to be flattened, elongated and significantly larger. The authors make no comment on whether this phenomenon could be a result of the methods used to induce porosity or if it is an effect which would normally be expected during production. Further work was conducted by Jones and Stone (1976) to examine the use of attenuation data on differing fibre-resin systems with the same fibre volume fraction. The aim of this work was to produce calibration curves which could be used across a variety of composites and accurately determine the porosity content. The attenuation was measured at a 7 MHz centre frequency for a variety of void concentrations for the composite examined by Stone and Clarke as well as a new sample with the same fibre volume fraction. Later Jones and Stone (1976) confirmed these results in a different set of samples.

Further treatment of the results presented by Stone and Clarke was provided by Martin (1976). By making the assumption that the voids were spherical Martin aimed to provide a relationship between the ultrasonic attenuation and the void diameter. Martin found that the through-composite attenuation could be related to the cube of the void radius.

In contrast to this, work by Martin, Hsu and Nair (1987) produced a model, which by assuming elliptical cylindrical voids, aimed to relate the slope of the attenuation against frequency curve to the percentage void content. The authors found a good agreement between the porosity content estimated ultrasonically and the values measured destructively by acid digestion. The authors also noted that the presence of porosity had an effect on the centroid frequency of the received signal. It was found that the presence of 5% by volume porosity caused a decrease in the centroid frequency of approximately 50% when compared to the void free case.

Hale and Ashton (1988) produced a model for attenuation of ultrasonic compression waves propagating in fibre reinforced plastics containing small voids. The authors considered the model provided by Martin and made alterations to calculate the attenuation due to scattering for small spherical voids following the work of Ying and Truell (1956). The primary addition made to the model by the inclusion of expressions from Ying and Truell is to allow the inclusion of distributions of scatterers. The attenuation was predicted to increase linearly with increasing void volume fraction, and for low concentrations of voids this was found to be acceptable as shown in figure 2.8.

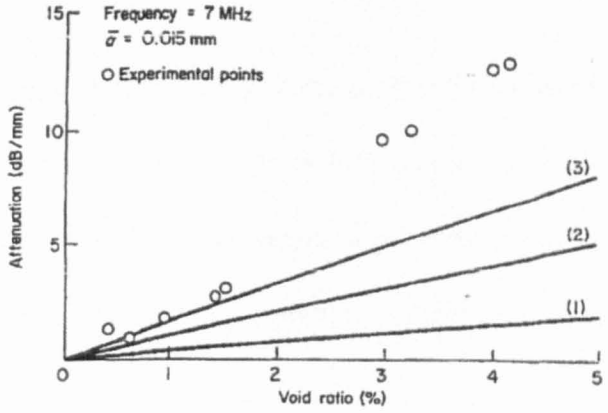

Figure 2.8 The effect on ultrasonic attenuation for a distribution of voids. (Reproduced from Hale and Ashton (1988)).

In the figure the lines (1), (2) and (3) represent a normal distribution of voids of radius 0-0.03mm, 0-0.1mm and 0-0.2mm respectively. The authors hypothesised that the discrepancy between modelled and experimental attenuation shown in figure 2.8 was due to the voids changing shape as the concentration increased, from spherical to disc type, as had been previously observed by Stone and Clarke. The authors modified the model to include disc shaped scatterers for void concentrations higher than 1.5%, and found a better match with experimental results as shown in figure 2.9.

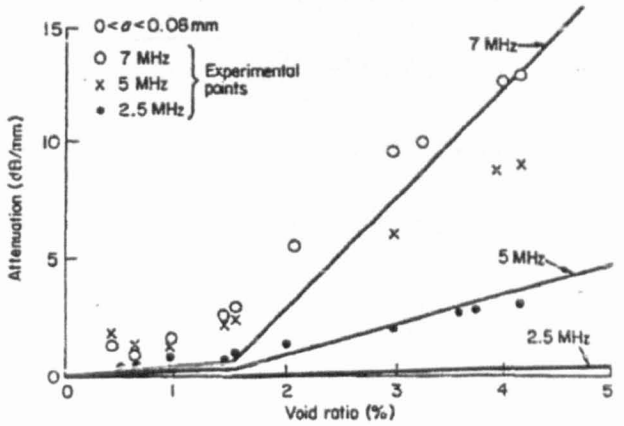

Figure 2.9 The effect on ultrasonic attenuation for disc shaped scatterers for increasing void concentrations. (Reproduced from Hale and Ashton (1988)).

Mouritz (2000) investigated the validity of the models proposed by Hale and Ashton. The effect of increasing void content from 0-30% on the ultrasonic attenuation coefficient of glass fibre reinforced composite was investigated. Similar experimental results were found to those obtained by previous authors as shown in figure 2.10.

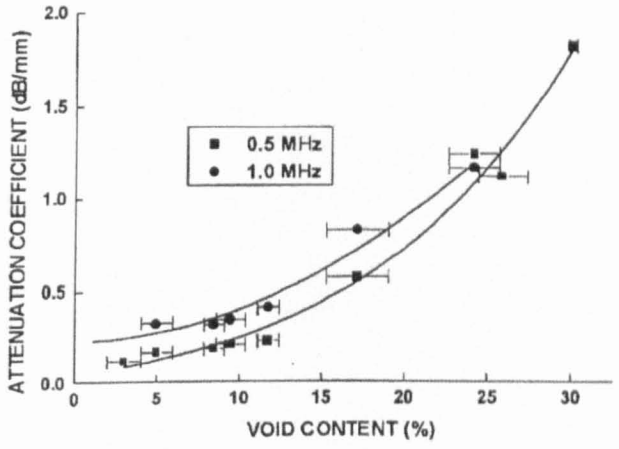

Figure 2.10 Variation in attenuation with void content. (Reproduced from Mouritz (2000)).

Mouritz found that for highly porous composites the model suggested by Martin and modified by Hale and Ashton was not an accurate representation of the observed attenuation. Mouritz found that below 10% void volume fraction the model was valid. The differences between modelled and experimental data were attributed to the scattering by the pores being non-Rayleigh like at high volume concentrations, the distribution of void sizes, and the scatterer morphology.

Daniel et al (1992) conducted a series of experiments on graphite-epoxy composite in pulse-echo and through transmission modes. Measurements of the variation in ultrasonic attenuation were taken with increasing levels of porosity. The author found

results similar to previous authors, and an increase in void content led to an increase in ultrasonic attenuation as shown in figure 2.11.

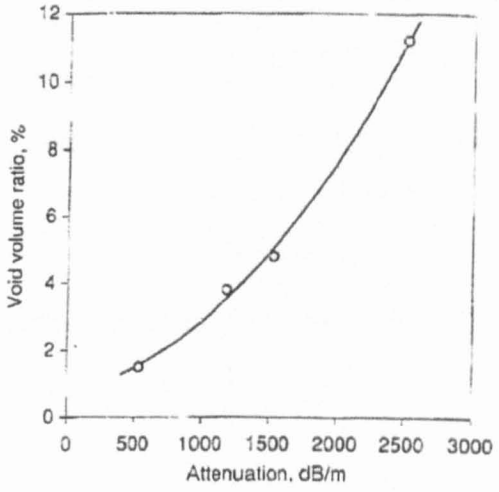

Figure 2.11 Variation in ultrasonic attenuation with increasing levels of void content at 5MHz. (Reproduced from Daniel et al (1992)).

In the figure the circles represent experimental values and the solid line represents a line of best fit to the data. The authors also considered the frequency dependence of the attenuation for different void contents. The material attenuation was found to increase with frequency in the range 3 – 8 MHz as shown in figure 2.12.

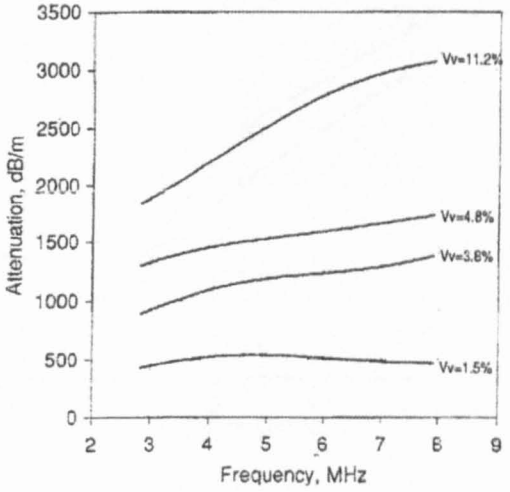

Figure 2.12 Variation of ultrasonic attenuation with increasing frequency. (Reproduced from Daniel et al (1992)).

In the figure *Vv* is the void volume fraction. Guo and Cawley (1994) examined the potential of using an attenuation measurement obtained from the back wall echo response rather than a through transmission or double through transmission technique. A back wall echo may be the only measurement method available when the component is in-service or when the geometry of the component prevents immersion. Comparisons were made between double through transmission techniques and back wall echo measurements for components in immersion. The results of attenuation measurement with increasing void content are shown in figure 2.13.

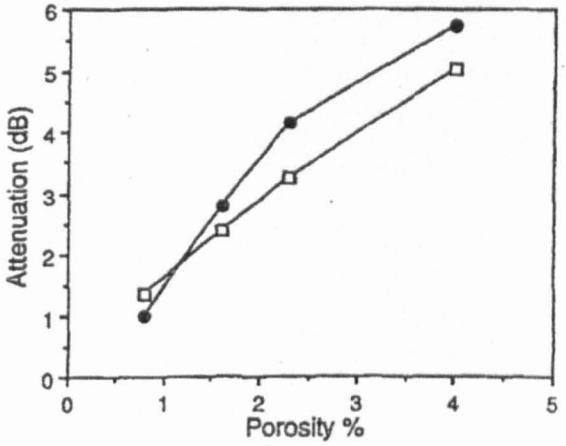

Figure 2.13 Effect of increasing void content on ultrasonic attenuation for double through transmission (square) and back wall echo (circle) measurements. (Reproduced from Guo and Cawley (1994)).

The authors concluded that the two techniques produced equivalent results. Investigation of a large number of test samples produced under many different conditions indicated that by careful control of the construction process the void content could be restricted to a maximum of 2% voids by volume.

The results published in the literature for the relationship between ultrasonic attenuation and void content are summarised in figure 2.14.

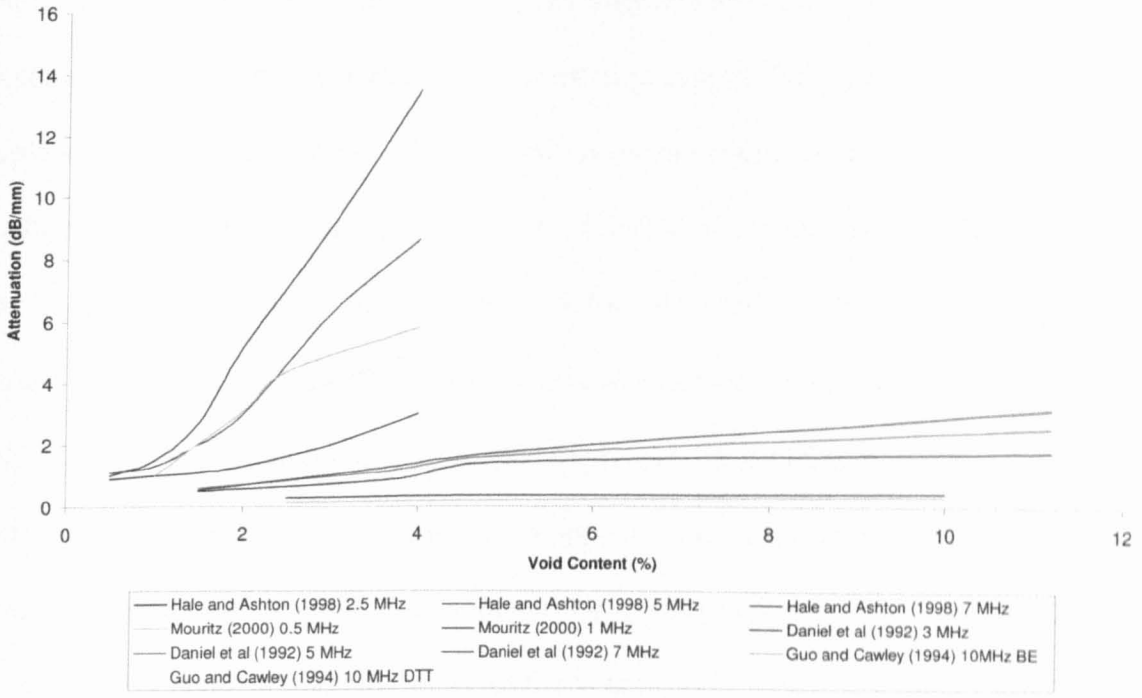

Figure 2.14 Effect of increasing void content on ultrasonic attenuation.

Figure 2.14 shows that although the results from the literature do not match exactly they do all show similar trends. The differences may be attributable to different composites being used with differing material properties such as fibre volume fraction. From this it may be concluded that: (i) the ultrasonic attenuation increases with increasing void content; (ii) the attenuation function is not linear with respect to void content; (iii) for comparable levels of void content the attenuation is greater at higher frequencies.

Given the reliability and repeatability of the results, measurement of through sample attenuation has been the favoured technique for production testing of composites in the aerospace industry. In recent times however, there has been a marked increase in the usage of composite structures to deliver cost savings and reduce weight. This potential for increased amounts of composite has led to a re-examination of the methods of testing which have traditionally been employed. Since this method was first proposed

there has been a marked increase in the capability and availability of computing systems, which has brought with it the potential to capture full waveform data. There have also been improvements which allow advanced data processing techniques (for example time-frequency analysis) to be conducted with a relatively small time penalty. Jeong and Hsu (1995) provided a framework for calculation of the ultrasonic attenuation based upon a local form of Kramers-Kronig relations (see for example O'Donnell et al 1978), and this formulation is investigated in greater detail in Chapter 3. However, the authors showed that the attenuation due to porosity was linear with frequency and the slope of this function increased with increasing levels of porosity. The function was also found to be dependent upon the shape of the voids.

Signal processing based techniques for assessing where in the depth of the composite porosity occurs have been proposed by Smith and Buoncristiani (1986) with later extensions to this method by Smith (1990). The method proposed involved conducting a Fourier deconvolution of the signal received from the pulse-echo analysis of the test subject with the transducer response. The resultant waveform was filtered and the analytic magnitude calculated, to provide the backscattered signal. This signal was found to have a peak where porosity was present, providing an indication of the depth of the porosity.

More recent work by Dominguez (2006) and Mascaro (2006) has investigated both the global (across the test sample) and local (within a gated part of the signal) attenuation effects due to porosity. Mascaro found that the attenuation versus frequency was linear and varied with the type of composite. For typical composite with unidirectional fibres the attenuation was found to vary from 0.16 to 0.22 $dBmm^{-1}MHz^{-1}$ dependent upon the

composite employed. Other authors have investigated the frequency dependence of attenuation in epoxy resin (see for example Rokhlin et al (1986), Kline (1984) and Challis et al (2000)) and found a linear relationship. A recent study by Challis et al (2009) demonstrated that the loss in cured epoxy resins was equivalent to an attenuation based linear dependence on frequency over 5 decades. The result from Mascaro implies that the attenuation in the epoxy resin dominates and that the attenuation from the fibres can be neglected. The attenuation in a composite layer consisting of resin and fibres can be approximated using simple mixture rules (Martin (1976)), and since the loss in the fibres is much less than in the resin, these rules would lead to attenuation being a linear function of frequency in the resin/fibre mix. Mascaro conducted investigations to determine the effect of variation in void volume fraction, void size and void morphology. He found that as the void volume fraction increased the attenuation increased. This increase was found to increase with increasing frequency as shown in figure 2.15.

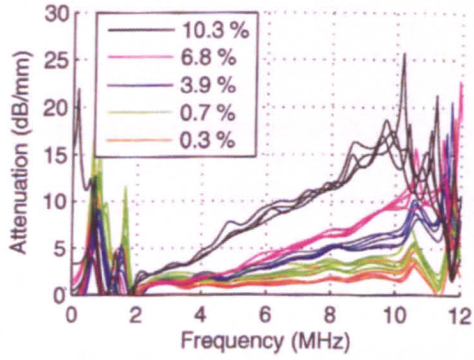

Figure 2.15 Ultrasonic attenuation for different porosity levels for a unidirectional composite. (Reproduced from Mascaro (2006)).

The signals show a large variation for values below 2 MHz and above 10 MHz; these fluctuations are due to conducting the attenuation calculation outside of the bandwidth

of the transducer where the signal to noise ratio is poor. For cylindrical scatterers Mascaro found that the ratio of the height of the cylinder (a) to the width of the scatterer (b) was important in determining the attenuation due to the scatterers. As the scatterer size increased so too did the attenuation. The results of the variation in these two variables are shown in figure 2.16.

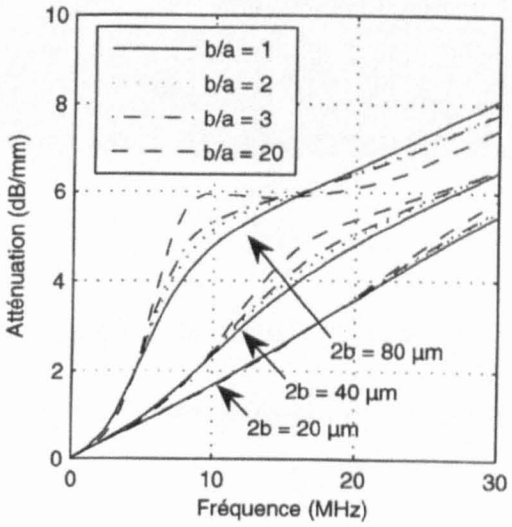

Figure 2.16 Variation in ultrasonic attenuation due to scatterer size and shape. (Reproduced from Mascaro (2006)).

In the figure, the variable a represents the minor axis of the ellipsoidal scatterer and b represents the major axis of the scatterer. Mascaro also investigated methods designed to locate porosity in three dimensions, using a system to analyse the spectral content of the received signal with time. The rationale behind this method is that the uniform nature of the composite structure should provide resonances (due to inter-ply reverberations) which should be constant, unless the resonance is distrupted by the presence of a defect such as porosity. Results of the time-frequency analysis for unflawed and defect containing composite are shown in figure 2.17.

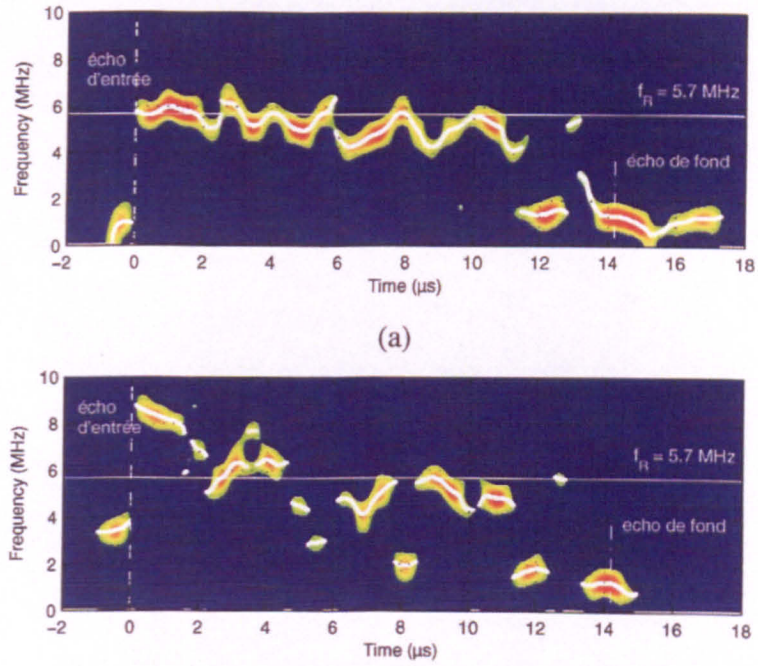

Figure 2.17 Time-frequency analysis for unflawed composite (top) and composite containing porosity in the central 8 plies (bottom). (Reproduced from Mascaro (2006)).

Observation of the time-frequency analysis reveals that in the presence of porosity the frequency response shifts to a lower frequency due to the change in material properties. Analysis was also conducted for the same sample but investigating the amplitude of the reflected signal. It has long been observed that in the presence of porosity there is an increase in the locally reflected energy. By application of a Hilbert transform to the reflected signal Mascaro aimed to provide a measure of this increase in reflection as shown in figure 2.18.

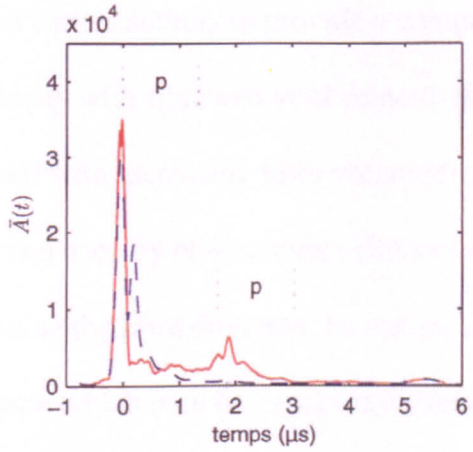

Figure 2.18 Measures of energy reflected from the composite specimen calculated using the Hilbert transform for composite containing porosity near the front surface (blue line), and composite containing porosity near the centre (red line). (Reproduced from Mascaro (2006)).

From figure 2.18 we can see that there is an increase in the reflected energy for porous composite; Mascaro found that as the level of the porosity present was increased the magnitude of the reflected energy increased. The regions highlighted by "*p*" are the regions where porosity is present.

These results presented have shown that the presence of porosity has a measurable effect on the attenuation, and that this effect is detectable locally. The recent developments in processing power and availability have led to the very real possibility that 3-D detection and characterisation of porosity may now be achievable.

2.3 Conclusions

This chapter has provided an overview of the world experience of the use of ultrasound for the detection of fibre volume fraction changes and the presence of porosity. Martin

(1977) built on the work of earlier authors to provide a comprehensive model of the variation of ultrasonic velocity with fibre and void content. His work showed that the ultrasonic velocity increased with increasing fibre volume fraction. Velocity measurements have also been used by other authors (for example Kline (1990) and Stijnman (1994)) to determine the fibre direction. However, the measured velocity change is within the variation which may be expected for temperature changes in the water coupling. Using velocity measurements to calculate fibre volume fraction is problematic for this reason.

Williams et al (1980) investigated the frequency dependence of the ultrasonic attenuation for unflawed composite, and found that it varied as frequency squared. The variation in attenuation with fibre content was later investigated by Kim and Park (1987) who found a small decrease in attenuation with increasing fibre content. These measurements provide only a global indication of the level of fibre content and are not able to provide a localised measure. Global changes in fibre volume fraction are of interest if a layer of fibres has been removed completely, however there may also be structural implications for a local increase in fibre volume fraction (from, for example, a folded ply) and these methods would have difficulty detecting such local changes.

Martin (1977) also investigated the dependence of velocity on void content. He found that there was a 20% decrease in velocity for compression waves when 5% voids were added across the composite structure. Reynolds and Wilkinson (1978) found similar observations. Both these methods however, can be used to give a global measure of porosity but are not able to detect localised changes, and as such these methods are of no use for the development of a system to monitor porosity in 3-D.

Traditionally the favoured method of detection and quantification of porosity within CFRPs has been based upon through sample ultrasonic attenuation methods, led by the research work conducted by Jones and Clarke (1975) and carried on by others. Rapidly this method spread to become the industry standard. For calibration, reference blocks were constructed with known levels of porosity and comparisons were made between the attenuation in these blocks and the sample under investigation. Although these methods have proved to be robust, giving a whole structure indication of the void content, recent developments in this field have led to the potential for better characterisation. The non destructive evaluation techniques already in place to test for porosity look for an increase in through-thickness attenuation for a CFRP, but this increase in attenuation could potentially be affected by an increase in fibre volume fraction which would lead to the two effects being offset and no change being observed.

Methods developed by Smith and Buoncristiani (1986), Smith (1990), Dominguez (2006) and Mascaro (2006) worked to analyse the full waveform received from the composite structure. Increased computing power and data capture equipment have meant that this kind of data analysis is now possible in a production setting. Indeed in many industries the equipment in use has this capability but the operators use the equipment with this functionality switched off. Location of regions of voids in three dimensions now seems possible, however, the methods for detection and classification are as yet immature. There is a need for an examination of possible techniques for better material characterisation, and so the focus of this thesis is to locate and quantify porosity within three dimensions.

Chapter 3 examines the development of a model to examine the effect that porosity has on ultrasonic attenuation via scattering of incident wave energy. This model is necessary to allow the effect of different quantities and morphologies of porosity to be determined so that the performance of any methods developed can be examined.

Chapter 3

Development of Scattering Models of Porosity

3.1 Introduction

The model for calculating attenuation due to multiple scatterers currently in use at the University of Nottingham is based upon the work of Epstein and Carhart (1953), Allegra and Hawley (1972), and is named ECAH in recognition of this fact. It does, however, also include the formulation of Ying and Truell (1956). The actual computer code used for evaluation of these models is a combination of the three, the equivalence of which was demonstrated by Challis et al (1998). This chapter will detail the methodology employed in making this assumption as well as demonstrating that, through recent alterations, this combined model has been adapted to simulate the scattering due to gaseous inclusions which may be cylindrical after Nair et al (1989), as well as spherical. Also detailed is the work of Adler et al (1986) on the applications of scattering models for quantifying porosity in aluminium castings; further work in this area by Ghaffari et al (2004) and its implications in respect of quantifying porosity in CFRPs is reviewed. A comparison between the results of these models and those of the ECAH model used at the University of Nottingham is presented. Finally the output of the ECAH model is examined and the potential applications for modelling within this project are discussed.

3.2 Physical Properties Determining Scattering from a Particle

In order to allow discussion of the various models for scattering from a distribution of particles it is first necessary to consider the behaviour of a single suspended particle to an incident compression wave. It is useful to examine the physical phenomena which are likely to influence reflection, refraction and continued propagation of the wave after it has interacted with the scatterer. These physical phenomena result from the scattering particle having different physical properties from the surrounding medium, that is, the continuous phase.

The first such phenomenon is that of material substitution; that is the effect of having inclusions of different attenuation and phase velocities in the medium. In order to take account of these differences it is necessary to take the weighted average of the attenuation and phase velocity in the two phases, taking account of the diffraction effects at the particle boundary and the mismatch in characteristic acoustic impedance at the boundary between the particles and the continuous phase.

The differences in compressibility between the inclusions and the continuous phase surrounding them has an effect on the phase shift and the attenuation caused by interactions between the propagating wave and the inclusions. If the particle is more or less compressible than the surrounding medium then it will contract by a greater or smaller volume than that medium in response to the pressure fluctuations in the wave. This differential expansion/contraction causes the particle to act as a source of radiation – at the same frequency as that of the incident wave. If the particle is small compared to the wavelength and spherical the particle will act as a monopole source.

Thermal contrasts between the particles and the surrounding medium, resulting from differences in thermal conductivity, specific heat capacity and thermal expansion coefficient result in a similar effect. In this case a monopole acoustic wave pattern results from differential expansion of the particle with respect to the surrounding medium. If the particle and the continuous phase heat and cool at different rates, causing heat flux between the two, this behaves as a monopole source of thermal waves which decay rapidly with distance away from the particle.

There exists the potential for further loss of amplitude and phase changes if the densities differ greatly between the particle and the continuous phase. Cyclic pressure gradient variations in the local pressure gradient, because of differences in inertia between particles and the surrounding medium, result in the particle oscillating with respect to the continuous phase. This causes loss of amplitude and phase due to viscous effects; these changes are modelled as shear forces which die rapidly with distance from the particle. The reaction of the continuous phase to this movement causes re-radiation of acoustic energy in a dipole pattern if the particle is small with respect to the incident wavelength.

If the particles under examination are relatively large with respect to the wavelength of the incident compression wave then there is a possibility that the particles will resonate in several different modes. The number and form of these different vibration modes will depend on both the shape and physical properties of the particle. These vibrations are likely to result in additional losses in ultrasonic energy within the medium. The particles themselves are likely to reradiate sound in multipole patterns due to the many vibration

modes. The vibrations will also cause a loss in energy from fluid flows around the boundary of the particle. Finally the vibrations will cause losses in energy due to friction losses inside the particle.

In the case of porosity, material substitution and differential compressibility are the phenomena that dominate. This is because of the large difference in material properties between the air inclusions and the fibre/resin mixture.

3.3 Construction of a Mathematical Model of Scattering

3.3.1 Epstein and Carhart Formulation

By consideration of the physical phenomena governing the response of a scatterer to an incident compression wave it is possible to construct a model capable of estimating the attenuation that would be caused by a layer of scatterers. From the behaviour described in section 3.2 we would expect the particle to react to the incident compression by converting some of the energy to thermal waves, some to shear waves and finally some scattered compression wave energy as shown in figure 3.1.

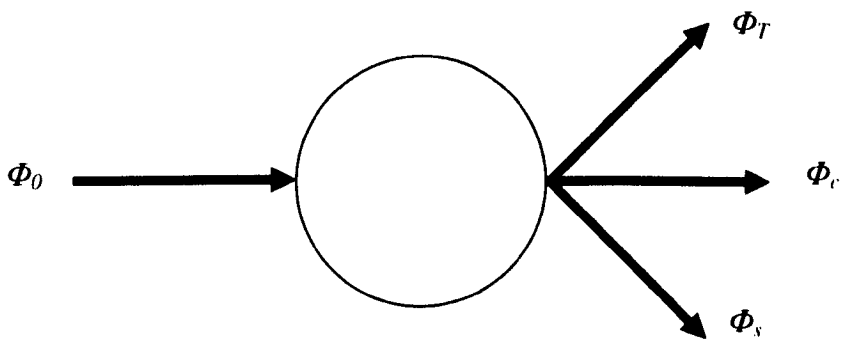

Figure 3.1 Reaction of a particle to an incident compression wave.

In figure 3.1 ϕ_c and ϕ_T are scalar potentials representing compression and thermal disturbances, and ϕ_s is the scalar component of the original vector potential which represents shear motions.

Initial work in this area was conducted by Epstein and Carhart (1953) who assumed that liquid particles were suspended in a liquid surrounding medium; these particles were considered to be elastic and free to move in the surrounding fluid. The particles were smaller than the compression wavelength and randomly distributed throughout the surrounding medium. The distance between the particles was much greater than the wavelengths of the viscous and thermal evanescent modes.

Epstein and Carhart began by deriving wave equations for compression, shear and thermal waves which could exist in both the scattering particles included and the surrounding medium. Given these expressions it was possible to describe a plane compression wave incident on a suspended particle in terms of the sum of spherical harmonics of the partial velocity potentials.

$$\phi_i = \sum_{n=0}^{\infty} i^n (2n+1) j_n(k_c r) P_n(\cos\theta) \qquad \textbf{(3.1)}$$

Where $j_n(k_c r)$ is a spherical Bessel function, k_c is the compression wave number and P_n is a Legendre polynomial. r is the distance from the centre of the particle and θ is the angle with respect to the axis of propagation of the incident wave. Similarly it is possible to write equations for the compression, shear and thermal waves reflected away from the particle:

$$\phi_c = \sum_{n=0}^{\infty} i^n (2n+1) A_n h_n (k_c r) P_n (\cos\theta) \tag{3.2}$$

$$\phi_s = \sum_{n=0}^{\infty} i^n (2n+1) C_n h_n (k_s r) P_n^1 (\cos\theta) \tag{3.3}$$

$$\phi_T = \sum_{n=0}^{\infty} i^n (2n+1) B_n h_n (k_T r) P_n (\cos\theta) \tag{3.4}$$

Where A_n, B_n and C_n are partial wave amplitudes, h_n is a spherical Hankel function. The equations for the compression, shear and thermal waves refracted into the particle are as follows:

$$\phi_c' = \sum_{n=0}^{\infty} i^n (2n+1) A_n' j_n (k_c' r) P_n (\cos\theta) \tag{3.5}$$

$$\phi_s' = \sum_{n=0}^{\infty} i^n (2n+1) C_n' j_n (k_s' r) P_n (\cos\theta) \tag{3.6}$$

$$\phi_T' = \sum_{n=0}^{\infty} i^n (2n+1) B_n' j_n (k_T' r) P_n (\cos\theta) \tag{3.7}$$

To calculate an effective wavenumber for the two different phases in the medium it is necessary to calculate the partial wave amplitudes A_n. To achieve this boundary conditions are applied at the particle surface as follows; that the velocity component is conserved both normal and tangential to the direction of travel, that the stress component is conserved both normal and tangential to the direction of travel and finally that temperature and heat flux is conserved within the system. Applying these conditions results in a matrix equation relating the unknown partial amplitudes to the incident compression wave.

$$[\mathrm{M}]_{EC}\begin{bmatrix} A_n \\ C_n \\ A_n' \\ C_n' \\ B_n \\ B_n' \end{bmatrix} = -\begin{bmatrix} a_c j_n'(a_c) \\ j_n(a_c) \\ \eta[a_s^2 j_n(a_c) - 2a_c^2 j_n''(a_c)] \\ \eta[a_c j_n'(a_c) - j_n(a_c)] \\ g j_n(a_c) \\ \kappa g a_c j_n'(a_c) \end{bmatrix} \tag{3.8}$$

Where a_c and a_s are the products of the particle radius R multiplied by the compression or shear wavenumber respectively, g is a thermal term, κ is the thermal conductivity and $[\mathrm{M}]_{EC}$ is a matrix as shown in Appendix A. A_n, B_n and C_n are the partial wave amplitudes outside the particle; A_n', B_n' and C_n' are the partial wave amplitudes within the particle. The coefficient G from the formulation for $[\mathrm{M}]_{EC}$ (see Appendix A) is defined as follows:

$$G = -\frac{\rho C_p}{\beta_T \kappa} \tag{3.9}$$

Where β_T is the coefficient of volume expansion. By developing explicit solutions for the A_0 and A_1 terms in the long wavelength limit, neglecting terms higher than second order of compression wavenumber an expression for the attenuation coefficient:

$$\alpha_1 = 4\pi N k_c^{-2} \,\mathrm{Re}(A_0 + 3A_1) \tag{3.10}$$

Where N is the dispersed particle number density. A_0 depends on heat conduction since transverse wave potentials do not enter the particle boundary for $n = 0$. A_1 incorporates

the viscous component of the attenuation and corresponds to an earlier result obtained by Epstein (1941).

3.3.2 Allegra and Hawley Formulation

Further developments of the model devised by Epstein and Carhart were made by Allegra and Hawley (1972), these modifications were necessary to allow the inclusion of elastic particles which could be solid. For solids the wave potentials were interpreted as displacement potentials; for liquid particles Epstein and Carhart had allowed the shear viscosity to tend to infinity, while using a fluid stress tensor in the remainder of their derivations. In this formulation the shear waves are no longer simply viscous.

As in Epstein and Carhart a solution was derived for the three wave types at the particle boundary, by application of continuity of normal and tangential velocity, normal and tangential stress, temperature and heat flux. Similarly a system of six equations was obtained.

$$[\mathrm{M}]_{AH}\begin{bmatrix} A_n \\ C_n \\ A_n' \\ C_n' \\ B_n \\ B_n' \end{bmatrix} = -\begin{bmatrix} a_c j_n'(a_c) \\ j_n(a_c) \\ \eta\left[\left(a_s^2 - 2a_c^2\right) j_n(a_c) - 2a_c^2 j_n''(a_c)\right] \\ \eta\left[a_c j_n'(a_c) - j_n(a_c)\right] \\ b_c j_n(a_c) \\ \kappa a_c b_c j_n'(a_c) \end{bmatrix} \tag{3.11}$$

Where $[\mathrm{M}]_{AH}$ is a matrix as shown in Appendix A. The formulation provided by Allegra and Hawley offers greater generality of solution by making fewer assumptions than the formulation of Epstein and Carhart.

3.3.3 Ying and Truell Formulation

A related model of scattering was provided by Ying and Truell who derived a model for spherical elastic solids in an elastic continuous phase.

The compression and shear waves were described using displacement potentials; at the boundary to the particle assumptions were made to preserve normal and tangential displacement and normal and tangential stress. Application of these boundary conditions led to a system of equations which was similar in structure to that obtained previously:

$$[\mathrm{M}]_{YT}\begin{bmatrix} A_n \\ C_n \\ A_n' \\ C_n' \end{bmatrix} = \frac{(-i)^{n-1}}{k_c}(2n+1)\times\begin{bmatrix} a_c j_{n+1}(a_c) \\ j_n(a_c) \\ \mu\left[a_s^2 j_n(a_c) - 2(n+2)a_c j_{n+1}(a_c)\right] \\ \mu\left[(n-1)j_n(a_c) - a_c j_{n+1}(a_c)\right] \end{bmatrix} \tag{3.12}$$

Where $[\mathrm{M}]_{YT}$ is a matrix as shown in Appendix A.

3.3.4 Combined Formulation

The similarity of these formulations provided the possibility that an equivalent solution between these three distinct solutions might exist; the existence of such a solution would provide a model of scattering which could be used in a variety of situations. The desirability of such an over-arching solution led to the development of a combined formulation by Challis et al (1998).

Similarities were observed between the two formulations of Epstein and Carhart and Allegra and Hawley and the equivalence of the two models was demonstrated by making modifications to the matrices $[M]_{EC}$ and $[M]_{AH}$, leading to a revised matrix for the Allegra and Hawley formulation $[M]_{AH1}$ which is contained in Appendix A. Challis et al demonstrated the equivalence of $[M]_{AH1}$ and $[M]_{EC}$ by comparing the individual terms of the each of the respective matrices.

In a similar manner comparisons were made between the formulations of Allegra and Hawley and those provided by Ying and Truell. Modifications were made to the matrix $[M]_{AH1}$ to remove the thermal terms forming a new matrix $[M]_{AH2}$, this was necessary to allow equivalence between the two models to be demonstrated.

The two systems of equations were shown to be equivalent apart from the common factors, $-i\omega$, which arose from the definition of A_n and B_n as velocity potentials in the Allegra and Hawley formulation, as distinct from the displacement potentials used throughout the derivation provided by Ying and Truell. The Allegra and Hawley equations will provide the A_n, which are the same as those expected from the theory of Epstein and Carhart. The removal of the thermal terms, appropriate scaling and choice of elastic constants in the Allegra and Hawley formulation also yielded the A_n which was expected from the Ying and Truell formulation.

This equivalent formulation can be used to model the frequency dependent attenuation due to scattering from porosity by choice of appropriate physical properties. An

example of the frequency dependent attenuation obtained from this formulation for various percentages of porosity in epoxy resin are shown in figure 3.2.

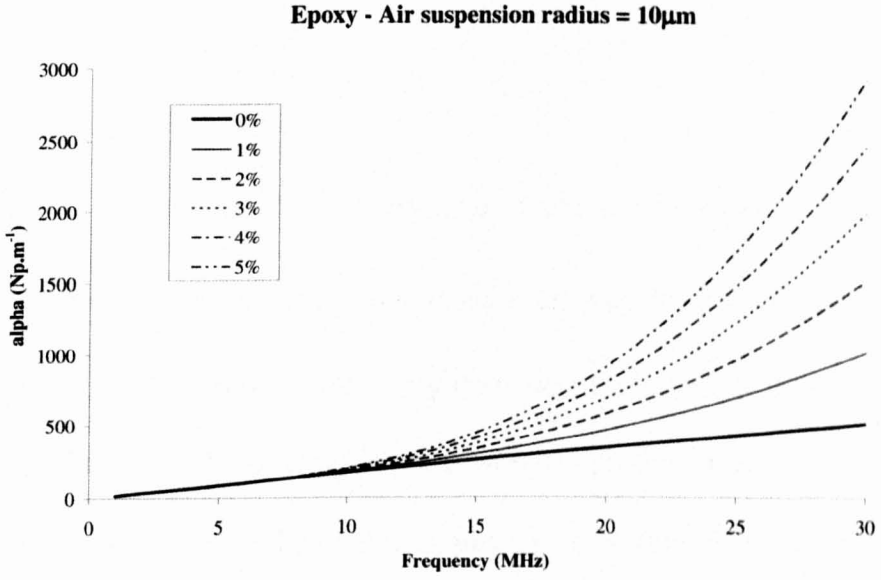

Figure 3.2 Frequency dependent attenuation for a suspension of porosity in epoxy resin obtained from the ECAH model.

Later, further consideration will be given to the attenuation due to porosity in mixtures of epoxy resin and carbon fibres in chapter 4.

3.4 Alternative Models of Scattering

Alternative methods exist to estimate the scattering due to porosity. One such method with applications to this work is that developed by Adler et al (1986). Considerations were made of microscopic gas porosity within aluminium castings. Approximations were made to the amount of energy scattered by dilute porosity (up to 6%) uniformly dispersed in an isotropic elastic space, by making a link between the cross-section of the

scatterers and the frequency dependent attenuation. Attenuation in this case is measured as a function of the longitudinal wave vector k, which is defined as:

$$k = \frac{2\pi f}{v_L} \tag{3.13}$$

Adler defines two regions, $ka_p < 1$ where a_p is the scatterer radius, is the long wavelength region, and $ka_p > 1$ which is the short wavelength region. In the long wavelength limit the sample is relatively transparent to ultrasound, this is a consequence of the power scattered by individual pores which is proportional to k^4. At higher frequencies where $ka_p > 1$ the scattering process is described by both ray concepts and the cross-section of the flaw; the attenuation, reflection and transmission coefficients become more independent of frequency and hence the material becomes more opaque to ultrasound.

Adler et al cite the following equation from Evans et al (1978) for attenuation in porous media:

$$\alpha(k) = \frac{1}{2} n\gamma(k) \tag{3.14}$$

Where n is the number density of pores and $\gamma(k)$ is the cross section of the scatterers. Further investigations of this equation were made by Gubernatis and Domany (1984) who found that the formulations provided by Evans et al accurately described the attenuation due to porosity and that the attenuation weakly depended upon the distribution of pore radii.

In the long wavelength region the cross section $\gamma(k)$ was expressed as:

$$\gamma(k) = 2\pi a_p^2 \Gamma(ka_p) \tag{3.15}$$

Where $\Gamma(ka_p)$ is the reduced cross section, in the long wavelength region, this function was described via:

$$\Gamma(ka_p) = \beta(\eta) k^4 a_p^4 \tag{3.16}$$

Where η is the ratio of shear to longitudinal velocities ($\eta = v_s / v_L$) and $\beta(\eta)$ is a known function as shown by Ying and Truell (1956) to be:

$$\beta(\eta) = \frac{4}{3} + 40\frac{2+3\eta^5}{\left[4-9\eta^2\right]^2} - \frac{3}{2}\eta^2 + \frac{2}{3}\eta^3 + \frac{9}{16}\eta^4 \tag{3.17}$$

By using the expression $\Gamma(ka_p)$ we can substitute into equation 3.14 to give the expression:

$$\alpha(k) = \frac{3}{4}\left(\frac{c}{a_p}\right)\Gamma(ka_p) \tag{3.18}$$

Where,

$$c = n\left(\frac{4\pi a_p^3}{3}\right) \tag{3.19}$$

In the short wavelength region the cross section $\gamma(k)$ was expressed as:

$$\gamma(k) = 2\pi a_p^2 \tag{3.20}$$

In this region the ray concepts may be applied and hence the cross-section is related to the geometric cross-section. Adler et al assumed that all rays which strike the scatterer were scattered, providing a reflection of the incident sound and a "shadow" where no sound is forward scattered, this gives the factor of 2 present in equation 3.20. The geometric cross section $\Gamma(ka_p)$ approached unity as $ka_p \to \infty$, and as such did not feature in equation 3.20. The attenuation due to scatterers in the short wavelength limit was thus shown to be:

$$\alpha(ka_p) = \frac{3}{4}\left(\frac{c}{a_p}\right) \tag{3.21}$$

where,

$$c = n\left(\frac{4\pi a_p^3}{3}\right) \tag{3.22}$$

Although equations had been developed for both the long and short wavelength regions by Adler et al, the interaction between the two regions was not defined, it was necessary

therefore to define the attenuation in the region between the long and short wavelength regions.

Work was conducted by Robert Smith (2008) to examine the relationship in the transition region between the long and short wavelength limits. Smith started the transition when $ka < 0.7$, and a ratio of $(0.7/ka)^3$ was used to match the graphs of scattering cross-section generated by Adler. The relationship was defined thus for $ka > 0.7$:

$$\alpha(k) = \frac{3c}{4a_p}\left[\left(\frac{0.7}{ka_p}\right)^3 \beta(0.7)^4 + \left[1 - \left(\frac{0.7}{ka_p}\right)^3\right]\right] \tag{3.23}$$

Comparisons between the attenuation curves generated using this formulation and the original results for reduced cross-section produced by Adler were conducted by Smith and good agreement was found.

To test the equivalence between the method described by Adler and ECAH, comparisons were made as shown in figure 3.3.

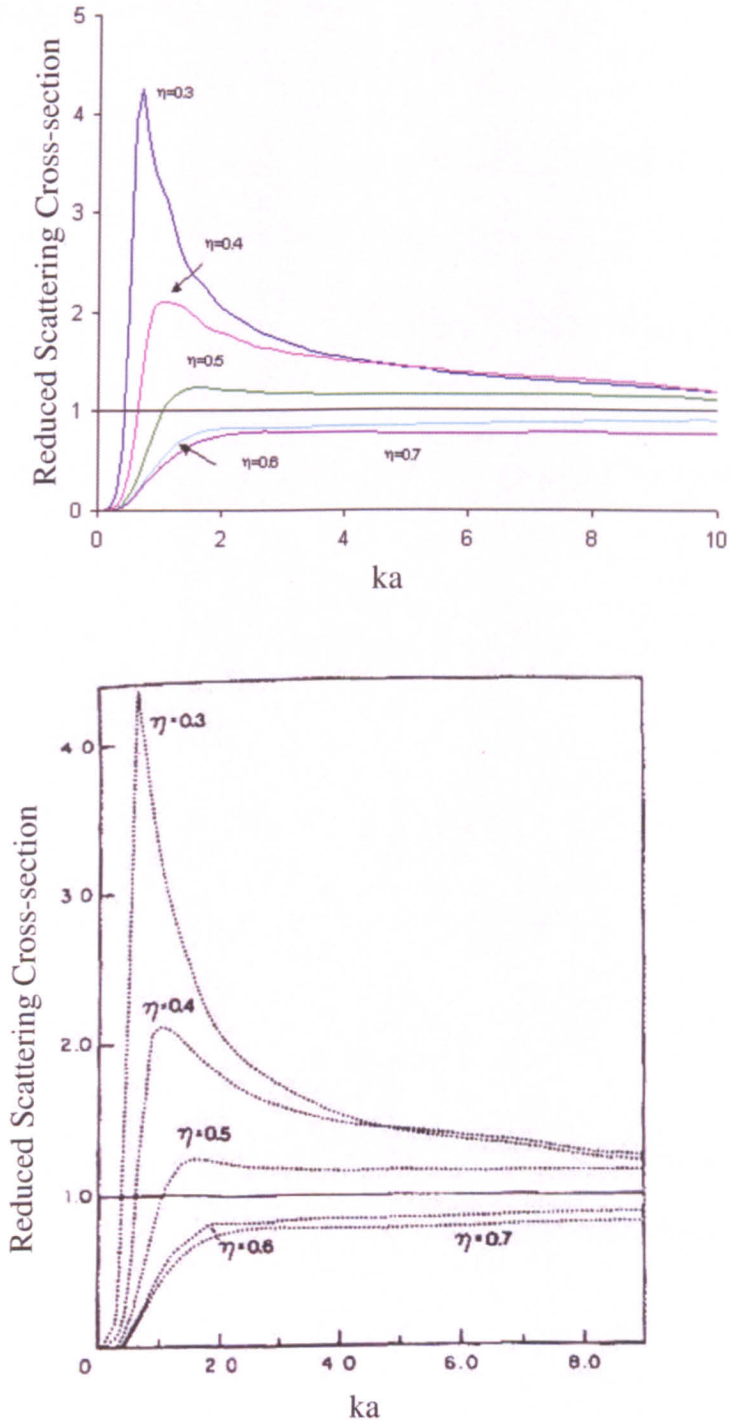

Figure 3.3 Comparison between model outputs of the ECAH scattering model produced at the University of Nottingham (top) and Adler et al (1986) (bottom) for various values of η.

Figure 3.3 shows that there is good agreement between the modelled output given by ECAH and that originally shown by Adler.

Application of this method for comparison with experimental data for porosity in aluminium castings was then undertaken by Adler. By removing the scattering due to the grain structure of the aluminium it was found that a good match could be made between the experimentally determined frequency dependent attenuation and that obtained from modelling. An example of the comparisons drawn is shown in figure 3.4.

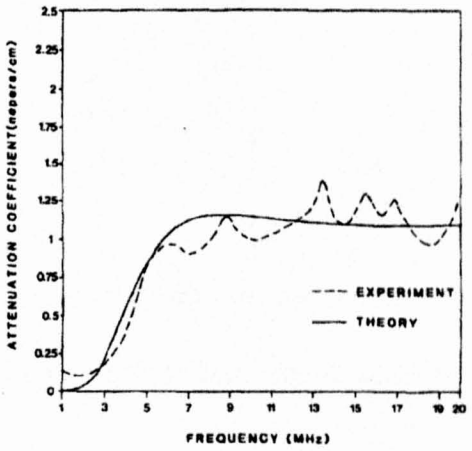

Figure 3.4 Comparison between experimental and theoretical frequency dependent attenuation, for a distribution of porosity in an aluminium casting. (Reproduced from Adler et al (1986)).

Rose et al (1985) investigated the possibility of using Kramers-Kronig relationships to characterize porosity. Rose derived a model which related the attenuation due to porosity to the shift in ultrasonic wave velocity. The porosity was assumed to be spherical voids of various radii which were uniformly and randomly distributed and of

low void volume fraction (ϕ_v < 5%). Rose provided the following equation for attenuation:

$$\alpha(\omega) = \frac{2\pi}{k}\int_0^\infty n(a)\,\mathrm{Im}(A(k,a))da \tag{3.24}$$

Where $n(a)$ is the number of pores per unit volume with radii a and $A(k,a)$ is the compression wave forward scattering amplitude. The ratio of the velocity shift to the velocity of ultrasonic compression waves in unflawed material is defined as:

$$\frac{\Delta V(k)}{V_0} = -\frac{2\pi}{k^2}\int_0^\infty n(a)\,\mathrm{Re}(A(k,a))da \tag{3.25}$$

By drawing on Kramers-Kronig relations (see for example O'Donnell et al 1978) an algorithm relating the void volume fraction to the frequency dependent attenuation was derived as follows:

$$\phi_v = \frac{4}{3\pi A_2}\int_0^\infty \frac{\alpha(k')}{k'^2}dk' \tag{3.26}$$

Where A_2 is a dimensionless constant related to the Poisson's ratio of the material. This formulation was used to provide an estimate of the void volume fraction of various test samples and this result was then compared against the void volume fraction defined by density measurements. A good qualitative agreement was found between the theoretical and experimental values but discrepancies were found between the two results and it was hypothesised that this was due to the use of spherical scatterers and that the

distribution was assumed to be uniform, which might not have been the case experimentally.

Nair et al (1989) considered infinitely long cylindrical pores, the profile of which could be circular or elliptical. Adaptations were made to the existing equations for frequency dependent attenuation developed by Adler et al,

$$\alpha(k) = \frac{1}{2}\int_0^\infty n(a)\gamma(k,a)da \qquad \textbf{(3.27)}$$

by changing the expression for the total scattering cross-section γ per unit length. For circular cylindrical scatterers γ depends on η, the ratio of shear to compression wave velocity in the medium, and *ka*, the wavenumber multiplied by the radius of the cavity. γ for infinitely long circular cylindrical scatterers is defined thus in terms of the reduced cross-section:

$$\gamma(ka,\eta) = 4a\Gamma(ka,\eta) \qquad \textbf{(3.28)}$$

The total scattering cross-section is shown by Lewis et al (1975) to be:

$$\Gamma(ka,\eta) = q_{cc} + q_{cs} \qquad \textbf{(3.29)}$$

Where,

$$q_{cc} = \frac{2}{ka}\sum_{n=0}^{\infty} e_n \left|(A_n)_c\right|^2 \tag{3.30}$$

and

$$q_{cs} = \frac{2}{ka}\sum_{n=0}^{\infty} e_n \left|(B_n)_c\right|^2 \tag{3.31}$$

$e_n = 1$ for $n = 0$ and $e_n = 2$ for $n \geq 1$, and A_n and B_n are complex numbers which represent the scattered wave coefficients. Figure 3.5 shows results for reduced scattering cross-section were obtained by Nair et al for various values of η.

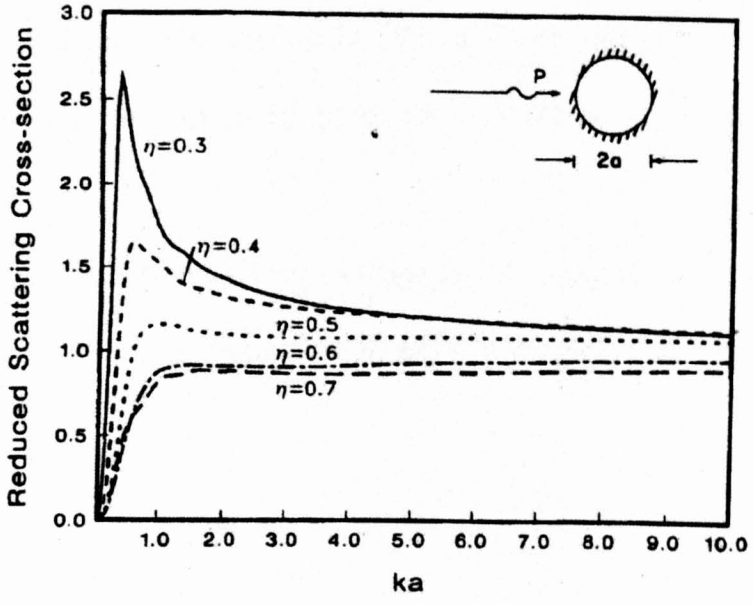

Figure 3.5 Reduced scattering cross-section for infinitely long circular cylindrical scatterers for various values of η. (Reproduced from Nair et al (1989)).

At the University of Nottingham comparisons were drawn between the modelled output shown by Nair and the output of a modified version of ECAH using the equations of Habeger (1982) for a cavity in a solid and good agreement was found, figure 3.6.

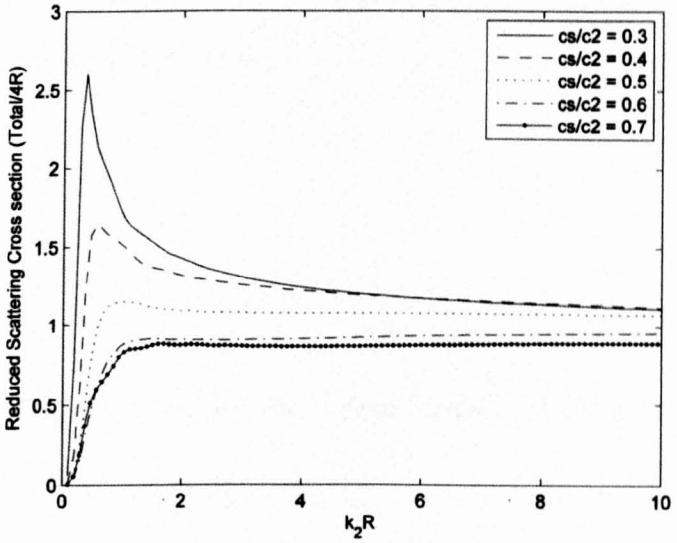

Figure 3.6 Reduced scattering cross-section for infinitely long circular cylindrical scatterers for various values of η. (Reproduced from Habeger (1982)).

For cylindrical scatterers which have a radius a on the smallest axis and b on the greater axis, the total scattering cross-section for an incident compression wave,

$$\underline{u}^{in} = \underline{U}^{p} \exp(ik\underline{\hat{\alpha}} \cdot \underline{x}) \tag{3.32}$$

$\underline{U}^{p}$ is the wave amplitude vector, $\underline{u}^{in}$ is defined in terms of particle displacements thus:

$$\gamma\left(k, \hat{\alpha}, \frac{b}{a}, b, \eta\right) = \frac{1}{k} \mathrm{Im}\left[\frac{\underline{U}^{p*} \cdot \underline{X}^{p}(\hat{\alpha})}{\underline{U}^{p} \cdot \underline{U}^{p*}}\right] \tag{3.33}$$

Where $\underline{X}^{p}(\hat{\alpha})$ is given by,

$$\underline{X}^{p}(\hat{\alpha}) = \frac{-ik}{\lambda + 2\mu}\hat{\underline{\alpha}}\int_{0}^{2\pi}\left\{\lambda(\underline{u}^{sc}\cdot\hat{\underline{n}}) + 2\mu(\underline{u}^{sc}\cdot\hat{\underline{\alpha}})(\hat{\underline{\alpha}}\cdot\hat{\underline{n}})\right\}\exp(-ik\hat{\underline{\alpha}}\cdot\underline{x})s(\tilde{\eta})d\tilde{\eta} \qquad \textbf{(3.34)}$$

The reduced cross-section is given as,

$$\Gamma = \frac{\gamma}{4b} \qquad \textbf{(3.35)}$$

The reduced scattering cross-section for various ratios of shear to compression wave velocities (η) is shown in figure 3.7.

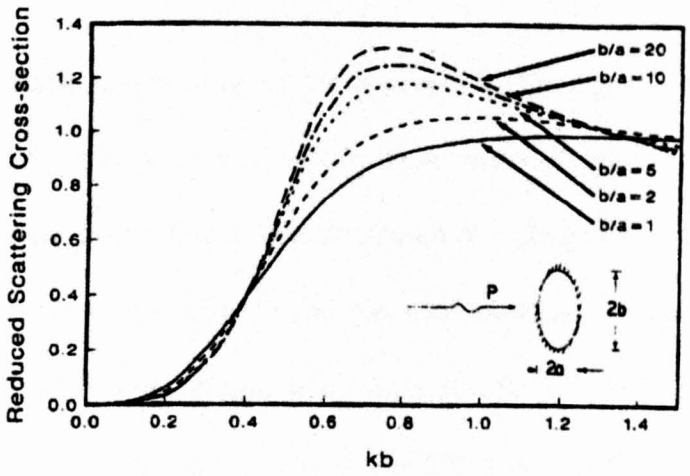

Figure 3.7 Reduced scattering cross-section for infinitely long eliptical cylindrical scatterers for various values of η. (Reproduced from Nair et al (1989)).

Experiments were conducted by Nair et al to match the modelled frequency dependent attenuation that resulted from small parallel circular holes drilled into aluminium blocks

to simulate porosity. The results obtained for an effective volume fraction of 1.82% porosity are shown in figure 3.8.

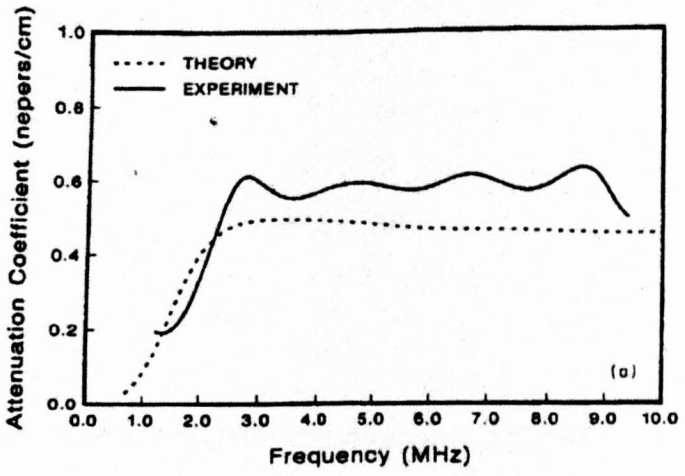

Figure 3.8 Frequency dependent attenuation for modelled and experimentally measured data for 1.82% porosity in an aluminium block. (Reproduced from Nair et al (1989)).

Nair et al then did further work to apply the concepts outlined previously to carbon fibre composite panels. Assumptions were made to allow simplification of the problem, namely that the composite medium could be treated as isotropic in a direction perpendicular to the plane of the fibres, and this was achieved by making the assumption that the fibres were aligned in a single direction, that the fibres were uniformly distributed and that the diameter of the fibres was assumed to be much smaller than the wavelengths which were under observation. The ultrasonic beam was modelled as an incident plane wave propagating perpendicular to the axes of the fibres, porosity was modelled as infinite elliptical cylinders which were aligned parallel to the direction of the fibres. By making these assumptions the composite could be modelled

as a transversely isotropic solid. Nair then showed that the stiffness matrix for this medium was as follows:

$$[C]=\begin{bmatrix} C_{11} & C_{12} & C_{12} & 0 & 0 & 0 \\ & C_{22} & C_{23} & 0 & 0 & 0 \\ & & C_{22} & 0 & 0 & 0 \\ & & & \frac{1}{2}(C_{22}-C_{23}) & 0 & 0 \\ & & & & C_{55} & 0 \\ & & & & & C_{55} \end{bmatrix} \tag{3.36}$$

Where the subscript 1 denotes the fibre direction, the subscript 2 is transverse with respect to direction of fibres and the subscript 3 is normal to 2. These material constants can be used to give the relationship between stress and strain; simplifications are possible since displacements occur only in a direction perpendicular to the scatterers, as shown below:

$$\begin{bmatrix} \sigma_{22} \\ \sigma_{33} \\ \sigma_{23} \end{bmatrix} = \begin{bmatrix} C_{22} & C_{23} & 0 \\ C_{23} & C_{22} & 0 \\ 0 & 0 & \frac{1}{2}(C_{22}-C_{23}) \end{bmatrix} \begin{bmatrix} \varepsilon_{22} \\ \varepsilon_{33} \\ \varepsilon_{23} \end{bmatrix} \tag{3.37}$$

This description of the stress-strain relation by two material constants is equivalent to the stress-strain relations of isotropic materials as shown in Reynolds and Wilkinson (1978). The equations defined for scattering cross-section used earlier can therefore be used to estimate the frequency dependent attenuation due to porosity in a composite.

Micrographs were taken of a vertical cross-section of a unidirectional composite, containing carbon fibres in epoxy, and with a porosity volume content of 1.14%. Comparisons were made between the frequency dependent attenuation predicted via the model and those obtained experimentally, the results of this comparison are shown in figure 3.9.

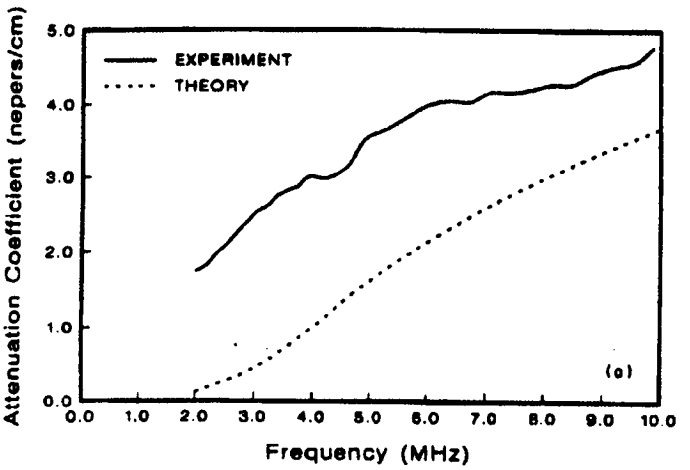

Figure 3.9 Frequency dependent attenuation for modelled and experimentally measured data for 1.14% porosity in a carbon fibre reinforced panel. (Reproduced from Nair et al (1989)).

There is a large discrepancy between the measured and simulated attenuation which was attributed to approximations which were made during the computation process. The layered nature of the solid was neglected, the shape of the scatterers was approximated to a smooth ellipse and it was assumed that the location of scatterers and infinetly long voids was randomly distributed. The authors also noted that the micrograph from which scatterer distribution was calculated was taken at a different location from where the attenuation measurements were taken, this could further have contributed to the attenuation discrepancy.

Ghaffari et al (2004) made comparisons between modelled data generated using the method outlined by Adler and experimental data for porosity in aluminium castings. Distributions of scatterers of different sizes were considered. It was noted that the exact scattering cross-section of the scatterers present in the aluminium castings was not accurately represented by the model since the experimental scatterers did not have a simple spherical morphology. Attempts were made to represent the experimental distribution of the scatterers with an equivalent distribution of spherical pores.

Test samples for comparison were made of aluminium; the volume fraction of porosity was estimated by estimating the density of cubes cut from the test sample after ultrasonic measurements had been taken. The morphology and size distributions of the pores was estimated by fracturing the test samples at various locations and imaging the pores present with a field emission scanning electron microscope. The data obtained could then be used to generate theoretical frequency dependent attenuation.

Ultrasonic scans were taken of the test samples immersed in water and comparison of the front and back wall echoes allowed the determination of the frequency dependent attenuation for the test sample under consideration. Corrections were made for impedance mismatches, surface roughness and diffraction effects. The measurements taken were processed to give an inferred volume fraction of porosity. These values were then compared to the values obtained from density measurements as shown in figure 3.10.

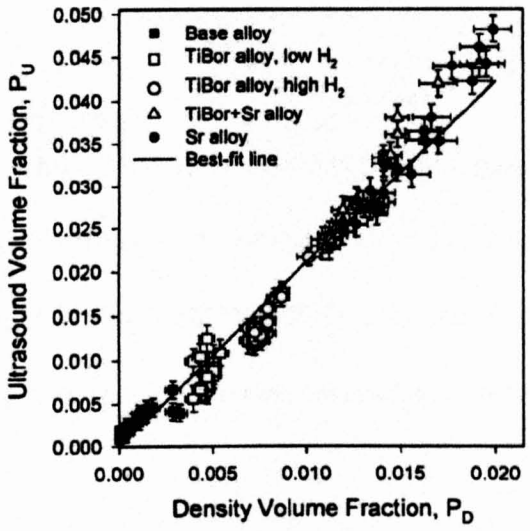

Figure 3.10 Comparison of volume fraction of porosity calculated from ultrasonic data and from density measurements for differing metal alloy blocks. (Reproduced from Ghaffari et al (2004)).

Figure 3.10 does not show a ratio of unity between the ultrasonically calculated porosity and that determined via density measurements. Having verified that the ultrasonic frequency dependent attenuation measurements were numerically correct, it was speculated that the differences in the two methods was a result of the complex morphology present in the castings which could not be completely simulated by the scattering models.

3.5 Conclusions

The physical properties which determine scattering from a particle have been given and their implications for development of a scattering model examined. Three scattering models which arise from this approach, that of Epstein and Carhart, of Allegra and Hawley and that of Ying and Truell have been described and the equivalence between the models demonstrated.

Alternative methods of calculating scattering from inclusions have been described; these methods have been based on the scattering cross-section of the distributions of scatterers. Equivalence between the ECAH model and that developed by Adler et al and Nair et al was demonstrated. Close matches between modelled output for spherical and elliptical scatterers was found, this would indicate that a model which used spherical scatterers should provide an adequate method of modelling porosity within carbon fibre reinforced panels. In some cases, for example Nair et al it was found that the absolute magnitude of the frequency dependent attenuation was underestimated. However, the shape of the function was accurately described and these results provide a basis for modelling, providing the difference in magnitude is noted. The results presented by Nair et al would seem to indicate that when modelling scattering within carbon fibre reinforced composites it is necessary to consider the layered structure of the media. A long standing multi-layer model *Propmat* is in use at the University of Nottingham, to which the output from ECAH could be incorporated. The next chapter will detail the modifications made to this multi-layered model to allow modelling of the interaction between ultrasonic compression waves, the layered structure of the carbon fibre reinforced panel and porosity.

Chapter 4

Development of a Model for Ultrasonic Propagation in Layered Media

4.1 Introduction

In order to develop of methods to successfully detect, identify and quantify porosity and other defects within carbon fibre reinforced panels (CFRPs) it was necessary to develop a method of modelling the interaction of ultrasound with the layered structures that form typical composites. This chapter details a model for simulating ultrasonic wave propagation in a multi-layered composite. It was originally developed by Freemantle (1995) as part of his PhD programme and was named *Propmat*. It was fairly basic in form and was restricted to a small number of layers; this was not a problem at the time because its principal application was to adhesively bonded strip metal structures in the automotive industry. The computer code ran under the DOS operating system. The software simulates acoustic wave propagation in layered media based on a well-established transfer matrix formulation which originated from the works of Thompson (1950), Haskell (1955), Knopoff (1964) and Pialucha (1992). This chapter will examine the history of this model, as well as alterations which were made to place it within a Windows® environment. Comparisons are made between structures simulated with the Windows® based client and the original benchmarks for the model. Analysis of the composite structure which will be modelled is conducted and simplifying assumptions are discussed. A modelling exercise is then conducted to verify that the model generates A-scan lines consistent with experimental data from composite structures.

4.2 Model Formulation

Many years ago acoustic wave propagation in layered media was modelled on the basis of a well established transfer matrix model which originated in the works of Thompson (1950), Haskell (1953), the original use being to model the behaviour of seismic waves. The aim of these works was to derive wave equations which described the behaviour of waves in terms of a transfer matrix which related the field present at the front surface of a layer to the field present at the rear surface of a layer. The matrices for multiple layers could then be cascaded to model the behaviour of a multi-layered structure. Instability problems were identified with the numerical implementation of these methods by Dunkin (1965), when modelling conditions which provided the sum of very large or very small numbers within the field matrix solution of the equations. A global matrix routine which contains one matrix containing the equations for all of the layers was developed by Knopoff (1964); this increases computation time and has memory issues with large structures since the whole structure must be simulated in memory at one time. Although this formulation was also employed by Freemantle (1995) and formed part of the software package developed by him, the size of the structures which would be simulated in this application made employment of the global matrix method undesirable. Early investigations showed that for the frequencies and material properties used the transfer matrix performed adequately and this was the method which was employed. Adaptations were later made to the transfer matrix method by Pialucha (1992), to model the behaviour of a finite sized transducer. The model described here and in use in the Applied Ultrasonics Laboratory at the University of Nottingham followed the earlier work of Freemantle (1995). We have not made significant changes to the core formulation, which has been previously demonstrated to function in a variety

of situations; rather we have concentrated on ways to define the properties of the material layers and the ergonomics of inputting these to the software. However, changes were made to the core code to allow an arbitrary number of layers to be input. The original had placed restrictions on the number of layers to preserve the limited memory available in computers at the time. There were also memory management issues with the original code which resulted in the code only being able to be run a limited number of times before the random access memory of the computer was full. Memory management routines were added to the code to allow many simulations to be run consecutively. The emphasis of this chapter is on the functioning of the model in the context of this project. A review of the transfer matrix formulations upon which the model is based was published by Lowe (1995), to which the reader is referred for an in-depth treatment. The final form of the model that resulted from these developments is known as *MLM-Propmat.*

The basic modelling situation was to consider the bulk wave stress and displacement on either side of each boundary between two layers, this can then be extended on a sequential basis to allow for a many layered system. In this case we consider a perfectly elastic medium. The simple modelled situation is shown in figure 4.1.

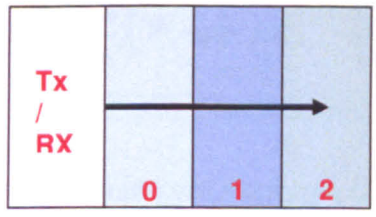

Figure 4.1 Three layered system

For the three layered system shown in figure 1, we make the assumption that the bounding layers 0 and 2, are semi-infinite and are in perfect contact with layer 1. Layer 1 is assumed to be a homogenous medium as well as isotropic, which is not strictly true for the fibre and resin layers in the transverse plane; the layers are assumed to support both compression and shear wave disturbances. The transducer is assumed to be a plane compression wave source, with its aperture parallel to the layers in the assembly. If layer 1 has a thickness x the following equation applies,

$$F_0(0)A_0 = F_2(x)A_2T_1 \tag{4.1}$$

where F_0 and F_2 are the field matrices for the layers bounding layer 1, A_0 and A_2 are the wave amplitude coefficients either side of layer 1 and T_1 is the transfer matrix for layer 1. This equation can then be solved for A_2, the unknown coefficient which corresponds to the compression and shear wave reflection coefficients for the layer. The basic field matrix F_2 for an elastic case is as follows:

$$\begin{bmatrix} j\left(\frac{\omega}{v_c}\right)D_1\exp[-j\omega Y] & j\left(\frac{\omega}{v_c}\right)D_1\exp[j\omega Y] & -j\left(\frac{\omega}{v_s}\right)D_2\exp[-j\omega Z] & j\left(\frac{\omega}{v_s}\right)D_2\exp[j\omega Z] \\ -j\left(\frac{\omega}{v_c}\right)D_2\exp[-j\omega Y] & j\left(\frac{\omega}{v_c}\right)D_2\exp[j\omega Y] & -j\left(\frac{\omega}{v_s}\right)D_1\exp[-j\omega Z] & -j\left(\frac{\omega}{v_s}\right)D_1\exp[j\omega Z] \\ -\left(\frac{\omega}{v_c}\right)^2 W_c\exp[-j\omega Y] & \left(\frac{\omega}{v_c}\right)^2 W_c\exp[j\omega Y] & \left(\frac{\omega}{v_s}\right)^2 X_s\exp[-j\omega Z] & \left(\frac{\omega}{v_s}\right)^2 X_s\exp[j\omega Z] \\ \left(\frac{\omega}{v_c}\right)^2 X_c\exp[-j\omega Y] & \left(\frac{\omega}{v_c}\right)^2 X_c\exp[j\omega Y] & \left(\frac{\omega}{v_s}\right)^2 W_s\exp[-j\omega Z] & -\left(\frac{\omega}{v_s}\right)^2 W_s\exp[j\omega Z] \end{bmatrix} \tag{4.2}$$

The terms of the matrix have the common factors $\exp[j\omega x_1 D_1]$ and $\exp[j\omega t]$. Where,

$$W_c = \rho v_s^2 2D_1D_2 \qquad X_c = \rho v_c^2\left(1-2v_s^2\frac{D_1^2}{v_c^2}\right) \qquad W_s = \rho v_s^2 2D_1D_2$$

$$X_s = \rho v_s^2 \left(1 - 2v_s^2 \frac{D_1^2}{v_s^2}\right) \qquad Y = x_2 D_2 v_c^{-1} \qquad Z = x_2 D_2 v_s^{-1}$$

where ρ is the density, v_c and v_s are the compression and shear wave velocities in the medium and D_1 and D_2 are the direction cosines defined as:

$$D_1 = sc \qquad D_2 = (1 - c^2 s^2)^{0.5} \tag{4.3}$$

where c is the compression or shear wave velocity, and s is Snell's constant given by:

$$s = \frac{\sin\phi}{c} \tag{4.4}$$

ϕ is the angle of the compression or shear wave to the normal to the boundary. The unknown amplitude coefficient matrix A_2 is as follows:

$$\begin{bmatrix} A^F \\ A^R \\ B^F \\ B^R \end{bmatrix} \tag{4.5}$$

A^F and A^R are the complex forward and reverse travelling compression wave amplitudes and B^F and B^R are the complex forward and reverse travelling shear wave amplitudes. T_1 the transfer matrix for layer 1 is given by:

$$T_1 = F_1(0)^{-1} F_1(x) \tag{4.6}$$

$F_l(0)$ and $F_l(x)$ are the field matrices at the front and rear surfaces of the layer respectively. By cascading these transfer matrices the total transfer matrix for a system of N layers can be obtained.

$$F_0(0)A_0 = F_{N+1}(x_N)A_{N+1}T_1T_2T_3....T_N \tag{4.7}$$

From this the overall reflection and transmission coefficients for the layered structure in the frequency domain can be determined. Further assumptions are made at this stage, namely: all of the layers are parallel to each other and perfectly bonded to their neighbours, and stress is conserved across the assembly.

Modifications may be made to the field matrix of 4.2 to account for effects such as viscosity, scattering and viscoelastic loss effects, as found in the inelastic case. This is achieved by modifying the terms with coefficients derived from the complex wave number. An example for the first term of the matrix is as follows:

$$j\left(\frac{\omega}{v_c(\omega)}\right)D_1 \exp[-j\omega Y]\exp[\alpha(\omega)] \tag{4.8}$$

Where $\alpha(\omega)$ is the frequency dependent attenuation and $v_c(\omega)$ is the frequency dependent velocity. These inputs are supplied to the model as data files, and as such can support a variety of modelled attenuations or alternatively experimental data. Further consideration to the form of these coefficients is given in section 4.4.3. We note at this point that this method provides for the inclusion of frequency dependent attenuation due

to scattering. Upon solution the four unknown amplitude coefficients are mapped to Fast Fourier Transform (FFT) arrays for analysis. Subsequent inverse FFT yields the equivalent time domain responses. *MLM-Propmat* is built into a software package which takes as its inputs the thickness, density and frequency dependent attenuation and phase velocity for each constituent layer.

4.3 Conversion of Original Code to Windows®

4.3.1 Conversion of Code

The original numerical processing code written by Freemantle was written in Unix 'C' and was called *Propmat*. Whilst performing perfectly adequately when simulating structures there were significant draw backs when modelling large structures due to the lack of a convenient user interface. It was decided that conversion of the original code to work from a Windows® interface would have significant benefits; the construction of a user friendly interface would not only increase the speed of simulation but allow interaction of the code with other modelling codes which had been developed within the laboratory such as the ECAH scattering code. The original 'C' code was compiled into a dynamic link library (DLL) using Microsoft Visual C++ .NET. Limitations had been placed in the original code, to limit the number of layers which could be modelled within a test structure, to preserve computer memory and limit computation time. Given the considerable increase in computer processor speed and memory size of the average computer, these limits were not considered to be as critical as previously thought. Thus these limits were removed and alterations to the code made to allow any number of layers to be simulated. A user interface was constructed using Visual C++ .NET, this language being chosen for its compatibility with the latest Windows® systems, and for

ease of development. The new code was named multi-layer model *Propmat (MLM-Propmat)* in recognition of the original source of the programmed code.

4.3.2 Modelling of Transducer Response

The code was modified to output only the frequency response, rather than also performing a convolution with a transducer response; the aim of this change was to take advantage of an existing code which could create an arbitrary transducer pulse of any centre frequency developed by Challis (1984, unpublished) and digitally implemented by Phang (2006). A piezoelectric transducer was modelled using the z-transform and digital filter theory. The transducer is regarded as a digital filter, which takes as its input a unit impulse, the output signal provided is a series of impulses which alternate in sign representing the fundamental acoustic reverberations within the piezo-electric element of the transducer. A recurrence relationship was derived based on the acoustic impedance of the transducer element and the backing materials either side of it. This output can then be convolved with a half cycle of a sine wave to give a full transducer response. Phang compared the transducer waveforms obtained using this method with actual transducer responses and found that the waveforms compared favourably. A sample waveform obtained from this process is shown in figure 4.2.

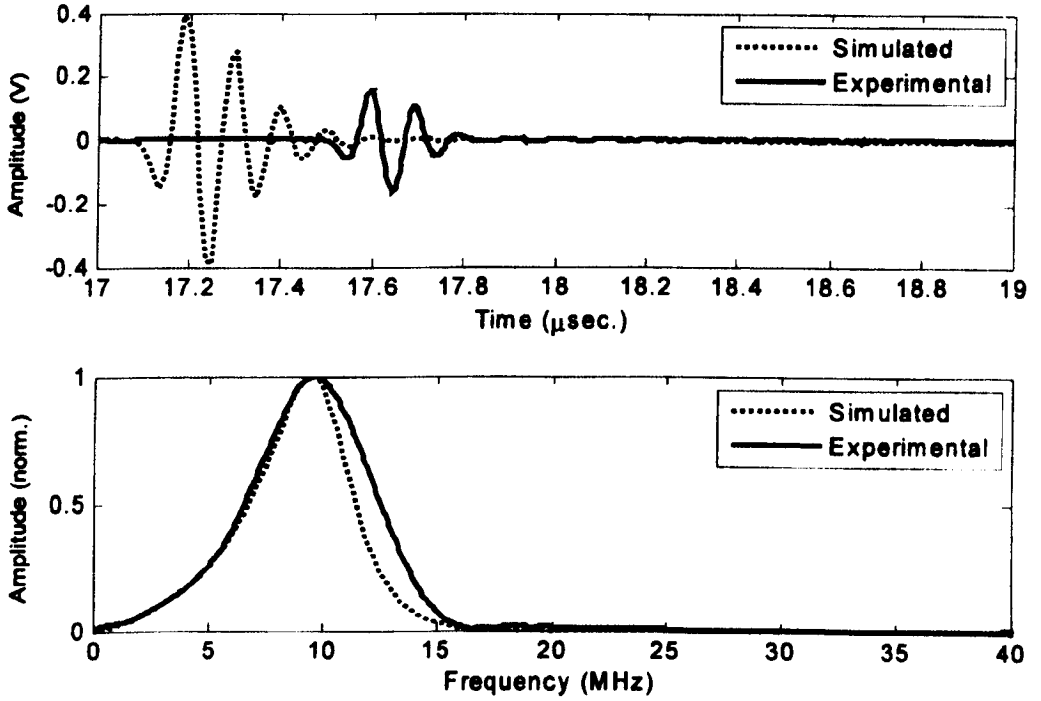

Figure 4.2 Comparison between10MHz Centre frequency transducer response obtained from transducer model and experiment for time domain (top) and frequency domain (bottom), reproduced from Phang (2006).

The output obtained from *MLM-Propmat* is transformed into the time domain by use of an inverse FFT, and the time domain impulse response can then be convolved with the transducer response obtained from the model.

4.3.3 Verification of Functionality

Given that changes had been made to the original *Propmat* code to allow an arbitrary number of layers and to allow compatibility with Windows® it was necessary to verify that the changes which had been made had not impaired the functionality of the simulation code. The original *Propmat* code had been compared by Freemantle to a variety of published results from other transfer matrix based models, for single and

multiple layers at normal and angled incidence. The updated version of the model was benchmarked against the original comparisons. The first modelling situation was a time domain simulation for a single 2mm thick ideal elastic plate immersed in an ideal liquid. The response originally generated by Freemantle is compared against that obtained from the updated code in figure 4.3.

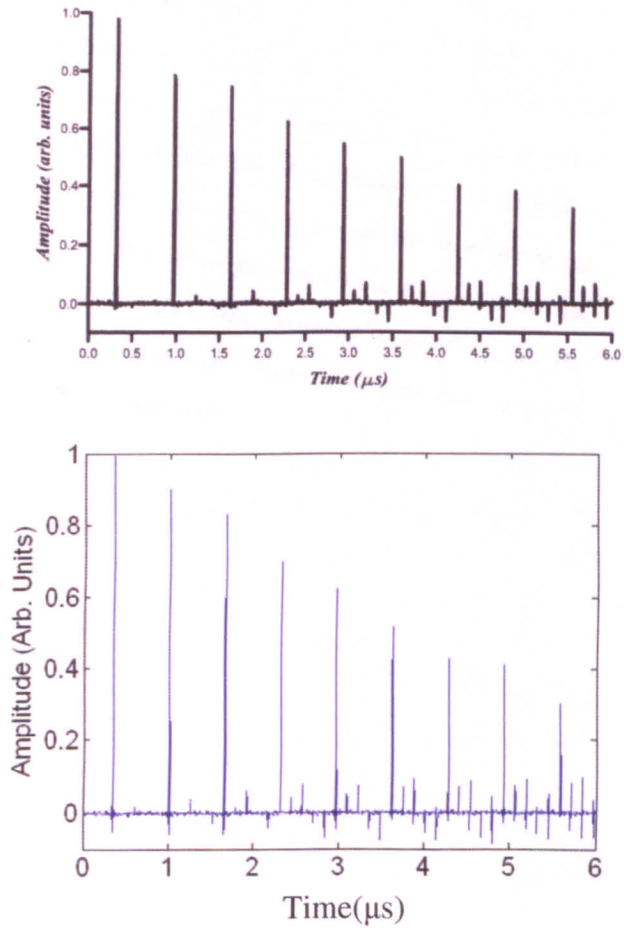

Figure 4.3 Time domain waveforms for a 2mm steel plate immersed in water from Freemantle (1995) (top), and the *MLM-Propmat* transfer matrix model (bottom).

Figure 4.3 shows that the comparison between the original model and the updated version was found to be good with a high degree of correlation. The models were also compared to each other using responses generated as a function of angle of incidence

for a fixed frequency. The original responses had been compared to a modelling situation generated by Pialucha (1992) for a 5mm plate immersed in water; the fixed frequency which was used was 6MHz. The complex reflected compression wave moduli were compared and the results are shown in figure 4.4.

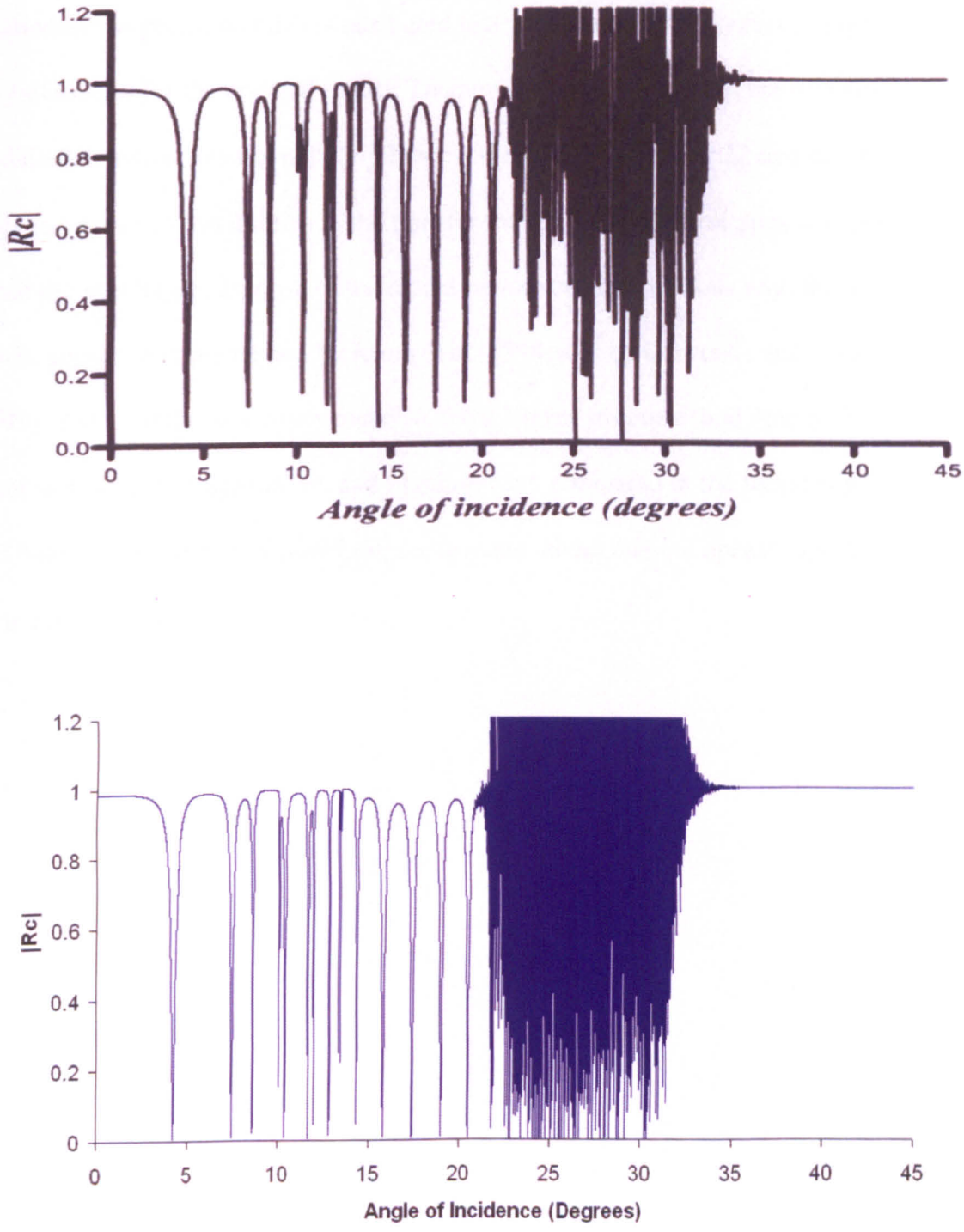

Figure 4.4 Predicted angular reflected response for a 5mm aluminium plate immersed in water at 6MHz, for original model *Propmat* (top) and updated model *MLM-Propmat* (bottom).

Figure 4.4 shows that there is good qualitative agreement between the original model and the updated model. There are some differences in the magnitude and precise location of the peaks, and this is attributed to a greater number of points being used in the calculation for the updated model. The number of points used in the original modelled situation was not noted by Freemantle. The noise above 22 degrees in both cases is a result of instabilities in the transfer matrix model at these angles. Freemantle tested the multilayer response of the model by making comparisons with the transfer matrix approach implemented by Kinra et al (1994) and by Cervenka and Challande (1991). The modulus frequency response for a 3 layer structure modelled by Kinra, of water surrounded by aluminium and titanium were compared in the frequency range 0 to 10MHz. The results obtained from the original model and the updated model are shown in figure 4.5.

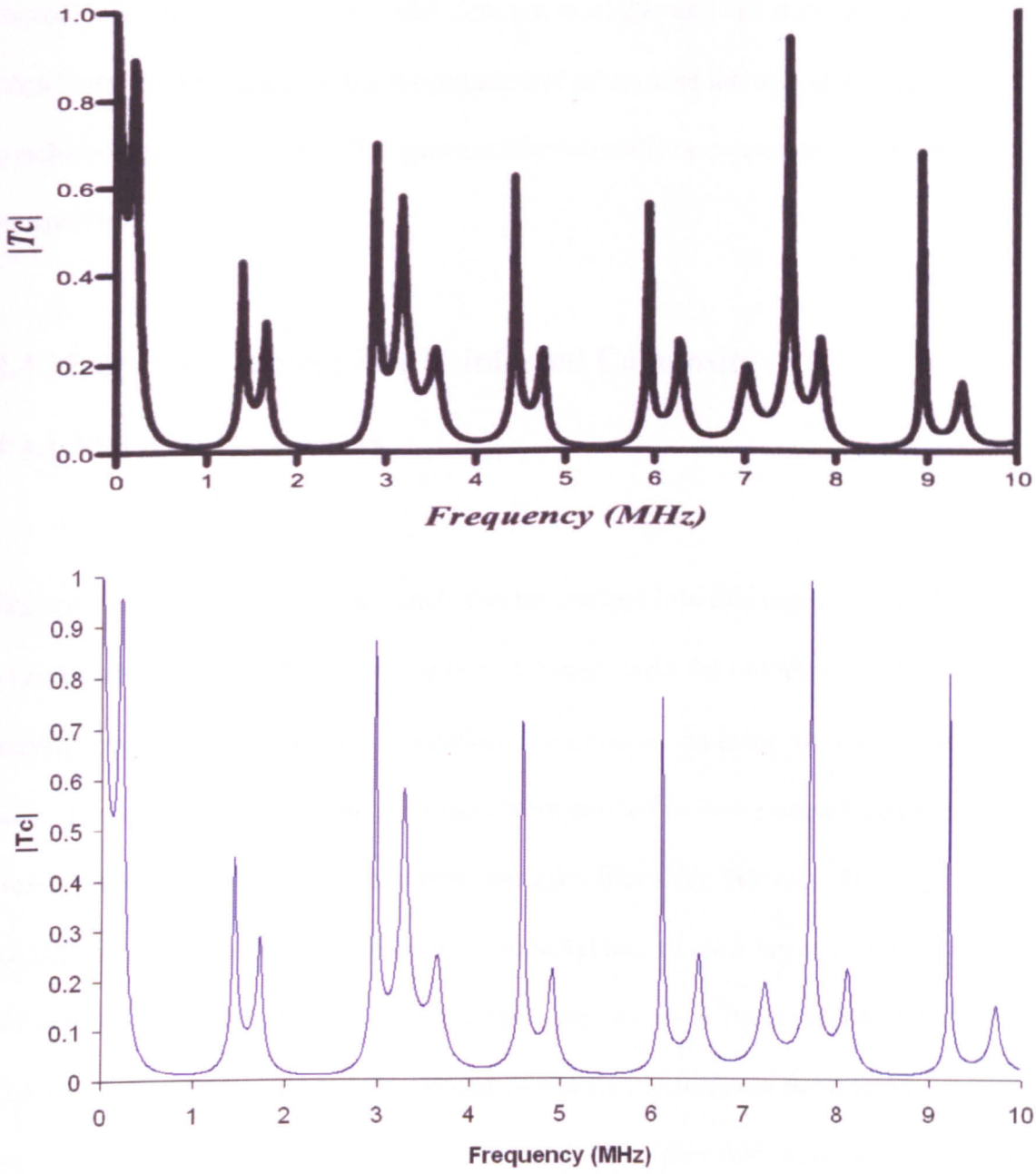

Figure 4.5 Predicted normal incidence transmitted response for the three layer system of Kinra, for the original model *Propmat* (top) and the updated version *MLM-Propmat* (bottom).

Figure 4.5 shows that the results obtained agreed well with the earlier model; the differences in magnitude of the peaks are attributed to differences between the number of points used when calculating the response in the original and the updated models; this quantity was not defined in the original work. The exact reflection coefficients used for

this calculation in the original model were not available and this may also have contributed to differences in the magnitude and location of the resonant peaks. It is concluded that the quality of the agreement between the two versions of the model is acceptable.

4.4 Modelling Carbon Fibre Reinforced Composite

4.4.1 Material Parameters

The constituent materials of the panels can be grouped into two regions, resin layers and a resin/carbon fibre mixture. In order to gain benchmarks for model performance and stability, as rapidly as possible, simulations were conducted using simplified mixture rules. The layers that constitute the model were defined as being one of four types: resin alone, resin and porosity, resin and fibre, or resin, fibres and porosity. There was a requirement to model the compression wave behaviour of each layer to arrive at the phase velocity and the attenuation for compression waves as functions of frequency. Comprehensive formulations for propagation velocity in terms of the relative concentrations of the constituent materials (resin, fibre, porosity) have been derived by Greszczuk (1971) and Martin (1977). In this chapter we will be using a very much simplified formulation for effective media to represent each of the layers; the performance of this simplified formulation for modelling propagation in a CFRP is examined later in this chapter. Appendix B has been added to show the equivalence or otherwise between the simple mixture rules used for the body of this work and these more comprehensive formulations. The compression modulus and density of each layer are arrived at from simple linear mixture rules. Thus for resin containing voids

$$M_{rv} = \phi_v M_v + (1-\phi_v) M_r \tag{4.9}$$

Where M_r is the modulus of the resin alone, φ_v is the void volume fraction and M_v is the bulk modulus of the voids, which we can assume to be negligible, yielding

$$M_{rv} = (1-\phi_v) M_r \tag{4.10}$$

Here we assume that the voids are small in relation to wavelength and layer thickness. For a fibre and resin layer we get

$$M_{fr} = \phi_f M_f + (1-\phi_f) M_r \tag{4.11}$$

where M_f is the compression modulus of the fibre material and φ_f is the volume fraction of the fiber in the layer. If the resin is to be modelled as porous then M_{rv} from equation 4.9 is substituted for M_r in equation 4.11. In a similar manner the densities become, for porous resin

$$\rho_{rv} = \phi_v \rho_v + (1-\phi_v) \rho_r \tag{4.12}$$

and for resin and fibre

$$\rho_{fr} = \phi_f \rho_f + (1-\phi_f) \rho_r \tag{4.13}$$

Here again ρ_m can be substituted for ρ_r in equation 4.13 for the case of fibres and porous resin. The compression wave velocity c is then obtained from the modulus M and density ρ appropriate to the constituents of the layer.

$$c^2 = \frac{M}{\rho} \tag{4.14}$$

The values for compression wave velocity c and density ρ for the constituent materials of the mixture are as given in Appendix C.

4.4.2 Material Attenuation

To accurately model the A-scan response which would be obtained it was necessary to insert attenuation into the model; this attenuation would take two forms, first the inherent attenuation in the resin, and second the addition of frequency dependent attenuation due to porosity. The attenuation of epoxy resin has been well characterized by previous works Rokhlin et al (1986), Kline (1984) and Challis et al (2000) and has been found to be linear with frequency as shown in figure 4.6.

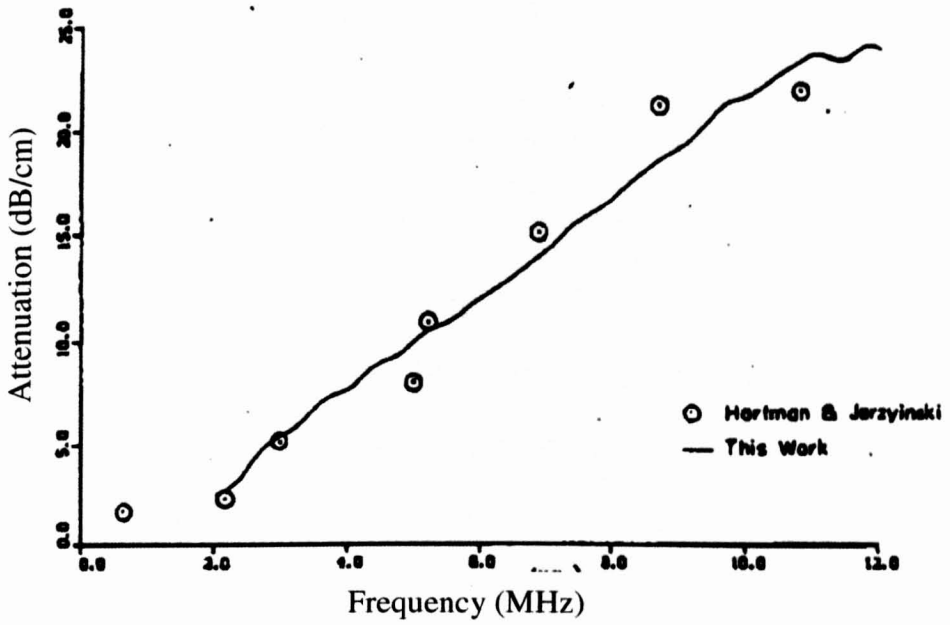

Figure 4.6 Attenuation for polyethylene. (Reproduced from Kline (1984)).

These functions may be obtained by use of an ultrasonic spectrometer-cum-goniometer instrument applied to thin slabs of cured material as shown by Freemantle et al (1998) and Challis et al (2000). Using typical values for attenuation in epoxy resin, an attenuation function was added to the resin layers within the model; the function was empirical representation of the proportionality between attenuation and frequency as follows:

$$\alpha_r = kf \text{ dBmm}^{-1} \tag{4.15}$$

Where $k = 0.15$, and f is the frequency at which the attenuation is to be calculated in MHz. This attenuation could then be added to the fibre/resin mixture by making the assumption that the attenuation due to the fibres was so small that it was negligible. The following relationship was used:

$$\alpha_{fr} = \phi_r \alpha_r \tag{4.16}$$

Where ϕ_r is the fractional volume of the resin in the fibre/resin mixture and α_r is the attenuation function. In the presence of porosity attenuation is added by using the ECAH scattering model described in chapter 3. Spherical scatterers were modelled in a layer of epoxy resin producing attenuation curves which could be used as an input by *MLM-Propmat*. An example of the output attenuation curves which were used is shown in figure 4.7.

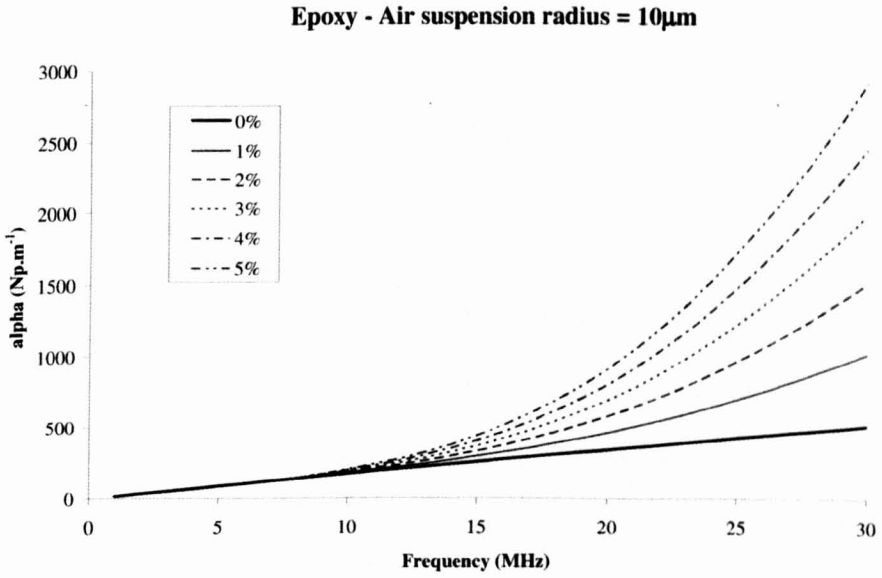

Figure 4.7 Frequency dependent attenuation for a suspension of porosity between 1% and 5% by value in epoxy resin obtained from the ECAH model.

The attenuation functions as shown in figure 4.7 may then be added directly to the resin layers, or alternatively added to the fibre/resin mixture using of the relationship defined in equation 4.16. It is noted when using this relationship that the percentage porosity

used as an input to the ECAH scattering model is not the same as will be in the final fibre/resin mixture. The final porosity volume fraction is given by:

$$\phi_{pfr} = \frac{\phi_p}{\phi_r} \tag{4.17}$$

Where ϕ_r is the resin volume fraction in the mixture and ϕ_p is the porosity volume fraction in the resin used within the mixture. It is concluded therefore, that care must be taken when conducting a simulation to ensure the porosity specified actually corresponds to the physical characteristics of the layer being modelled.

4.4.3 Layer Thickness Randomisation

Early comparisons between the model output and real data from CFRP A-scans showed that the inter-ply resonances seen in the model output were more regular in form than those in experimental data as shown in figure 4.8. The time of arrival of the signal is slightly different between the two traces; this was not significant and is merely due to the unknown thickness of the water layer between the specimen and the transducer in the experimental case.

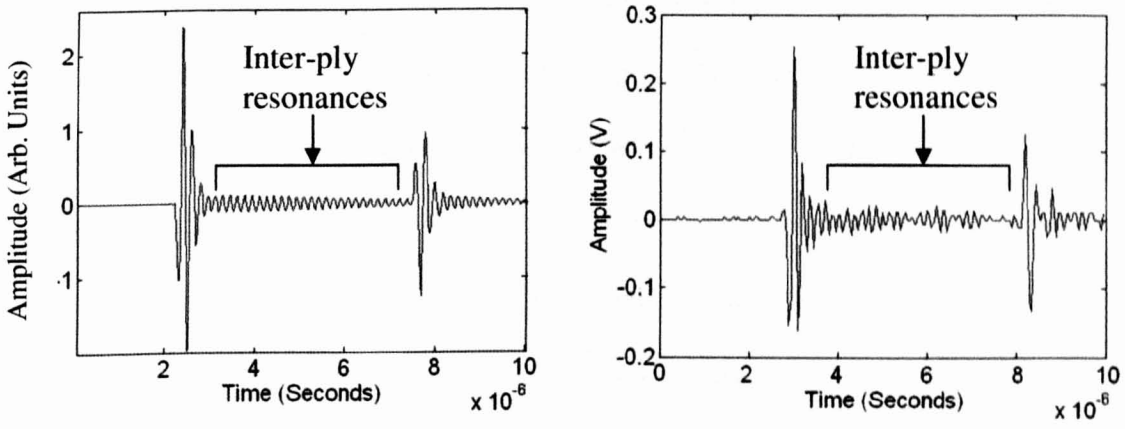

Figure 4.8 Time domain response for a modelled signal (left) and experimental data (right).

It was hypothesized that this was due to small but finite randomness in the thickness of the real ply layers. Micrographs were analysed, and the results of the analysis supported this theory. An example micrograph which was examined is shown in figure 4.9.

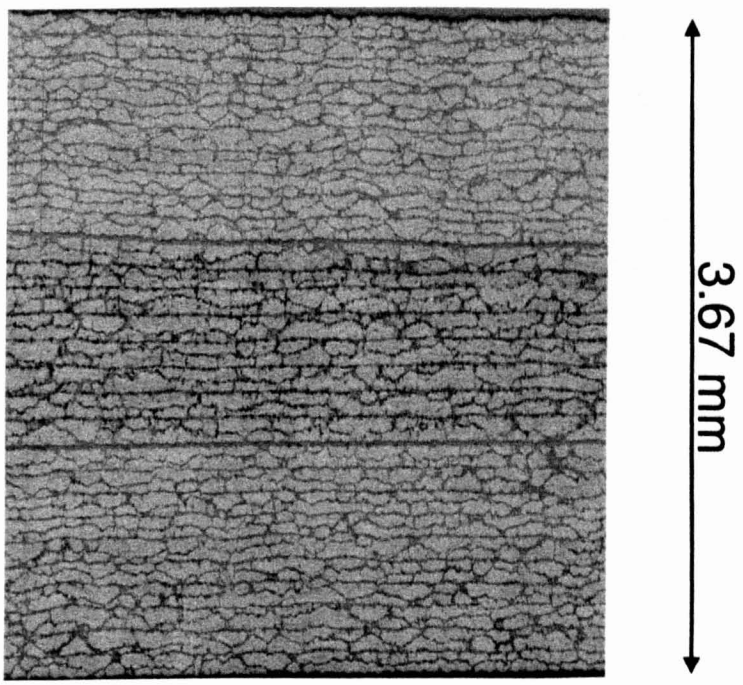

Figure 4.9 Sample micrograph of a carbon fibre reinforced panel. (Reproduced from Dominguez (2006)).

The micrograph shown in figure 4.9 was one which was modelled by Dominguez (2006). The panel was constructed to contain porosity by curing 8 plies of 8 plies per mm composite at a lower pressure before adding 10 plies to both sides of the 8 ply composite and re-curing the entire structure under normal conditions. This panel presented an excellent opportunity to compare the model with other work since during his project Dominguez modelled the micrograph shown using the modelling package CIVA. Measurements were taken of the thickness of the resin and ply/resin layers from a micrograph magnified for ease of measurement, and from these values a mean and standard deviation calculated. The results of this analysis are shown in table 4.1.

	Mean (mm)	Standard Deviation (mm)
Resin	0.15	0.049
Fibre/Resin	3.04	0.415

Table 4.1 Calculated mean and standard deviation of layer thickness for composite modelled by Dominguez (2006).

Since 8 plies per mm of depth were used, corresponding to a ply thickness of 125μm by use of the data in table 4.1 we can calculate the mean resin layer thickness which was 6μm. The randomness was represented in the input to the *MLM-Propmat* model by the following equation for layer thickness.

$$t_i = t_p\left[1 + p\frac{r-4.5}{4.5}\right] \qquad \textbf{(4.18)}$$

Where t_i is the randomized thickness, t_p is the nominal thickness, p is the allowed percentage variation and r is a random number between 0 and 9. By observation of table 4.1, the percentage variations allowed were 33% for the resin layer thickness, and 14% for the ply/resin mixture. Comparisons were made between *MLM-Propmat* using the data derived from table 4.1 and the original A-scan waveforms generated originally by Dominguez, the results are shown in figure 4.10.

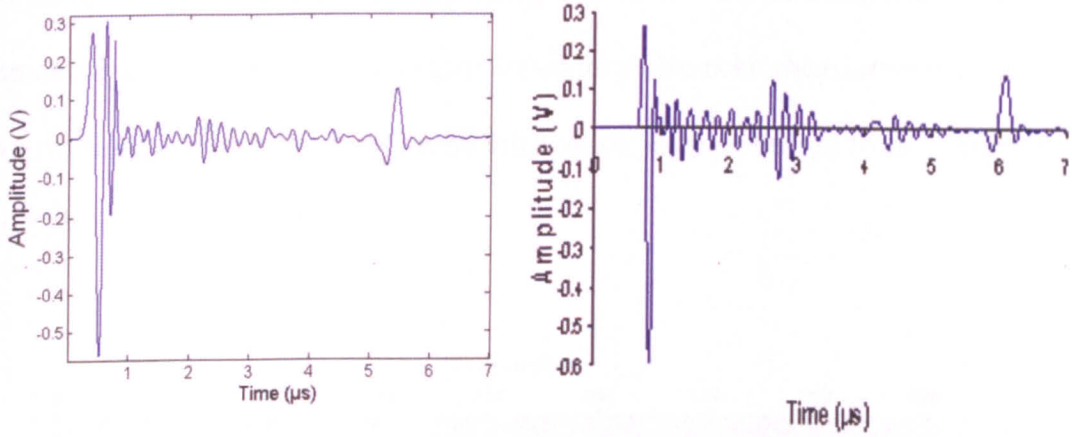

Figure 4.10 Comparison between waveform using *MLM-Propmat* (left) and given by Dominguez (2006) (right).

Observation of figure 4.10 shows that the waveform generated by the model (left) compares favourably with the waveform produced by Dominguez (right). It is noted that there are features in the A-scan waveform at 2μs and 3.8μs; these are the boundaries to the central plies, at which points the resin layers have been cured twice. The material properties at these points were changed to better reflect resin which had been cured in this way by increasing the compression modulus of these layers (Challis et al (2000)).

4.5 Comparison with Experimental Data

Experiments were conducted on specimen carbon fibre reinforced panels supplied by Airbus UK to provide a basis for comparison between *MLM-Propmat* and real data. The test panel contained 31 plies of fibres at 8 plies per mm. The panel contained varying degrees of porosity, ranging from areas which had no porosity to areas where the porosity was so great it could be approximated to delaminations. The panels were immersed in water and were scanned using a 10 MHz focused transducer (10mm element size, 15 – 60mm focal length) set up for pulse-echo measurements. Areas of low, medium and high back wall echo attenuation were identified from C-Scans of the panel shown in figure 4.11.

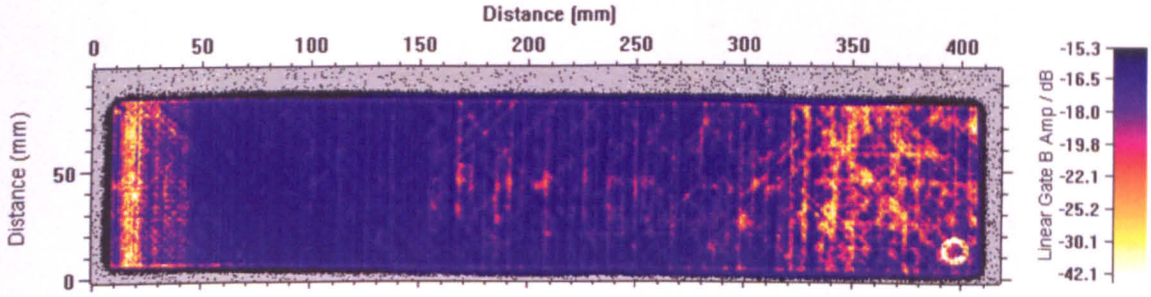

Figure 4.11 C-scan of a carbon fibre reinforced panel produced under normal conditions.

In figure 4.11 the lighter colours represent a decrease in back wall echo amplitude, and are hence areas where defects are suspected to exist. *MLM-Propmat* was used to simulate the selected A-scan waveforms, with no porosity for the area of low attenuation, 5% porosity for the area of medium attenuation and 20% porosity for the area of high attenuation. The thickness of the layers and the nominal deviation about these mean values was calculated from micrographs of similar composite. The impulse

response was convolved with a transducer response obtained from the transducer used in experiment. The water stand-off in the model was varied so that the front wall echoes of the modelled waveforms were at the same point in time as the experimental data. The original waveforms and the results from *MLM-Propmat* are shown in figure 4.12.

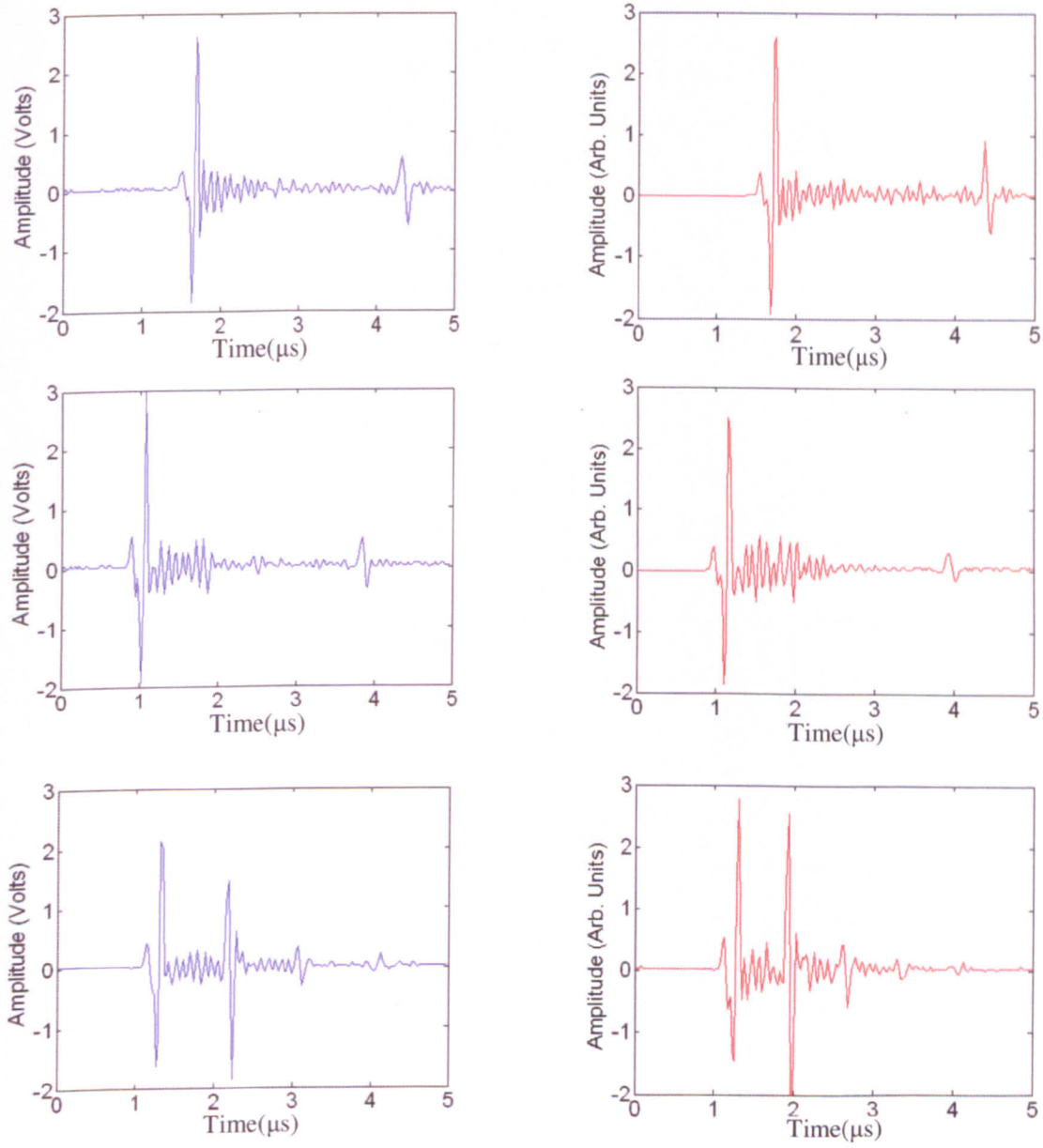

Figure 4.12 Waveforms from experiment (left) and MLM-Propmat (right), low attenuation (top), medium attenuation (middle), high attenuation (bottom).

Figure 4.12 shows that the modelled waveforms compare favourably with the experimental waveforms and that the assumptions made previously, and the material properties used, resulted in a useable representation of real test data. The results presented in figure 4.12 provide a strong indication that the mixture rule proposed produces an A-scan response similar in form to that which may be obtained from experiment, and a more complicated method such as that proposed by Greszczuk (1971) and Martin (1977). These results also provide confidence that the model in its current form can accurately provide predictions of the A-scan for differing concentrations of scatterers.

4.6 Conclusions

The original transfer matrix code written by Freemantle was developed to work in the Windows® environement. Changes were made to the code to allow any chosen number of layers to be given as an input and simulated. The functionality of this converted code was tested against the original benchmarks, and the code was found to be functioning satisfactorily. Simple models of material properties were derived, which in conjunction with a novel transducer model and knowledge of the composite structure allowed structures to be modelled which gave results similar to other results modelled on the same structure. Comparisons were made between *MLM-Propmat* and results obtained experimentally. The results presented were encouraging in that the multi-layer propagation model *MLM-Propmat* gives simulated A-scans that are close in form to experimental data from a CFRP panel with porous inclusions. The model provides a flexible platform for the rapid simulation of A-scan data for any defined panel lay-up, with or without porosity included, and will be used in future chapters to gain an insight

into how the ultrasonic responses of defects interact with the normal ultrasonic response to produce significant signals.

In the next chapter the *MLM-Propmat* model is used to develop an algorithm which allows time domain analysis of the signal received from a composite structure through the use of envelope analysis. The method employs filters to suppress the ply resonance and remove visco-elastic losses. Experimental results are analysed and it is found that in the time domain the presence of a thick resin layer can produces a response similar to porosity.

Chapter 5

Location of Porosity in Three Dimensions: Envelope Analysis

5.1 Introduction

Whilst current non-destructive methods for identifying porosity within carbon fibre reinforced panels (CFRPs) are reliable for locating faults in two dimensions they are unable to locate the depth of anomalous features within the CFRP. Also, a back wall echo is required to conduct the analysis, and this signal may not always be available in, for examples, some aircraft rudder assemblies. There is a need to identify where faults occur within the depth of a CFRP; this information will allow scrutiny by materials engineers and stress analysts to discover how the manufacturing process may be changed to eliminate the introduction of these faults, as well as to determine whether these defects are critical to the structure. With increasing use of CFRPs in more complex shapes it is becoming increasingly more difficult to conduct analysis which requires a back wall echo to draw a conclusion. Methods are therefore essential which do not need a back wall echo for their success; such a method would allow the relatively simple process of pulse-echo analysis to be employed without resulting to more complex, time consuming and expensive techniques.

In this chapter a background review of the parameters governing the expected signal structure is given. Further to this an explanation of the Hilbert transform and its application in this setting is given; also, a review is included of filtering techniques which were needed to prepare the signal for further analysis. Methods for displaying the results of the filtering techniques are then examined. The organisation of the system

developed for A-scan analysis is then detailed, followed by a trial of the technique to assess its effectiveness for locating defects within real CFRPs. A technique to calibrate the signal by giving the instantaneous reflection coefficient for a volume in space derived from the unmodified Hilbert Transform is also presented. The potential was investigated for a system which could utilise this method to estimate a back wall echo where one was not present. Finally, conclusions are drawn and the effectiveness of the new system is assessed.

5.2 Expected Signal Structure

Before the designing a system to detect changes within the structure, it is necessary to determine what effects would be expected within the received signal. The study will focus on compression wave ultrasound, this being the mode in use for the majority of non-destructive tests on composite components.

The technique used for ultrasonic evaluation of a material is the pulse-echo method in which a short pulse of ultrasound is propagated into a sample. This propagates until it meets a boundary between two different materials, for example epoxy resin and carbon fibre. When the pulse meets a boundary the energy is split between that which is transmitted into the next medium and that which is reflected back to the source. An example of a three layer system showing the first three reflections received is given in figure 5.1.

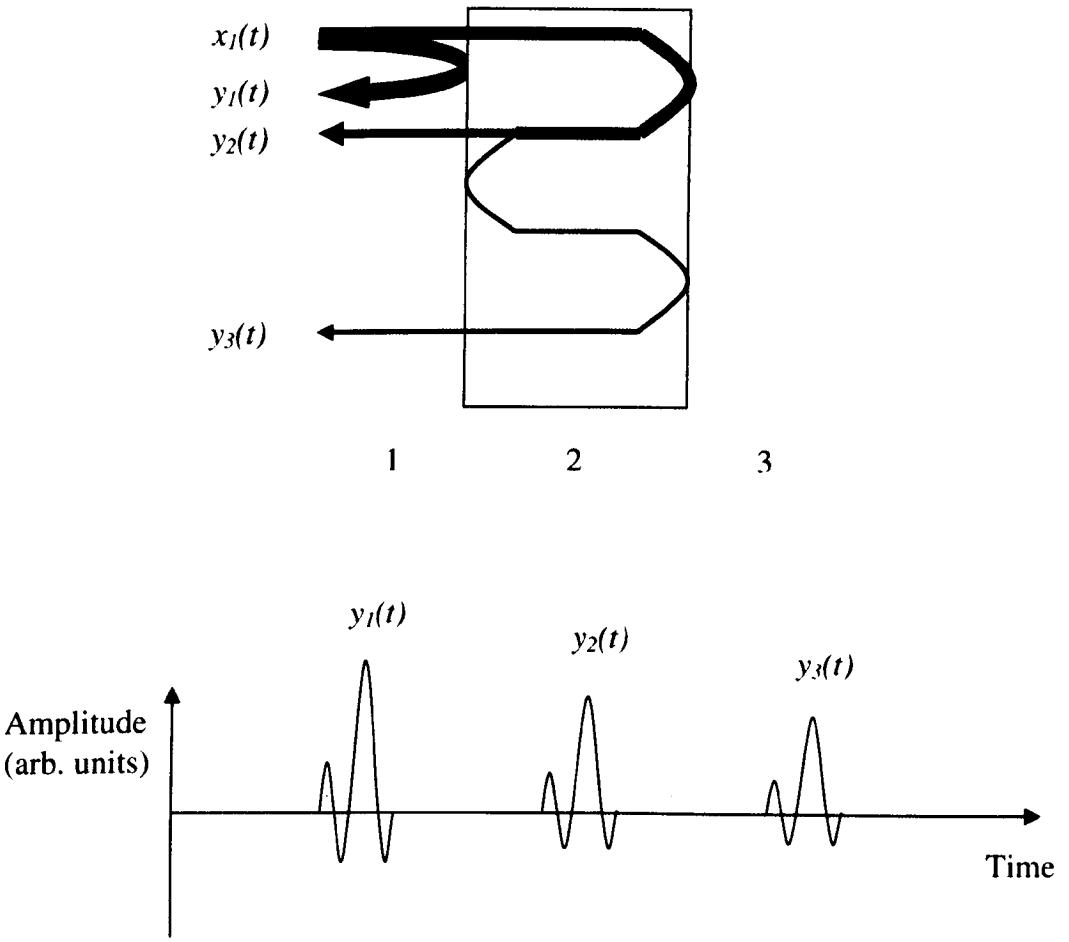

Figure 5.1 The path taken by an ultrasonic pulse in a three layered system (top) and the response obtained (bottom).

As may be seen in figure 5.1, when a signal $x(t)$ is transmitted into the structure reflections from the various boundaries are received back at the transmitter. An ultrasonic scan of this type is known as an A-scan. Other types of ultrasonic scans are the B-scan where a transverse section of the test subject is taken by combing many A-scans, and the C-scan where data is collected from A-scans in 2 dimensions to form an image of the test sample at a specific depth. It is possible to determine the amplitude of the peaks at each boundary which depend on a reflection coefficient determines how much of the energy is transmitted into the medium and how much is reflected. For the pressure associated with the wave this is defined as:

$$r_{ij} = \frac{Z_j - Z_i}{Z_j + Z_i} \tag{5.1}$$

Where Z is the acoustic impedance of the medium, subscript i represents the medium in which the wave is incident and subscript j represents the medium into which part of the incident energy is transmitted. The numerical value of the acoustic impedance of the medium may be calculated if the density of the medium and the speed of sound in the medium are known:

$$Z = \rho c \tag{5.2}$$

The speed of sound in the material may itself be defined in terms of the physical properties of the medium:

$$c^2 = \frac{M}{\rho} \tag{5.3}$$

Where M is the modulus governing propagation, which for compression waves is defined by:

$$M = K + \frac{4G}{3} \tag{5.4}$$

Where K is the bulk modulus and G is the shear modulus. Given these equations it is possible to derive an expression for the amplitude of the first peak $y_1(t)$:

$$y_1(t) = r_{12}x(t) \tag{5.5}$$

Where r_{12} is the reflection coefficient from medium one to medium two. The corresponding transmission coefficient is:

$$t_{12} = \frac{2Z_2}{Z_1 + Z_2} \tag{5.6}$$

The magnitude of the peak $y_2(t)$ expressed in the frequency domain yields $Y_2(\omega)$:

$$Y_2(\omega) = t_{12}r_{23}t_{21}H(\omega)X(\omega) \tag{5.7}$$

$H(\omega)$ is a frequency function representing compression wave propagation in a homogenous isotropic material. $H(\omega)$ has the form:

$$H(\omega) = e^{-\alpha(\omega)x}e^{-j(x/c(\omega))} \tag{5.8}$$

$\alpha(\omega)$ is the frequency dependent absorption coefficient and $c(\omega)$ is the phase velocity which generally shows a small dependence on frequency, causing a slight dispersion in the frequency components in the pulse. x is the twice the thickness of layer 2 when considering pulse-echo. The attenuation caused by $\alpha(\omega)$ arises from viscoelastic losses and also from scattering of the wave within the substance. To summarize, we would expect consecutive peaks to show a decay in amplitude based upon a geometric progression, any deviation from this expected result would expose changes to the

attenuation slope which are present as a result of an unexpected structure within the component; this could be a consequence of localized porosity or fibre-resin effects.

5.3 Determination of the Envelope of the Signal

In order to identify the time of arrival of anomalous peaks in an A-scan it is necessary to perform an analysis that yields the envelope of the signal. In the days of analogue flaw detectors this was achieved by a simple diode-plus-filter amplitude demodulator. Where software based analysis is used, as in all modern testing instruments, more sophisticated and better, methods become available. In this section we present the Hilbert transform as our chosen method. For completeness, this is followed by a software based amplitude demodulation, and a comparison is made between the two.

5.3.1 Hilbert Transform

The Hilbert transform is based on the relationship between the real and imaginary parts of causal signal. It is used first to produce an analytic signal followed by the effective signal envelope.

The mathematical representation of the Hilbert transform is as follows:

$$\hat{s}(t) = \int_{-\infty}^{\infty} s(\tau)h(t-\tau)d\tau \qquad \textbf{(5.9)}$$

where,

$$h(t) = \frac{1}{\pi\ t} \tag{5.10}$$

In order to understand the process of a Hilbert transformation it is useful to remind oneself of how simple signals are represented in the frequency domain.

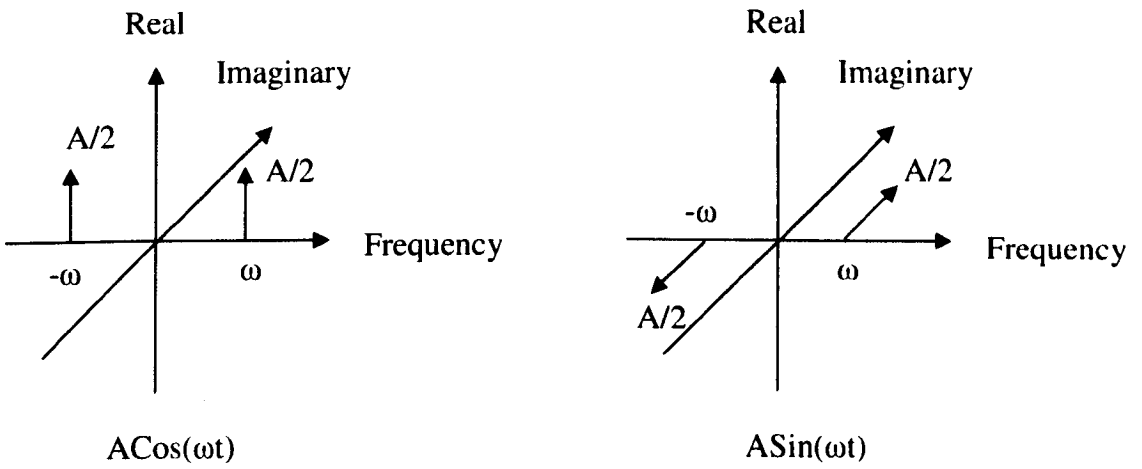

Figure 5.2 Frequency domain representation of cosine and sine waves at a single frequency.

Figure 5.2 shows that if the amplitude and frequency of the cosine and the sine wave are the same then the only difference is that the sine wave is entirely in the imaginary plane, the positive frequency component on the positive part of the imaginary plane (+*j*), the negative frequency component on the negative part of the imaginary plane (-*j*), whilst the cosine wave is entirely in the real plane. The Hilbert transform shifts all positive frequency components by +90 degrees about the frequency axis, and all negative frequency components by -90 degrees. If we consider the case of a cosine wave at a single frequency, the result of the Hilbert transform is a sine wave at the same frequency. If this process is repeated the results are as follows:

$$\cos(\omega t) \longrightarrow \sin(\omega t) \longrightarrow -\cos(\omega t) \longrightarrow -\sin(\omega t) \longrightarrow \cos(\omega t)$$

Figure 5.3 Results of repeated Hilbert Transforms on a simple cosine wave.

The analytic signal is the complex signal created by the addition of the Hilbert transform to the original signal and is defined as follows:

$$g_+(t) = g(t) + j\hat{g}(t) \tag{5.11}$$

If we determine the analytic signal for a simple cosine wave at a single frequency, the use quickly becomes apparent.

$$g_+(t) = \cos(\omega t) + j\sin(\omega t) = e^{j\omega t} \tag{5.12}$$

The result is a phasor and this is represented in the frequency domain as follows:

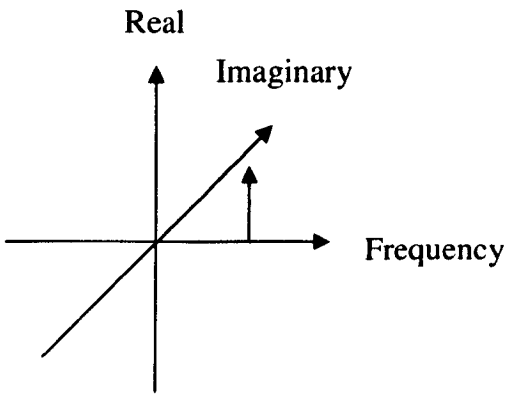

Figure 5.4 Representation of a positive phasor in the frequency domain.

Similarly for a sine wave:

$$g_+(t) = \sin(\omega t) + j\cos(\omega t) = e^{-j\omega t} \tag{5.13}$$

The analytic signal for a sine wave is also a phasor, albeit a negative complex exponential. This highlights the useful property of analytic signals – although the sine and cosine have a two sided spectrum the analytic signal always has a one-sided spectrum which is in the positive frequency part of the frequency domain.

Following on from this we can define a property known as the complex envelope of the signal:

$$\tilde{g}(t) = g_+(t)e^{-j\omega_c t} \tag{5.14}$$

That is the analytic signal multiplied by a phasor at the carrier frequency; multiplication with a phasor in the time domain results in a frequency shift in the frequency domain, in this case the shift is to the baseband removing the carrier frequency and resulting in the complex envelope of the original signal. Taking the magnitude of this gives the envelope across the real and imaginary axes. To simplify, if a signal consists of the sum of a sine and cosine (represented in the real and imaginary planes of the frequency domain), then taking the Hilbert transform and then the complex envelope gives the instantaneous magnitude of the signal. This is easier to see in diagrammatic form:

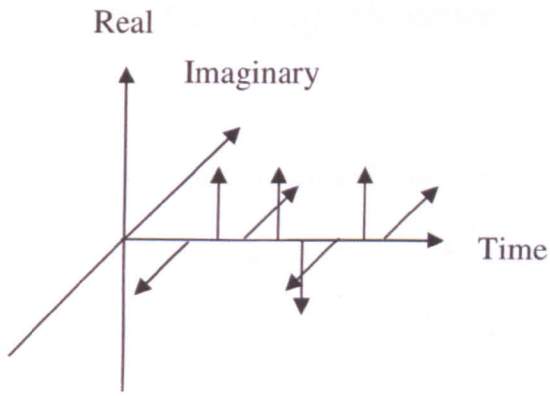

Figure 5.5 Phasor representation of a signal varying in time.

It is sometimes more convenient to imagine the envelope detection process using the Hilbert transform as the surface which would be created if a helix was added to the above diagram connecting all of the phasors. The magnitude of the helix is equivalent to taking a cross-section of this surface along the real axis. A sample waveform from experimental data and its Hilbert transform are shown in figure 5.6.

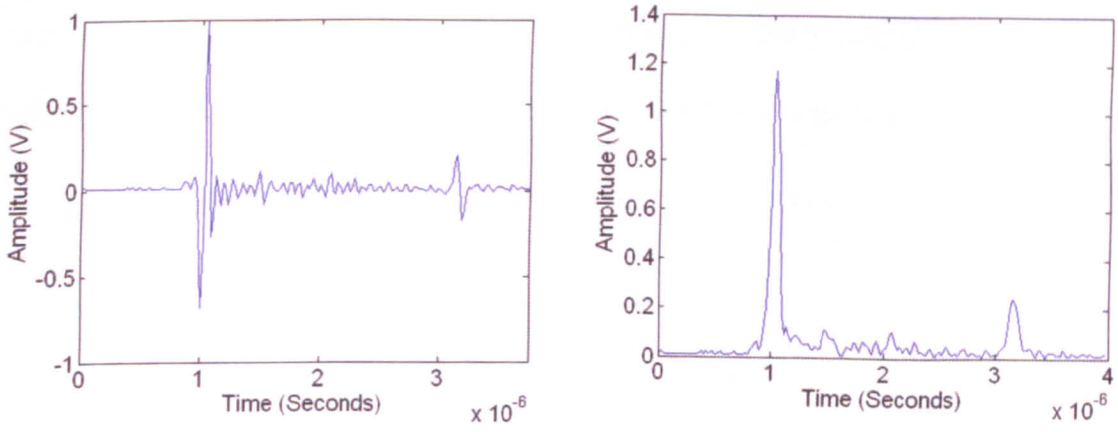

Figure 5.6 Typical waveform before Hilbert Transform (Left) and after Hilbert Transform (Right).

5.3.2 Alternative Method of Envelope Detection

Although the Hilbert transform method described above is a very accurate method of determining the envelope of the signal, it does require Fourier transformation of the signal. Although application of this process may not take a long time in isolation, performing many iterations could slow down the operation of the analysis system. A faster approximation to this method may be needed; one such method is based on amplitude demodulation. We imagine that the segment of the A-scan signal between front wall and back wall echoes can be represented as a conventional amplitude modulated (AM) record as shown in figure 5.7a.

$$x(t) = K[1 + m\cos\omega_m t]\cos\omega_c t \tag{5.15}$$

Here ω_m represents one component of the modulating envelope and ω_c represents the carrier, which we regard as the oscillatory components due to interply resonances. We require to detect the envelope components ω_m, and this is achieved by squaring $x(t)$ in the time domain. For convenience we set K=1; $x^2(t)$ becomes

$$\begin{aligned} x^2(t) = {} & \frac{m^2}{2} + \frac{1}{2} + m\cos\omega_m t + \frac{m^2}{4}\cos 2\omega_m t + \left(\frac{m^2}{4} + \frac{1}{2}\right)\cos 2\omega_m t \\ & + \frac{m}{2}\cos(2\omega_c t - \omega_m t) + \frac{m}{2}\cos(2\omega_c t + \omega_m t) \\ & + \frac{m^2}{8}\cos(2\omega_c t - 2\omega_m t) + \frac{m^2}{8}\cos(2\omega_c t + 2\omega_m t) \end{aligned} \tag{5.16}$$

This spectrum is plotted on figure 5.7b with m set to 0.5.

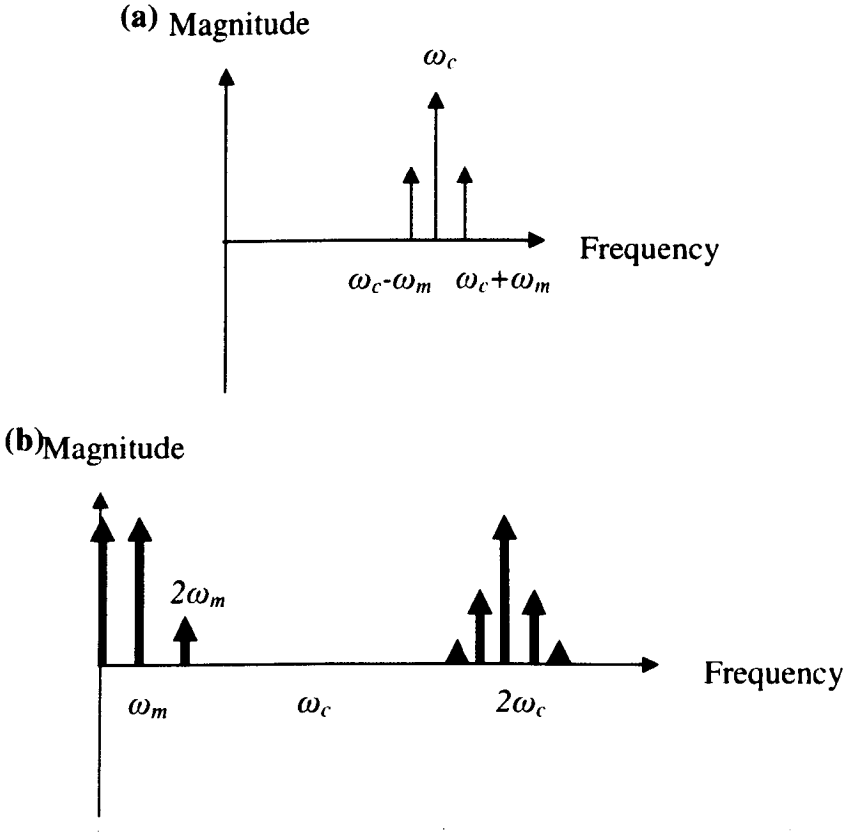

Figure 5.7 (a) The original spectrum of an ideal amplitude modulated signal; (b) The result of envelope detection by square-law demodulation.

On the figure we identify a large zero frequency component and a dominant component at ω_m, which represents the signal envelope. There are also components at twice the carrier frequency, together with sidebands at $\pm\omega_m$ and $\pm 2\omega_m$. The small component at $2\omega_m$ will distort the measure of the amplitude of ω_m. In order to extract ω_m a bandpass filter will be required to reject dc and the components around $2\omega_c$. The square root of the signal is then taken to give the original magnitude of the amplitude. This method is advantageous since it can be carried out in the time domain and is hence much faster. Unfortunately the signal is not as detailed as the envelope detection method using the Hilbert transform.

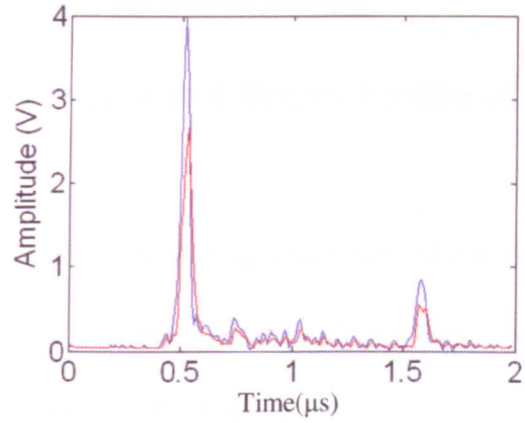

Figure 5.8 Comparison of methods of envelope detection – Hilbert Transform (Blue Line), amplitude demodulation (Red Line).

Figure 5.8 shows that although the amplitude modulation method provides a good estimation to the envelope of the signal some definition is lost in terms of the measured amplitude of the envelope. This is because some of the energy is removed by the band pass filter identified previously. In practice this method works for signals where the change in amplitude is relatively large, however, it was found in practice that this method was less sensitive to smaller changes in amplitude. The changes in amplitude in the time domain signal that are caused by the presence of porosity tend to be quite subtle and hence as high a definition of the envelope as is possible is required. Consequently the original Hilbert transform method was employed since if a small number of points were used in the FFT array then extra time taken to determine the Hilbert transform was negligible.

5.4 Filter Requirements and Specification

5.4.1 Low-Pass Filter Design and Determination of Parameters

Whilst the Hilbert transform results in a representation of the change of the envelope of the signal, further processing is required to provide a signal which is suitable for automated analysis for the identification of features.

It can be seen in Figure 5.6 that many small peaks occur in the transformed waveform as well as the principal peaks. These small peaks could be regarded merely as high frequency noise, although they most probably represent the expected back-scattering behaviour of the multi-layered composite which results from inter-ply resources. Figure 5.9 shows the result from another A-scan, in which the time domain peaks in the signal show as ripples after the first noise peak. If such ripples are thought not to be of diagnostic significance then an appropriate low-pass filter is required to remove them. In order to properly specify such a filter the expected frequencies back-scattered in the A-scan have been examined using *MLM-Propmat* as outlined in Chapter 4.

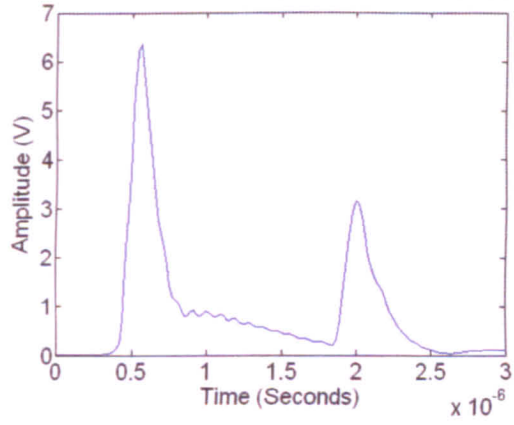

Figure 5.9 Signal after Hilbert Transform demonstrating high frequency ripple after the first principal peak.

The theoretical frequency response for a sample with 4 plies per mm is shown in figure 5.10, which

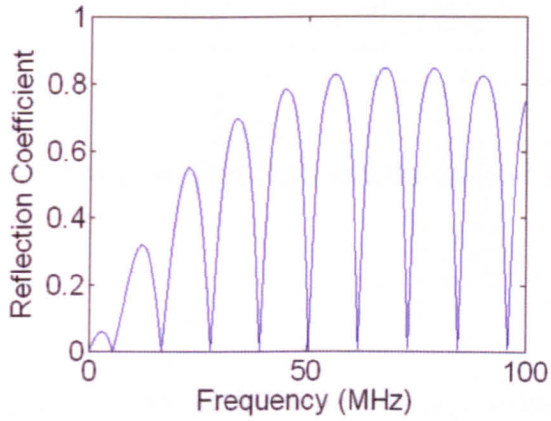

Figure 5.10 Theoretical frequency response for a sample with 4 plies per mm.

shows resonant peaks of differing magnitude, the high frequency ripple present in the signal shown in figure 5.9, is due to the second resonant peak around 12 MHz. This may be removed by simply low pass filtering the signal, removing the second and all subsequent resonances, whilst preserving the information contained within the first resonance. The simplest low pass filter is modelled on a first order Butterworth resistor-capacitor network. The circuit diagram and the transfer function of the filter are shown in figure 5.11.

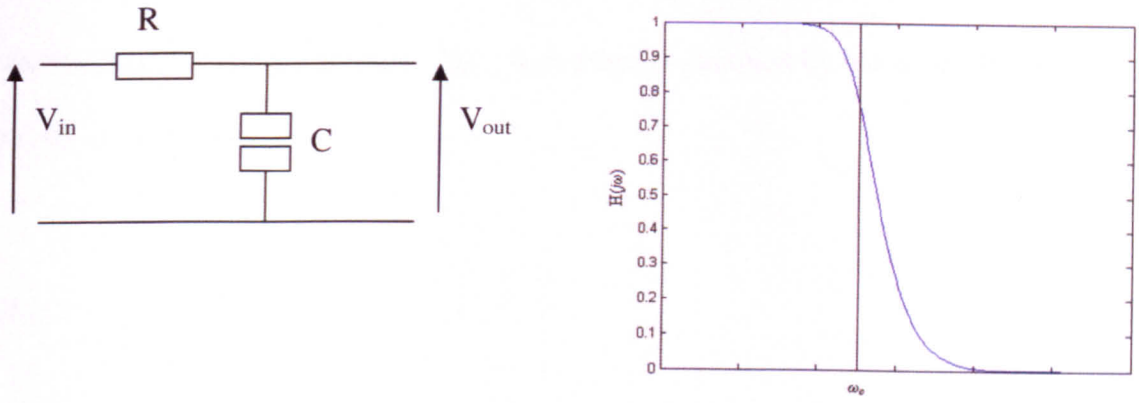

Figure 5.11 A simple RC low pass filter (left) and the transfer function of the filter (right).

For a Butterworth filter the gradient of the slope ($\omega > \omega_c$) is determined by the order of the filter. To increase the order of the filter additional poles are added to the s-plane. For the simplest case of a first order filter the slope is 20dB/decade and the transfer function is given below.

$$H(s) = \frac{\omega_0}{s + \omega_0} \tag{5.17}$$

Where ω_0 is the cut-off frequency which cuts at 3dB ω_0. A Butterworth filter was chosen due to its simplicity, providing easy implementation digitally. The filter provides good pass band characteristics, with no "ripple", and performs better than other filter types (i.e. Chebyshev). The phase response for this type of first order Butterworth filter is more linear in the pass band than other comparable filter types and "rolls-off" from 0 to -45 degrees at ω_0.

In order to use this filter digitally a z-transform is used to derive a recurrence relationship in the time domain. The z-transform is obtained by use of the bilinear transform as follows:

$$H(z) = \frac{\omega_0}{\frac{2}{T}\left[\frac{1-z^{-1}}{1+z^{-1}}\right] + \omega_0} \tag{5.18}$$

Where T is the time period between samples. This is equivalent to:

$$\frac{Y(z)}{X(z)} = \frac{\omega_0}{\frac{2}{T}\left[\frac{1-z^{-1}}{1+z^{-1}}\right] + \omega_0} \tag{5.19}$$

Rearranging yields:

$$\frac{2}{T}Y(z) - \frac{2}{T}Y(z)z^{-1} + \omega_0 Y(z) + \omega_0 Y(z)z^{-1} = \omega_0 X(z) + \omega_0 X(z)z^{-1} \tag{5.20}$$

Solving for Y(z) gives:

$$Y(z) = \frac{\frac{2}{T}Y(z)z^{-1} - \omega_0 Y(z)z^{-1} + \omega_0 X(z) + \omega_0 X(z)z^{-1}}{\frac{2}{T} + \omega_0} \tag{5.21}$$

From which follows the recurrence relationship in the time domain:

$$y(n) = \frac{\frac{2}{T}y(n-1) - \omega_0 y(n-1) + \omega_0 x(n) + \omega_0 x(n-1)}{\frac{2}{T} + \omega_0} \tag{5.22}$$

Rearranging gives:

$$y(n) = ay(n-1) + b[x(n) + x(n-1)] \tag{5.23}$$

Where,

$$a = \frac{1 - \frac{\pi\omega_0}{\omega_s}}{1 + \frac{\pi\omega_0}{\omega_s}} \qquad b = \frac{\frac{\pi\omega_0}{\omega_s}}{1 + \frac{\pi\omega_0}{\omega_s}}$$

Where ω_s is the sampling frequency. By carefully selecting ω_0 the ripple caused by the second resonance can be removed; ω_0 is set so that the second resonance is 40dB below the pass band of the filter, removing it completely.

The filter was extensively tested with theoretical data for various values of plies per mm, to determine the optimum value of ω_0. It was found that the first order performance in terms of magnitude (slope of 20dB/decade) was sufficient to remove the undesired frequency components. Figure 5.12 shows an experimentally generated signal after application of the Hilbert Transform and low pass filter.

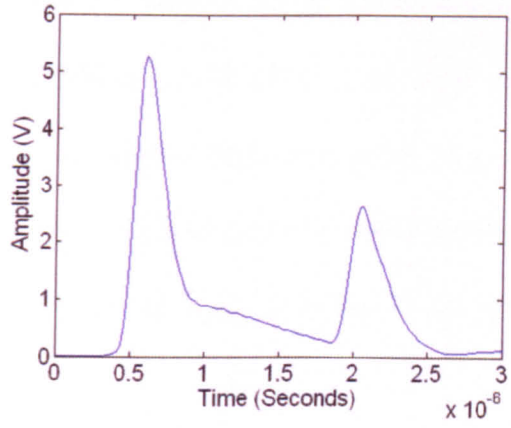

Figure 5.12 Modelled data for a sample of 4 plies per mm, 20 plies thick, after application of the Hilbert Transform and low pass filter.

By modelling the frequency response for one ply for various values of plies per mm, and assuming constant resin layer thickness, the values of the frequency of the first and second resonant peaks were obtained. This was achieved by using a simple MATLAB function which determined the frequency of each of the peaks. The error associated with this calculation is related to the number of points used in the frequency arrays of the model. In this case 2048 points were used to represent 50 MHz. The calculation error is simply ± ½ of the frequency spacing (error of ± 0.012 MHz). The results of this analysis are shown in table 5.1.

Plies per mm	First Resonant Peak (MHz) (f_1)	Second Resonant Peak (MHz) (f_2)
1	0.4	1.6
2	0.8	3.2
4	1.6	6.4
8	3.2	12.9
16	6.4	25.7

Table 5.1 Values of the resonant frequency for differing values of plies per mm.

The most commonly occurring structures are of 4 or 8 plies per mm, for which the same value of f_0 may be used (5 MHz). For numbers of plies per mm higher than this a higher value of f_0 must be used since the first resonant peak occurs at a higher frequency and using this filter would result in loss of information from the first resonant peak. When applied to experimental data similar results are obtained as shown in figure 5.13.

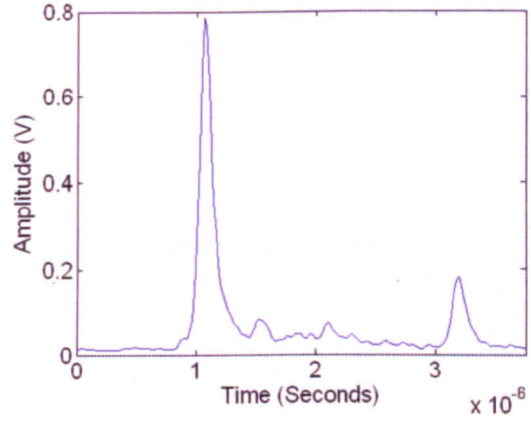

Figure 5.13 Experimental data, a 4 plies per mm CFRP 31 plies thick – f_{r2} = 6.43 MHz, f_0 = 5 MHz.

5.4.2 Removal of Falling Trend

A normal signal response for a CFRP with no significant features such as porosity has an approximately exponential decay in signal amplitude between the peak which represents the front wall echo and the peak which represents the back wall echo. This decay is caused by reflections between the layers within the composite as well as attenuation of the signal within these layers. Any features that are present within the structure, for example due to porosity, will appear as either a peak or a trough within this decay. The major obstacle to automated identification of these variations is the

slope of the decay itself. If it were possible to remove this slope then any variations will be easier to identify. If we assume that the decay is exponential then:

$$h(t) = e^{\frac{-t}{\tau}} \tag{5.24}$$

If this is transferred to the s-plane then we get the following equation:

$$H(s) = \frac{\omega_0}{s + \omega_0} \tag{5.25}$$

To remove the slope we multiply this by the inverse:

$$H(s) = \frac{s + \omega_0}{\omega_0} \tag{5.26}$$

This equation can then be transformed onto the z-plane and a recurrence relationship derived to allow the function to be used digitally. Performing the bilinear transform results in:

$$H(z) = \frac{\frac{2}{T}\left[\frac{1 - z^{-1}}{1 + z^{-1}}\right] + \omega_0}{\omega_0} = \frac{Y(z)}{X(z)} \tag{5.27}$$

Which simplifies to:

$$\omega_0 Y(z) + \omega_0 Y(z)z^{-1} = \frac{2}{T}X(z) - \frac{2}{T}X(z)z^{-1} + \omega_0 X(z) + \omega_0 X(z)z^{-1} \quad \textbf{(5.28)}$$

Solving for *Y(z)*:

$$Y(z) = \frac{\frac{2}{T}X(z) - \frac{2}{T}X(z)z^{-1} + \omega_0 X(z) + \omega_0 X(z)z^{-1} - \omega_0 Y(z)z^{-1}}{\omega_0} \quad \textbf{(5.29)}$$

Converting back into the time domain gives:

$$y(n) = \frac{\frac{2}{T}x(n) - \frac{2}{T}x(n-1) + \omega_0 x(n) + \omega_0 x(n-1) - \omega_0 y(n-1)}{\omega_0} \quad \textbf{(5.30)}$$

Rearranging gives:

$$y(n) = a_0 x(n) + a_1 x(n) - by(n) \quad \textbf{(5.31)}$$

Where,

$$a_0 = \frac{\omega_s}{\pi\omega_0} + 1 \qquad a_1 = 1 - \frac{\omega_s}{\pi\omega_0} \qquad b = \omega_0$$

This recurrence relationship was initially tested on an exponential curve generated in Matlab®, the result was a horizontal line provided that the correct value of ω_0 was chosen. If the value of ω_0 chosen was too low then the filtered signal followed the

original signal, however, if the value of ω_0 was greater than the optimum value (ω_{opt}) then the filtered signal began to resemble the inverse of the original signal, as shown in figure 5.14.

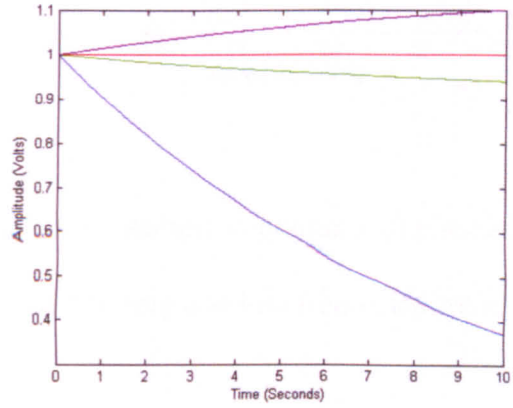

Figure 5.14 Response of the filter to an exponential decay. The blue line is the original signal, the red line is the optimum value of ω_0, the purple line is for $\omega_0 < \omega_{opt}$, the green line is for $\omega_0 > \omega_{opt}$.

To determine which value of ω_0 to use a routine was devised which analysed the output of the filter. The average of the first five points of the output was compared to the average of the last five points of the output. If the first average was higher than the second average then the value of ω_0 which was chosen was too low, if the opposite was true then the value was too high. The value was then adjusted automatically and the filter reapplied to the original signal. Once the averages were within a specified percentage difference of each other (5%), then the corresponding value for ω_0 was used. The filter was then tested with modelled data. An example is shown in figure 5.15.

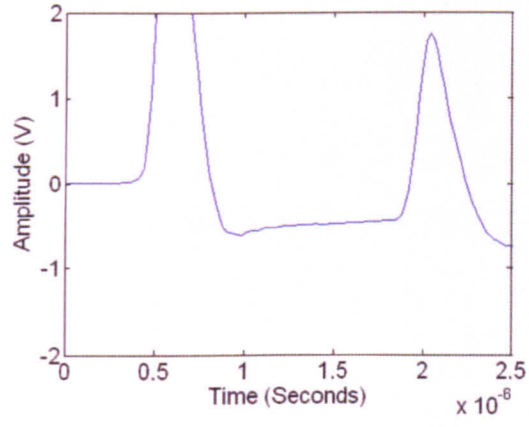

Figure 5.15 Modelled data for a sample containing 20 plies at 4 plies per mm, after Hilbert Transform, low pass filtering and low frequency trend removal.

Although the filter was able to produce the desired effect, the frequency required varied from sample to sample, sometimes the process of calculating the correct value of ω_0 to use greatly delayed the processing of the signal. Finally, the extra variations in the signal caused by variations in the resin thickness in real data made it almost impossible to reliably remove the exponential slope present in the signal. Therefore, whilst the filter worked well for theoretical data and could produce excellent results for experimental data given appropriate time to calculate parameters, it was felt that another faster and more reliable method was needed.

5.4.3 High-Pass Filter Design and Determination of Parameters

If we consider the approximation of the decay in amplitude of the signal cause by reflections and attenuation within a CFRP:

$$y(t) = e^{\frac{-t}{\tau}} \tag{5.32}$$

If τ is large then the equation approximates to a straight line with a constant gradient. Given this, then taking the derivative of the signal will give a horizontal line, any variations in the signal due to features within the structure will be revealed since they will appear as deviations from the constant gradient.

Differentiation may be achieved by high pass filtering the signal providing the cut off frequency is low enough to not interfere with the first resonant peak. The structure of a simple high pass filter is very similar to the structure of a simple low pass filter. A first order high pass filter constructed from a resistor-capacitor network, and the transfer function of the system is shown in figure 5.16.

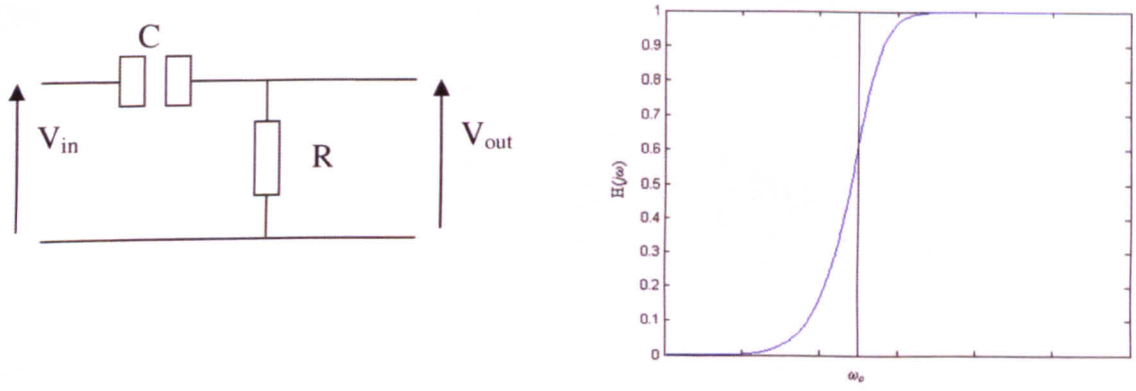

Figure 5.16 A simple RC high pass filter (left) and the transfer function of the filter (right).

The transfer function for the filter is shown below:

$$H(s) = \frac{s}{s + \omega_0} \tag{5.33}$$

In a similar fashion to the low pass filter derived earlier, a z-transform must be performed before a recurrence relationship can be obtained for use in the time domain.

The phase response for this type of first order Butterworth filter is also 0 degrees in the pass band and "rolls-off" to +45 degrees at ω_0.

Applying the bilinear transform gives:

$$H(z) = \frac{\frac{2}{T}\left[\frac{1-z^{-1}}{1+z^{-1}}\right]}{\frac{2}{T}\left[\frac{1-z^{-1}}{1+z^{-1}}\right]+\omega_0} = \frac{Y(z)}{X(z)} \tag{5.34}$$

This simplifies to:

$$\frac{2}{T}Y(z)-\frac{2}{T}Y(z)z^{-1}+\omega_0 Y(z)+\omega_0 Y(z)z^{-1} = \frac{2}{T}X(z)-\frac{2}{T}X(z)z^{-1} \tag{5.35}$$

Solving for *Y(z)*:

$$Y(z) = \frac{\frac{2}{T}X(z)-\frac{2}{T}X(z)z^{-1}+\frac{2}{T}Y(z)z^{-1}-\omega_0 Y(z)z^{-1}}{\frac{2}{T}+\omega_0} \tag{5.36}$$

Transforming back into the time domain:

$$y(n) = \frac{\frac{2}{T}x(n) - \frac{2}{T}x(n-1) + \frac{2}{T}y(n-1) - \omega_0 y(n-1)}{\frac{2}{T} + \omega_0} \tag{5.37}$$

Rearranging gives:

$$y(n) = ay(n-1) + b[x(n) - x(n-1)] \tag{5.38}$$

Where,

$$a = \frac{1 - \frac{\pi\omega_0}{\omega_s}}{1 + \frac{\pi\omega_0}{\omega_s}} \qquad b = \frac{1}{1 + \frac{\omega_0}{\omega_s}}$$

On the basis of table 5.1 (first resonant peak) it is possible to select a value for ω_0 that will always be appropriate no matter what number of plies per mm within the CFRP. A value for ω_0 of 100 kHz was chosen to be below all of the significant peak frequencies. This was then tested extensively with theoretical as well as experimental data, to ensure adequate functionality. Examples of the responses obtained are shown in figure 5.17.

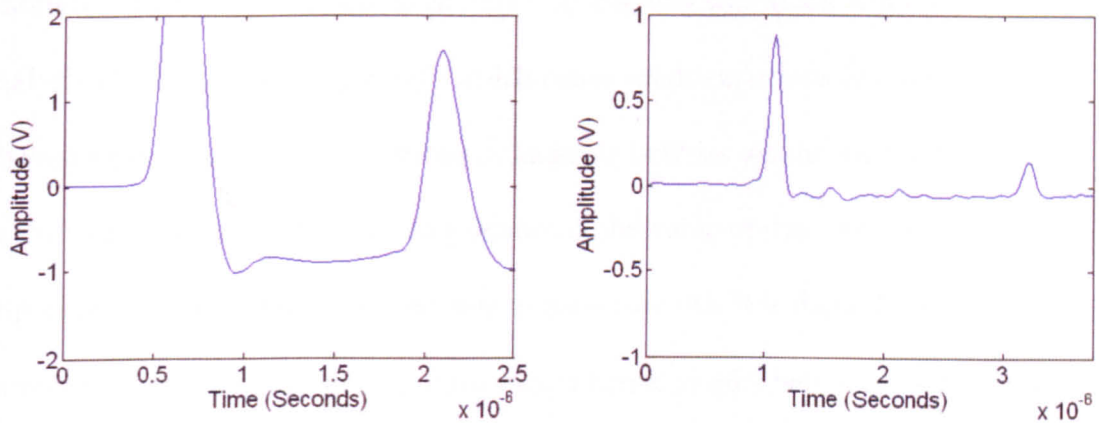

Figure 5.17 Modelled data 4 plies per mm, 20 plies thick, after Hilbert Transform, low pass filtering and high pass filtering (left). Experimental data, a 4 plies per mm CFRP 31 plies thick – $f_{r2} = 6.43$ MHz, $f_0 = 5$ MHz (right).

Figure 5.17 shows that the high pass filter removes the low frequency trend resulting in a near-horizontal base line. Changes in amplitude slope will be reflected in this line as either peaks or troughs. The filter was therefore suitable for use in the analysis system.

5.5 Identification and Classification of Features within the Signal

Having developed a system to reliably process the signal ready for analysis it was necessary to devise a method of identifying features in the signal. To enable the identification of features, first critical flaws or "showstoppers" must be highlighted, since if a critical fault is present then the more subtle considerations such as porosity or changes in fibre-resin effects would not warrant further study. "Showstoppers" refer to large echoes that represent major flaws such as voids or inclusions which, if present, would imply scrapping of the component. It was decided that the most effective way of differentiating between showstoppers and secondary considerations was to assign a colour scale to the processed signal. At low levels this colour scale was to have a high

resolution with lower resolutions at higher levels, this was to allow more detailed analysis of effects such as porosity which cause small variations in amplitude. Showstoppers such as delaminations or large air bubbles would cause a large variation in amplitude at the point which they occurred, the value of this variation is less important; the system must just be able to recognise that it is there. In order to demonstrate this we consider the three experimental results below for a good area, a porous area and a critically flawed area of composite, Figure 5.18.

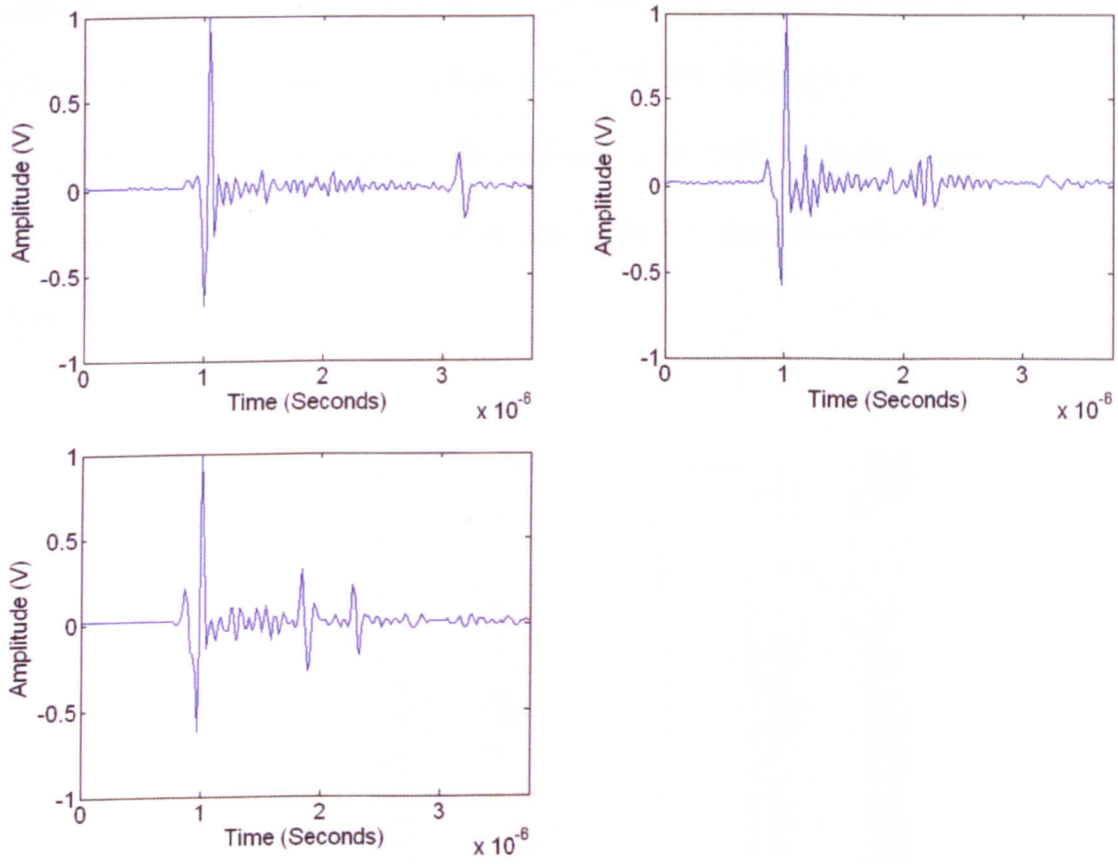

Figure 5.18 Plies per mm, 31 plies CFRP, good area (top left), porous area (top right), critically flawed area (bottom).

From figure 5.18 it can be seen that the critically flawed area requires little further analysis; however, there is much information in the waveforms of the good and porous

area which would warrant detailed analysis to assess the implication of any features within the waveform. A non-linear classification system is therefore required. Fortunately, Andscan® (NDT imaging software package developed by QinetiQ (Farnborough, UK). It is described by Appendix D) has two inbuilt methods which can aid in this process.

First the user can assign different colour palettes to the colour scale. These can be conventional with a gradual change from white to black or alternatively a highly contrasting colour can be placed at any point in the scale. For example green could be moved from the middle of the colour scale to the top. In this case large amplitudes would appear green and would contrast highly with the surrounding colours. This provides a method to identify "showstoppers" easily. Sample colour scales are shown in figure 5.19.

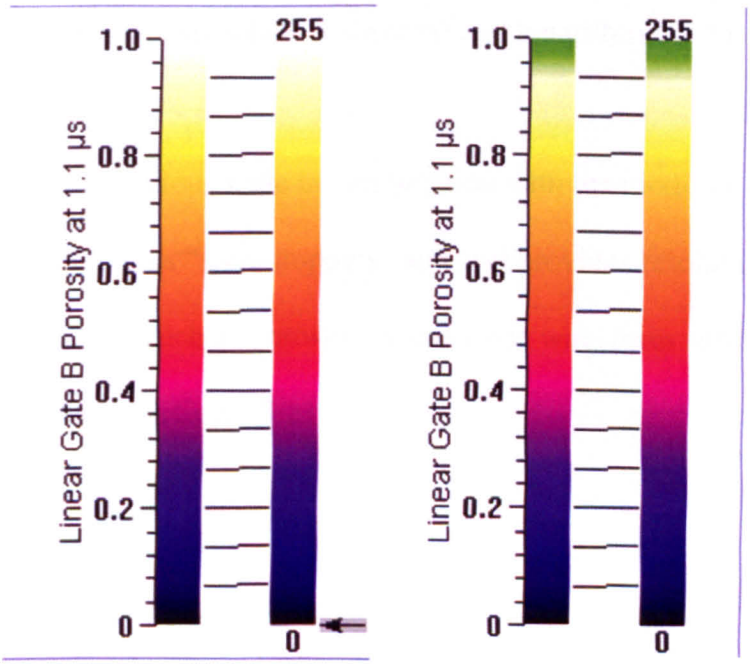

Figure 5.19 Normal Colour Scale (Left) and Modified Colour Scale (Right).

Further to this, the colour scale may be manually adjusted to cover all or part of the amplitude range, and it may also be set to a logarithmic scale to cover the bottom of the amplitude range in greater detail than the top. These colour scales are shown in figure 5.20.

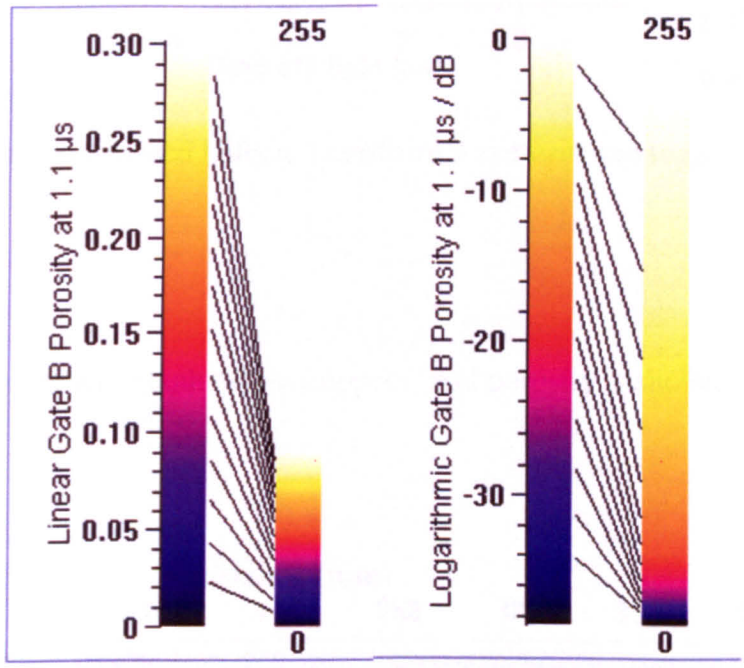

Figure 5.20 Manually adjusted colour scale (left) and logarithmic colour scale (right).

By using the logarithmic colour scale in combination with the modified palette a system is produced which highlights "showstoppers" and still provides resolution to determine changes caused by factors such as porosity. A specimen waveform and the mapping to this colour scale is shown in figure 5.21.

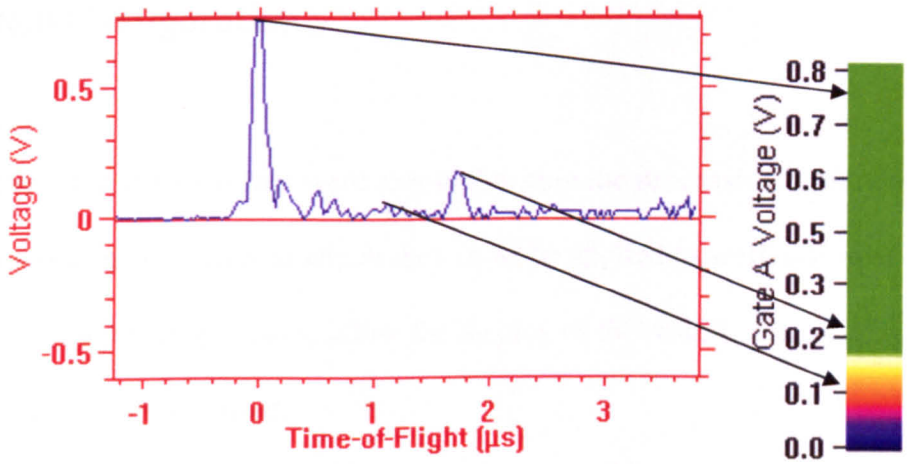

Figure 5.21 Relation between Hilbert Transform waveform and logarithmic colour scale.

A sample B-scan showing both "showstoppers" and porosity is shown in figure 5.22.

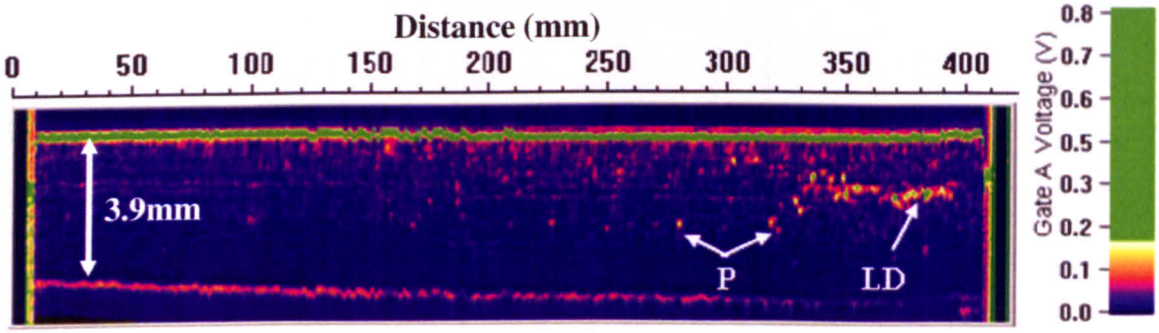

Figure 5.22 A B-scan for a panel containing both large scale defects ("LD") and porosity ("P").

For the detection of large scale defects and porosity the colour scale was set so that the back wall echo is highlighted in green, thus meaning that gross defects such as a delamination should also show in green where as small scale defects like porosity should show in the remaining colours of the colour scale.

5.6 System Configuration

Having identified the steps that were required during the processing of the data it was necessary to define the order in which they must be applied as well as how the software would interact with Andscan® to allow the display of the results. The system model shown in figure 5.23 was used:

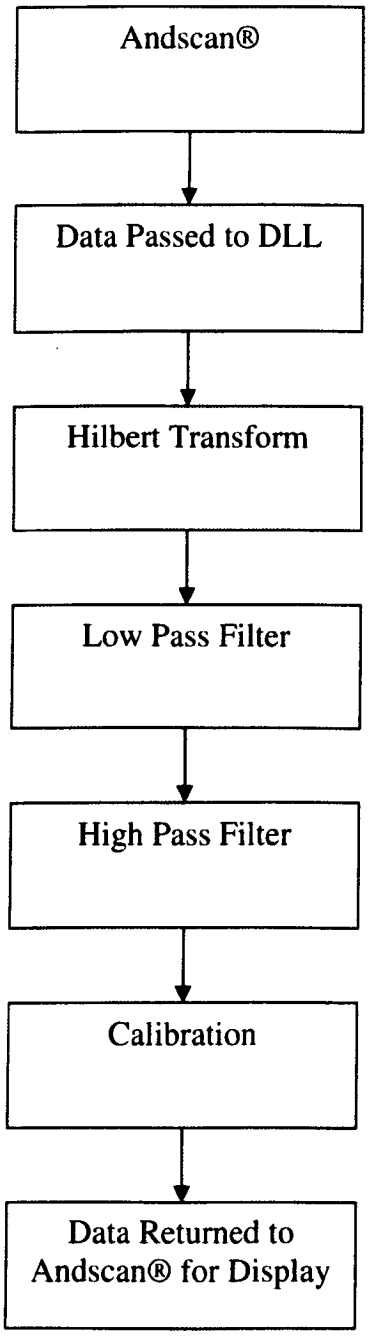

Figure 5.23 System model for analysis of A-scan data.

Data display in Andscan® can be in one of four formats; initially the time-domain waveform for a single point is shown as an A-scan. Secondly this time-domain waveform can be gated to display the amplitude or the time of flight at a particular point within the data set; this data is plotted in two dimensions with a varying colour to represent the parameter being measured (a C-scan). Thirdly the variation in amplitude or time of flight may be presented as a function of one spatial variable against time, this is known as a B-scan.

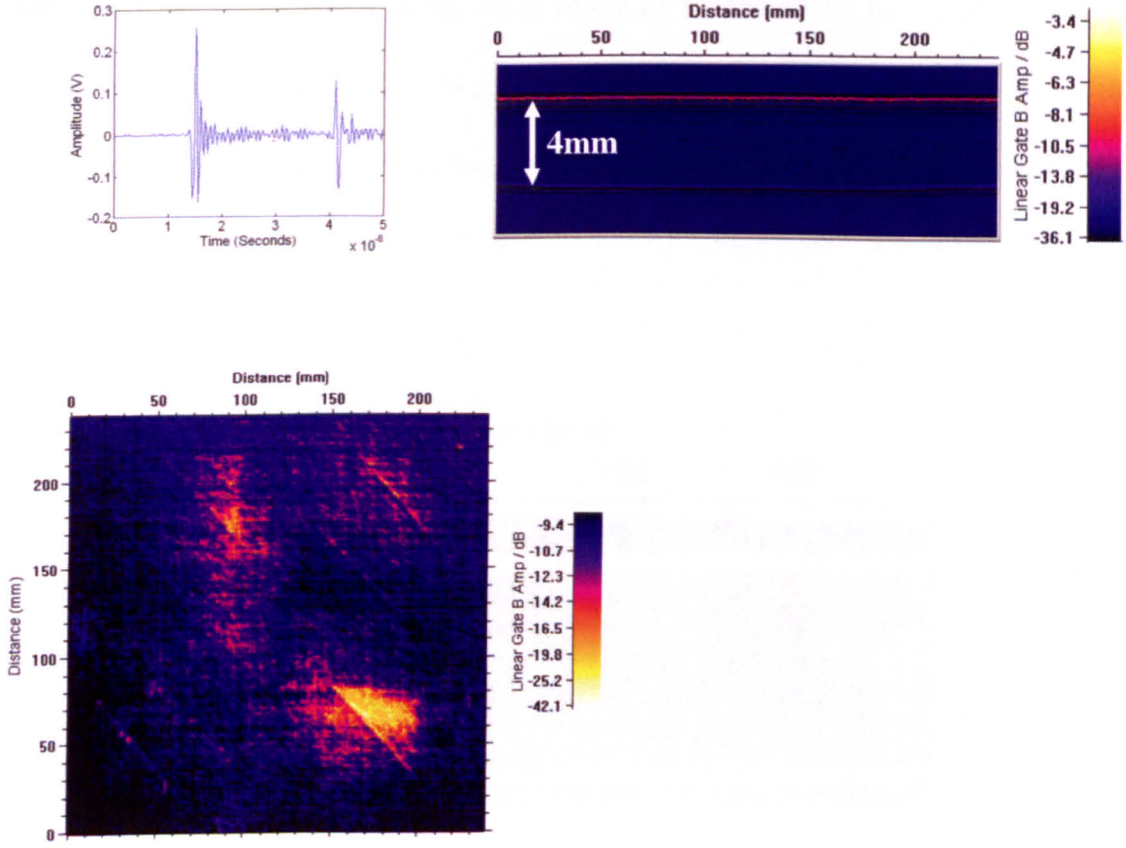

Figure 5.24 A typical A-scan (top left), B-scan (top right) and C-scan (bottom).

Finally, a 3-D profile may be generated by applying a small gate to the waveform and generating C-scans of the amplitude within the gate at each depth. This results in a set

of C-scans for each depth from which B-scans are also generated giving cross sections both horizontally and vertically across the panel.

The use of A-scan data to highlight defects within a CFRP is fraught with difficulties, and so the user must be highly versed in examination of such waveforms, and even then identification may prove difficult as well as time consuming. C-scans are useful for highlighting areas which may require further investigation. For example a plot of back wall amplitude will show the gross attenuation variation over the sample; areas of abnormal attenuation will require further study. This method can be performed rapidly but, it will not reveal where in the depth of the CFRP the defect is, and also it cannot be performed when a back wall echo cannot be obtained. It is for this reason that during the testing of the software, a C-scan was used to draw attention to areas which needed further scrutiny; a B-scan was then used to show the depth and structure of such areas.

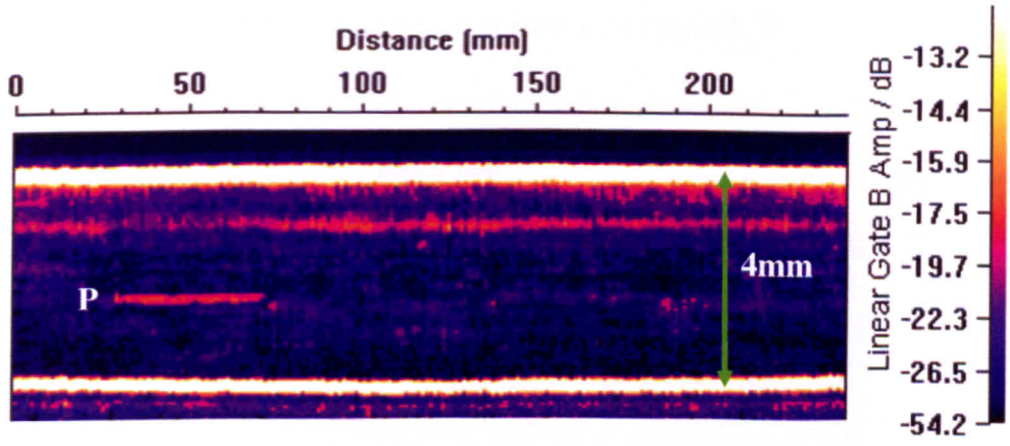

Figure 5.25 Sample B-scan identifying suspected area of porosity ("P").

For the final system 3-D profiles are employed; the user can identify layers of porosity from either the C-scan (as in testing) or via the B-scan. Clicking on the B-scan takes the

user to the C-scan at that layer. This allows analysis of the spread of porosity at a specific depth or the spread of porosity in depth at a particular cross-section.

5.7 Experimental Results

To examine the effectiveness of the method it was extensively tested with experimental data, results from three samples are presented here. Detailed descriptions of the components along with sample C-scans of the ultrasonic back wall echo response are contained within Appendix E.

The first sample was designed and constructed at Airbus (Sample 1, Appendix E); it contains two layers of glass micro spheres at different depths, to simulate layers of porosity. Although glass micro spheres provide a much larger reflection than would be expected from porosity, the sample does provide a useful opportunity to locate such a defect within a CFRP. The initial C-scan is shown in figure 5.26.

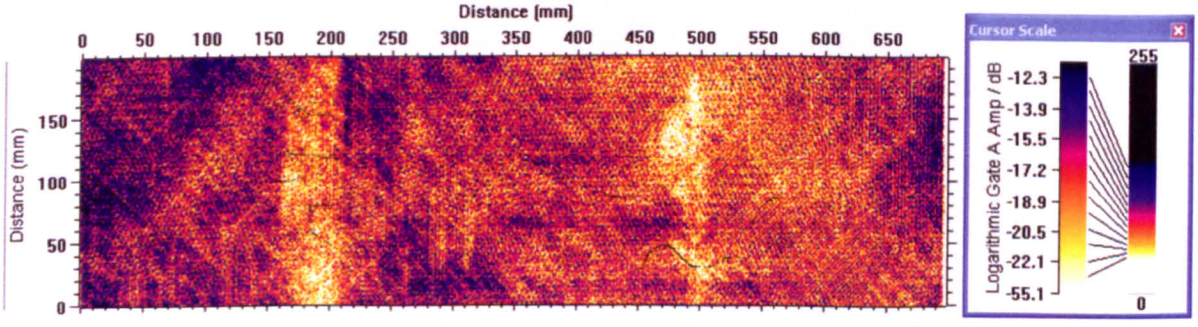

Figure 5.26 Initial C-scan of back wall amplitude for Sample 1.

Figure 5.26 reveals that there are two areas of high attenuation, one at 200mm and the other at 500mm on the x-axis, both running vertically down the sample; it is not

immediately clear where the boundaries of these layers are since there is a relatively high level of attenuation all over the panel. Further analysis using a simple B-scan plot of amplitude, along a horizontal line at a point 100mm in the vertical direction provides little clarification as to the location of the defects or their magnitude.

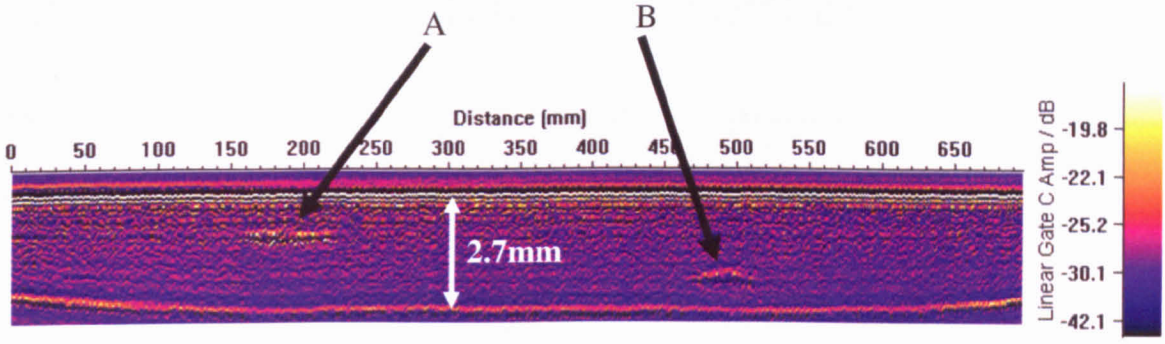

Figure 5.27 Amplitude B-Scan of Sample 1 horizontally at 100mm, showing layers of glass microspheres (marked "A" and "B").

From figure 5.27 we can see the first layer of glass microspheres visible as a dark region with lighter coloured edges within the B-scan (marked A), the second and deeper layer of glass microspheres are barely visible (marked B) – the difference in colour between this layer and the surrounding regions is less discernable.

Application of the Hilbert Transform method with filtering and application of the logarithmic colour scheme further highlights the areas which contain the glass micro spheres, making them more visible as well as giving a clear indication of their location and spread within the sample.

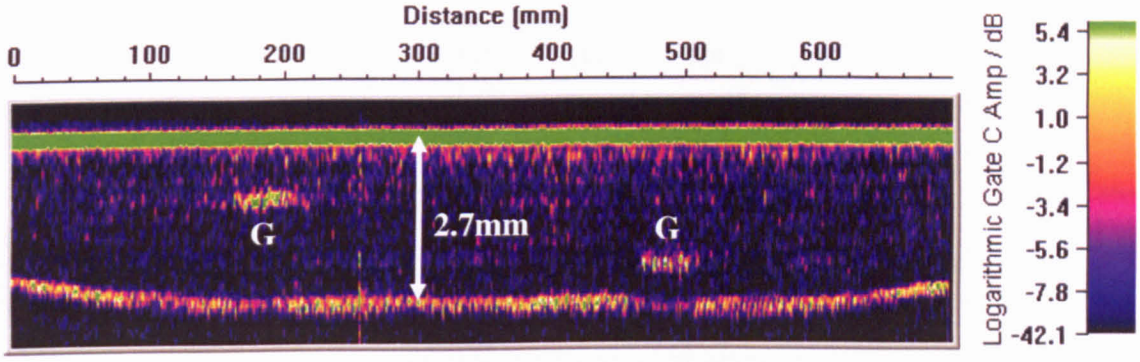

Figure 5.28 Hilbert Transform method with filtering and application of the logarithmic colour scheme B-scan for Sample 1, showing glass microspheres ("G").

From figure 5.28 it can clearly be seen that there are two areas of micro spheres within the panel; the reflections from the glass microspheres are so large that in places they are identified as "showstoppers" (green colours). There also appears to be some level of general porosity all over the panel, which was not identified by the first B-scan (figure 5.27), but are now visible due to the methodology employed.

Sample 2 (Appendix E) was also examined in this fashion. The C-scan of the back wall echo amplitude shows areas of defects on the right hand side as shown in figure 5.29.

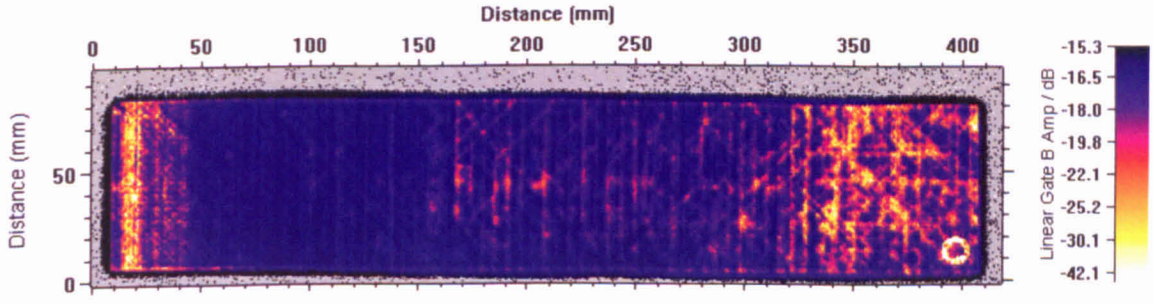

Figure 5.29 C-Scan of back wall echo amplitude for Sample 2.

Again B-scans were conducted across the panel, sample results are shown in figure 5.30.

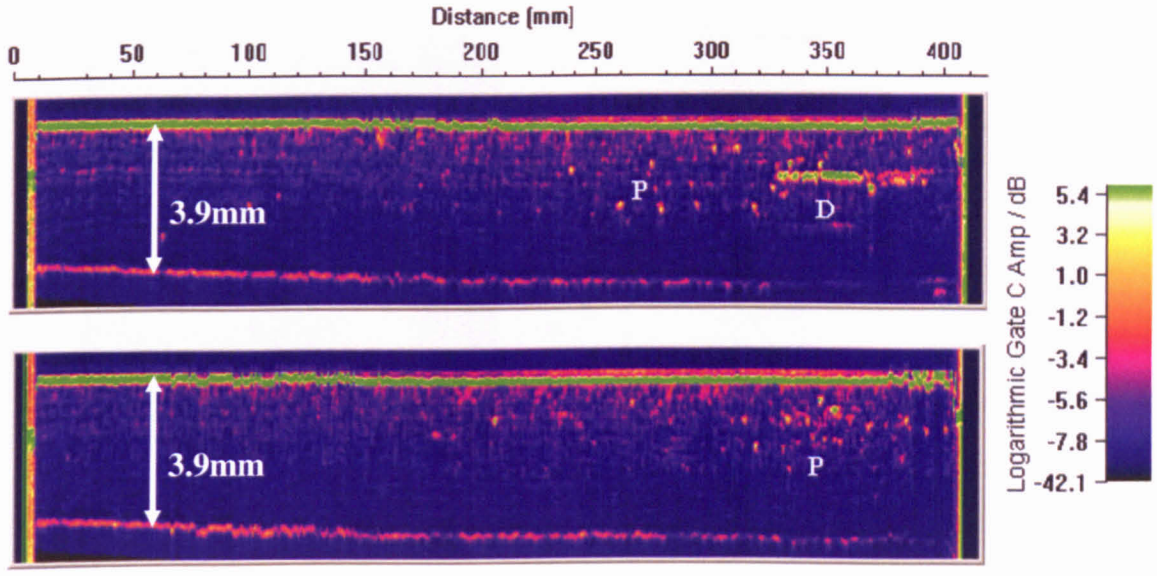

Figure 5.30 Hilbert Transform method with filtering and application of the logarithmic colour scheme B-Scans from Sample 2 showing porosity ("P") and delaminations ("D").

The upper B-scan in figure 5.30 shows general low level porosity (shown as point like indications) with a region on the right hand side which appears to show a large and persistent defect. This is consistent with A-scan results for this panel which suggest that there are delaminations within this part of the panel. The lower B-scan in figure 5.30 shows some scattered regions of low level porosity across the panel (shown as point like indications). Towards the right hand side there is more concentrated porosity (marked "P"), this is where the C-scan (figure 5.29) suggests the greatest density of defects is to be found.

Sample 3 (Appendix E) was also examined as previous. Initially a C-scan was plotted showing the variation in back wall echo amplitude across the sample.

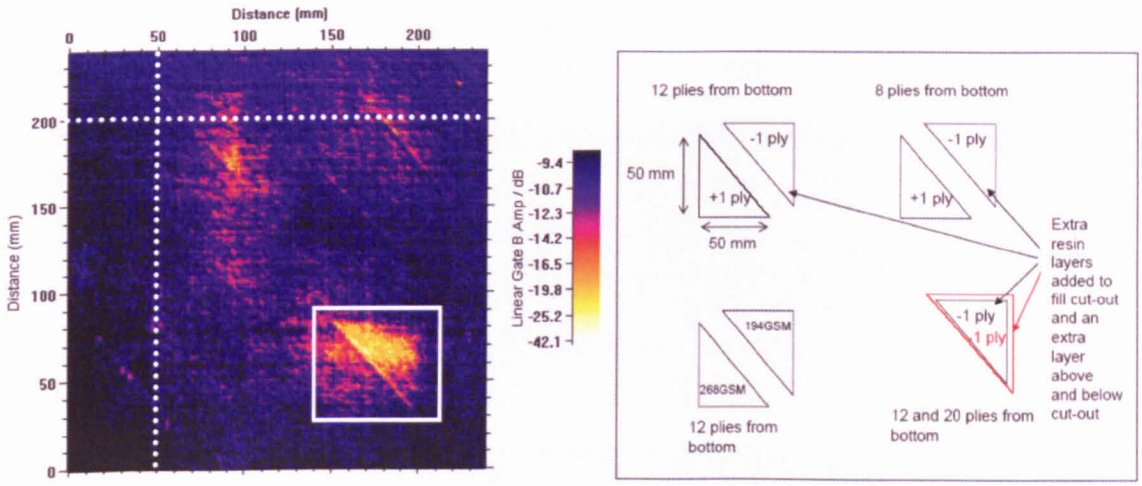

Figure 5.31 C-scan of combined fibre volume fraction and porosity panel for Sample 3 (left) and design of the panel showing defect positions (right).

From figure 5.31 it can be deduced that there are anomalies within the panel, shown by a decrease in the back wall echo response (see for example the area in the white box); these are most readily observed when a ply has been removed from the panel. These are the areas where porosity would be expected. To confirm these expectations B-scans were obtained at points across the panel. Figure 5.32 shows two of these; the first is a vertical cross section at a point 50mm on the horizontal axis (indicated by the vertical white line on figure 5.31), the second is a horizontal cross section at a point 200mm on the vertical axis (indicated by the horizontal white line on figure 5.31).

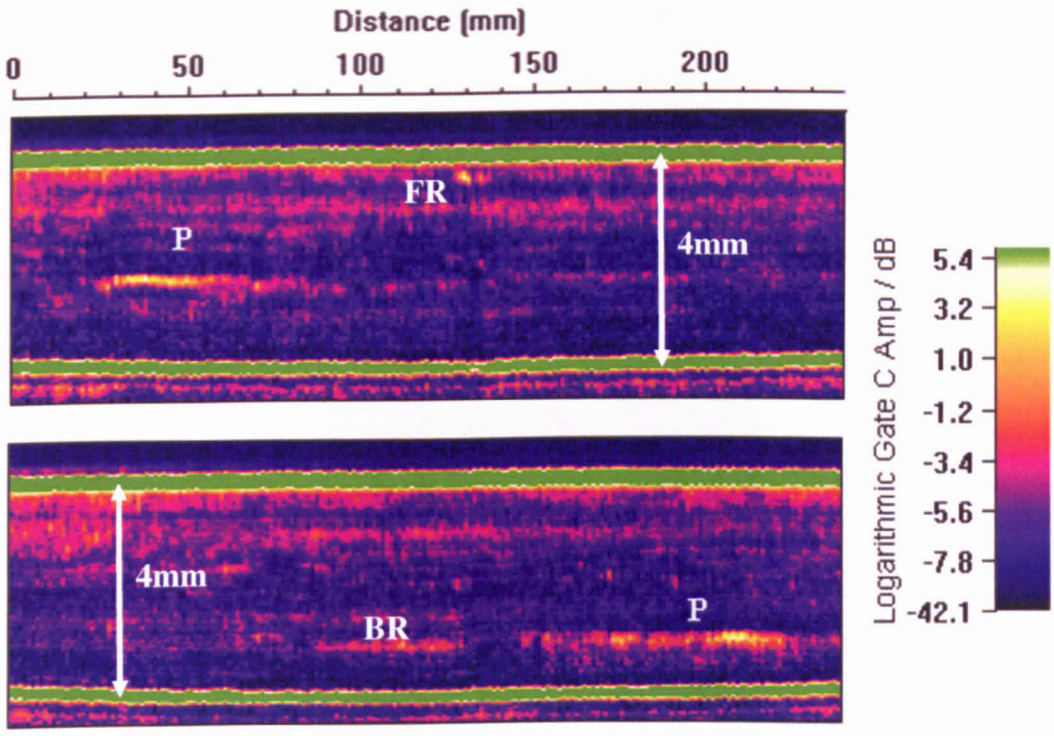

Figure 5.32 Hilbert Transform method with filtering and application of the logarithmic colour scheme B-scan images from a panel containing both thick resin layers and porosity – showing suspected porous regions "P" and unidentified responses near the front wall "FR" and back wall "BR".

From the upper B-scan in figure 5.32 it is possible to see an area on the left which corresponds to the point where the ply has been removed. This is to be expected since the C-scan (figure 5.31) shows a higher through sample attenuation on the left hand side at this point and therefore we would expect a higher level of porosity. The two green lines represent the front and back wall echoes. The lower B-scan in figure 5.32 shows a large area which appears to be porosity on the right hand side and which again corresponds to the area where a ply has been removed. Both B-scans show low level responses notably in the top B-scan near the front wall (marked "FR") and in the bottom B-scan near the back wall (marked "BR"). These features were not revealed in the C-scan of back wall echo size and indicate a disruption in the structure of the composite.

Such defects would not be detected by existing methods and may be structurally significant. Having compared the section taken by the B-scan with a micrograph of the same area it was found that the area of highlighted as porosity was in fact a thick resin layer as shown in figure 5.33.

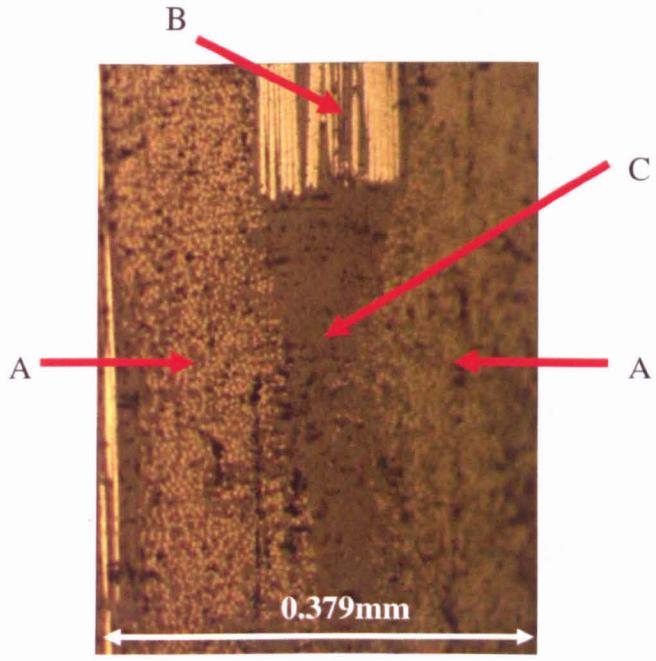

Figure 5.33 Micrograph of area covered by second B-scan showing thick resin layer – showing fibres "A" and "B", and resin "C".

Figure 5.33 shows fibres running parallel to the plane of the micrograph marked by B, fibres running perpendicular to the plane marked as A and the area of the cut-out filled by resin marked as C. Modelling of one ply surrounded by resin reveals why there is an increase in amplitude in the signal. For a typical system of a 0.25mm ply surrounded by 5μm resin layers the resonance response calculated by *MLM-Propmat* is as shown in figure 5.34.

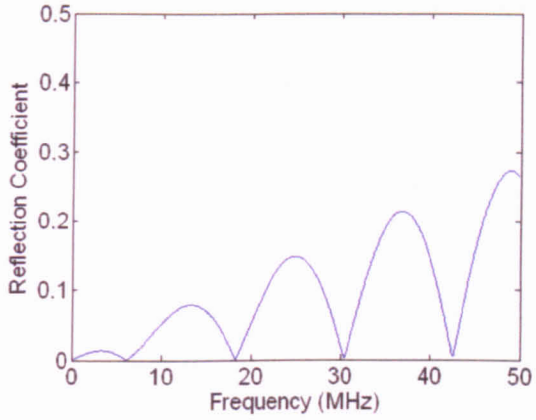

Figure 5.34 Frequency response for a typical ply resonance system.

When porosity is added to the central ply there is an increase in amplitude of the resonant peaks, as well as a shift upwards in resonant frequency from a quarter wave towards a half wave resonance, in the range 0 – 20MHz, which is the range most likely used for ultrasonic measurements. This is shown in figure 5.35 which is a modelled system with 10% porosity.

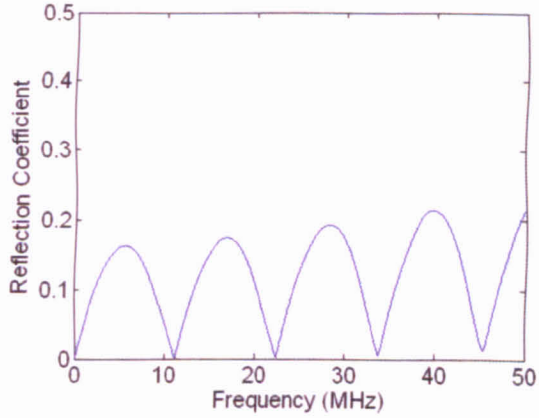

Figure 5.35 Frequency response for a typical ply resonance system with 10% porosity in the ply.

The increase in reflection at the resonant peak as well as the shift into the bandwidth of the transducer causes a large reflection which is detected via envelope analysis. Upon

examination of the frequency response with a resin layer thickness of 20 μm increased from a nominal value of 5 μm (figure 5.36) it becomes apparent that a thick resin layer also causes an increase in reflection coefficient which will be detected by the envelope analysis method.

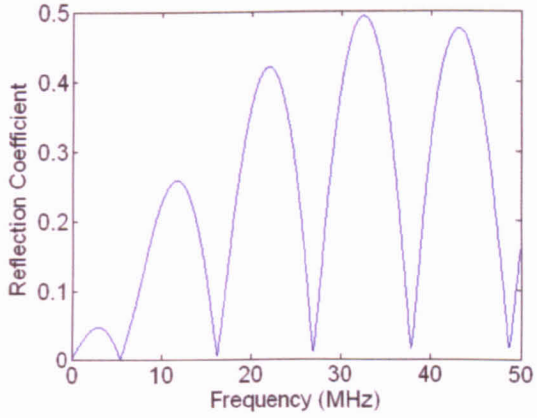

Figure 5.36 Frequency response for a typical ply resonance system with 20μm thick resin layers.

From figure 5.36 it can be seen that the amplitude of the resonant peaks has increased, whilst the frequency of the peaks has decreased slightly, these changes cause an increase in the effective reflection coefficient which is detected by the envelope analysis method.

It is important therefore to note that the envelope technique also highlights areas of differing fibre-resin effects; however, it only does this when a local change in fibre volume fraction occurs. Where an additional ply of the same density has been added, the fibre volume fraction change is averaged over the thickness of the panel and this change is not highlighted. Thus there is an important requirement to determine the difference between thick resin layer changes and those attributable to porosity. The evaluation of

methods that have potential for making this differentiation form the basis of the rest of this thesis.

From the above experiments it would appear that the system can differentiate between large structural defects such as delaminations and smaller anomalies such as porosity or fibre volume fraction changes. The system cannot in this format currently make a distinction between porosity and fibre-resin changes.

5.8 System Calibration

To provide a measurement of porosity it is necessary to identify a feature in the A-scan signal by which this might be achieved. The localised reflection coefficient from a volume of interest appears to provide such a measure, since it will vary depending on the material properties within the CFRP. This would be independent of measures which consider the frequency of inter ply resonances because the frequency of such peaks depends upon the thickness of the layers (plies and resin). By calibrating the signal to give the localised reflection coefficient we can provide a basis for calculation of the porosity distribution or thick resin within the CFRP.

It is necessary to make some assumptions to enable computation of the localised reflection coefficient. The first such assumption is that the response at a particular time in the waveform is dominated by the reflection coefficient multiplied by the incident energy at the corresponding depth. This is only the case where multiple reflections from earlier depths are much lower in amplitude than the primary reflection at that depth. We must also assume that the transducer beam profile is constant over the distance

measured. Finally, we must assume that the instantaneous acoustic intensity is proportional to the acoustic pressure squared. This is the case when a plane or spherical wave is used; also the use of Hilbert Transform earlier in the process removes the effect of phase, this minimises the effect using a focussed transducer probe.

By integrating the pressure-squared which is equivalent to the transducer voltage squared in the waveform up to the time of interest we can determine the reflected energy and hence determine the remaining incident energy at each volume element. The square root of this can be used to determine the reflection coefficient at each volume element.

By using conservation of energy:

Incident Energy = Reflected Energy to Time t + Transmitted Energy Beyond Time t + Energy absorbed and converted into heat.

The transducers which have been used in the experimental work in this thesis have been focussed within the centre of the composite and a relatively long focal length has been used. By inspecting the sample in this way diffraction losses are minimised and for the purposes of this discussion these losses have been neglected. Where experimental work has been conducted using different amplitudes, the frequency responses have not been observed to change and hence the transducer can be assumed to be linear for the purposes of this work. Although we do not know the incident energy we can calculate it with knowledge of the reflection coefficient at the front surface, R_1 which is calculated as 0.5295 for a 75% fibre volume fraction. This value is chosen because it is the average

of 80% and 70% fibre volume fraction, the most common range of fibre volume fraction in real modern composites. To give an approximate initial incident energy we can integrate the front wall echo amplitude squared, then divide by the intensity reflection coefficient R_1^2.

The reflected energy density (energy per unit area across the beam), E_r prior to each time τ is given by:

$$E_r = \frac{1}{\rho c}\int_0^{\tau} p^2 dt \qquad \textbf{(5.39)}$$

For the front surface reflection, the reflected energy density, E_{r1} is calculated as below:

$$E_{r1} = \frac{1}{\rho c}\int_0^{t_1} p^2 dt \qquad \textbf{(5.40)}$$

Where p is the instantaneous acoustic pressure in the beam, ρ is the density, c is the phase velocity, and t_1 is the time of the end of the front-surface reflection.

Hence the incident energy density, E_i is:

$$E_i = \frac{E_{r1}}{R_1^2} = \frac{1}{\rho c R_1^2}\int_0^{t_1} p^2 dt \qquad \textbf{(5.41)}$$

Then the transmitted energy density at each time τ, $E_t(\tau)$ is given by:

$$E_t(\tau) = E_i - E_r(\tau) = E_i - \frac{1}{\rho c}\int_0^{\tau} p^2 dt \tag{5.42}$$

To calculate the instantaneous reflection coefficient (from each volume element) we need to calculate the instantaneous intensity *I*, where:

$$I = \frac{p^2}{\rho c} \tag{5.43}$$

In order to convert from energy density in the incident pulse into instantaneous intensity, we have to assume that the maximum instantaneous energy in a pulse is what is produced by the filtered Hilbert Transform squared. To achieve this we define an effective pulse length T_{eff}, which converts from the integrated energy density in the pulse into the maximum instantaneous intensity. For the front wall reflection this is calculated as:

$$T_{eff} = \frac{E_{r1}}{I_{\max}} \tag{5.44}$$

Where I_{max} is the maximum instantaneous intensity in the incident pulse. Therefore, the reflection coefficient at each time τ, $R(\tau)$ is given by:

$$R(\tau) = \sqrt{\frac{p^2 T_{eff}}{\rho c E_1(\tau)}} \tag{5.45}$$

This provides the instantaneous reflection coefficient for each volume element which varies from 0 for total transmission to unity for total reflection of the remaining incident energy. This has the advantage of providing a distance amplitude correction, allowing direct comparison of anomalies regardless of the depth within the structure they occur. However, for this to be accurately measured we need to correct for the effect of visco-elastic attenuation within the sample; fortunately, a simple distance amplitude correction can be made for this, at a constant rate with depth. This is not already accounted for by the Hilbert Transform method outlined in this chapter since the filtering method used takes account of the energy reflected/transmitted at an interface not the visco-elastic loss within the structure.

This method was not pursued since it was realised that although the filtered Hilbert transform can highlight both regions of porosity and thick resin it is unable to differentiate between the two. A method which can achieve this is important since the two defects may have very different effects on structural integrity. These methods are identified and developed in Chapters 6, 7 and 8.

5.9 Estimation of the Size of a Back Wall Echo

As stated earlier, a commonly used technique to asses the porosity content of composite is to monitor the amplitude of the back wall echo. When the size of the back wall echo falls by a certain predetermined amount, the component is assumed to have a level of porosity which means that it must be rejected. Obviously, for adequate functioning of this method, then access to a back wall echo is paramount; there are, however, situations where it might not be possible to gain a back wall echo, such as where composites are

backed by honeycomb structures. A method is required to provide an estimate of the back wall echo in such situations. On the basis of an emergent issue at Airbus (Bremen, Germany) an empirical study was conducted to develop a method that estimated the size of the back wall echo based upon the energy reflected between the front and back wall echoes and to investigate how such a method might perform.

We consider ultrasonic echo signals from the body of the composite, between the front wall and the point in time which would correspond to a BWE if it existed. In an unflawed sample, these echoes would have an expected range of amplitudes which could be defined for any given material type or component. If the sample were flawed then we would expect these amplitudes to increase. Thus it is likely that the energy in the back-scattered signal, integrated over a time window corresponding to the thickness of the composite, could give an indication of significant flaws. Figure 5.37 shows an ultrasonic A-scan edited so as to appear not to have a BWE, for the purpose of illustration.

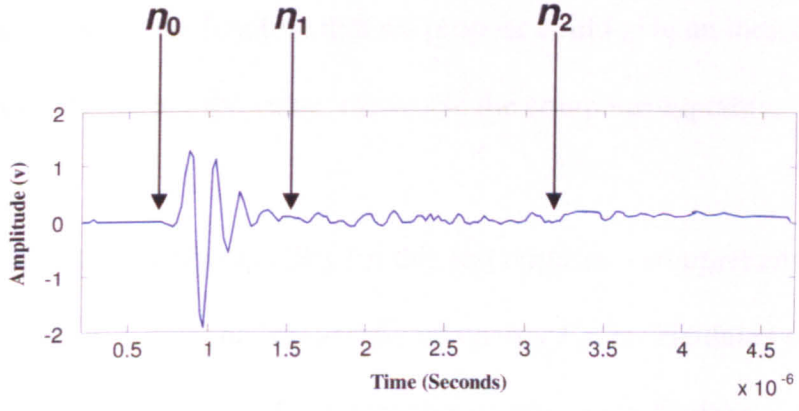

Figure 5.37 Illustration of an A-scan with no BWE. The times n_0 and n_1 mark the start and end of the front wall echo, and n_2 marks the end of the time window corresponding to echoes from the body of the composite.

A measure of the energy from the body of the material is

$$E_{BS} = \int_{n_1}^{n_2} x^2(t)dt \tag{5.46}$$

$x(t)$ is the time domain signal and the limits n_1 and n_2 correspond to the beginning and end of the window of interest. When dealing with digitised data, the time variable n becomes the sample number and the signal $x(t)$ is in discrete form $x[n]$. Equation (5.46) becomes

$$E_{BS} = \sum_{n_1}^{n_2} x^2[n] \tag{5.47}$$

This energy may be expressed logarithmically in dB

$$E_{BS}^{L} = 10\log_{10} \sum_{n_1}^{n_2} x^2[n] \tag{5.48}$$

It is the value of this function that we propose could give an indication of the presence of flaws – the higher the value, the worse the component quality.

The establishment of feasibility for this test requires a comprehensive study of real components in which the back-scattered energy E_{BS} is calculated and related to physical damage either by X-ray or by destructive examination. Neither of these were possible over the limited time scale of this project, so an alternative strategy was adopted.

We have examined composite components which were known to contain flaws and which *did* exhibit a significant BWE. Figure 5.38 gives an illustration of the A-scan with times n_1 and n_2 marked as before, as well as time n_3 which marks the end of the BWE.

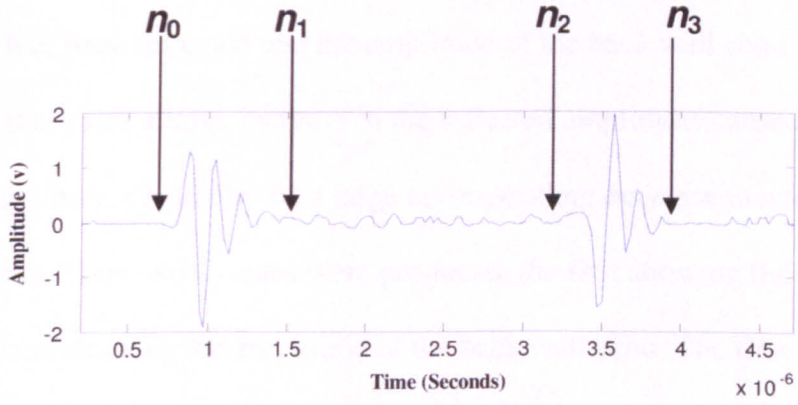

Figure 5.38 Illustration of an A-scan with a significant BWE. The times n_0 and n_1 mark the start and end of the front wall echo, and n_2 marks the end of the time window corresponding to echoes from the body of the composite, and n_3 corresponds to the end of the BWE.

The energy in the BWE is

$$E_{BWE} = \sum_{n_2}^{n_3} x^2[n] \qquad \textbf{(5.49)}$$

or, logarithmically

$$E_{BWE}^{L} = 10\log_{10} \sum_{n_2}^{n_3} x^2[n] \qquad \textbf{(5.50)}$$

We would expect there to be a negative correlation between the energies E_{BS} and E_{BWE}. Flawed components with a low BWE would exhibit a high back-scattered energy. If

such a correlation can be shown to be robust then high back-scattered energy would indicate the presence of flaws.

To assess the feasibility of this method, experimental data was analysed, from samples in which a back wall echo was present for comparison. The energy between the front and back wall echo was calculated in order to allow a comparison between the energy which had been reflected and the amplitude of the back wall echo. It was predicted that where there was a large increase in the reflected amplitude, caused for example by porosity, there would also be a large corresponding decrease in amplitude of the back wall echo. Thus two C-scans were produced, the first showing the reflected energy and the second showing the amplitude of the back wall echo. The first experimental sample examined was designed and constructed at Airbus and contained glass micro spheres as described in section 5.7 and shown in figure 5.25. The colour scales were selected so that a large amount of energy present in the gate or a large reflected amplitude from the back wall are both shown as a light colour, the expectation is that an area depicted as a light colour on one C-scan would be shown as a dark area on the other and vice versa. The results of this analysis are shown in figure 5.39.

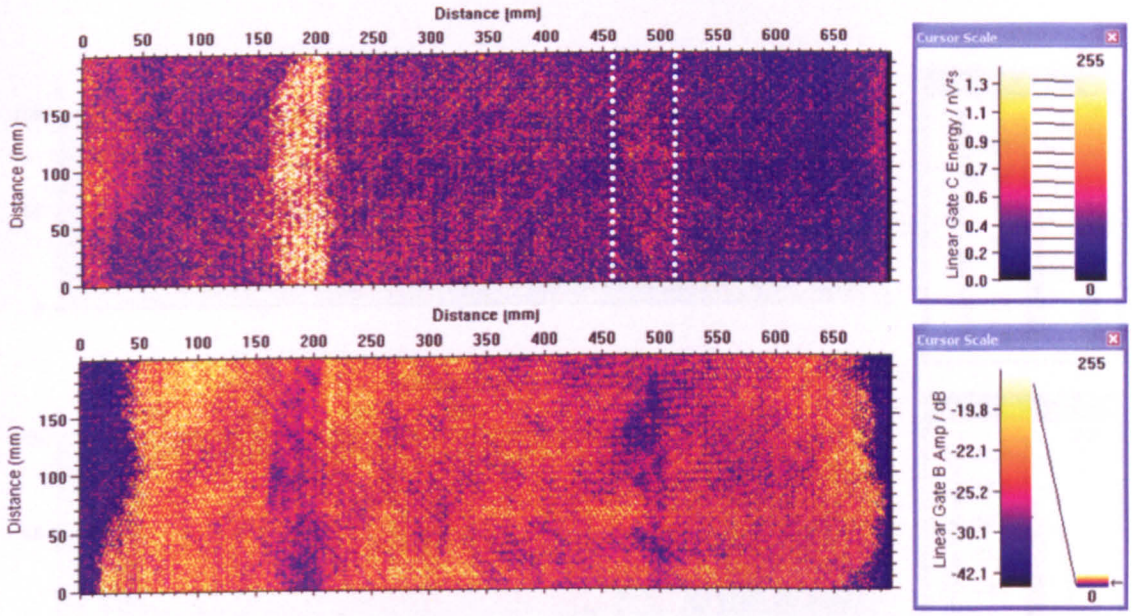

Figure 5.39 C-Scans for energy reflected between the front and back wall echo (top), and back wall echo amplitude (bottom).

Figure 5.39 shows that the two layers of glass microspheres can be seen as light regions the first, easily visible and running vertically from points 200mm on the horizontal axis indicating an increase in reflected energy in the top scan. The second is less visible and is present between the two dashed white lines in the top image. The maximum energy measured in this region is 1.0 nV^2s compared to a background average value of 0.5 nV^2s. Similarly in the back wall echo C-scan, these regions are depicted as a dark area indicating a decrease in amplitude. There are two significant features at either end of the panel which are shown as light regions on the energy C-scan which may be porosity; significantly these regions are shown as dark areas in the back wall echo C-scan indicating a decrease in the amplitude of the back wall echo reflection. The second panel which was investigated was produced by Airbus using standard production techniques, as described in section 5.7 and shown in figure 5.28. The results obtained are shown in figure 5.40.

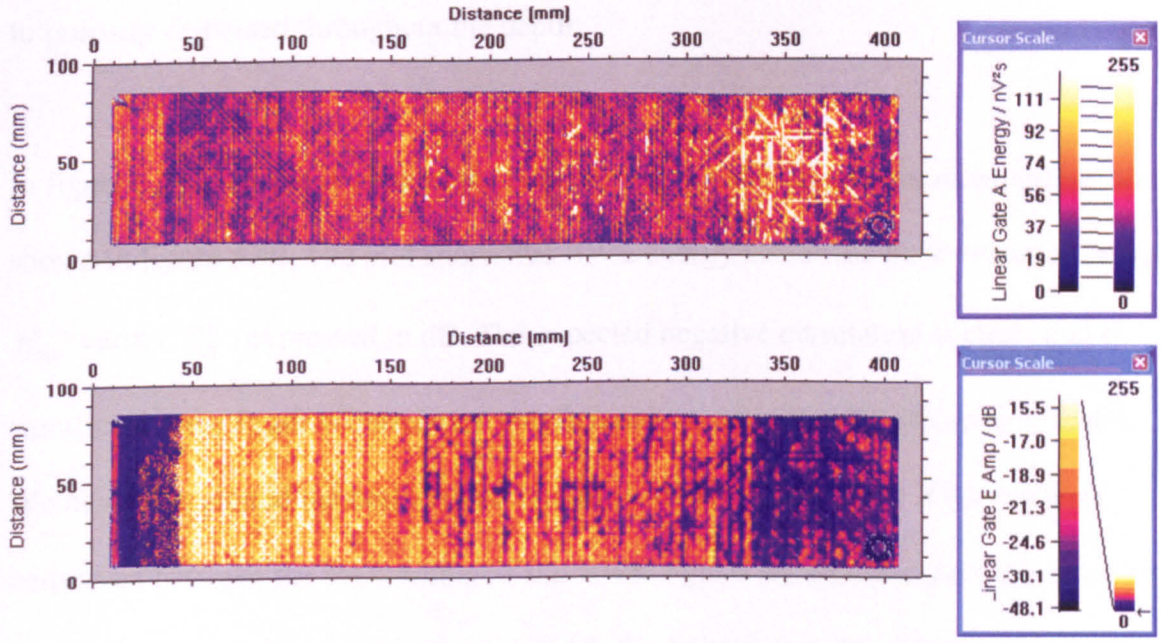

Figure 5.40 Energy C-scan (top) and back wall echo C-scan (bottom) obtained for a panel produced using standard production techniques.

Figure 5.40 shows a large area which contains lines of increased reflected energy from 325mm to 400mm on the horizontal axis. This is the area of the panel which is suspected to contain porosity and large voids, similarly the back wall echo C-scan shows a decrease in back wall echo in these regions. In the area from 150mm to 300mm on the horizontal axis there are lines which indicate an increase in the reflected energy (represented by lighter colours), inspection of the A-scan lines in these regions indicates large groups of porosity are present running parallel to the direction of the fibres at the depth to which the porosity is present. This kind of "worm-hole" porosity has been observed previously (Robert Smith, personal communication). The back wall echo C-scan shows these regions in a darker colour indicating that there is a decrease in the back wall echo at these points. There is also present an area of increased reflected energy from 10mm to 40mm on the horizontal axis, this is shown as a dark region on

the back wall echo C-scan. The precise cause of this effect is unknown but may be due to porosity dispersed throughout the depth.

In figure 5.41 we have compared the two energies for the sample discussed earlier and shown in figure 5.40. The plot shows the BWE energy versus the back-scattered energy, E^{I}_{bwe} versus E^{L}_{BS}, expressed in dB. The expected negative correlation is clear, and is significant – the Pearson correlation coefficient is -0.61 with a significance of 0.006. We have also plotted the best straight line fit (LMS) on figure 5.41. If energy were conserved between the back-scattered and BWE signals we would expect this slope to be -1, whereas the observed value was -0.58. We believe that this difference is due to energy which is absorbed by the composite and lost as heat.

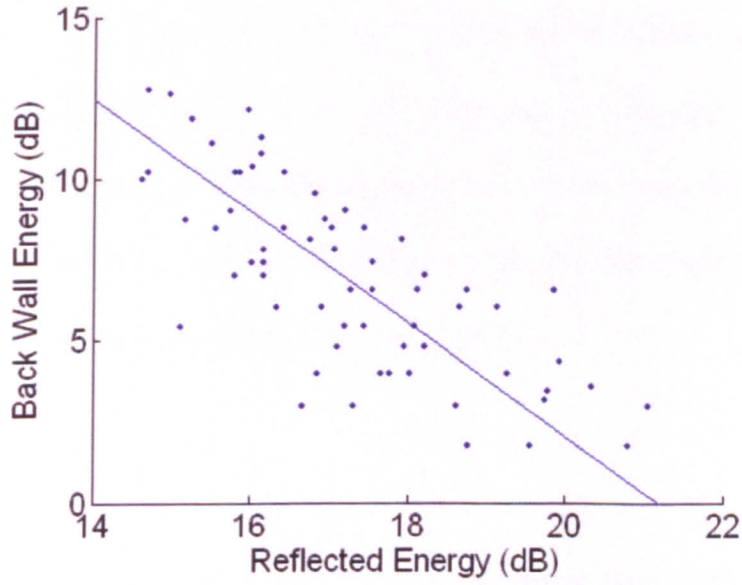

Figure 5.41 Logarithmic plot of the BWE energy versus back-scattered energy. The straight line is the LMS fit to the data.

Initial investigations into the feasibility of the method have shown that where porosity is present there is an increase in the reflected energy between the front and back wall echoes, this is accompanied by a decrease in the reflection from the back wall echo. Statistical analysis of the data obtained showed that there is a negative correlation between back wall echo amplitude and reflected energy; this correlation was found to be statistically significant. The results of this initial study are encouraging. It is suggested that further work be done to establish the statistical performance of the technique, specifically:

(i) Repeat the studies outlined above on a broader range of samples.

(ii) Empirically relate the back-scattered energy to attenuation estimated on the basis of the BWE. This would quantify the equivalence with current procedures.

(iii) Carry out studies on components which do not exhibit a BWE, but BWE enabled by a saw cut at the back of the region being tested.

(iv) Develop a formal theoretical justification for the technique.

(v) Use the theory of (iv) to investigate any risks that might exist due to ill-conditioning in the statistical calculation.

5.10 Conclusions

Using the techniques described in this chapter a method of identifying anomalies within the envelope amplitude was presented. Investigations were performed into various methods of filtering the signal and it was established that a low pass filter was required to remove the high frequency ripple which was present as a result of inter ply resonances. The parameters for the filter were defined and would remain constant for most normal values of plies per mm. A high pass filter was required to remove the low

frequency trend within the panel. The parameters of this filter were defined and could be kept constant regardless of the technical specifications of the panel. The use of non-linear and user modified colour scales allowed the system to identify gross defects with a high level of reliability and was able to locate these defects within the depth of the substance. Smaller defects could be identified and positioned in 3D space using the Hilbert Transform based envelope method applied to raw A-scans. These are regarded as significant in the industry because they are most likely to represent porosity in the sample, although excessively thick resin layers could lead to similar features as porosity. In the form established so far, the system is unable to differentiate between porosity and other defects such as localised fibre-resin changes. The system is not affected by fibre volume fraction changes which are spread across the depth of the panel. The remainder of this thesis concentrates on methods to differentiate between the presence of a thick resin layer and porosity.

The observations provided in section 5.7 give a basis for a method to allow the difference to be shown. If a measurement of resonant frequency were made, then in the case of porosity we would see an increase in resonant frequency, and conversely in the case of a thick resin layer we would see no change in resonant frequency. For such an analysis to be achieved examination of the time dependent frequency content of the signal is necessary; the next chapter examines time frequency analysis of the received signal. A method to calibrate the system to provide the instantaneous reflection coefficient was outlined. This provides the potential for a system to estimate what the back wall echo would have been if it were present. The technique would be useful for providing estimates of global porosity via attenuation of this back wall echo, or a local porosity measure by analysis of the instantaneous reflection coefficient. This would be

useful in situations where the presence of thick resin layers is not important. The possible presence of thick resin layers indicates that other methods designed to be sensitive to porosity or thick resin layers only are required. The next chapter examines the process of determining the time dependent frequency content of the signal as well as determining how changes in the frequency content can provide indications of the presence of either porosity or a thick resin layer in the composite.

Chapter 6

Location of Porosity and Excess Resin in Three Dimensions: Short Gate Time-Frequency Analysis

6.1 Introduction

Investigation of the envelope analysis method for detecting flaws within composite structures (chapter 5) showed that issues arose when trying to determine the difference in terms of received ultrasonic signals between porosity and thick resin layers. Analysis of expected ultrasonic signals using *MLM-Propmat* showed that, although in both cases an increase in the amplitude of the reflected signal would be expected, the frequency content of these signals differed. Methods were developed to extract the frequency spectra from received signals from composite, based upon the use of short time-domain gates (duration approx 1½ plies) to extract signal segments for analysis. Further analysis is then developed to differentiate between the two principal flaw types – porosity and thick resin.

In this chapter modelling is conducted to assess the nature of the local resonances within the composite (section 6.2) under different flaw conditions, an overview of a method for time-frequency analysis is given (section 6.3.1), together with a support modelling exercise (section 6.3.2). The characteristics of these measures are assessed in an investigation on experimental data (sections 6.5 and 6.6). The sensitivity of these measures to various defects is investigated and the minimum detectibility determined by further modelling (section 6.7).

6.2 Local Resonance Modelling

In order to understand changes in A-scans that result from diffuse porosity and lay-up anomalies such as a thick resin layer, it was necessary to model local acoustic conditions around a single anomalous layer. It was proposed that changes to the resonant system associated with a single flawed resin/ply layer would act as a source of change in the A-scan signal which would propagate back to the receiver through the intervening composite material. The basic system under consideration was as shown in figure 6.1, it consists of a single ply layer (125μm) which is a mixture of fibres and resin, following simple mixture rules as shown in chapter 4, section 4.4.1, sandwiched between two resin layers (5μm). This local 3-layer assembly is in turn sandwiched between two semi-infinite half spaces of unflawed ply. We imagine a local observer in the form of a transmitter/receiver (Tx/Rx on figure 6.1), placed in one of the half spaces. *MLM-Propmat* is used to generate the frequency domain response of this elemental structure.

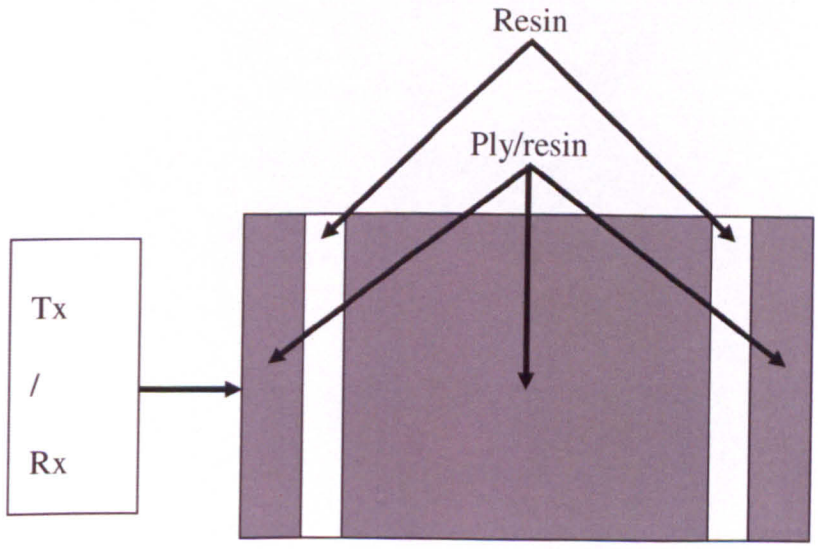

Figure 6.1 Five Layer system analysed to determine parameter variation, for ply/resin mixture thickness (125μm), resin thickness (5 μm).

Frequency dependent attenuation was added to the resin, and by simple linear mixture rules to the resin/ply mixture. The attenuation was linear with respect to frequency and the functions which were used were obtained empirically from an ultrasonic spectrometer-cum-goniometer. Attenuation due to porosity may be added to these layers by use of the ECAH scattering model as described in chapter 3, section 3.3.4. The local resonance for flawed/unflawed composite could then be examined. The frequency response for unflawed composite is shown in figure 6.2.

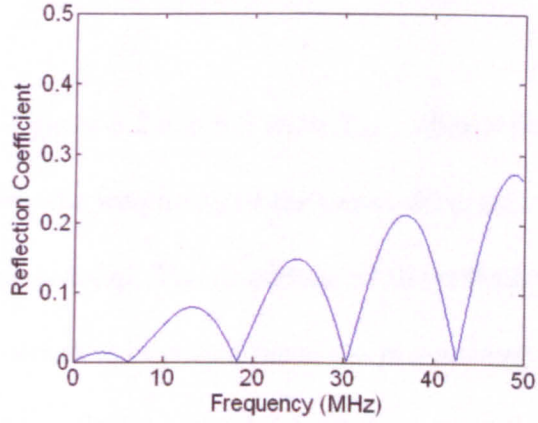

Figure 6.2 Frequency response for unflawed composite.

Defects may be added to the model and their effects on the frequency response of the system can then be examined. The presence of thick resin layers was simulated by varying the thickness of the second resin layer shown in figure 6.1. The values of the thickness of the resin layer which were simulated were 1, 2, 5, 10 and 20 microns. The fibre volume fraction of the ply/resin mixture layer was kept constant whilst the thickness of the layer was reduced; this is equivalent to the fibres being displaced horizontally across the layer by the presence of the thick resin layer, maintaining the

overall thickness of the element. The frequency response obtained is shown in figure 6.3.

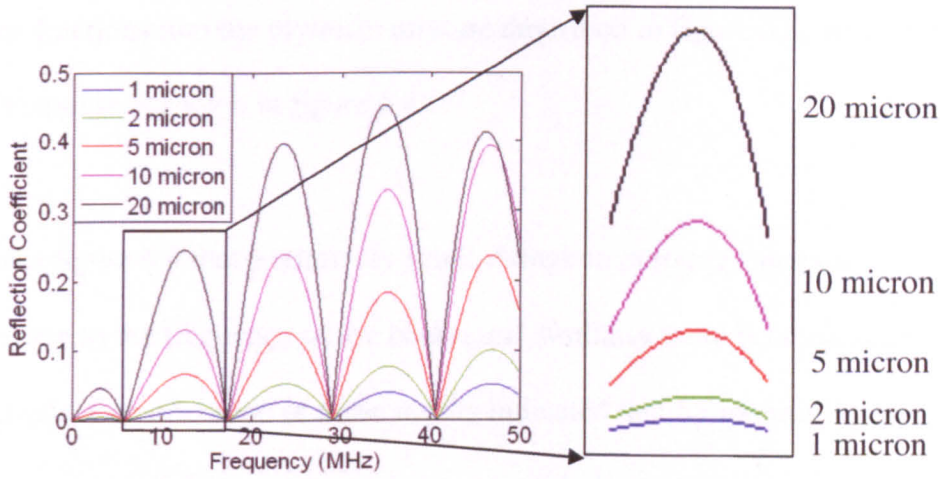

Figure 6.3 Frequency responses for the resin thickness shown in the key.

Comparisons between figures 6.2 and 6.3 show that, when a thick resin layer is introduced to the system, the frequency of the peaks decreases by a small, but nevertheless measurable amount. The amplitude of the reflections increases as resin thickness is increased, which is expected since the presence of a thick resin layer is detected by the envelope analysis method described in chapter 5.

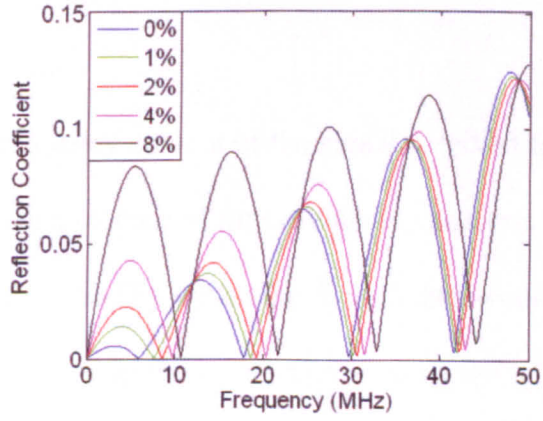

Figure 6.4 Frequency responses from 5 layer system, varying porosity level as shown in the key.

To provide an indication of how porosity might be differentiated from resin layer, thickness simulations were conducted introducing spherical porosity of radius 10μm and varying volume fractions into the ply/resin mixture described in figure 6.5, the effect on the frequency response is shown in figure 6.4.

It is evident from figure 6.4 that a relatively small change in porosity causes a significant increase in the frequency of the peaks, and similarly there is an increase in reflected amplitude. Consideration of these results indicated that by monitoring the change in the frequency of the resonance, an area identified as anomalous by use of the envelope analysis method outlined in chapter 5 could be categorised as either a layer of porosity or a layer of thick resin. This would be possible since a decrease in resonant frequency would be expected where a thick resin layer is included and an increase in resonant frequency would be expected in the presence of porosity. A method to measure the resonant frequency of this peak is examined in section 6.3.1.

6.3 Modelling of the Whole Signal Path

6.3.1 Time-Frequency Analysis

In order to allow the frequency content of the signal received from local features in a composite to be analysed a method of time-frequency analysis was necessary. Initial studies focussed on the method by which the A-scan data would be gated for further analysis. Two methods of gating the signal were considered; either the signal could be gated with consecutive gates which could be of a length defined by the user, or alternatively the signal could be gated with overlapping gates the length and overlap of

which could again be defined by the user. Figure 6.5 shows the two possible implementations.

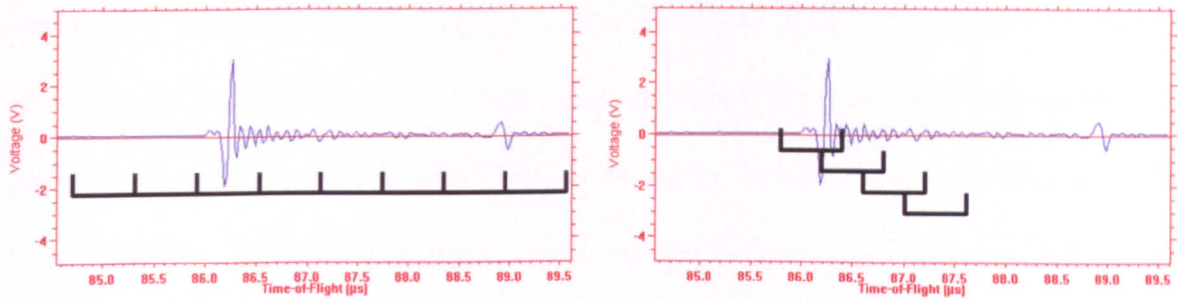

Figure 6.5 A-Scan signal gated with consecutive gates (left), and with overlapping gates (right).

It was found that when consecutive gates were applied to the signal there was a significant loss of resolution. This results from the gates having a minimum length in time, this length is defined by the width of the plies, the gate having to be at least the length of a ply and hence defined as:

$$\tau_{\min} = \frac{x}{c} \tag{6.1}$$

Where x is the thickness of the ply and c is the velocity of compression waves in the ply/resin mixture. The value of this velocity is based upon the simple mixture rules described in chapter 4, section 4.4.1. There is a necessity for a minimum gate width since the methods described within this chapter depend on the inter-ply resonance. In practice a gate width equivalent to 1.5 plies was used to ensure that any variation in ply width would not result in a loss of resonance data for analysis and to mimic a system as shown in figure 6.1. The use of consecutive gates therefore would imply that there

would be one frequency spectrum obtained for each ply, in practice this does not provide a high enough resolution, since there are factors in the composite which may occur across gates or alternatively at the boundary between gates. Therefore, for experimental data overlapping gates were used, to ensure maximum resolution the gate was stepped through the A-scan by one sampling period at a time. With overlapping gates it is possible to increase the lengths of the gates without losing resolution as in the case of consecutive gates. However, increasing the length of the gate above 2 ply widths leads to interference between the resonances from both plies, and the resulting frequency spectrum of this gate would be the averaged effect of two plies, and as such an individual effect from a single ply would be more difficult to see. There are however, advantages to the use of a long gate time-frequency analysis which will be examined later in chapter 7; this chapter will be restricted to gates shorter than two plies.

Data is gated from the signal by windowing sections of the original A-scan with a Hanning window. This ensured that the output of the Fourier Transform was not distorted by any sharp transitions in the signal. This type of window represents a compromise between rectangular windows which respond well if the different frequencies of the signal have similar amplitudes and other windows which have a high dynamic range but respond poorly to noise. The Hanning window has low aliasing; however, it does decrease the resolution achievable in the frequency domain, since the lobes are widened slightly. An example gate of an A-scan is shown in figure 6.6, the Hanning window function applied to the gated data is shown in grey.

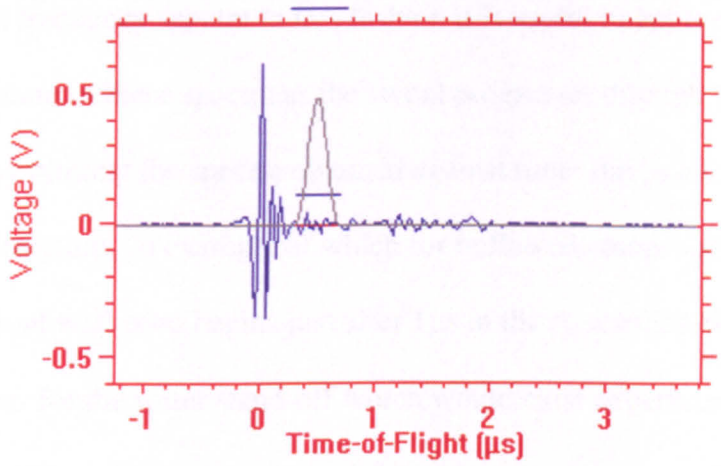

Figure 6.6 Typical A-scan signal, showing gate (blue), and Hanning window within the gate (grey).

An FFT is then taken of the data within this gate to provide the frequency response for the gated signal segment; this is equivalent to the inter-ply resonance examined in the model provided that the gate length is greater than or equal to the width of a ply and the surrounding resin layers. This process is known as the Short-time Fourier Transform (STFT). A typical frequency response obtained from data gated in this fashion is shown in figure 6.7.

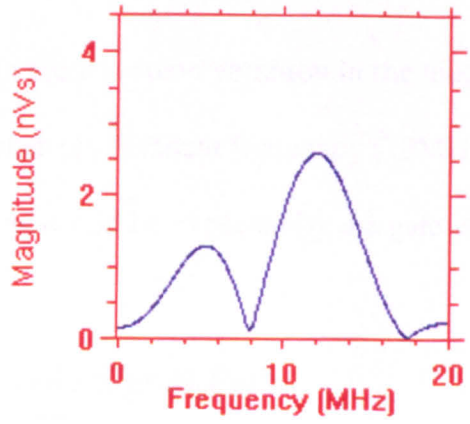

Figure 6.7 Typical frequency response obtained from gated A-scan.

Having obtained frequency spectra in this fashion it is useful to apply further analysis. The changing nature of these spectra as the signal progresses through the composite may be shown by plotting the spectra obtained against time; this is conventionally known as a spectrogram, an example of which for unflawed composite is shown in figure 6.8 The front wall echo begins just after 1μs in the A-scan, as distinct from time = 0. This accounts for the water stand-off which would exist experimentally.

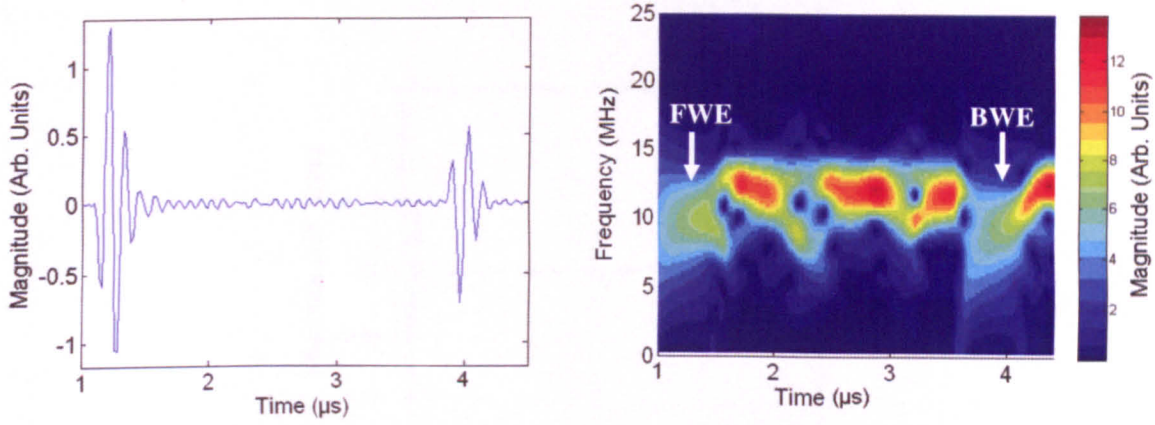

Figure 6.8 Example A-scan (left) and example spectrogram (right) showing the variation in frequency content for unflawed composite, showing front wall echo ("FWE") and back wall echo ("BWE").

Figure 6.8 shows that although there is some variation in the magnitude of the frequencies surrounding the inter-ply resonant frequency (12MHz), the response is dominated by this resonance, as would be expected by the gate width chosen.

6.3.2 Modelling of the Whole Signal Path

The changes in expected elemental spectra due to anomalies in the composite have been detailed in section 6.2. To better understand how the real A-scan would change due to

these flaws a further modelling exercise was done using *MLM-Propmat.* A 32 ply system immersed in water was simulated for normal composite, or in the presence of defects such as a single ply containing porosity or a single thick resin layer as outlined in section 6.2. A typical transducer pulse of finite bandwidth and centre frequency of 10MHz was used as the signal source. This pulse when transmitted into the medium produced a modelled output in the time domain. A sample response obtained via this modelling method is shown in figure 6.9.

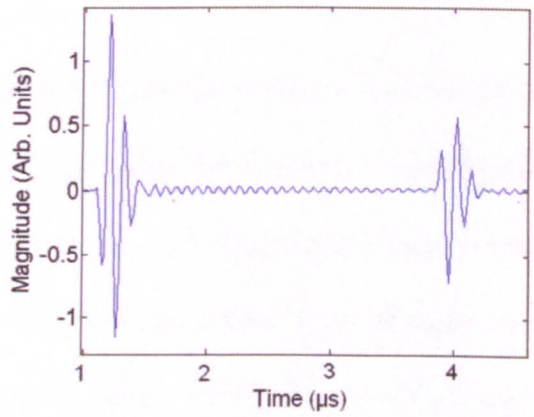

Figure 6.9 Modelled A-scan data from an unflawed panel 32 plies thick.

The response obtained from the model could then be gated as in shown in section 6.3.1 and time-frequency analysis applied to the A-scan, Figure 6.10.

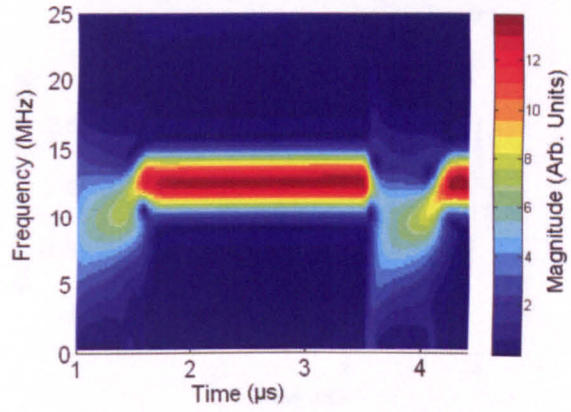

Figure 6.10 Time-frequency analysis of modelled A-scan data from a panel 32 plies thick.

It can be seen from figure 6.10 that the response is dominated by the inter-ply resonance which occurs at 12MHz. The modelled situation is slightly different to the experimental case shown in figure 6.8. In the experimental case there are variations in the ply and resin thicknesses, this results in disruption of the inter-ply resonance. In the modelled case, a constant resonance is expected since there is no randomness within the resin layer thickness and hence the inter-ply resonance dominates. Modelling the panel in this fashion, whilst not necessarily identical to an experimental situation, will highlight changes introduced when defects are added, rather than inherent irregularities in the signal due to randomness in ply lay-up. To examine the effects of porosity, a porous layer of 10% volume fraction spherical scatterers of radius 10μm was inserted within the 10^{th} ply and time-frequency analysis applied to the resulting A-scan as shown in figures 6.11 and 6.12.

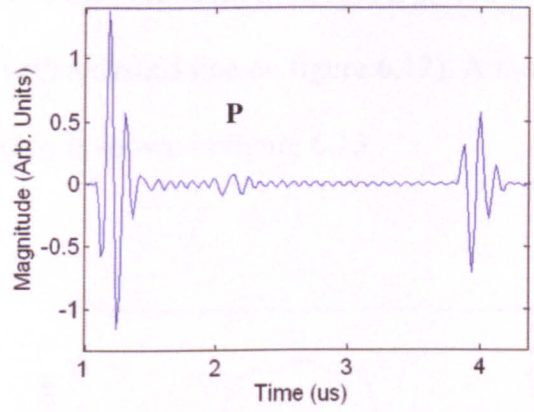

Figure 6.11 Modelled A-scan data from a panel 32 plies thick with 10% porosity within layer 10 ("P"), corresponding to t = 2μs.

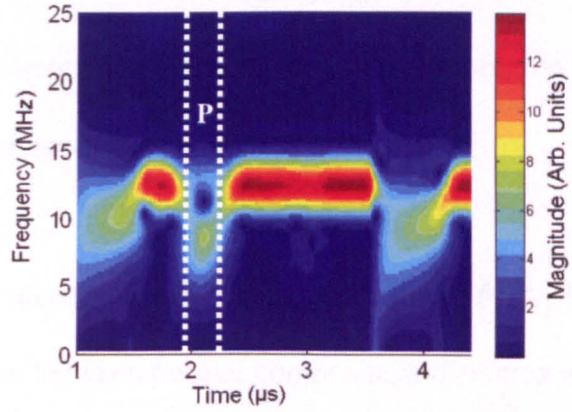

Figure 6.12 Time-frequency analysis of modelled A-scan data from a panel 32 plies thick with 10% porosity within layer 10 ("P"), corresponding to t = 2μs.

As was demonstrated experimentally in section 6.3.2 there is a shift in dominance of the resonances from the second resonance normally present at 12MHz to the first resonance normally present at 6MHz under the influence of porosity. This is due to the second resonance moving upwards out of the transducer bandwidth whilst the first resonance begins to move upwards into the transducer bandwidth. This causes an apparent decrease in resonant frequency, and is expected from earlier modelling. The time-frequency analysis suggests that whilst the resonance is transferring either to or from the

resonance associated with the porous layer there is a period where both resonances have an influence (marked with a dashed line on figure 6.12). A modelled frequency response from this transition region is shown in figure 6.13.

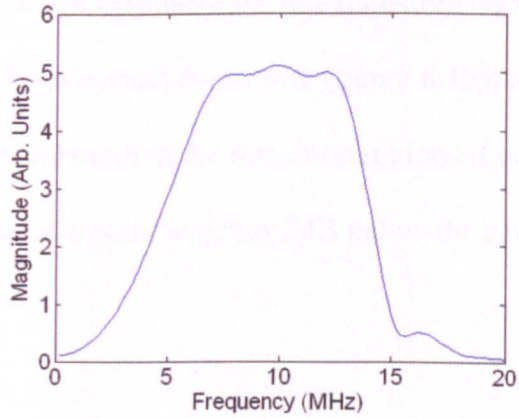

Figure 6.13 Modelled frequency response for a transition region from normal composite to a porous region.

This effect is also seen experimentally as shown in figure 6.14 which is a frequency response for a transition between normal composite and an area which appears to include porosity.

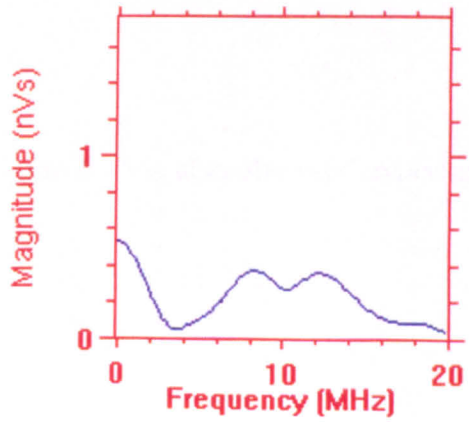

Figure 6.14 Experimental frequency response for a transition region from normal composite to a porous region.

Figure 6.14 shows a peak at 0MHz which is not present in the modelled spectrum; this is due to a DC bias in the experimental data, which can easily be removed by removal of the average value of the signal before conducting the Fourier transform. If a comparison is made between the modelled responses for this transition region and a typical response which may be obtained from normal composite (figure 6.15); it can be seen that there is an apparent increase in bandwidth in the transition regions if bandwidth were defined as the width of the spectrum at a point which is 3dB below the resonant peak in the spectrum.

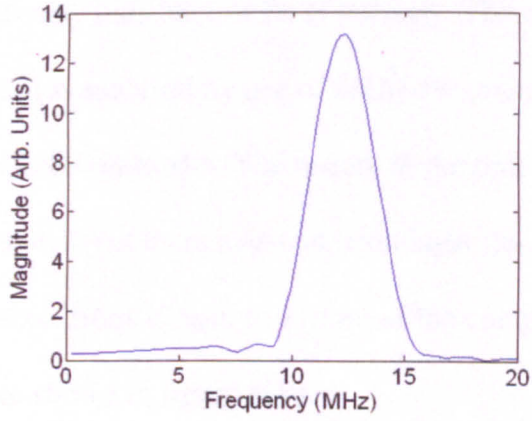

Figure 6.15 Modelled frequency response obtained from gated A-scan for good composite.

The resonance shown in figure 6.15 is also observed experimentally as shown in figure 6.16.

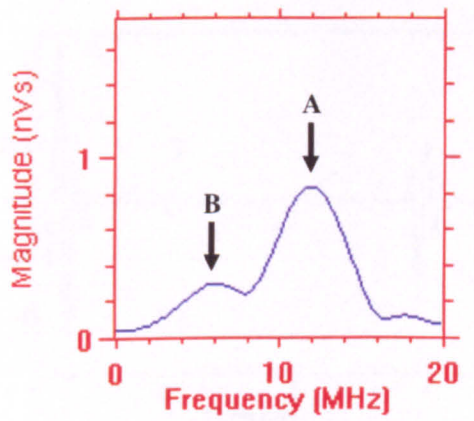

Figure 6.16 Experimental frequency response obtained from gated A-scan for good composite, showing inter-ply resonance ("A") and low level porosity ("B").

Figure 6.16 shows the main inter-ply resonance marked "A"; there is also a secondary peak marked "B" which may indicate low level porosity. The effects of the inclusion of a thick resin layer were also analysed by use of *MLM-Propmat* to see if there was a comparable increase in 3dB bandwidth. The results of the time-frequency analysis for a modelled A-scan (figure 6.17) of an increase in resin layer thickness from 5μm to 20μm and the associated decrease from 125μm to 110μm of the composite layer immediately below the resin layer are shown in figure 6.18.

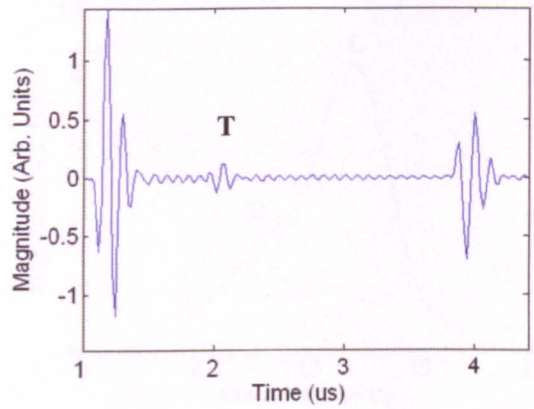

Figure 6.17 Modelled A-scan data from a panel 32 plies thick with a 20μm thick resin layer at layer 10 ("T").

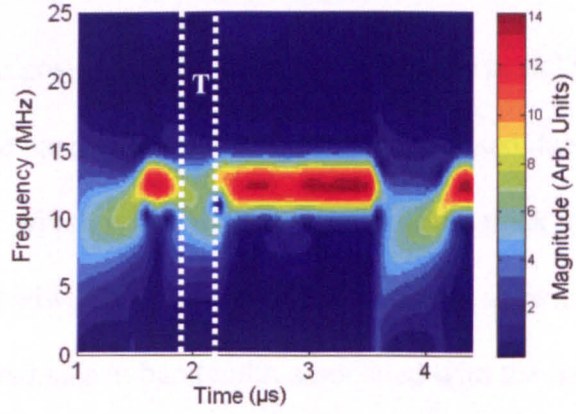

Figure 6.18 Time-frequency analysis of modelled A-scan data from a panel 32 plies thick with a 20 μm thick resin layer at layer 10, marked "T".

Analysis of the thick resin layer region shows that the 3dB bandwidth does increase slightly in this region but not as much as for porosity as shown in figure 6.19 which is a frequency response from modelled data for a thick resin layer.

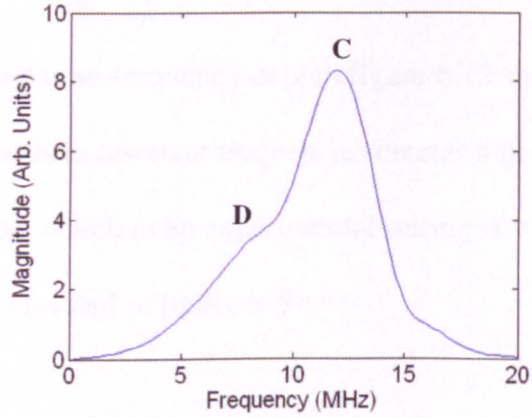

Figure 6.19 Modelled frequency response obtained from gated A-scan composite with a thick resin layer, showing ply resonance peak ("C") and thick resin layer response ("D").

Figure 6.19 shows that the position of the main ply resonance peak "C" has remained constant in frequency. The bandwidth of the signal has increased due to the appearance of another weak peak "D" which is due to the presence of the thick resin layer. Comparison of the 3dB bandwidths for the modelled cases as shown in table 6.1 indicates that there is an increase in bandwidth associated with the inclusion of a thick resin layer but this increase is relatively small when compared with that expected due to a layer of porosity.

Defect	Bandwidth (MHz)
Normal Composite	2.5
10% Porosity in One Layer	8
20μm Resin Layer	3.5

Table 6.1 Comparison of measured 3dB bandwidths for the inclusion of various defects in modelled composite.

Analysis of the modelled time-frequency data in figure 6.12 shows that in the region of porosity, the shift upwards in resonant frequencies creates a peak in the frequency spectrum close to 7MHz, which in an experimental setting is within the bandwidth of the transducer, as demonstrated in figure 6.20.

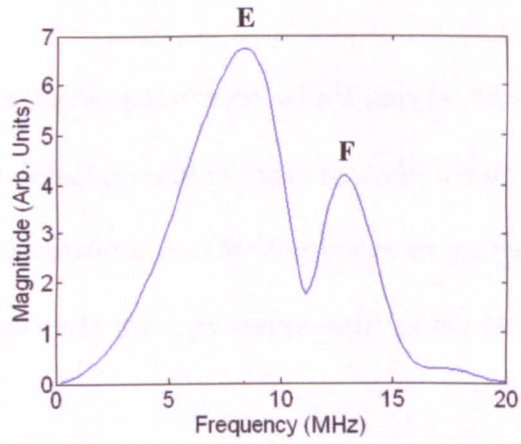

Figure 6.20 Modelled frequency response from porosity, showing peak due to porosity ("E") and inter-ply resonance ("F").

An alternative method which could differentiate between this spectrum and that obtained from a thick resin layer, as shown in figure 6.19, is to take the magnitude of the spectrum at the position of the peak caused by porosity ("E", figure 6.20), and divide it by the magnitude of the signal at the position of the normal ply resonance ("C", figure 6.19, "F", figure 6.20). For porosity this will provide a large value since the magnitude at the higher frequency will be much higher than the magnitude of the signal at the normal ply resonance frequency. For a thick resin layer the energy in the spectrum moves towards the resonance due to porosity but to a much lesser extent. This will cause a slight increase in the parameter value, but not on the same scale as that due to porosity. The values chosen for the two frequencies were 16MHz and 6MHz; the basis

was that 16MHz is above the expected inter-ply resonance value and hence at this value the magnitude of the signal will decrease quickly in response to a porosity flaw; 6MHz was chosen as the second value since this is close to the location of the peak expected under the influence of porosity ("E", figure 6.20) but away from the peak caused by the presence of a thick resin layer ("D", figure 6.19). It is noted that this value is far enough away in the spectrum that a difference will be seen even at low sampling frequencies.

Therefore there are three further parameters which may be measured to give an indication of the type of defect present in the composite: comparison between the resonant frequency, the bandwidth, and the frequency magnitude ratio should provide a method to identify and quantify the type and severity of the two commonest defects.

6.4 Parameter Measurement

6.4.1 Detection of Resonant Frequency

It was required to devise a method which could analyse the inter-ply reflections, and from that derive a measure of the resonant frequency. The spectrum shown in figure 6.21 shows the difficulty associated with calculating the resonant frequency in practice; there are present two resonant peaks which would confuse a simple peak finding algorithm.

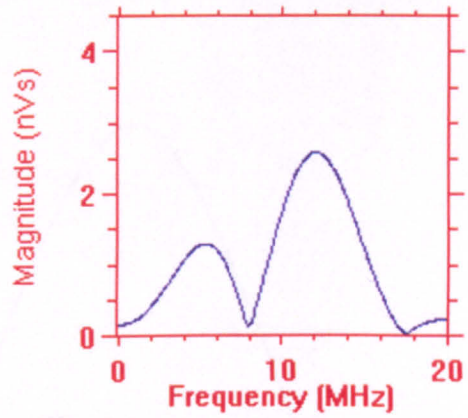

Figure 6.21 Typical frequency response obtained from gated A-scan.

Both peaks in the figure are due to the ply resonance for good composite (figure 6.2). The first peak shown in figure 6.21 is of little interest in this case since the frequency response will in practice be dominated by the resonances at the inter-ply resonant frequency (12 MHz). A method is therefore required which can consistently return a value of resonant frequency even if the result provided by the FFT is ambiguous.

One such method which has applications in this situation is to determine the centre of gravity or centroid of the spectrum; this is equivalent to taking the weighted average, and hence a greater consideration will be given to the frequencies around the resonant frequency of the plies than lower frequencies. This method is also advantageous since it always returns a result providing a spectrum is present to be analysed. A typical frequency response which could be analysed in this way is shown in figure 6.22.

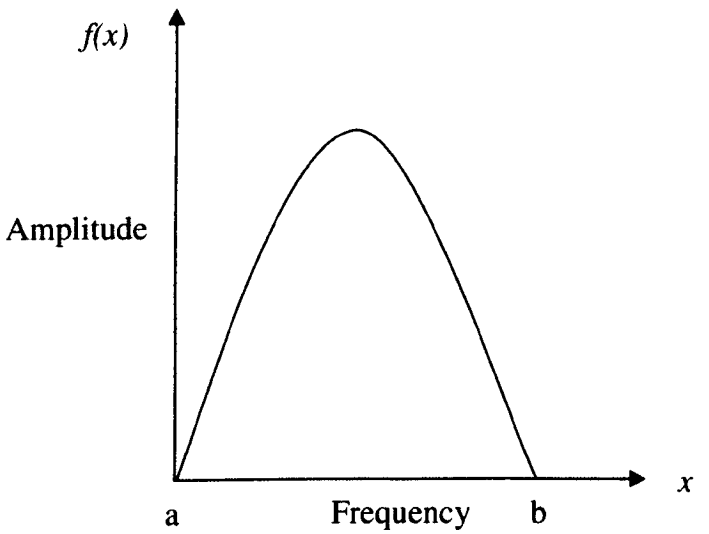

Figure 6.22 Typical frequency response from gated signal.

The area of the spectrum shown in figure 6.22 is given by,

$$A = \int_a^b f(x)dx \tag{6.2}$$

To calculate the centroid of a signal it is necessary to determine the first moment of area about each axis, this is simply the distribution of area of the spectrum in relationship to the x-axis. We can define the x-coordinate of the centre of gravity, which is equivalent to the centroid frequency.

$$\bar{x} = \frac{\int_a^b xf(x)dx}{\int_a^b f(x)dx} \tag{6.3}$$

Where a and b are the limits of integration. From equation 6.3 we can obtain a parameter which will vary as resonant frequency, since as the resonant frequency of the composite increases or decreases the energy within the spectrum will shift either upwards or downwards, affecting the measure obtained via equation 6.3. However, this measure will also be stable to abnormalities within the frequency spectrum, since it is unaffected by minima within the spectrum.

6.4.2 Detection of Bandwidth

A commonly used measure of bandwidth is at the point where the power in the signal has fallen to 3dB of the value at the peak. The 3dB point is used in preference to the 6dB point since in the frequency responses which are to be analysed the signal often does not fall to 6dB below the peak value. It is noted that the frequency spectrum which will be analysed will not necessarily be symmetrical about the peak as seen in previous modelled results. Therefore, a peak finding code was written which would identify the largest peak within the spectrum, and from this point the 3dB points which were at frequencies higher than and lower than the frequency of the peak were determined. The frequency difference between these two points was then calculated providing a measure of bandwidth.

6.4.3 Detection of Frequency Magnitude Ratio

Section 6.3.2 provided a method for comparing the magnitudes of different frequencies within the spectra generated from time-frequency analysis. The modelling exercises conducted indicated that this method would generate a mean value which would

increase strongly or weakly dependent upon the type of flaw present. Application of a colour scale which differed from the mean value towards one of two contrasting colours would allow ready detection and differentiation between these two types of defect. For example if the mean value were assigned to orange and values higher than this were green and values much greater than this were purple then defects would not only be readily visible but easily identifiable. A sample colour scale is shown in figure 6.23. the scale on figure 6.23 may be linear (amplitude) or logarithmic (nepers or dB) depending on the application.

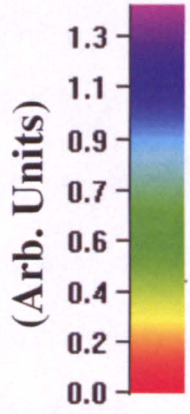

Figure 6.23 Specimen colour scale for use in frequency magnitude comparison method.

6.5 Experimental Results

6.5.1 Experimental Results for Resonant Frequency

The data obtained experimentally from the samples described in chapter 5, section 5.8, was reprocessed and the effect of resonant frequency examined. Sample 1 (Appendix E) was examined by means of a C-scan of back wall echo amplitude as in figure E.1. A B-scan of energy centroid frequency was taken along a horizontal line at a point 100mm on the vertical axis of figure E.1, and is shown on figure 6.24.

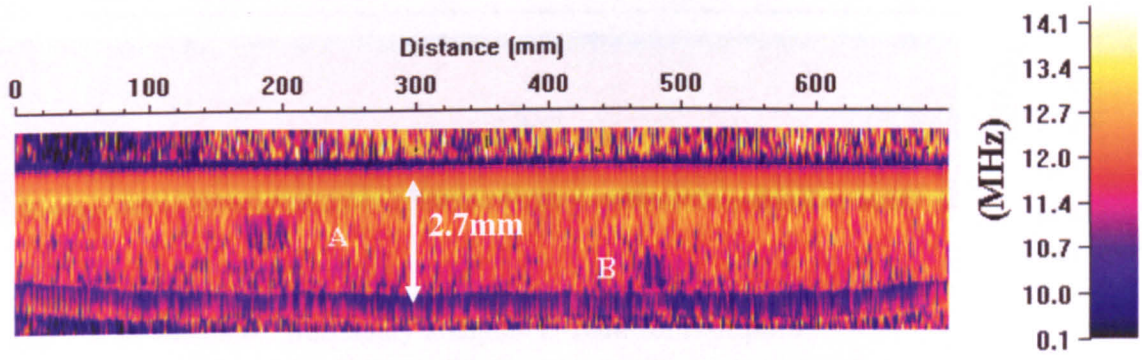

Figure 6.24 Resonant frequency analysis B-scan of Sample 1.

On this figure the dark areas indicate a decrease in resonant frequency, and are an indication of porosity, in this case the two dark areas A and B occur where the glass microspheres have been included in the panel. A decrease in resonant frequency is seen rather than the increase which theory suggests is present due to the bandwidth of the transducer used and the strength of the resonance from the microspheres. The strength of reflection from the microspheres is so great that the resonance quickly moves from a half wave to a quarter wave resonance taking the power in the spectrum out of the bandwidth of the transducer, the lower resonance moves into the bandwidth and begins to dominate causing an apparent decrease in resonant frequency.

Sample 2 (Appendix E) was re-examined using the resonant frequency method. Initially a C-scan of back wall echo amplitude was produced as in figure E.2. Specimen B-scans were produced across the panel as shown in figure 6.25.

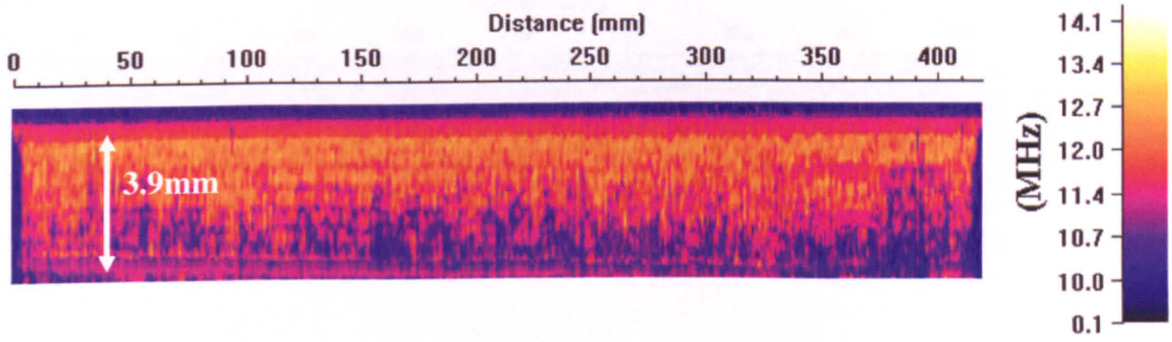

Figure 6.25 Resonant frequency analysis B-scan for Sample 2.

In figure 6.25 it is observed that there are many dark regions across the panel which correspond to a decrease in resonant frequency and hence might be suspected to be porosity. However, there are also large sustained dark regions towards the back wall of the panel; these can be explained if we consider the attenuation of typical carbon fibre composites. It would be expected that higher frequencies would attenuate more highly than lower frequencies, this effect causes energy to be lost from the spectrum at these higher frequencies (those towards the inter-ply resonant frequency) and hence the energy centroid frequency measured appears to decrease over larger propagation distances. This is a problem which may be resolved by application of a frequency and distance dependent amplitude correction. To examine the effectiveness of a resonant frequency measure for relatively short propagation distances (those less effected by attenuation) C-scans of the parameter at specific depths were produced. Figure 6.26 shows a C-scan at a depth of 1.6mm.

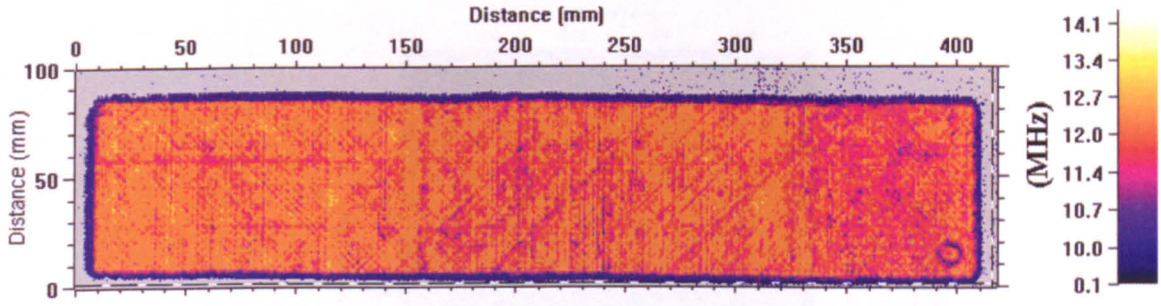

Figure 6.26 Resonant frequency analysis C-scan for Sample 2.

Figure 6.26 shows lines of porosity in parallel with the fibre direction, and this effect has previously been observed by analysis using the envelope analysis method as shown in figure 6.27 which is a C-scan for the same depth produced using the envelope analysis method.

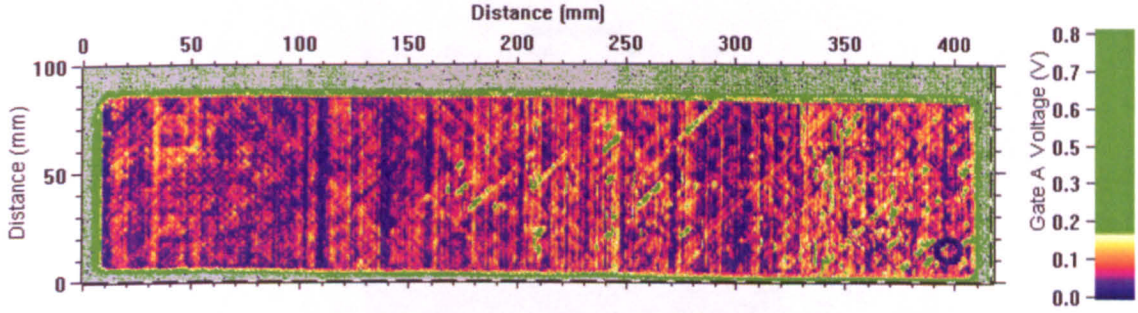

Figure 6.27 Envelope analysis C-scan for Sample 2.

Finally Sample 3 (Appendix E) was analysed and the effects on resonant frequency of porosity and thick resin layers was examined. To allow direct comparison of the resonant frequency method with the envelope analysis method C-scans were produced at a depth of 3.2 mm, it was at this depth that a thick resin layer was present which was detected by the envelope analysis method and mistaken for porosity. Figure 6.28 shows the C-scan produced via envelope analysis.

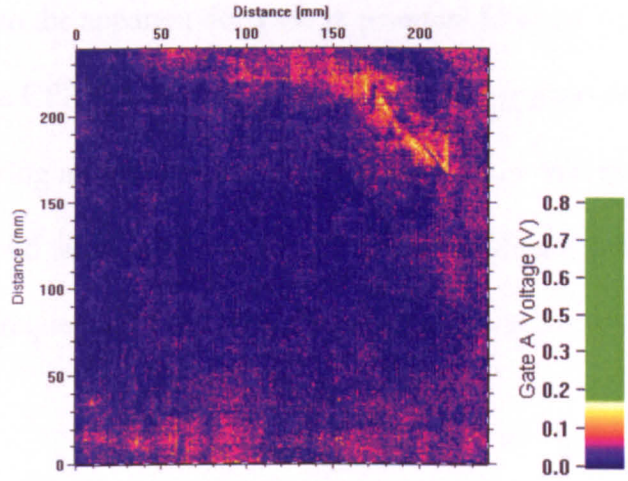

Figure 6.28 Envelope analysis C-scan for Sample 3.

The results of this analysis were then compared with those obtained when the sample was examined by use of the resonant frequency method, as shown in figure 6.29.

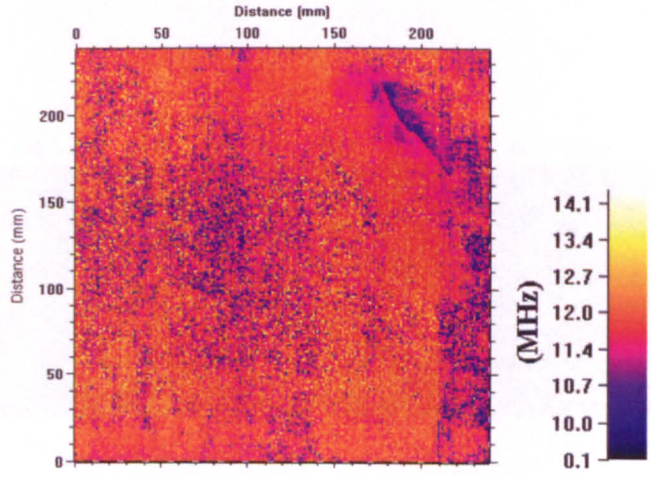

Figure 6.29 Resonant frequency analysis C-scan for Sample 3.

Comparison of the C-scans shown in figures 6.28 and 6.29 reveals that the resonant frequency method has also highlighted the thick resin layer as porosity. This effect results from the decrease in resonant frequency associated with thick resin layers as demonstrated in section 6.3.2; it is possible therefore to conclude from the experimental evidence that the change caused in resonant frequency from thick resin layers is of a

comparable magnitude to the apparent decrease in resonant frequency caused by porosity. Analysis of the CFRP produced by Airbus containing glass microspheres as well as that produced using normal production techniques show that the method is sensitive to both small and large scale porosity. There are problems however, associated with the loss at higher frequencies caused by the inherent attenuation within carbon fibre panels.

6.5.2 Experimental Results for Bandwidth Analysis Method

The experimental data obtained previously was re-examined using time-frequency analysis, and the 3dB bandwidth of the spectra obtained taken. A C-scan of Sample 1 was produced, figure 6.30.

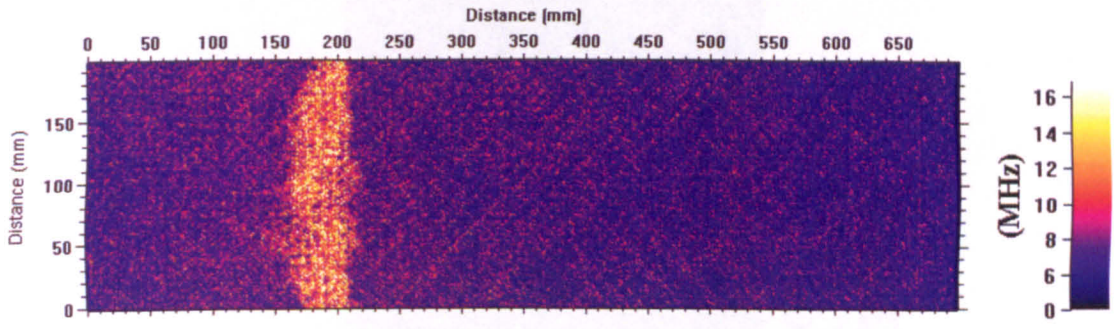

Figure 6.30 3dB Bandwidth C-scan for Sample 1.

In figure 6.30 the dark areas represent regions where the bandwidth has increased and which we might suspect to be porosity. In this scan the region of glass microspheres can be clearly seen running vertically at a point 200mm on the horizontal axis. A C-scan of suspected porosity in Sample 2 was produced as in section 6.5.1.

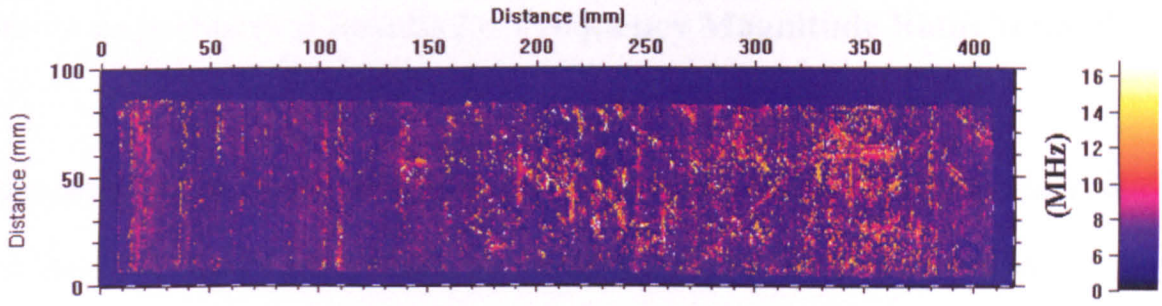

Figure 6.31 3dB Bandwidth analysis C-scan for Sample 2.

Figure 6.31 was produced at the same depth as figures 6.26 and 6.27 and compares favourably with them. The lighter areas represent an increase in bandwidth which would be expected in the presence of porosity. The apparent areas of porosity are parallel to the direction of the fibres as has been observed previously. Finally analysis of the area in Sample 3 showing a thick resin layer was conducted.

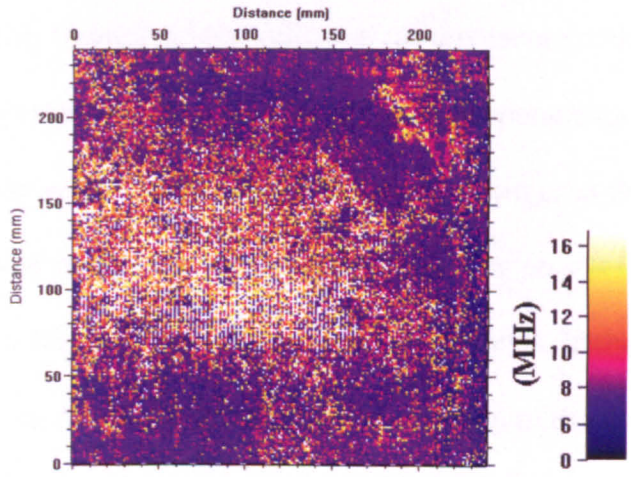

Figure 6.32 3dB Bandwidth analysis C-Scan for Sample 3.

Figure 6.32 appears to show that an increase in bandwidth has been detected in the area where the thick resin layer is present. The scan also shows scattered porosity across the panel.

6.5.3 Experimental Results for Frequency Magnitude Ratio Method

Comparisons were made between experimental results obtained previously and those utilising the frequency magnitude ratio method. Sample 2 was re-examined and a C-scan of frequency magnitude comparison as in section 6.5.1.

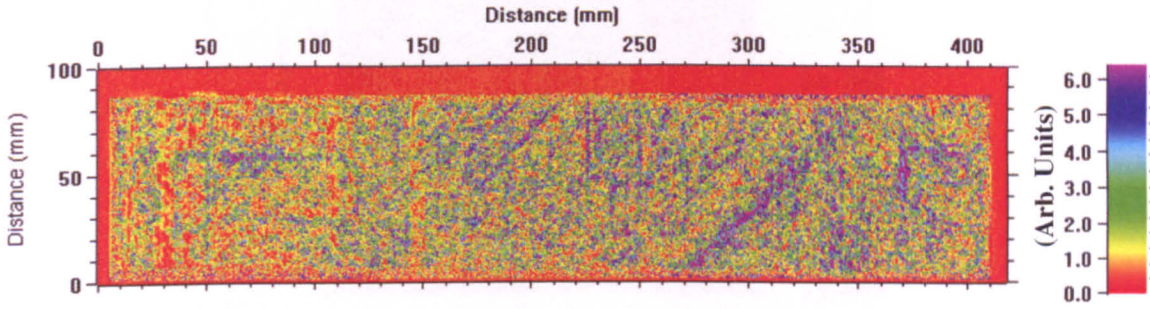

Figure 6.33 Frequency magnitude comparison C-scan for Sample 2.

In the C-scan shown in figure 6.33 the yellow areas represent good composite, the blue and purple areas represent an increase in the value of the parameter corresponding to porosity and the green and red areas represent a small changes in the value of the parameter and are most likely to be fibre resin effects. The results from this method would tend to agree with those obtained using other methods, in that porosity is detected across the panel in lines which are parallel to the direction of the fibre tows. However, there are areas which are marked in green/red which would indicate the presence of a fibre-resin effect. It is noted that a broadband response, such as that which would be obtained from a back wall echo, would cause a large value of the parameter to be returned which would be highlighted as porosity. This is because the energy in the signal shifts away from the higher frequencies at this point, reflecting the transducer pulse. This is currently only considered to have happened for large air voids, and as such this is seen as an acceptable result from the method.

A C-scan was conducted on Sample 3 which appeared to show a thick resin layer in the presence of porosity.

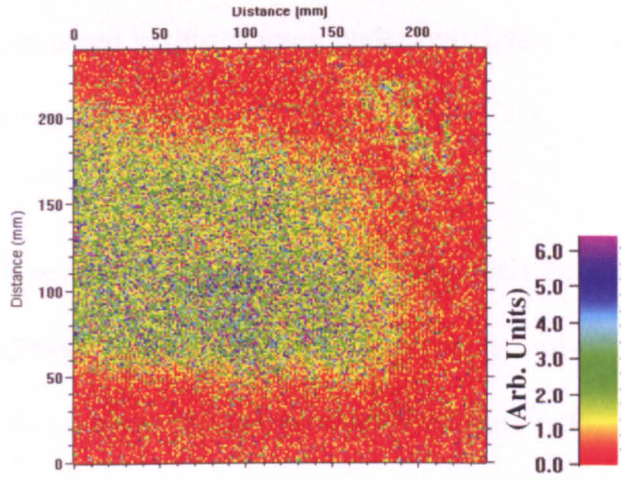

Figure 6.34 Frequency magnitude ratio C-scan for Sample 3.

The C-scan shown in figure 6.34 compares favourably with previous analysis of this panel; there appears to be a large region of porosity scattered across the panel, represented by blue and purple point like reflectors within the green area which indicates an area of increased resin thickness. This is similar to what was observed by the 3dB bandwidth analysis scan, which showed an increase in bandwidth in these areas. The area of the cut out is less well defined than in previous methods. This is attributed to loss within the signal at higher frequencies (since the cut-out is towards the rear of the panel), this loss causes the value of the parameter to be lower than would otherwise be expected.

6.6 Combined Method

The need for a combined method was illustrated by comparisons which were made between the envelope analysis method outlined in chapter 6, and the time-frequency dependent methods discussed in this chapter, under two defect conditions, porosity and the presence of a thick resin layer.

An area where a thick resin layer was present had previously been identified in a test sample provided by QinetiQ via use of a micrograph, as described in chapter 5 section 5.7, for convenience this micrograph is reproduced in figure 6.35.

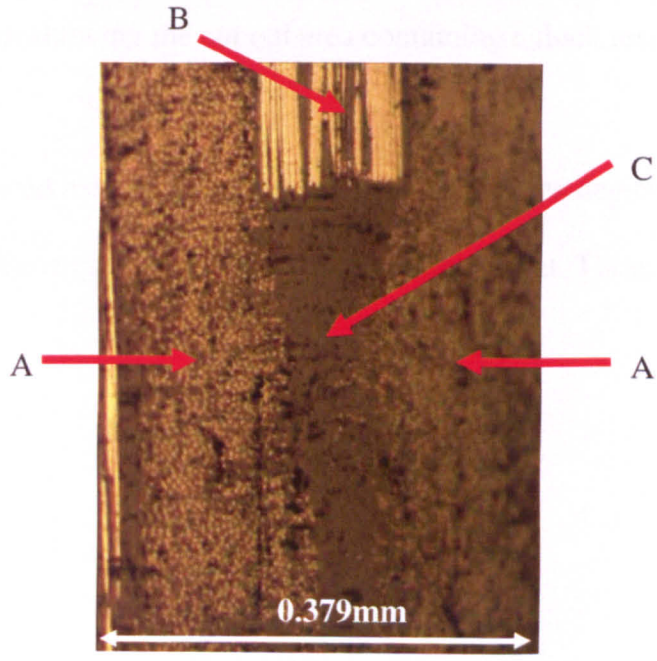

Figure 6.35 Micrograph of fibre cut out showing fibres "A" and "B", and resin "C".

Figure 6.35 shows fibres running parallel to the plane of the micrograph marked by B, fibres running perpendicular to the plane marked as A and the area of the cut-out filled by resin marked as C which decreases in thickness with distance away from the cut-out

boundary. There are also dark areas which may be low levels of porosity. The presence of both types of defects allows a convenient test region for analysing the performance of the various parameters which have been identified. A diagram showing the cut out area is shown in figure 6.36, where the area marked as "a" corresponds to normal composite, and the area marked as "b" corresponds to an area where the fibres from a ply have been removed.

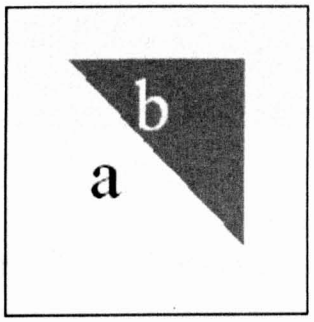

Figure 6.36 Diagram showing the cut out area containing a thick resin layer.

A C-scan was produced using each of the methods for the area depicted in figure 6.36, and at a depth which corresponded to the centre of the cut-out. These C-scans are shown in figure 6.37.

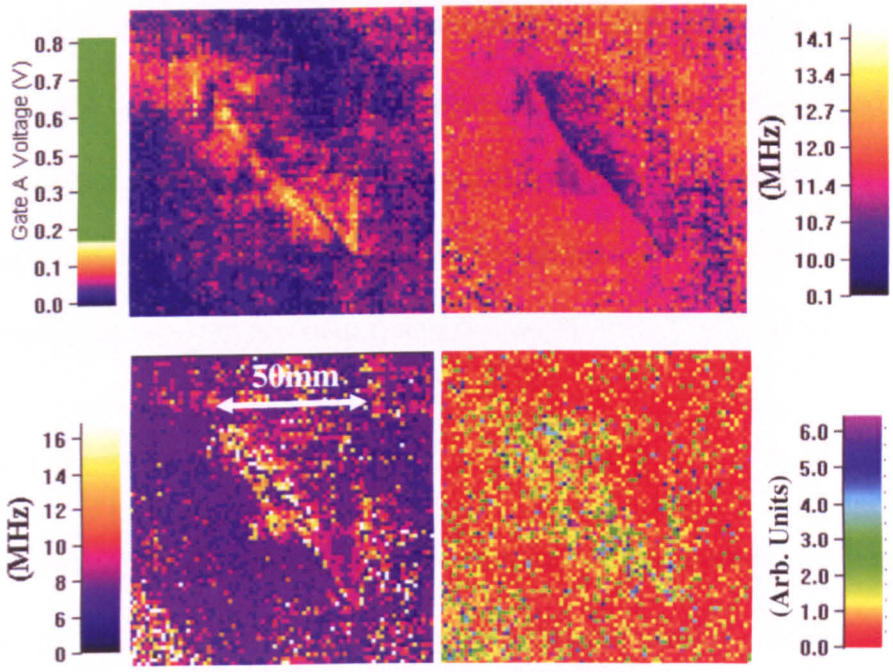

Figure 6.37 Parameter C-scans for envelope analysis (top left), resonant frequency (top right), 3dB bandwidth (bottom left) and frequency magnitude ratio (bottom right).

Figure 6.37 shows that the envelope analysis method (top left) produces a large response (shown as lighter colours) at the boundary between the fibres and the thick resin layer; this is equivalent to an increase in the reflected signal and would be expected in both the presence of porosity or a thick resin layer as demonstrated in the modelling of the local resonance (section 6.2). This corresponds to the region of the micrograph were there is a thick resin layer but also suspected porosity. There is also an increase in reflected amplitude detected via the envelope analysis method in the thick resin layer region ("b" in figure 6.36), this is again expected since there will be an increase in the energy reflected at this point.

The resonant frequency method (figure 6.37, top right), records a large decrease in resonant frequency (shown as a darkening in colour) at the boundary between the fibres

and the thick resin layer, this is indicative of porosity as described in section 6.5.1, and would support the assertion that the dark regions observed in the micrograph in figure 6.35 are in fact porosity. In the cut-out region ("b" in figure 6.36), a decrease in resonant frequency is also detected, although the colours are not as dark, indicating that there is a smaller decrease in resonant frequency which would indicate a thick resin layer.

The 3dB bandwidth measure (figure 6.37, bottom left), shows isolated regions of brightness at the boundary between the fibres and the cut-out, this corresponds to an increase in bandwidth, this would only be expected if porosity were present. In the cut-out region ("b" in figure 6.36), there are regions of brightness indicating that porosity is present, since the reflection from this area is not large when compared to the back wall echo.

Observation of the frequency magnitude ratio method (figure 6.37, bottom right) shows that on the boundary between fibres and resin a red colour is observed indicating that there is an increase in the thickness of the resin; there is also present a blue colour which would show the presence of porosity. In the cut-out region ("b" in figure 6.36), there is also a red colour indicating a thick resin layer, which gradually changes to orange, the base colour for unflawed composite. This would be expected since the resin layer gradually decreases in thickness at this point.

There are also responses from within the "good" composite area at the edges of the cut out for all of the methods analysed. This is most likely due to the cutting mechanism used on the fibres which tends to cause the fibres to spread at the edges of the cut out.

Comparison between the methods which have been determined has allowed the structure of this complex region to be better understood. It is noted that no single method is able to reliably determine the type of defect present in isolation, rather a comparison must be made between the methods to allow identification of the defect. A table has been constructed showing the performance of these methods in the presence of differing defects; this table highlights the need for comparison when making a decision on what type of anomaly is present.

	Porosity	**Increased resin thickness**	**No flaw**
HT	**1**	**1**	**0**
f_0	**-1**	**0**	**0**
Δf	**+1**	**0**	**0**
f_x/f_y	**+1**	**+0.5**	**0**

Table 6.2 Significant indications of porosity or increased resin thickness: from the Hilbert transform (HT), the frequency of the principal data peak (f_0), the bandwidth in the transition region (Δf) and the frequency magnitude ratio (f_x/f_y). **1** = strong indication, **+1** = significant increase, **-1** = significant decrease, **0** = no significant change.

6.7 Detectability of Defects

Variation of Parameters with Increasing Porosity Content

To examine the usefulness of a system to defects using these methods it was necessary to determine the minimum detectable defect quantity. A further modelling exercise was undertaken to provide an indication of the minimum defect quantity, the effect of depth on defect detectability and additionally the effect of the presence of multiple defects. A 32 ply system was created as in described in section 6.3.2. In the first exercise, porosity

or a thickened resin layer were inserted into the 10th ply. To better reflect experimental data, the thickness of the resin layers was randomized, using 50% randomization. Time-frequency analysis was then conducted on the resulting time-domain signals, the analysis methods outlined previously could then conducted, and the change due to the inclusion of the defect measured. For porosity, volume fractions of 0, 1, 2, 4, 8, 16 and 32% and radius 10μm were used. The results obtained for envelope analysis are shown in figure 6.38.

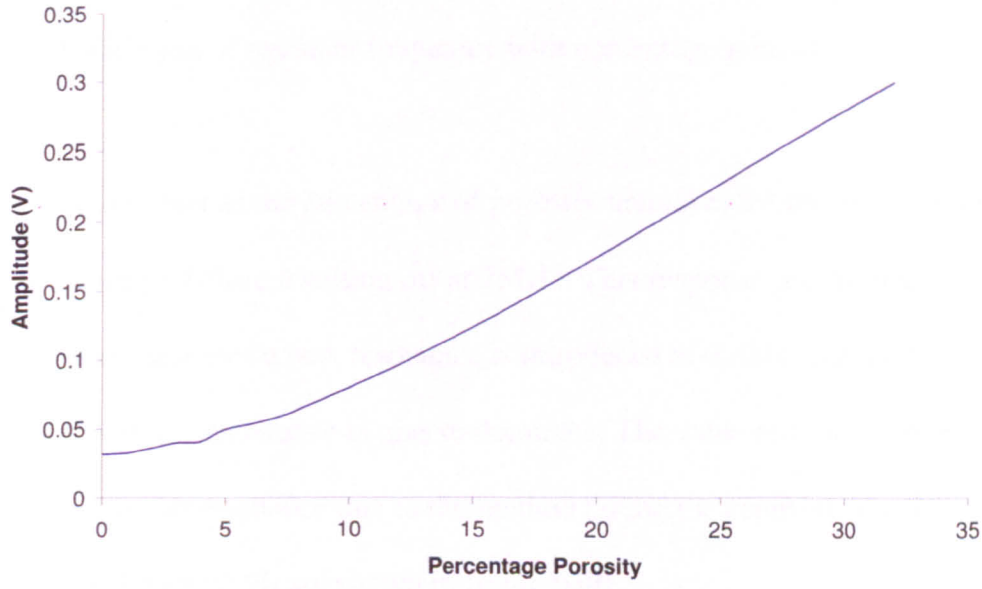

Figure 6.38 Variation of envelope analysis parameter with percentage porosity.

Figure 6.38 shows that where there is an increase in percentage porosity, there is an increase in amplitude of the signal at that point. This is as has been previously shown by modelling (section 6.2) and is expected. The results obtained for resonant frequency are shown in figure 6.39.

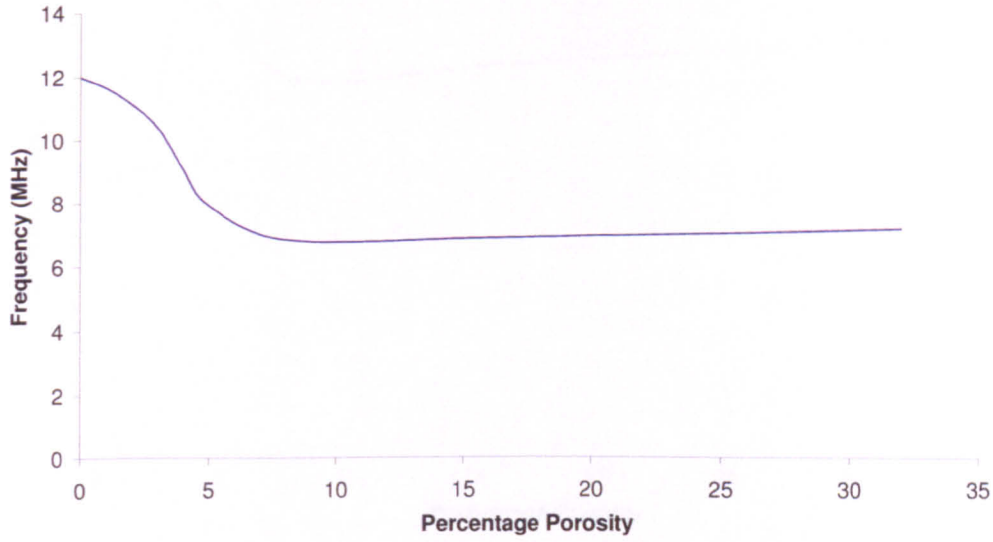

Figure 6.39 Variation of resonant frequency with percentage porosity.

Figure 6.39 shows that as the percentage of porosity increases the measured resonant frequency decreases before levelling off at 7MHz. This response is expected since as the level of porosity increases a new resonance is introduced at 6MHz, and as the volume fraction increases this resonance begins to dominate. The value returned is higher than the actual peak in the resonance due to the method taking the centroid. The results obtained for 3dB bandwidth are shown in figure 6.40.

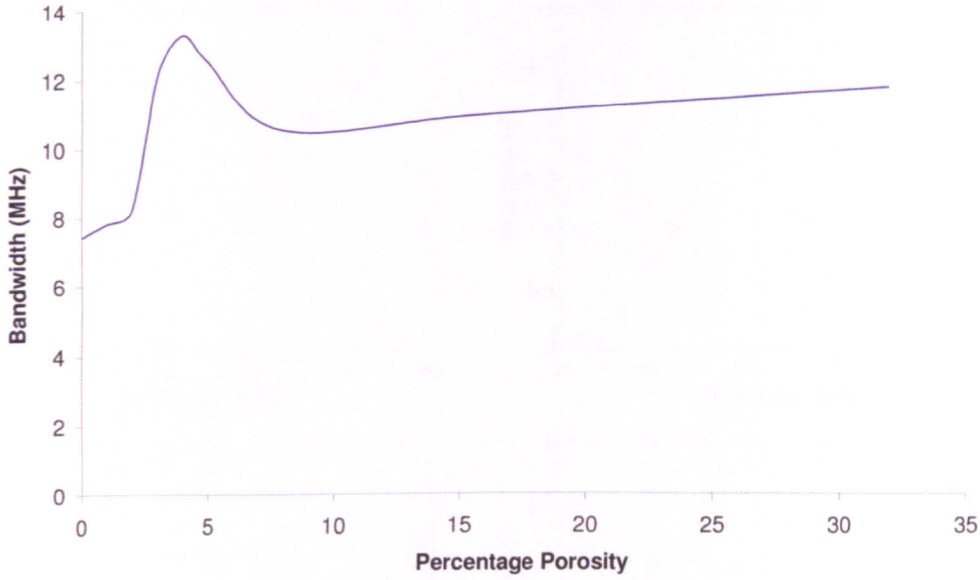

Figure 6.40 Variation of 3dB bandwidth with percentage porosity.

Figure 6.40 shows that as percentage porosity increases, the 3dB bandwidth increases also. A sharp increase in bandwidth begins at 1% porosity and reaches a peak at 4%, which then decreases until the percentage porosity is 8%. This result seems counterintuitive since one would expect the bandwidth to increase constantly, verification of this result was undertaken by measuring the value of bandwidth at additional volume fractions, and this shape was consequently verified. An explanation of this phenomenon is forthcoming if we examine the spectra which are generated in this transition region. The spectra for 0, 1, 2, 4, 8 and 16% porosity are shown in figure 6.41.

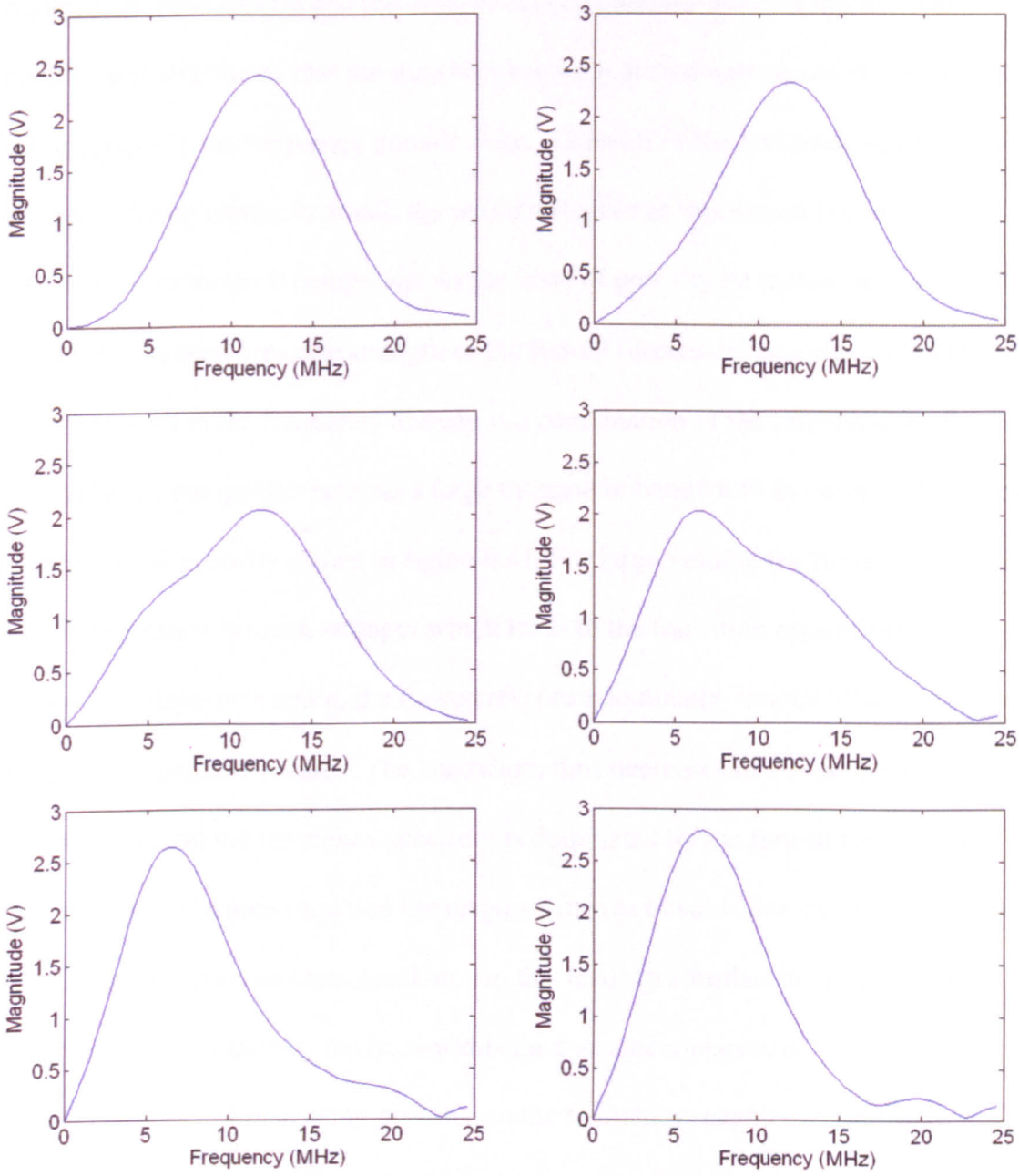

Figure 6.41 Frequency spectra obtained from the transition region for 0% (top left), 1% (top right), 2% (middle left), 4% (middle right), 8% (bottom left) and 16% porosity (bottom right).

Figure 6.41 shows that the spectra for 0% porosity is that which would be expected for unflawed composite, this gradually moves to a combination of the resonance for unflawed composite and the resonance for porous composite for 4% and 8% porosity; finally the resonance for flawed composite dominates for 8% and 16% porosity.

Analysis of these spectra and the time-frequency plots for these values of volume fraction porosity shows that the transition region is at first narrow in time, as well as being narrow in the frequency domain. This is a result of the flawed composite resonance being relatively small; the major influence in this region is therefore the resonance for unflawed composite. As the level of porosity increases the width of this region in time increases, the strength of the flawed resonance increases and hence the result obtained in the frequency domain is a combination of the responses for flawed and unflawed composite, causing a large increase in bandwidth as observed in the case of 2% and 4% porosity shown in figure 6.41. For large volume fractions of porosity the flawed resonance is much stronger which leads to the transition region becoming narrower in time once again, the flawed response dominates and the influence of the unflawed response decreases. The bandwidth thus decreases to 8% porosity as this effect begins and the frequency spectrum is dominated by the flawed response. For higher values of volume fraction the response moves towards that expected for a back wall echo and the resonances break down, this leads to a further increase in bandwidth as the frequency spectrum moves towards the transducer response.

Finally the effect of increasing porosity on the frequency magnitude ratio were investigated as shown in figure 6.42.

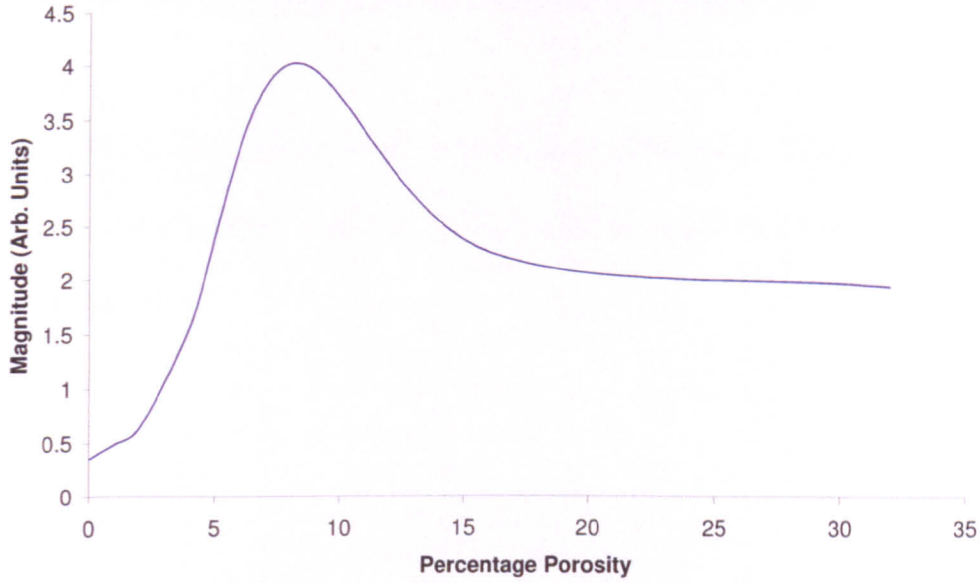

Figure 6.42 Variation of frequency magnitude ratio with percentage porosity.

Figure 6.42 shows that we see an increase in the measured frequency magnitude ratio, until the void volume fraction reaches 9%, after which we see a gradual decrease in the value of the parameter until a level is reached for values of porosity greater than 20%. An initial increase is observed since in the porous region the energy in the signal is decreasing at 16MHz as the flawed response becomes more like the flawed response which has a peak at 6MHz; the value at this frequency is hence increasing. Once a peak in the value of frequency magnitude is reached the value of this parameter begins to decrease as the spectrum becomes more like that of a back wall echo, which has a peak at a higher frequency, the energy at 6MHz thus decreases whilst the energy at 16MHz increases, decreasing the value of the parameter. This decline in parameter value is then halted when the reflection from the porosity is so large it is like a back wall echo; at this point the magnitude of the 6MHz and 16MHz components are both increasing but at a similar rate which allows the parameter to reach a final value.

Variation of Parameters with Increasing Resin Layer Thickness

To demonstrate the detectability of thick resin layers a thick resin layer of 1, 2, 5, 10, 15, 20 or 40μm was inserted at the 10th ply, the obtained result for envelope analysis is shown in figure 6.43.

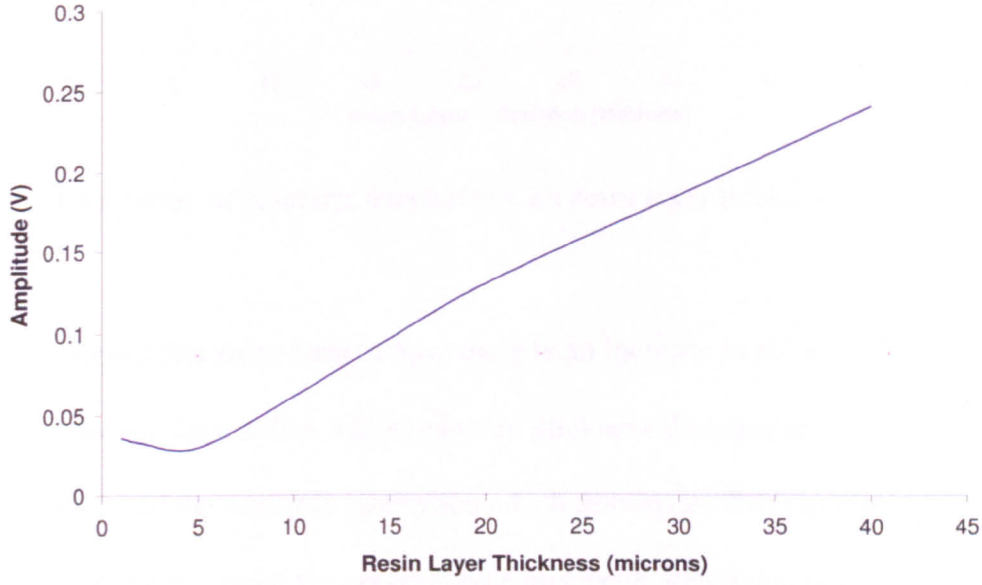

Figure 6.43 Variation of envelope analysis parameter with resin layer thickness.

Figure 6.43 shows that there is a near linear increase in amplitude of the envelope analysis parameter with resin layer thickness. This has been observed previously in modelling (section 6.2) and is as expected. The results which were obtained for resonant frequency are shown in figure 6.44.

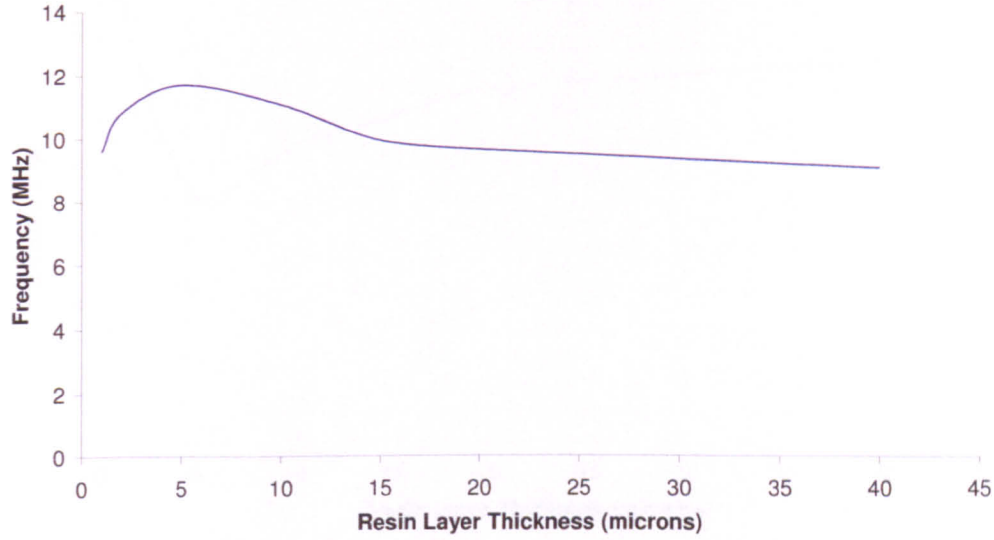

Figure 6.44 Variation of resonant frequency with resin layer thickness.

Figure 6.44 shows that from 1μm to 5μm there is an increase in resonant frequency, this would be expected since at low values of resin thickness the plies are almost in contact with each other and the inter-ply resonance which dominates the response is of a very high frequency. At this point the second resonance peak which dominates the spectrum is outside of the bandwidth of the transducer allowing the first and lower in frequency resonant peak to dominate. At higher values of resin layer thickness there is a decrease in resonant frequency which is expected and has been previously shown via modelling (section 6.2). The results for 3dB bandwidth are shown in figure 6.45.

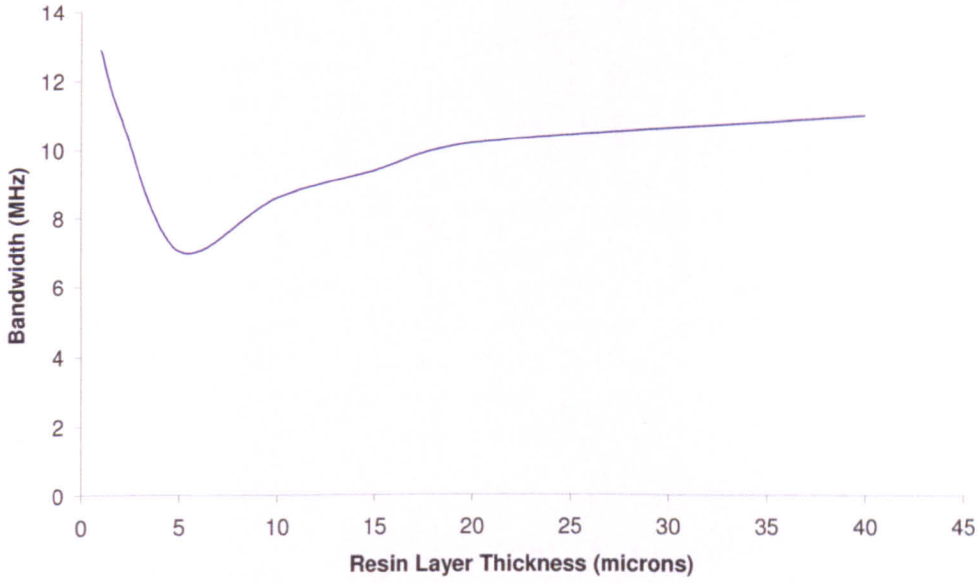

Figure 6.45 Variation of 3dB bandwidth with resin layer thickness.

Figure 6.45 shows that a large bandwidth is detected for low resin layer thicknesses, and this is due to the plies almost being in contact with each other which causes a large reflection. For values of resin layer thickness higher than 5μm an increase is seen. A small increase of 2.5MHz had previously been predicted by full wave-form path modelling and the final value of 11MHz is consistent with this. The effect of resin layer thickness on frequency magnitude ratio is shown figure 6.46.

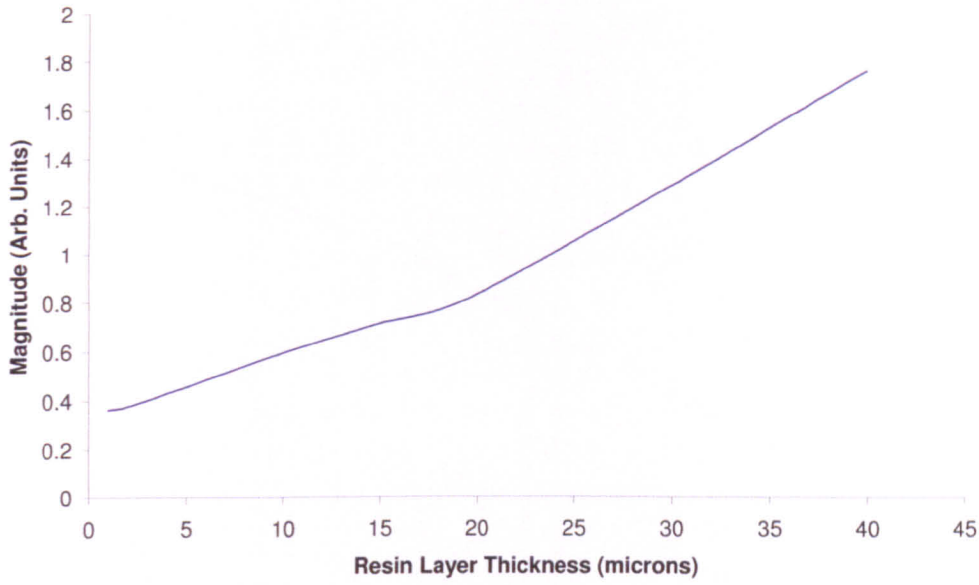

Figure 6.46 Variation of frequency magnitude ratio with resin layer thickness.

Figure 6.46 shows that an increase in frequency magnitude ratio is observed, but this is not of the same magnitude as that observed for porosity (figure 6.42). This increase is observed because the frequency of the resonance decreases, reducing the energy at 16MHz and increasing the energy at 6MHz.

Variation of Parameters with Porosity Depth

To examine the effect of depth on the detectability of a defect, a layer of porosity of 10% volume fraction and scatterers of radius 10μm was added to the composite at the 4^{th} ply, measurements were then made of the parameters. The results for the first 3 plies are not shown due to interaction with the front wall echo. The defect was then moved through the sample a ply at a time and further readings taken, the results obtained for envelope analysis are shown in figure 6.47.

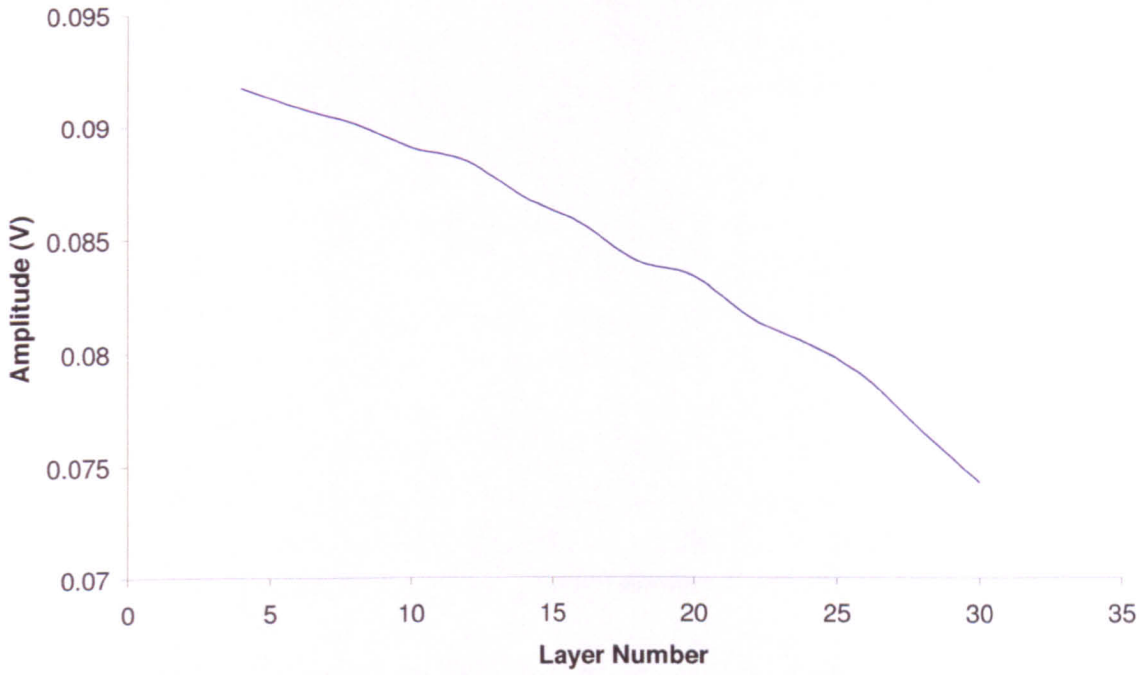

Figure 6.47 Variation of envelope analysis parameter with porosity depth.

Figure 6.47 shows that there is a decrease in the amplitude of the envelope analysis parameter with depth, this is expected and is due to loss of signal from reflections at previous plies as well as viso-elastic attenuation. This may be corrected with application of the distance amplitude correction discussed in chapter 5, section 5.6. The variation of resonant frequency with depth is shown in figure 6.48.

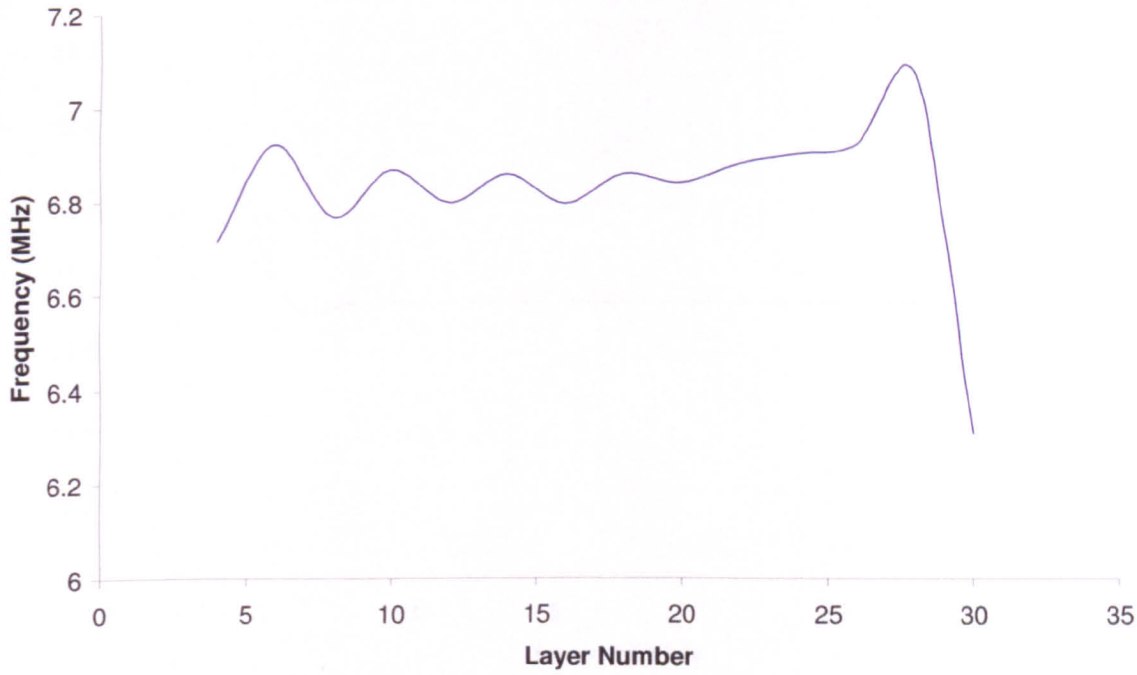

Figure 6.48 Variation of resonant frequency with porosity depth.

Figure 6.48 shows that there is no variation of resonant frequency with depth. The features observed at the 2nd and 28th layer are due to interference from the front and back wall echoes respectively. No variation was expected since the resonance which is being measured is at a comparatively low frequency of 6MHz so attenuation effects are not as marked as at higher frequencies. The resonance is also much stronger than the regular resonance observed for unflawed composite. There is some variation in the measured resonant frequency due to the randomness of the ply layer thicknesses used in the model; this is as shown in figure 6.8. The response obtained for 3dB bandwidth with depth of porosity is shown in figure 6.49.

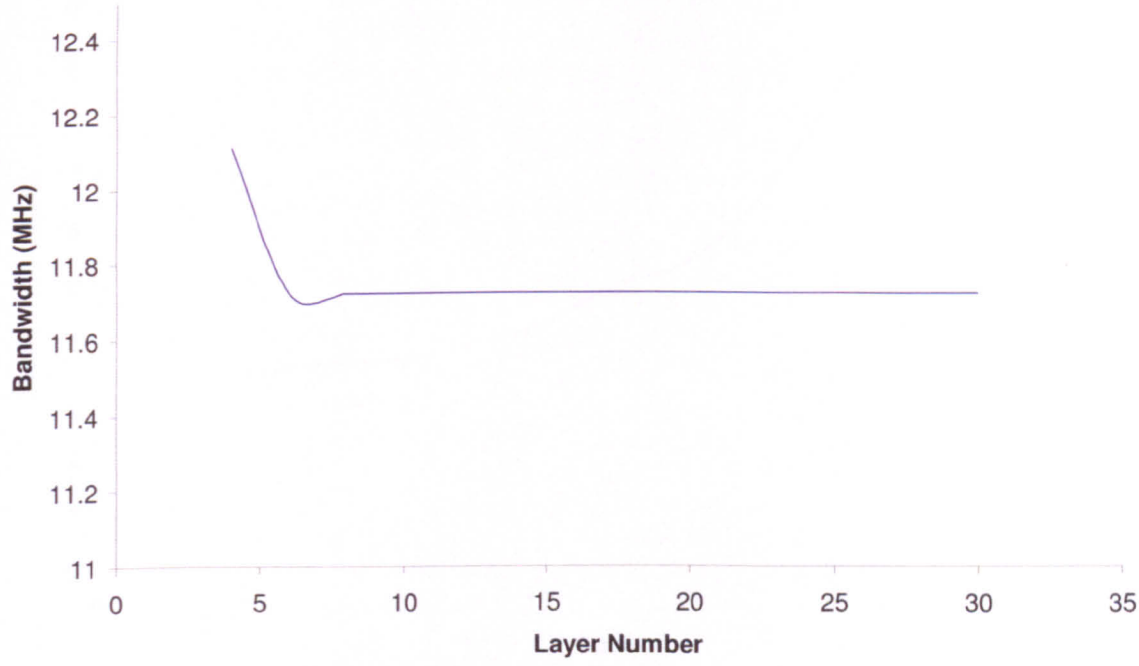

Figure 6.49 Variation of 3dB bandwidth with porosity depth.

Figure 6.49 shows that there is a feature near to the front wall, which is thought to be related to the front wall echo. The measured bandwidth remains constant throughout the depth, a slight decrease in bandwidth might have been expected due to attenuation at higher frequencies. However, at this level of porosity the spectrum is dominated by the porosity resonance, and hence most of the energy is at lower frequencies and the bandwidth remains the same. The effect of depth on the frequency magnitude ratio parameter is shown in figure 6.50.

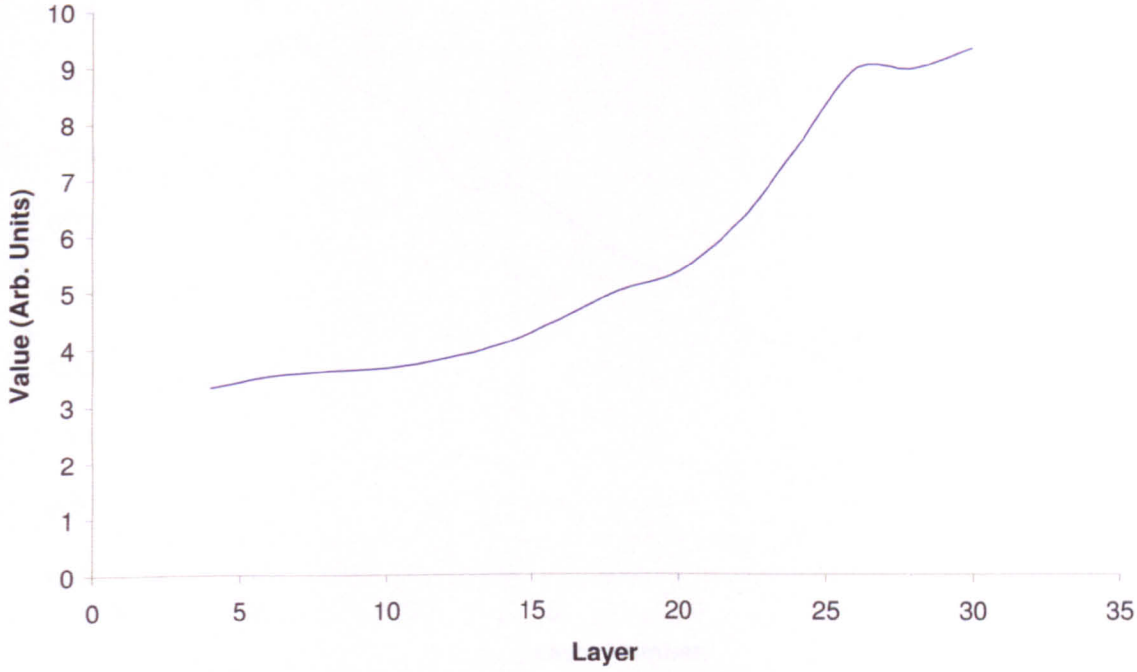

Figure 6.50 Variation of frequency magnitude ratio with porosity depth.

Figure 6.50 shows that the value of the frequency magnitude ratio parameter increases with porosity depth, this is attributed to greater attenuation at higher frequencies, reducing the value of the 16MHz value and hence increasing the value of the parameter.

Variation of Parameters with Thick Resin Layer Depth

The same procedure was then carried out using a thick resin layer of 20μm. The defect was then moved through the sample a ply at a time and further readings taken. The results for the first 3 plies are not shown due to interaction with the front wall echo and for all similar figures. The results obtained for envelope analysis are shown in figure 6.51.

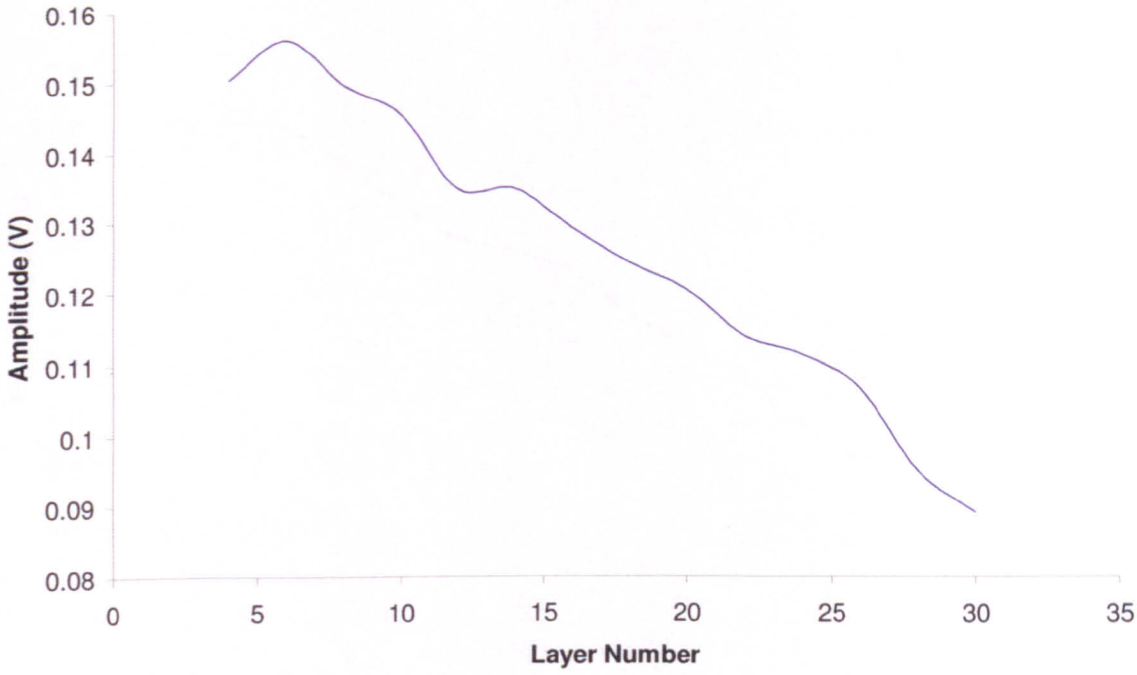

Figure 6.51 Variation of envelope analysis parameter with depth of thick resin layer.

Figure 6.51 shows that as the depth of the thick resin layer is increased there is a decrease in the value of the envelope analysis parameter. This is similar to what was observed in figure 6.50, and could be corrected using the methods described in chapter 5, section 5.6. The variation in resonant frequency with defect depth is shown in figure 6.52.

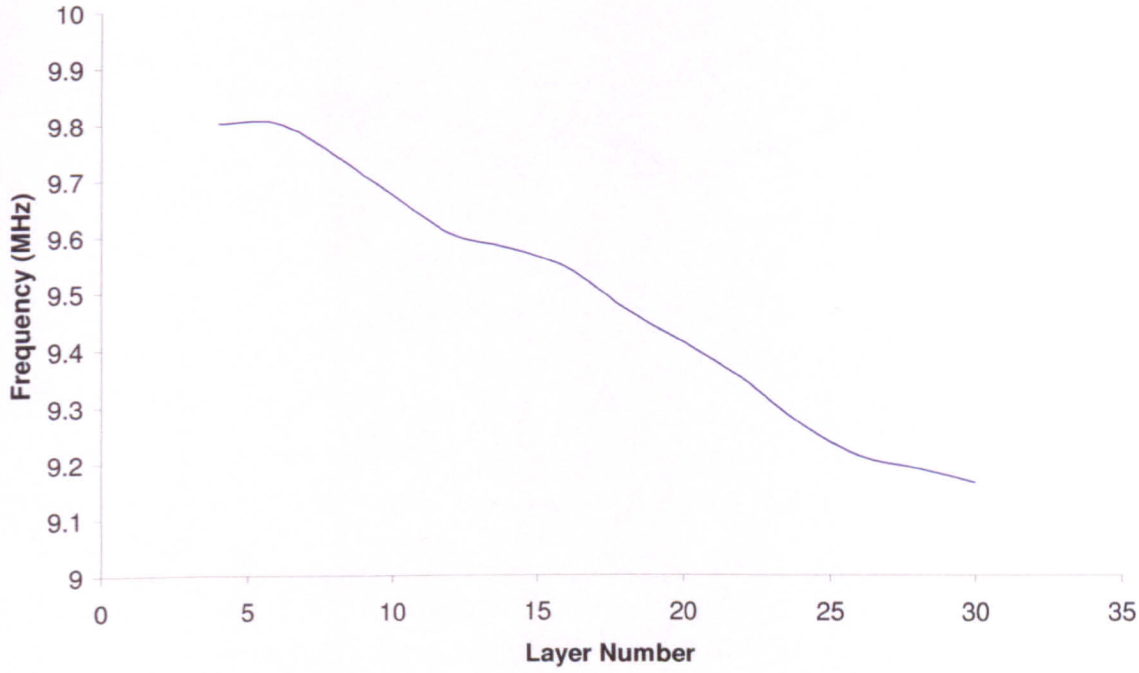

Figure 6.52 Variation of resonant frequency with depth of thick resin layer.

Figure 6.52 shows that there is a small decrease in resonant frequency with defect depth, although examination of the spectra shows that there is not a significant loss of energy from the resonant peak, it is considered that energy is lost from the higher frequencies via visco-elastic attenuation. Since the resonant frequency method takes the weighted average this will lower the measured resonant frequency. The effect on bandwidth is shown in figure 6.53.

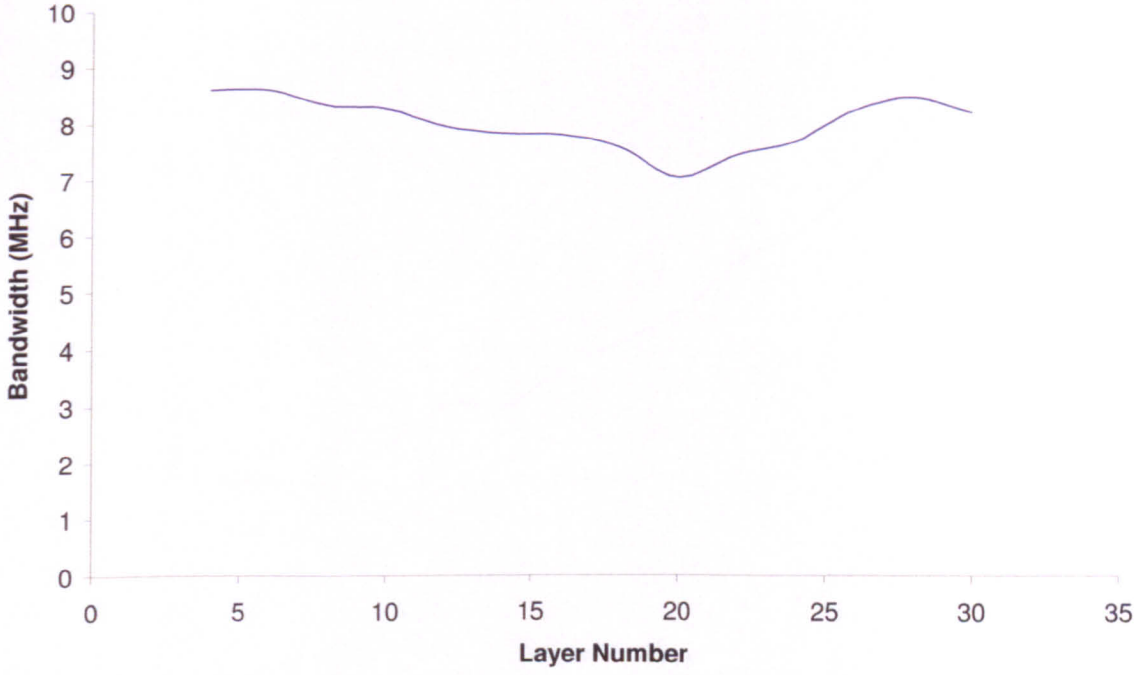

Figure 6.53 Variation of 3dB bandwidth with depth of thick resin layer.

Figure 6.53 shows that there is a small decrease in 3dB bandwidth with the depth of the thick resin layer; this is a result of increased loss at higher frequencies, reducing the energy and causing a decrease in bandwidth. There is an increase shown after layer 20; this is a result of the transition between the normal thick resin layer resonance in the body of the composite and the back wall echo. Figure 6.54 shows the frequency magnitude ratio with varying defect depth.

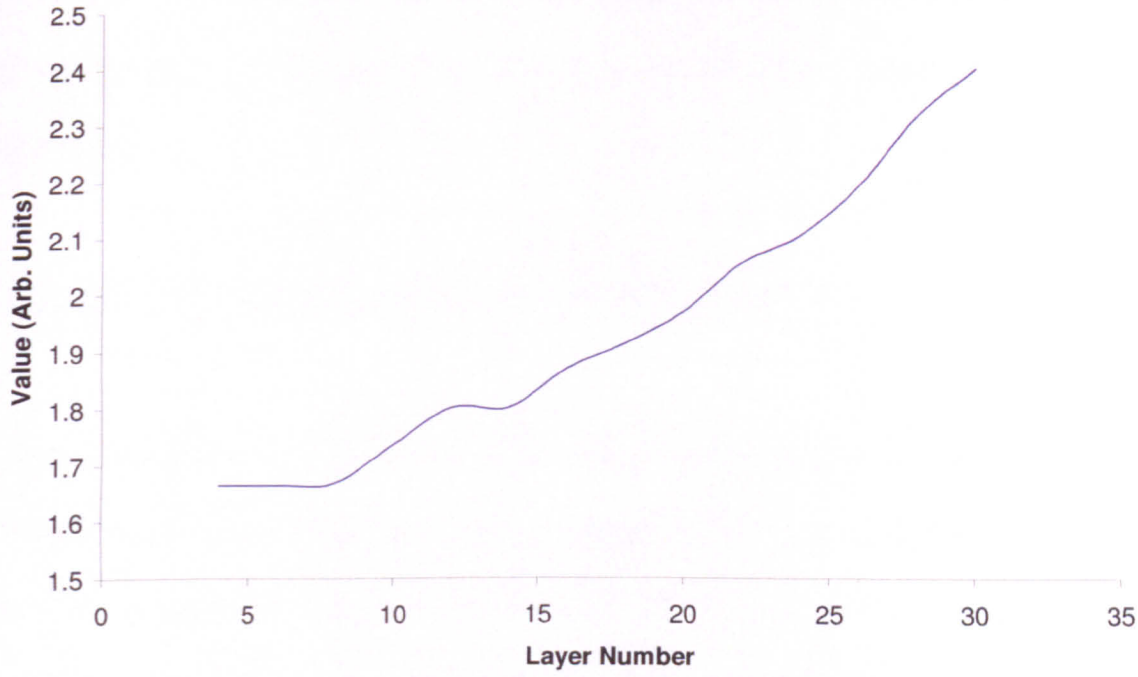

Figure 6.54 Variation of frequency magnitude ratio with depth of thick resin layer.

Figure 6.54 reveals an increase in the measured frequency magnitude ratio with depth similar to that observed for porosity in figure 6.50; this is thought to be due to loss of energy at higher frequencies increasing the value of this parameter.

The results presented have shown that the parameters are affected by the depth at which the defect occurs. When the defect is porosity, the only methods that are significantly affected are envelope analysis and the frequency magnitude ratio. The changes seen in the frequency magnitude ratio seem to be due to visco-elastic losses, which cause the higher frequencies to be attenuated more making the measured value of the parameter higher. When the defect is a thick resin layer the envelope analysis measure and the bandwidth are affected. It would be expected that the bandwidth measure would be affected by visco-elastic attenuation, since the centre frequency of the resonance associated with a thick resin layer is higher than that for a porous region. These

frequencies are more affected by visco-elastic loss. This effect could be compensated for by modifying the raw waveform with a frequency dependent distance amplitude correction.

Variation of Parameters in the Presence of Multiple Defects

Further modelling was done to analyse the effect of multiple defects on the values of the measured parameters. Simulations were conducted with two defects present in the simulated composite, one placed at layer 7 and one placed at layer 25. The defects used were a resin layer 20μm thick and a layer of porosity of 10% volume fraction and 10μm radius scatterers. Simulations were conducted for the possible defect combinations, porosity-porosity, porosity-resin, resin-resin and resin porosity. The results obtained for the effect on the second defect for envelope analysis are shown in table 6.3.

		Second Defect	
		Porosity	Resin
First Defect	Porosity	-8.10%	1%
	Resin	3.40%	-1.40%

Table 6.3 Percentage change in measured envelope analysis value.

Table 6.3 reveals that there is a change in the measured value of the envelope analysis parameter dependent upon which defect is present; where the defect is the same type as the defect preceding it there is a decrease and where the defect is of a different type there is an increase. Similarly for resonant frequency, table 6.4.

		Second Porosity	Defect Resin
First Defect	Porosity	-0.30%	2%
	Resin	-1.60%	-6.20%

Table 6.4 Percentage change in measured resonant frequency.

Table 6.4 shows that for resonant frequency there is a decrease in the measurement at the second defect, except if the second defect is a thick resin layer following a layer of porosity. The results for 3dB bandwidth are shown in table 6.5.

		Second Porosity	Defect Resin
First Defect	Porosity	0.00%	0%
	Resin	0.00%	-4.80%

Table 6.5 Percentage change in measured 3dB bandwidth.

Table 6.5 shows that there is no effect on bandwidth except in the case of a thick resin layer preceding another thick resin layer. For the frequency magnitude ratio method the following results were obtained, table 6.6.

		Second Porosity	Defect Resin
First Defect	Porosity	-28.00%	1%
	Resin	-75.00%	10.40%

Table 6.6 Percentage change in measured frequency magnitude ratio.

Table 6.6 shows that there is a marked decrease in frequency magnitude ratio for porosity if there is a preceding defect, for thick resin layers there is an increase, which is larger if the preceding defect is also a thick resin layer.

These results are most likely due to the earlier defect causing modifications to the incident waveform which are then carried forward into the test sample. These modifications are most likely frequency dependent and will vary with the severity of the first defect. Further work is required to evaluate the impact of these results for the use of these methods for the detection and analysis of defects. However, the methods outlined in this chapter are able to detect both kinds of defect even in the presence of multiple defects, the effect on the measured void volume fraction/layer thickness and whether this will cause an under/over estimate has been indicated and this can be taken into account during analysis.

6.8 Conclusions

Analysis of modelled data showed that the resonant frequency of an elemental area of composite was related to fibre volume fraction, resin layer thickness and porosity. It was suggested on the basis of modelling ,that porosity would cause an increase in resonant frequency but that fibre-resin effects would cause a decrease or negligible change which should be detected via analysis of the resonant frequency. Experimental analysis showed that there was an apparent decrease in resonant frequency in the presence of porosity. This was attributed to the resonant frequency shifting so far upwards that it moved out of the bandwidth of the transducer, allowing the system to detect the lower first resonance which is normally insignificant. Accurate detection of

resonant frequency becomes more difficult for longer propagation distances because the energy in the signal at higher frequencies is removed by visco-elastic attenuation and this leads to the first resonance dominating.

Modelling of a composite structure suggested that there might be an increase in the bandwidth of the received signal, immediately before and after the presence of porosity. It was expected that this increase in bandwidth would not be seen with the presence of fibre-resin effects. Experimental analysis shows that the 3dB bandwidth method is able to detect small scale porosity as well as larger defects. The method is able to differentiate between the two based on the magnitude of the bandwidth detected in the defect region as well as the quantity of indicated defects in a region. The method was less sensitive to fibre resin effects allowing the possibility that this method could be used to differentiate between porosity and fibre resin effects. However, there was a response from an area containing a thick resin layer on one panel, and this could either be the result of the thick resin layer or porosity contained within this thick resin layer. Further analysis is therefore required to test the sensitivity of this method in the presence of porosity and fibre-resin effects.

Any method based on an analysis of the spectrum from an elemental area should be able to provide contrasting responses for porosity and fibre-resin effects. The frequency magnitude comparison method performs well when detecting microscopic porosity, and testing of the method revealed that it was able to detect small scale porosity across differing test panels.

The experimental work for these methods has been promising and indicates that further testing of the methods should allow a route to detection and identification of anomalies within carbon fibre composites. The 3dB bandwidth method has been shown experimentally to be sensitive to porosity and large scale defects, and the difference between the two inclusions should be detectable on the basis of the magnitude of the bandwidth increase and the quantity of identified anomalies within a given area. However, further analysis of this method is required with both modelled and experimental data to confirm correct functionality. The 3dB bandwidth method seems less sensitive to fibre-resin effects – this provides evidence towards the response which was obtained in the presence of a thick resin layer being due to porosity. However, further analysis is needed under experimental conditions to confirm this. The frequency magnitude comparison method shows small scale porosity clearly, as well as providing an indication of changes in fibre resin effects.

Further work was conducted which looked at the detectability of defects within composite structures using these methods. It was found that changes occurred in the parameters when the porosity level reached 2% in one layer, this is much less than the level which would need to be detected in industry which is around 5%. The envelope analysis parameter was found to be almost linear with frequency above 10% porosity in one layer, however, there was a decrease in the value of the measured parameter as depth was increased. The resonant frequency was found to move quickly to the value which would be expected in the presence of porosity, and indicated that 5% porosity in one layer should be identifiable. Again, the value of this parameter was found to decrease with depth due to losses inherent in the composite structure. The bandwidth was found to produce an unexpected region between 2% and 8% porosity, where the

parameter was more sensitive to porosity, and this was attributed to features within the transition region between normal and porous composite. The value of the 3dB bandwidth was found to be independent of depth. The frequency magnitude ratio was found to increase with percentage porosity until 10%, the response then decreased back which was still higher than the original value as the spectrum moved to a broadband response. The frequency magnitude ratio was found to decrease with depth, due to viso-elastic attenuation in the composite.

In the case of a thick resin layer it was found that the envelope analysis parameter increased linearly with resin layer thickness above the nominal thickness of 5μm; visco-elastic losses in the composite caused this parameter to decrease with depth. The resonant frequency decreased with resin layer thickness as was predicted by earlier modelling; this parameter decreased with depth as shown in figure 6.44. The bandwidth of the signal increased with resin layer thickness (figure 6.45), but this increase was not on the same scale as that seen for porosity (figure 6.40). This was expected from previous modelling. The bandwidth was found to decrease with depth (figure 6.49); this is due to the resonant peak being much higher in the spectrum for a thick resin layer, and thus more susceptible to visco-elastic losses. The frequency magnitude ratio was found to increase with resin layer thickness, but this increase was not on the same scale as that experienced for porosity, and is as would be expected via modelling. The value of the frequency magnitude ratio was found to decrease with depth into the structure, due to losses within the composite. It has been hypothesised that the effect of defect depth could be compensated for with the addition of a frequency dependent distance amplitude correction.

The effects of the presence of two defects were examined. It was found for envelope analysis that if the preceding defect were the same as the defect being examined there was a decrease in the value of the parameter; however, if the defects differed, an increase was found. A decrease in the resonant frequency was observed in all cases except where a porous layer preceded a thick resin layer. The 3dB bandwidth was resistant to multiple defects and no change was observed except if there was a thick resin layer followed by another thick resin layer where a decrease in the value of the parameter was found. The frequency magnitude ratio was found to vary based upon the nature of the second defect; if the defect was porosity then a decrease was observed; if the defect were a thick resin layer then an increase in the value of the parameter was observed. Further work is required to evaluate these effects and their dependence on the severity of the first detected defect. The work thus far will provide an indication as to whether the second detected defect will be under/over estimated. Although it should be noted that there are other parameters which have not been varied, such as, defect separation, depth of both defects within the structure and proximity of front and back wall echoes. Further work in this area is therefore required to ascertain the effect of varying more than one of these parameters simultaneously.

The methods outlined in this chapter have shown that there is significant information contained within the frequency response obtained from a short time gate applied to the A-scan. However, there is some variation in these results, which is present due to inherent randomness within the composite, as well as gating issues, such as when the gate is between plies. The next chapter investigates the effect of increasing the length of the time domain gate to average out effects between plies.

Chapter 7

Location of Porosity in Three Dimensions:

Long Gate Time-Frequency Analysis

7.1 Introduction

Chapter six presented new frequency domain analyses of A-scans based on short time gates corresponding to a depth increment of less than the width of two plies in the composite. The rationale behind the short gate was that longer gates would average any observable effect over a greater number of plies, and possibly distort or de-emphasise important diagnostic information. However, there may still be advantages in using longer gates, particularly because the implied averaging over distance may reduce the effects of structural randomness in the ply lay-up.

This chapter investigates the frequency response which would be expected from a long time gate. Comparisons are drawn between data obtained using the *MLM-Propmat* model and data obtained experimentally from real physical samples. A theoretical expression for the response observed in the frequency domain is suggested and methods are investigated which uses filters to limit the effects due to the ply resonance and thick resin layers.

7.2 Modelling of Full Waveform Spectra

The spectra which result from a Fourier analysis of the full waveform between the front and back wall echoes contain the effects of interference between the various resonances present in the ultrasonic signal. This may be demonstrated by comparing varying gate widths when applied to the analysis of unflawed composite. In order to better explain the phenomena which are observed and to provide an indication of the performance of this form of analysis in the presence of various concentrations and morphologies of porosity, a modelling exercise was conducted using *MLM-Propmat*. To predict the expected frequency spectra the ply resonance was modelled on the basis of a 5 layered system, as shown in figure 7.1.

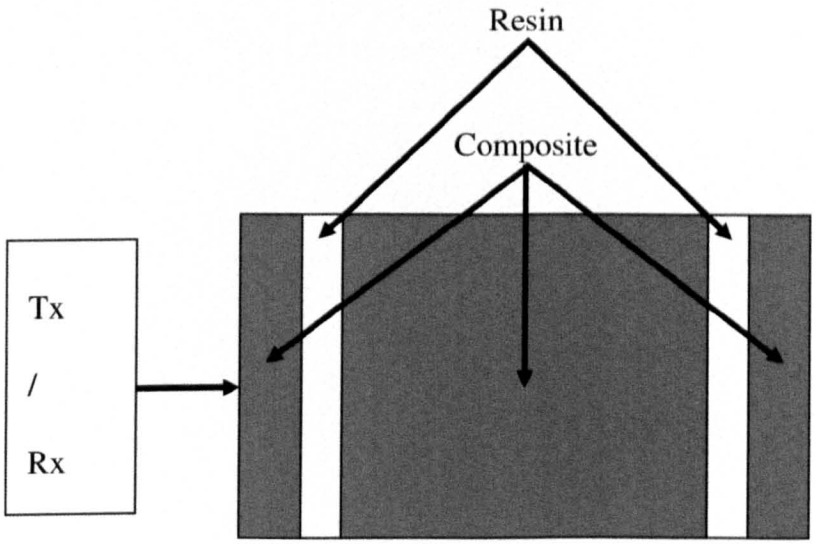

Figure 7.1 Five-layer system used to predict the inter-ply resonance.

The ply width used was 330 microns, the resin thickness was 2 microns, and the frequency response was not combined with a transducer response. The response which was obtained is shown in figure 7.2.

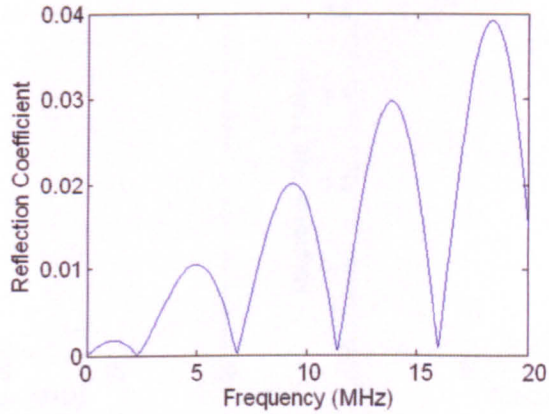

Figure 7.2 Frequency response for a five layered system.

By cascading this five layer system (elemental structure) several times it is possible to construct a simulation which accurately models the panels which were subject to experiment. Spectra were produced from gates containing 1, 2, 5, 10, 15 and 20 elemental structures of composite using the same method; the results are presented in figure 7.3.

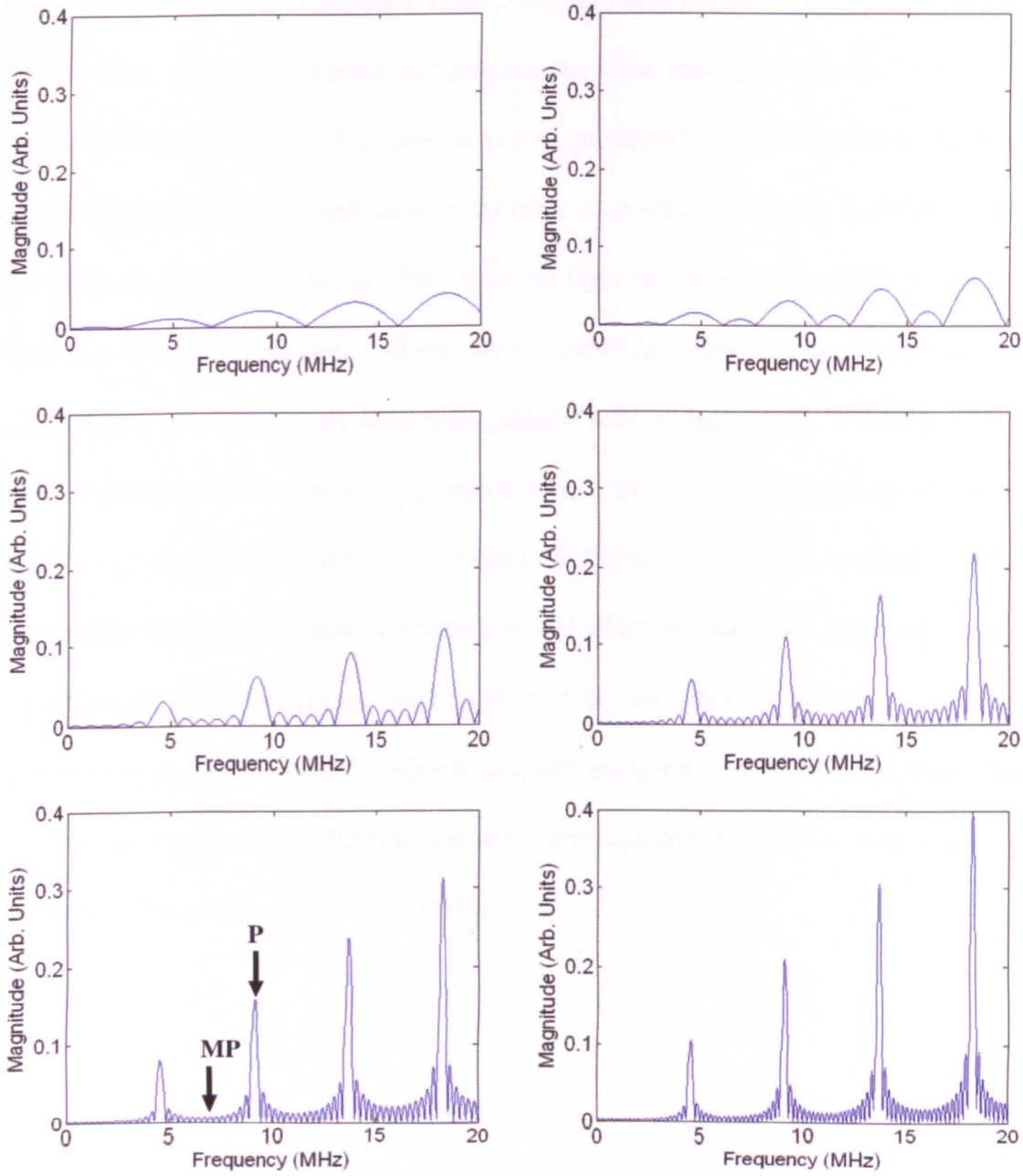

Figure 7.3 Frequency response for a elemental structure system, for composite containing 1 (top left), 2 (top right), 5 (middle left), 10 (middle right), 15 (bottom left), 20 (bottom right) elemental structures.

Figure 7.3 shows that as the number of plies in the system increases the resonances are superimposed upon each other. The result for greater number of plies is the combination of the previous resonance systems for lesser numbers of plies. The peaks become better defined as the resonances interact with one another ("P" in figure 7.3). The top left

image in figure 7.3 gives the basic resonance pattern in the elemental 3 layer structure. Two of these next to each other will produce the same basic ply resonance but destructive interference will be present at a frequency which corresponds to an overall π phase shift between the outer walls of the elemental structure. As the number of layers increases the overall thickness of the resonant layer increases, decreasing this through thickness resonant frequency and the interval between its harmonics, resulting in the minor peaks between the ply resonance peaks ("MP" in figure 7.3). The frequency spectra indicate that for the ply spacing of 330μm the expected frequencies of the ply resonances would be 4.9MHz, 9.8MHz and 14.7MHz. It was of considerable interest to examine how the presence of porosity would affect the long gate frequency analysis. Consequently, the modelling exercise was repeated for values of porosity of 0, 1, 2, 4, 8 and 16% in one layer (layer 7 within a structure using a 15 elemental structures), using a probe centre frequency of 10MHz and with 50% randomness present about resin thickness. The results are shown in figure 7.4.

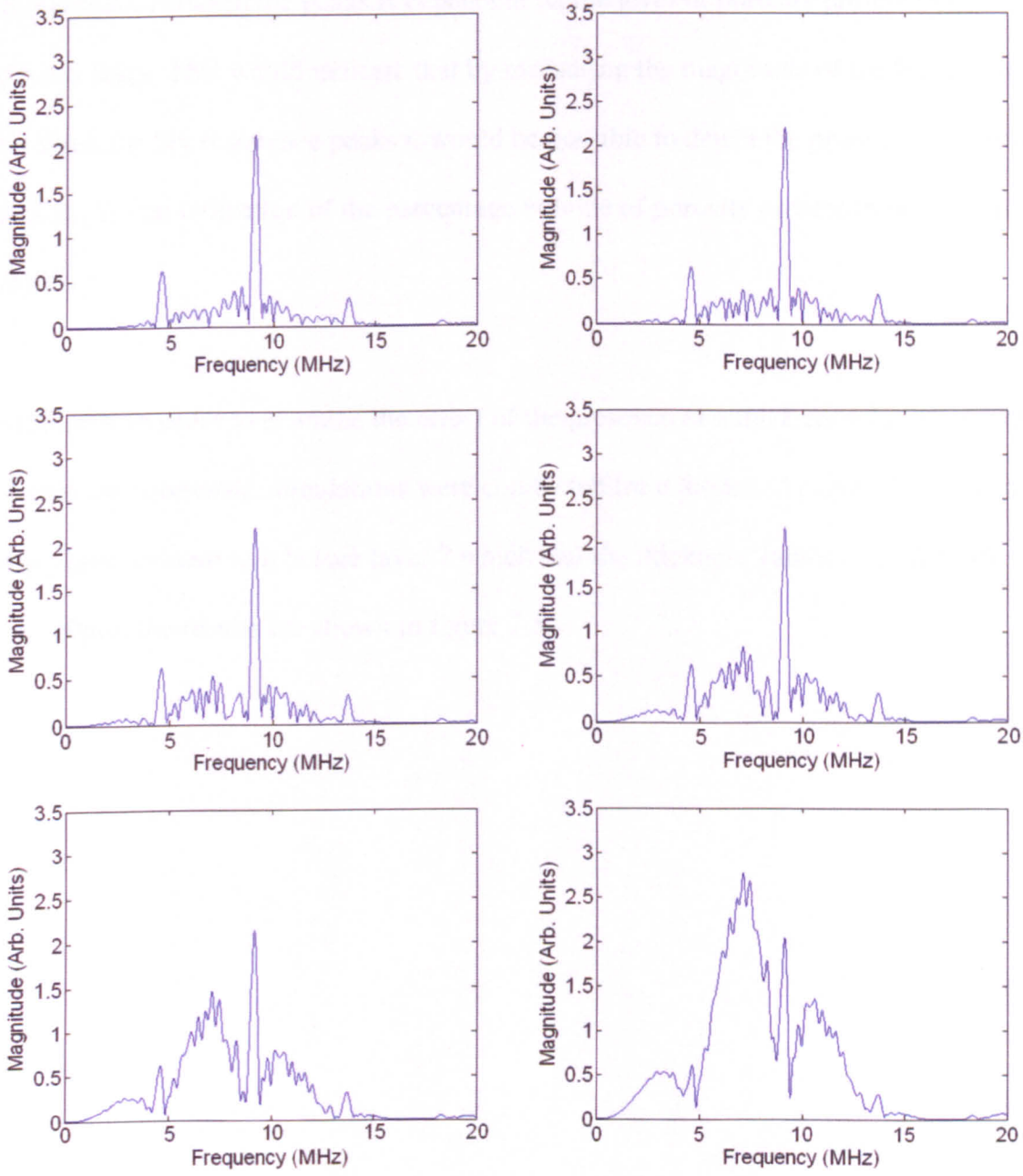

Figure 7.4 Frequency response for a 15 elemental structure system, for composite containing porosity contained in layer 7 and of percentage value 0% (top left), 1% (top right), 2% (middle left), 4% (middle right), 8% (bottom left), 16% (bottom right).

The frequency spectra in figure 7.4 all show the ply resonance peaks present at 4.9MHz and 9.8MHz, the magnitude of these peaks remains constant with the addition of porosity since there is an increase in the reflected energy which manifests itself in the appearance of separate peaks between the ply resonance peaks. The magnitude of the

frequencies between the peaks is dependent on the level of porosity present in the porous layer. This would indicate that by measuring the magnitude of the frequencies between the ply resonance peaks it would be possible to detect the presence of porosity and to give an indication of the percentage volume of porosity present in the porous layer.

Similarly, in order to examine the effect of the presence of a thick resin layer present within the composite, simulations were conducted for a modelled panel which had one resin layer present in it before layer 7 which had the thickness values of 1, 2, 5, 10, 15 and 20μm, the results are shown in figure 7.5.

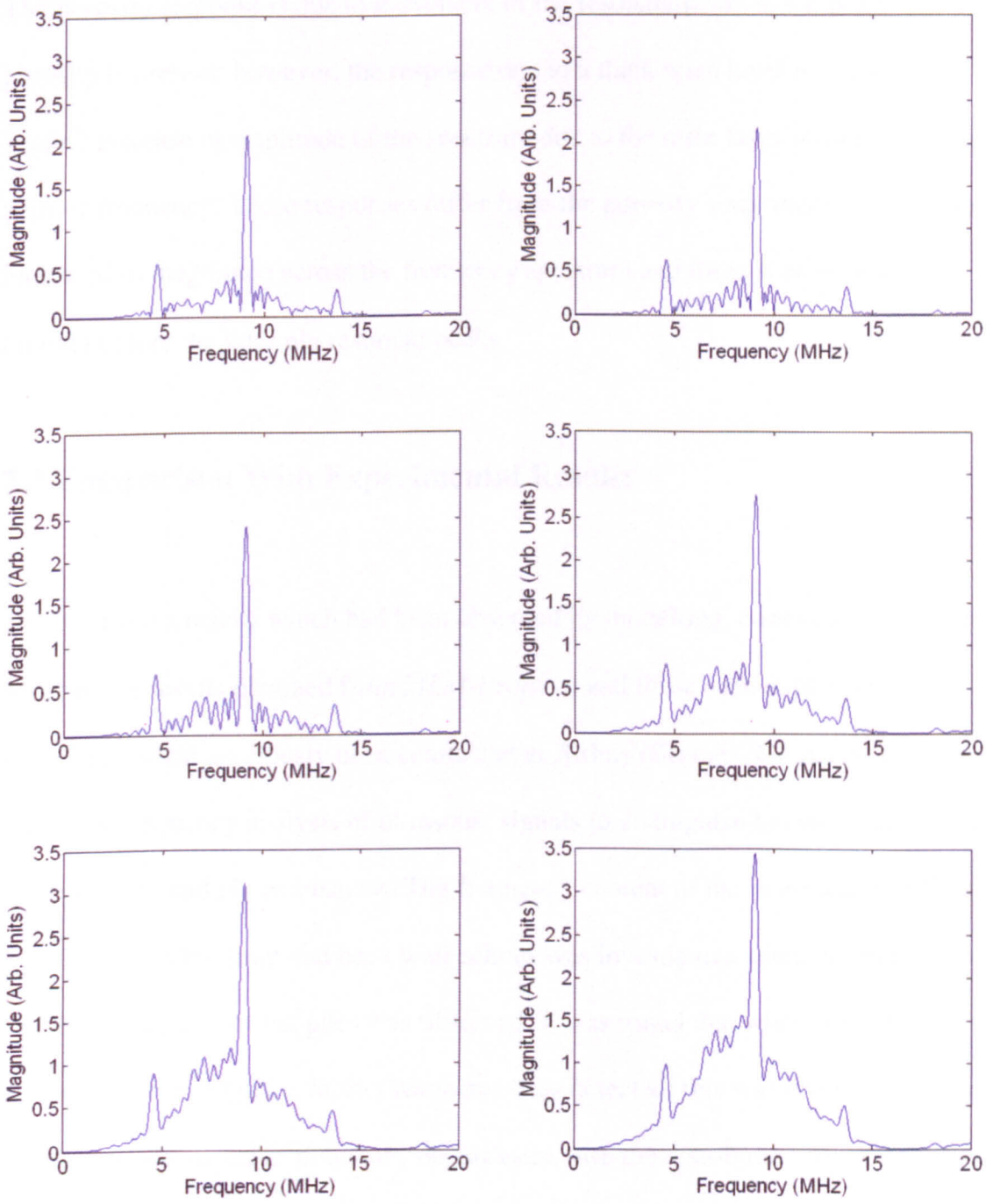

Figure 7.5 Modelled frequency response for a 15 elemental structure system, for composite containing one resin layer of thickness 1μm (top left), 2μm (top right), 5μm (middle left), 10μm (middle right), 15μm (bottom left), 20μm (bottom right).

The frequency spectra shown in figure 7.5 indicate that in the presence of a thick resin layer; there is also an increase in energy detected between the ply resonance peaks. From previous modelling it is known that these effects are due to different mechanisms.

The porosity response is due to movement of the resonant peaks at the point where the porosity is present; however, the response due to a thick resin layer is a result of a general increase in amplitude of the spectrum due to the resin layer resonance moving to a lower frequency. These responses differ from the porosity since there is a generalised increased in magnitude across the frequency spectrum and there is an absence of minima before the inter ply resonant peaks.

7.3 Comparison With Experimental Results

To confirm the results which had been observed by modelling, comparisons were done between the results obtained from *MLM-Propmat* and those seen experimentally. Experiments had previously been conducted at Airbus (Bremen, Germany) to evaluate the use of frequency analysis of ultrasonic signals to distinguish between back scatter from porosity and ply resonances. The frequency content of the intermediate reflected signal between the front and back wall echoes was investigated and a dependence on the resonant frequency of the plies was observed. It was found that when porosity was present in a test sample, a further resonance was detected; this was due to the presence of porosity and varied in frequency dependence with the distribution of the porosity in the test sample. The existence of this additional resonance when porosity was included within a test sample provides the basis for a method of detection of porosity which is not dependent on detection of the back wall echo. The first experimental sample was a carbon fibre reinforced panel (CFRP) without defects. Measurements were made using differing transducer centre frequencies to expose the resonant frequencies present in the reflected signal. The frequency spectra obtained by taking a fast Fourier transform

(FFT) of the intermediate signals for 5MHz, 10MHz and 17MHz centre frequency transducers are shown in figure 7.6.

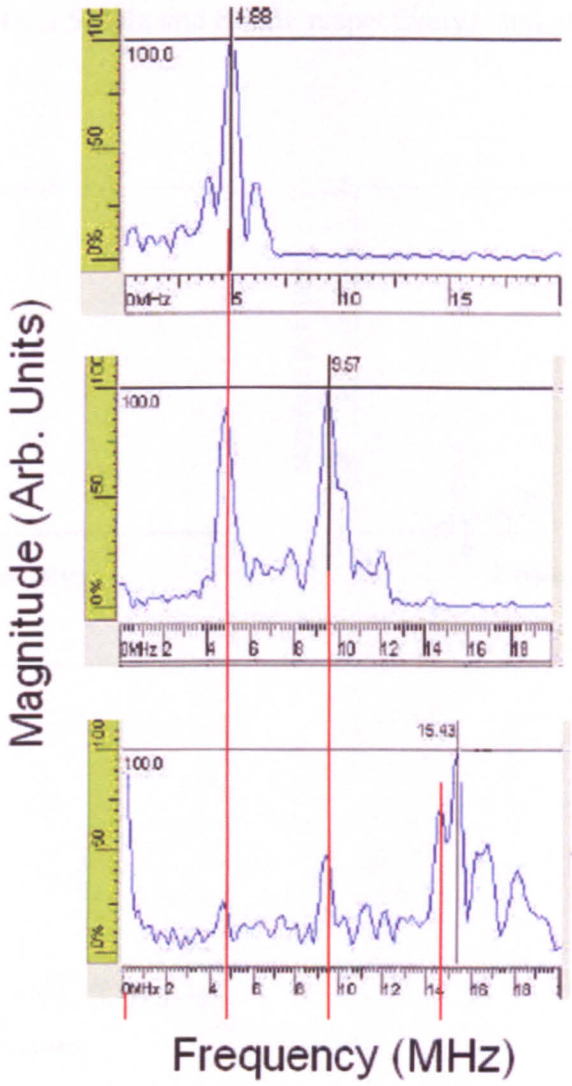

Figure 7.6 FFT spectra of intermediate signal for 5MHz (top), 10MHz (middle) and 17MHz (bottom) centre frequencies, conducted by Airbus, Bremen.

Figure 7.6 shows that resonant peaks can be observed at 4.88MHz, 9.57MHz and 14.6MHz as highlighted by vertical red lines. The heights of the peaks depend on the centre frequency and the bandwidths of the transducers used. To compare the spectra obtained from modelling with those seen experimentally the frequency spectrum for a

15 elemental structure system corresponding to the thickness of the panels used by Airbus were generated using *MLM-Propmat.* The results were convolved with transducer responses for 5MHz, 10MHz and 17MHz centre frequencies (with 3dB bandwidths of 2.25MHz, 3.5MHz and 8MHz respectively), and are shown in figure 7.7.

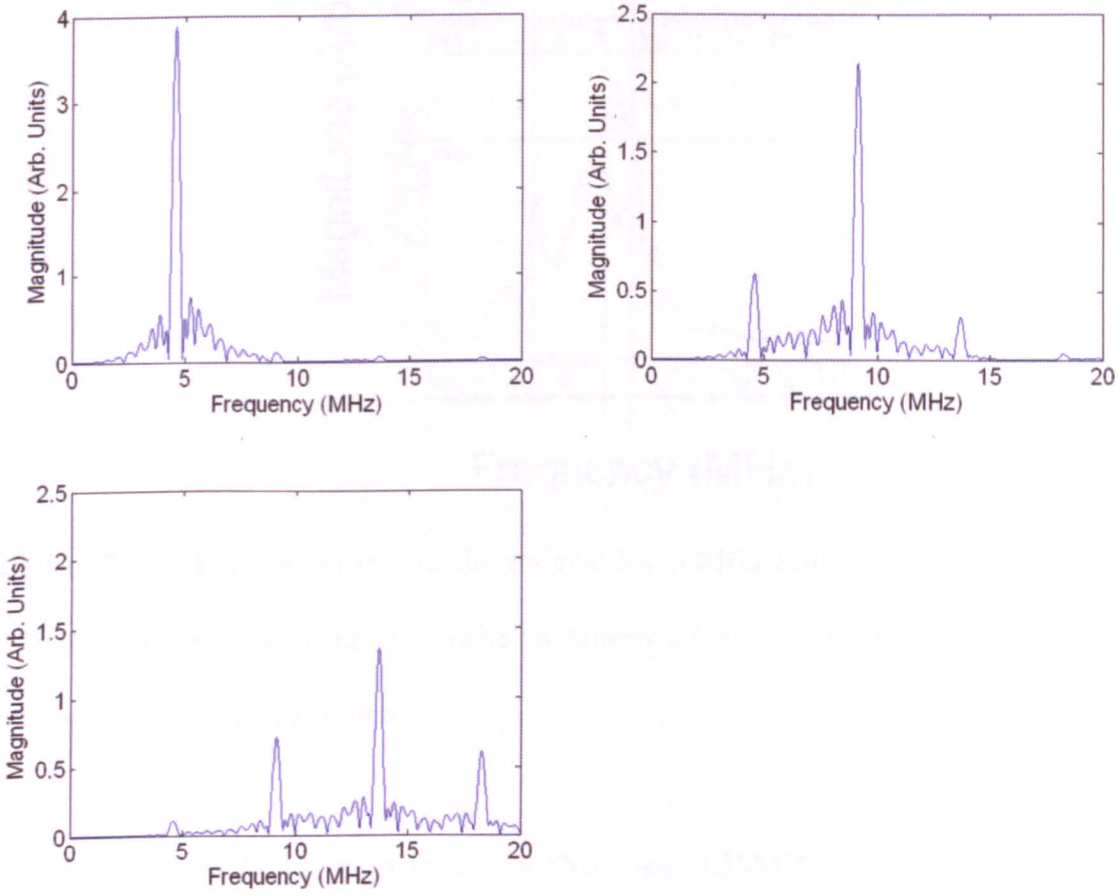

Figure 7.7 Modelled frequency response for a 15 elemental structure system, for a transducer centre frequency of 5MHz (top left), 10MHz (top right) and 17MHz (bottom left).

The frequency responses obtained from figure 7.7 compare well with those obtained experimentally shown in figure 7.6. To investigate the presence of a layer of porosity further experiments were conducted using a 10MHz centre frequency transducer array

on a CFRP containing one layer of porosity. Frequency spectra were obtained for normal and porous composite and are shown in figure 7.8.

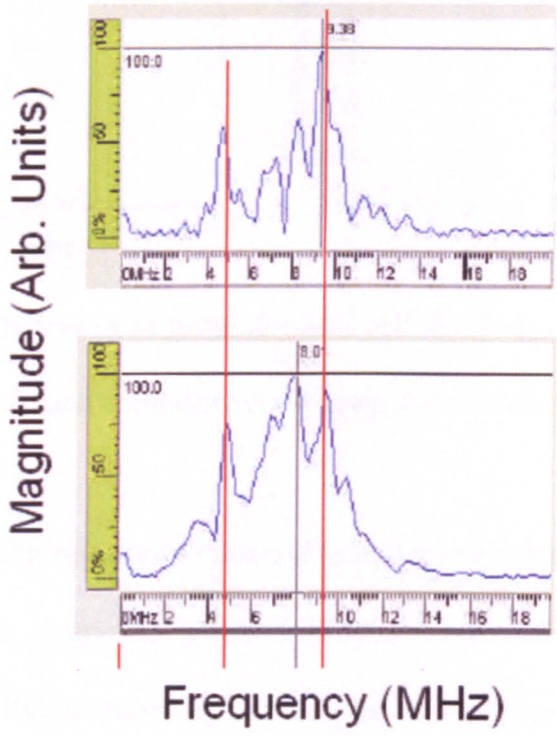

Figure 7.8 FFT spectra of intermediate signal for 10MHz centre frequency probe, for normal composite (top) and composite containing a layer of porosity (bottom) , conducted by Airbus, Bremen.

Figure 7.8 shows the ply resonances at 4.8MHz and 9.38MHz as highlighted by vertical red lines. In the presence of porosity the frequency response between the ply resonances increases, as has been observed in previous modelling (figure 7.4), the greatest magnitude is at 8.01MHz. It is noted that there is a generalised response between the inter-ply resonance peaks in the unflawed case; this may be due to the random nature of the ply spacing, or low levels of porosity within the panel. Modelling was again conducted using a 15 elemental structure system, similar to the experimental data a centre frequency of 10MHz was used for the transducer response. For the porous case one layer of 16% porosity was added in the 4th layer, the results are shown in figure 7.9.

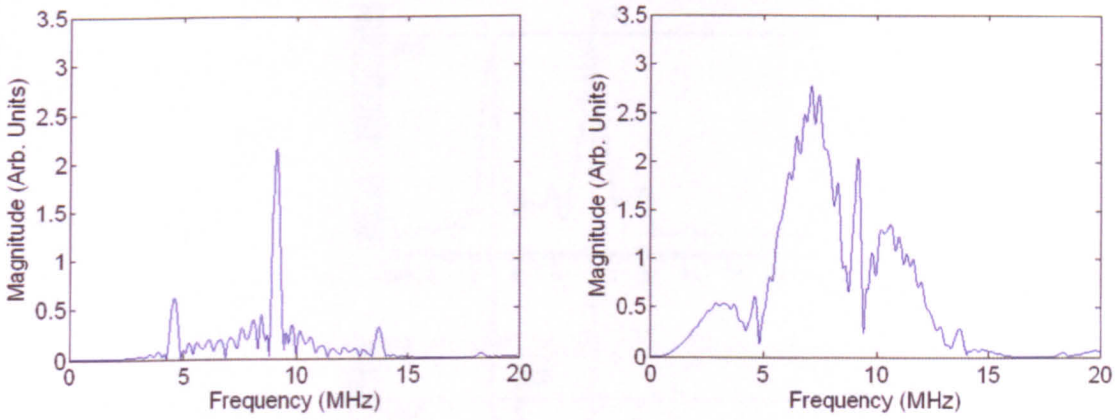

Figure 7.9 Modelled frequency response for a 15 elemental structure system, for unflawed composite (left) and composite containing one layer of porosity (right).

Figure 7.9 shows a similar response to those obtained experimentally and shown in figure 7.8. For unflawed composite, peaks in the spectrum are shown at values close to those seen experimentally; the response between the inter-ply resonance peaks is not of the same magnitude as that observed experimentally. For the case of porous composite an increase in the magnitude of the frequencies between the resonant peaks is observed; this is also found experimentally. A sample containing porosity dispersed across the depth of the panel was investigated using a 10MHz centre frequency transducer array. Frequency spectra were obtained for normal and porous composite and are shown in figure 7.10.

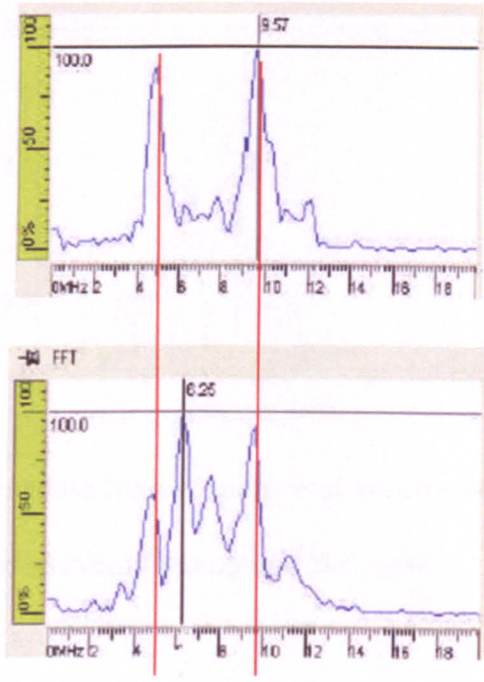

Figure 7.10 FFT spectra of intermediate signal for 10MHz centre frequency probe, for normal composite (top) and composite containing dispersed porosity (bottom) , conducted by Airbus, Bremen.

Figure 7.10 shows the ply resonances at frequencies of 4.8MHz and 9.57MHz as is predicted by the simplified modelling method used. Where dispersed porosity is present a new peak emerges at 6.25MHz as well as an increase in magnitude of the frequencies between the ply resonance peaks. Dispersed porosity was inserted into the model by adding porosity throughout the plies to draw comparisons with the panel produced by Airbus. The results obtained are shown in figure 7.11.

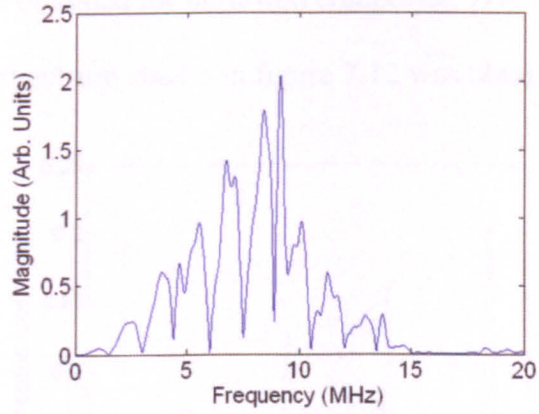

Figure 7.11 Frequency response for a 15 elemental structure system, for composite containing porosity dispersed evenly throughout the depth.

Figure 7.11 compares well with the experimental data shown in figure 7.10, the resonant peaks are visible at the expected values of 4.9MHz and 9.8MHz, and between these peaks there is an increase in magnitude of the response due to the porosity present throughout the panel.

The results of the modelled data indicate that the presence of an increased response between resonant peaks is due to the inclusion of porosity. For both dispersed and layer porosity there is an observable response which indicates the presence of the porosity.

7.4 Analysis of the Long Gate Frequency Response

The agreement between the modelled and experimental results for flawed and unflawed composite shown above implies that it should be possible to construct a method which is able to detect and quantify porosity defects. This will require some further understanding of the factors that lead to the observed phenomena. We begin by

analysing the response obtained for unflawed composite. For a 15 elemental structure system the frequency spectrum shown in figure 7.12 was obtained.

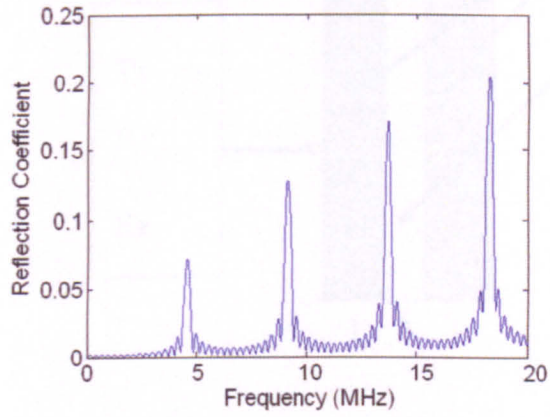

Figure 7.12 Modelled frequency response for an unflawed15 elemental structure system.

From figure 7.12 we can see that the superposition of resonances has narrowed the ply resonance peaks. This superposition of resonances leads to the development of an equation which provides for the cumulative effect of the various resonances within the composite. It is suggested that the frequency response of the system may be described thus:

$$F(\omega) = [S(\omega)R(\omega, t_{norm})] \qquad \textbf{(7.1)}$$

Where $S(\omega)$ is the ply resonance which results from the ultrasonic reflections at the front and the back wall of the composite layer and $R(\omega, t_{norm})$ is the effect due to the presence of the thin interstitial resin layers in the composite. By considering the resonance within one ply as shown in figure 7.13,

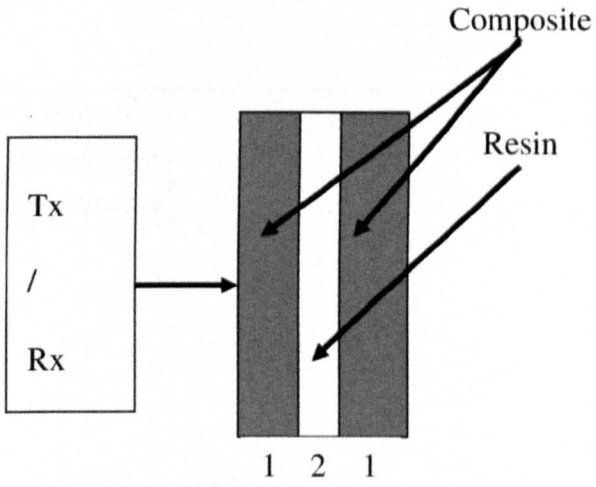

Figure 7.13 Three layer system used to predict the resin layer resonance.

by considering the multiple reflections that occur within layer 2 the function describing $R(\omega, t_{norm})$ may be written as (Smith 2008):

$$R(\omega, t_{norm}) = \frac{\left|(Z_2 - Z_1)(Z_2 + Z_1)\tan k_2 t_{norm}\right|}{\sqrt{4Z_2^2 Z_1^2 + \left(Z_2^2 + Z_1^2\right)^2 \tan^2 k_2 t_{norm}}} \tag{7.2}$$

Where Z is the acoustic impedance in the respective media, t_{norm} is the thickness of medium 2 and k is the wavenumber in the medium given by:

$$k = \frac{2\pi f}{c} \tag{7.3}$$

For a given compression wave velocity c at a frequency f. The shape of this resonance is superimposed upon the ply resonance $S(\omega)$, and varies in relation to the resin layer thickness as shown in figure 7.14.

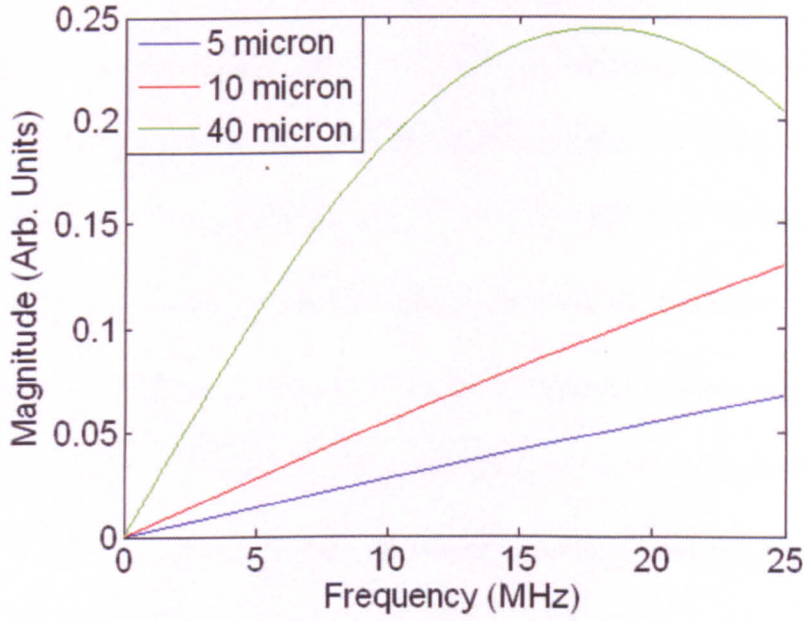

Figure 7.14 Resonance due to a thin resin layer for various layer thicknesses.

For small values of $k_2 t_{norm}$ ($k_2 t_{norm} << 1$) the value of $R(\omega, t_{norm})$ approximates to:

$$R(\omega, t_{norm}) = \frac{(Z_2 - Z_1)(Z_2 + Z_1)}{2Z_2 Z_1} k_2 t_{norm} \tag{7.4}$$

The constant acoustic impedances may be grouped into the constant Γ giving:

$$R(\omega, t_{norm}) = \Gamma k_2 t_{norm} \tag{7.5}$$

The averaged effect of these resin layer resonances for the entire composite system is a function of the average acoustic impedances for resin and the resin and fibre composite layer and the average thickness of the resin layers within the system.

To analyse the validity of this equation as a simplification of the spectra obtained from the full *MLM-Propmat* models, further analysis was applied to the modelled results. Frequency spectra were generated for various values of nominal resin layer thickness in a 15 elemental structure system. The magnitude of the peaks due to the ply resonance were observed; they have a magnitude due to $S(\omega)$ as well as the frequency dependent effect due to $R(\omega, t_{norm})$. $S(\omega)$ remains constant since the ply thickness and acoustic impedances remain the same throughout all of the simulations, hence we can investigate the effect due to $R(\omega, t_{norm})$. The resin layer thickness of all the resin layers was varied with values of 1, 2, 5, 10, 15 and 20μm, these results were plotted to allow comparison between the resonant peaks for constant resin layer thickness and to investigate the effect of increasing resin layer thickness as shown in figure 7.15.

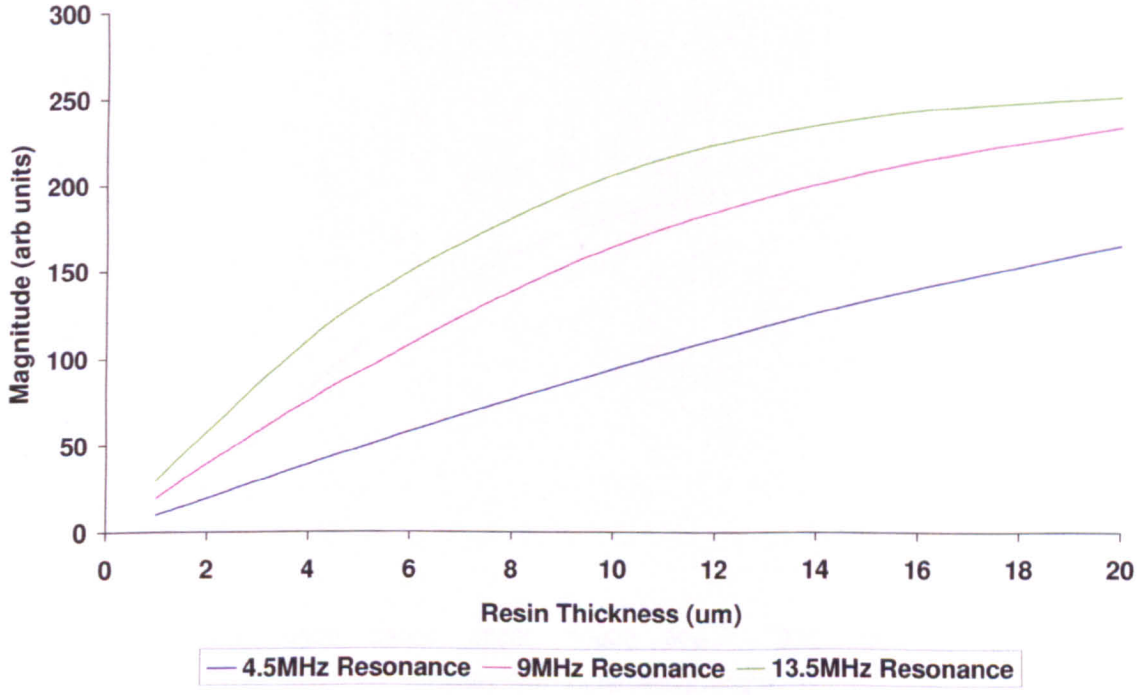

Figure 7.15 Magnitude of resonant peaks for a 15 elemental structure system for various values of nominal resin layer thickness.

Figure 7.15 shows that whilst the resin layer thickness is kept constant the magnitude of the resonant peaks due to the ply resonance differs due to the effect of the resonance within the resin layer as shown in figure 7.14. As the thicknesses of the resin layers are increased the position of the resonant peaks moves towards lower frequencies, this increases the magnitude of the ply resonance peaks. At higher frequencies the approximation of $kt_{norm} << 1$ no longer holds true and hence the magnitude curves are no longer linear, as shown in figure 7.15.

A comparison may be made between the different resonant peaks by dividing the nominal resin layer thickness by the wavelength of the wave at each resonant frequency. This allows the shape of the function $R(\omega, t_{norm})$ to be determined and the effect of this function on the frequency spectrum to be established, figure 7.16.

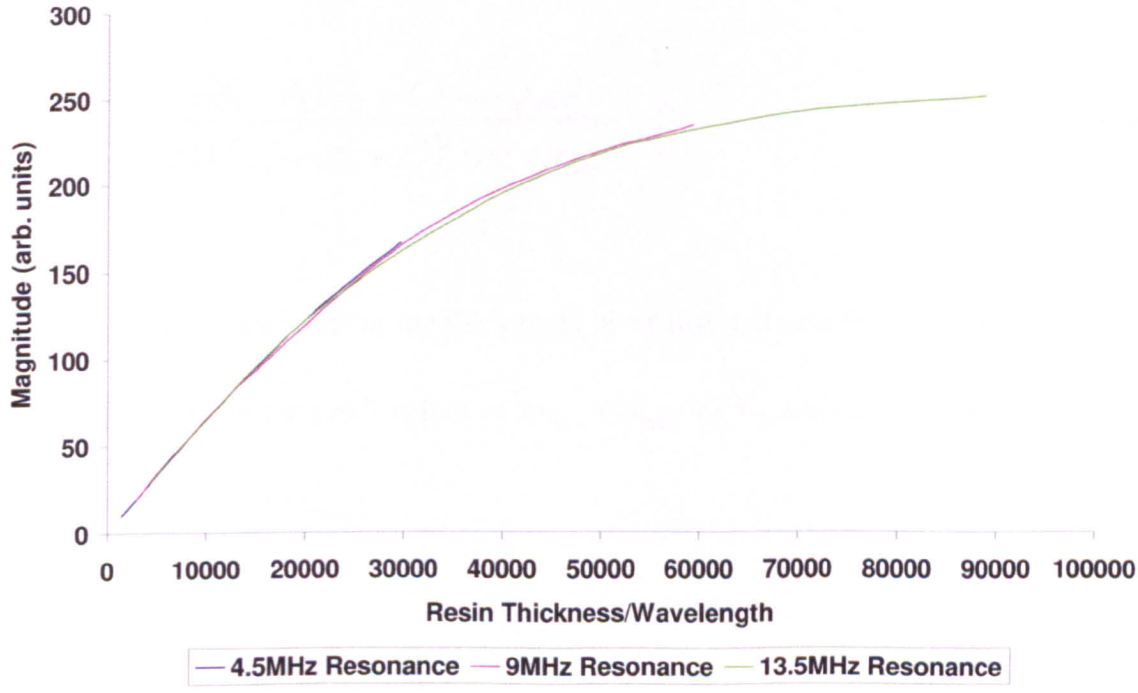

Figure 7.16 Magnitude of resonant peaks for a 15 elemental structure system for various values of nominal resin layer thickness divided by wavelength at the peak.

Figure 7.16 shows that as the nominal resin layer thickness is increased the change in magnitude across all frequencies follows the same curve, this would imply that $S(\omega)$ is modulated by $R(\omega, t_{norm})$ and that equation 7.1 is a reasonable approximation of the system. Had $R(\omega, t_{norm})$ been an additive component of $F(\omega)$, then plotting the magnitude of the resonant peaks against the resin thickness, divided by the wavelength, would have resulted in some difference between the functions describing how the magnitude of the resonant peaks varies with frequency.

Similar to the function describing the resonance due to thin resin layers within the composite, a new expression, $C(\omega, t_{thick})$, may be used to describe the resonance due to the inclusion of a single thick resin layer. By creating a system similar to figure 7.13 this function may be described thus:

$$C(\omega, t_{thick}) = \frac{\left|(Z_2 - Z_1)(Z_2 + Z_1)\tan k_2 t_{thick}\right|}{\sqrt{4Z_2^2 Z_1^2 + \left(Z_2^2 + Z_1^2\right)^2 \tan^2 k_2 t_{thick}}} \tag{7.6}$$

Where t_{thick} is the thickness of the thick resin layer inserted into the composite. Again we can approximate for small values of kt_{thick} ($kt_{thick} << 1$), which gives the simplification for $C(\omega, t_{thick})$:

$$C(\omega, t_{thick}) = \frac{(Z_2 - Z_1)(Z_2 + Z_1)}{2Z_2 Z_1} k_2 t_{thick} \tag{7.7}$$

The constant acoustic impedances may be grouped into the constant γ giving:

$$C(\omega, t_{thick}) = \gamma k_2 t_{thick} \tag{7.8}$$

It was proposed that when a thick resin layer was present in the system the effect was to modulate the signal with the resonance due to that thick resin layer as:

$$F(\omega) = [S(\omega)R(\omega, t_{norm})C(\omega, t_{thick})] \tag{7.9}$$

To test this hypothesis simulated frequency spectra were obtained using *MLM-Propmat*, for various values of an inserted thick resin layer within a 15 ply composite. So that the variation due to $C(\omega, t_{thick})$ could be observed the nominal resin layer thickness and the ply thickness were both kept constant, thus keeping $S(\omega)$ and $R(\omega, t_{norm})$ constant. The resultant magnitudes of the peaks due to $S(\omega)$ are shown plotted in figure 7.17.

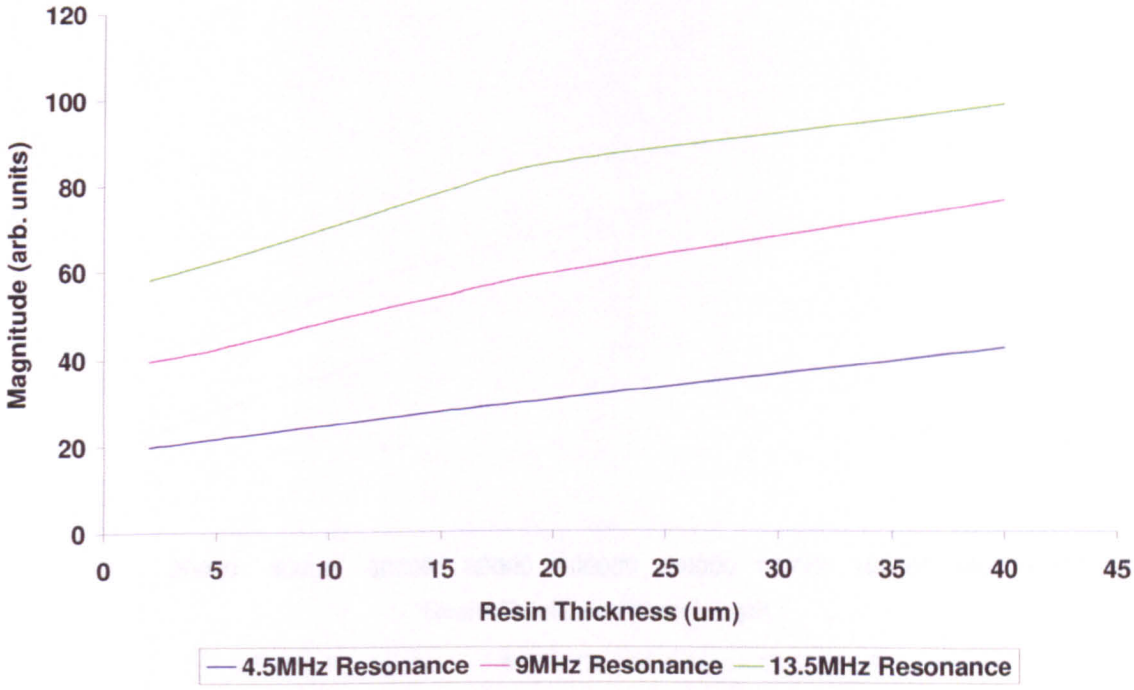

Figure 7.17 Magnitude of resonant peaks for a 15 elemental structure system for various values of thick resin layer thickness.

To compare between the different resonant peaks the thick resin layer thickness was divided by the wavelength at each resonant frequency. By plotting the modelled data in this fashion the hypothesis outlined in equation 7.9 may be tested. The results of this analysis are shown in figure 7.18.

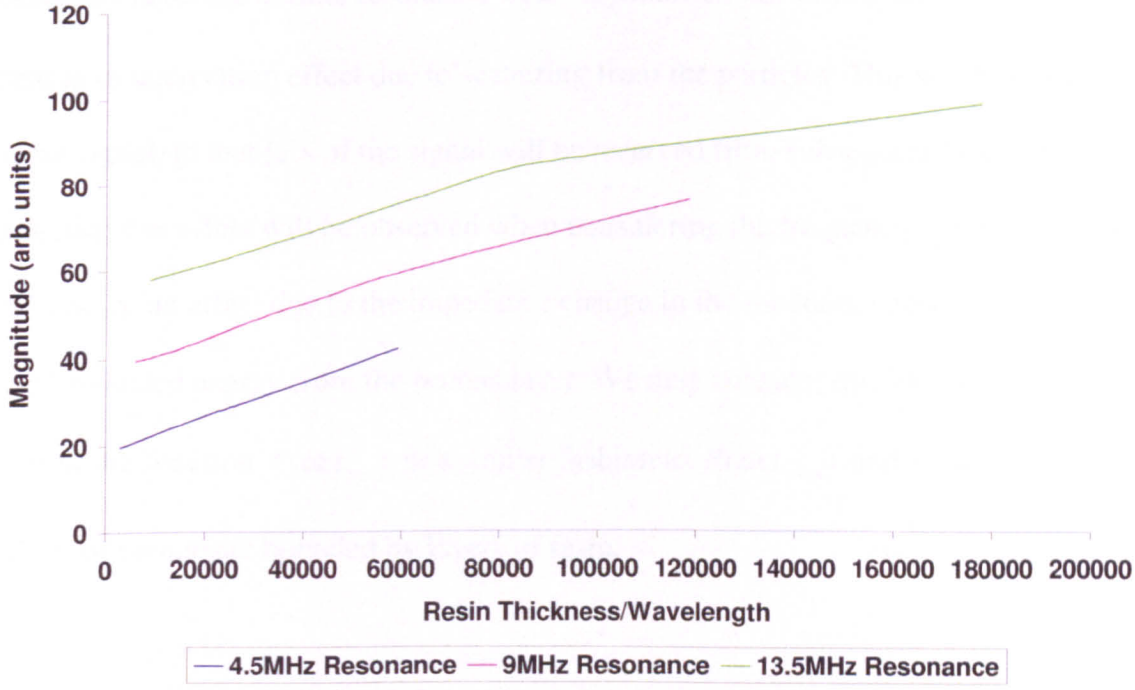

Figure 7.18 Magnitude of resonant peaks for a 15 elemental structure system for various values of thick resin layer thickness divided by wavelength at the peak.

It may be seen from figure 7.18 that, although the different resonances follow the same shape function, the magnitude of the resonances for comparable resin thickness divided by wavelength differs. This would indicate that the assumption made in equation 7.9, that the function $C(\omega, t_{thick})$ modulates the other resonances in the frequency spectra is not correct. Instead the function $C(\omega, t_{thick})$ interacts additively to the other resonances, providing:

$$F(\omega) = \left[S(\omega)R(\omega, t_{norm}) + C(\omega, t_{thick})\right] \tag{7.10}$$

We make the assumption that the function interacts additively for the purpose of developing an empirical model. There also exists a resonance $P(\omega, t_{ply})$, which is due to porosity being present within one layer of composite. When porosity is present in a

composite layer the normal resonance $S(\omega)$ is modified due to two processes: First there is an attenuation effect due to scattering from the particles. This will have an effect on the signal, in that less of the signal will be received from subsequent layers than expected; this effect will be observed when considering the frequency spectrum. There will also be an effect due to the impedance change in the medium, causing an increase in the reflected energy from the porous layer. We may consider this by looking at the form of the function $P(\omega, t_{ply})$ in a similar fashion to $R(\omega, t_{norm})$ and $C(\omega, t_{thick})$ but for a layer of composite bounded by layers of resin.

$$P(\omega, t_{ply}) = \frac{\left|(Z_2 - Z_1)(Z_2 + Z_1)\tan k_2 t_{ply}\right|}{\sqrt{4Z_2^2 Z_1^2 + \left(Z_2^2 + Z_1^2\right)^2 \tan^2 k_2 t_{ply}}} \tag{7.11}$$

In this case the subscript 1 denotes resin and the subscript 2 denotes composite. The effect of attenuation can be observed by conducting experiments for a three layer system as outlined in figure 7.13 with and without attenuation due to the porosity in the composite layer. The results of this analysis are shown in figure 7.19.

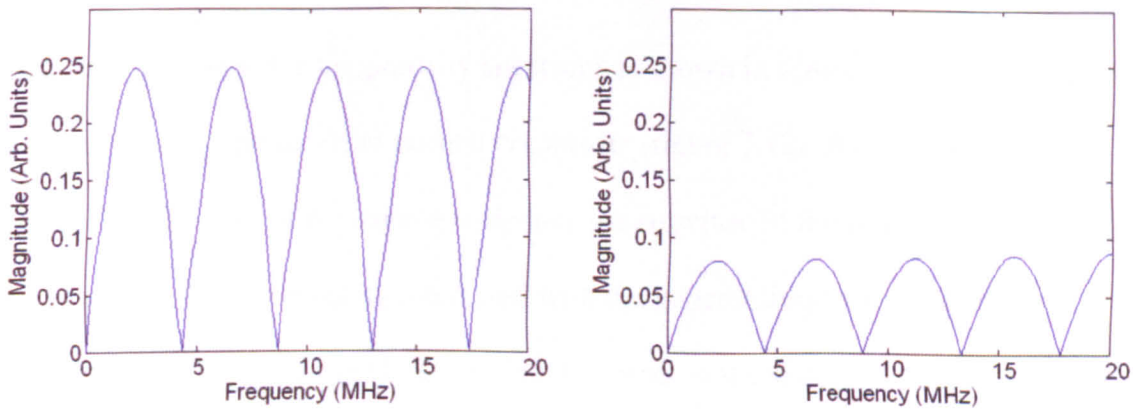

Figure 7.19 Frequency spectra for a 1 elemental structure system with 10% 10μm porosity without attenuation (left) and with attenuation (right).

It may be observed from figure 7.19 that the inclusion of attenuation reduces the amount of energy which is reflected by the porous layer, however for the frequencies considered it does not significantly affect the shape of the function.

The interaction of the resonance $P(\omega, t_{ply})$ with the function $F(\omega)$ was investigated by simulating a 15 elemental structure system containing one layer of porosity. The frequency spectrum for this simulation is shown in figure 7.20.

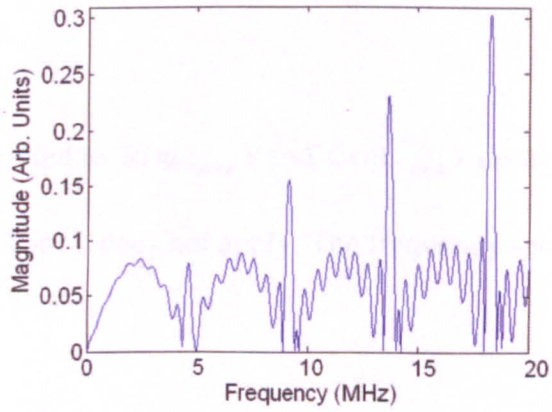

Figure 7.20 Frequency response for a 15 elemental structure system with 10% 10μm porosity in layer 7.

Figure 7.20 shows that the porosity spectrum as shown in figure 7.19 is superimposed over the basic response from normal composite (figure 7.12). By analysing this frequency response, it is possible to deduce the structure of the equation governing it. If the resonance due to porosity interacted with the general frequency response by multiplication then we would expect that the peaks in the spectrum due to $S(\omega)$, (4.5MHz, 9MHz, 13.5MHz), to disappear. This would occur because these are points in

the spectrum $P(\omega,t_{ply})$ which are minima, and so the resonance must be additive This leads to the following equation:

$$F(\omega)=\left[S(\omega)R(\omega,t_{norm})+C(\omega,t_{thick})+P(\omega,t_{ply})\right] \tag{7.12}$$

To asses the validity of this hypothesis the frequency response is divided by frequency to provide a frequency independent response, for equation 7.12 this leads to:

$$F(\omega)=\left[\frac{S(\omega)}{\omega}\Gamma t_{norm}+\gamma_{thick}+\frac{P(\omega,t_{ply})}{\omega}\right] \tag{7.13}$$

The simplifications applied to $R(\omega,t_{norm})$ and $C(\omega,t_{thick})$ do not apply to $P(\omega,t_{ply})$ since the assumption $kl<<1$ does not apply. The frequency spectrum which results is shown in figure 7.21.

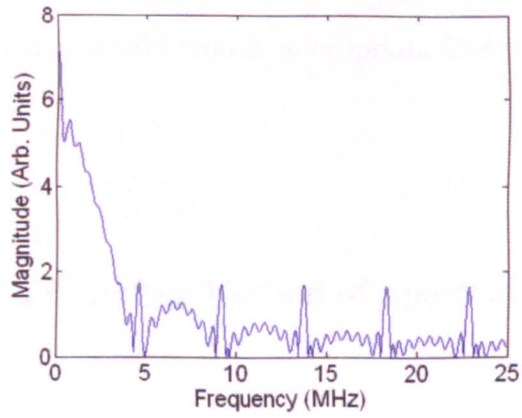

Figure 7.21 Frequency response divided by frequency for a 15 elemental structure system containing porosity.

It can be observed from figure 7.21 that dividing by frequency has reduced the term $R(\omega,t_{norm})$ to a constant (Γt_{norm}), this has the result that the peaks due to the ply resonance $S(\omega)$ are now equal in height. The porosity resonance $P(\omega,t_{ply})$ now shows a dependence on $1/\omega$, which would be expected if the term $P(\omega,t_{ply})$ was additive and so it is concluded that the final equation governing the combined frequency spectrum is:

$$F(\omega)=\left|S(\omega)R(\omega,t_{norm})+C(\omega,t_{thick})+P(\omega,t_{ply})\right| \tag{7.14}$$

With the inclusion of a transducer response which acts to filter the received signal this equation becomes:

$$F(\omega)=T(\omega)\left|S(\omega)R(\omega,t_{norm})+C(\omega,t_{thick})+P(\omega,t_{ply})\right| \tag{7.15}$$

This equation could form the basis of an inversion method to detect and quantify porosity or thick resin inclusions, by selectively filtering out components ($C(\omega,t_{thick})$ or $P(\omega,t_{ply})$. Such a procedure would require appropriate filtering schemes which are discussed next.

7.5 Development of a Filtering Method of Spectral Analysis

A method was developed to modify the frequency spectrum of experimental data to provide a spectrum which would vary with the presence and quantity of porosity / excess resin present in a sample. Notch filters were applied to remove the response due to $S(\omega)$, then the resulting spectrum was divided by frequency to provide a signal

which had constant components of nominal resin layer thickness and thick resin layer thickness resonances, as well as the porosity resonance. This spectrum could then be further studied to provide an indication for the presence and quantity of porosity present in the area of analysis.

In order to test this method on theoretical data, simulations were conducted using *MLM-Propmat* to simulate the response from the 15 elemental structure system as outlined in section 7.2. It was possible to vary the nominal resin layer thickness, insert one or more thick resin layers and insert one or more layers of porosity. Initially the study was carried out in the absence of the transducer response function, the frequency spectrum analysed being equivalent to the Fourier transforms of the reflection impulse response of the composite. This enabled the variation due only to $S(\omega)$, $R(\omega, t_{norm})$, $C(\omega, t_{thick})$ and $P(\omega, t_{ply})$ to be considered.

The dominant effect of $S(\omega)$ is to produce equally spaced frequency peaks as shown in figure 7.22, which is a 15 elemental structure system with a nominal resin layer thickness of 2μm and a nominal ply thickness of 330μm.

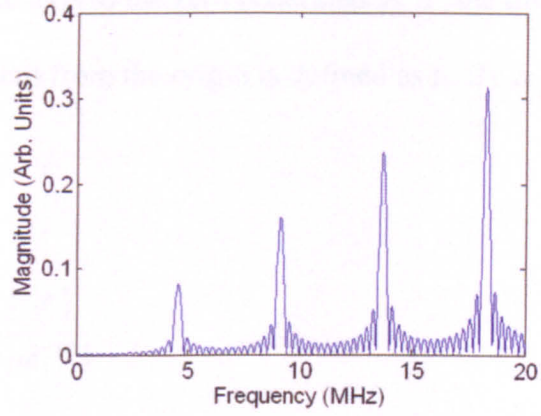

Figure 7.22 Frequency response for a 15 elemental structure system showing resonances due to $S(\omega)$.

A simple notch filter was developed by use of conventional z-plane techniques. Zeros were placed on the unit circle at a frequency corresponding to the required cut-off frequency ω_0. Poles were then placed close to the unit circle, on the same vector as the zeros to control the width of the notch in frequency space. A diagrammatic representation of this is shown in figure 7.23.

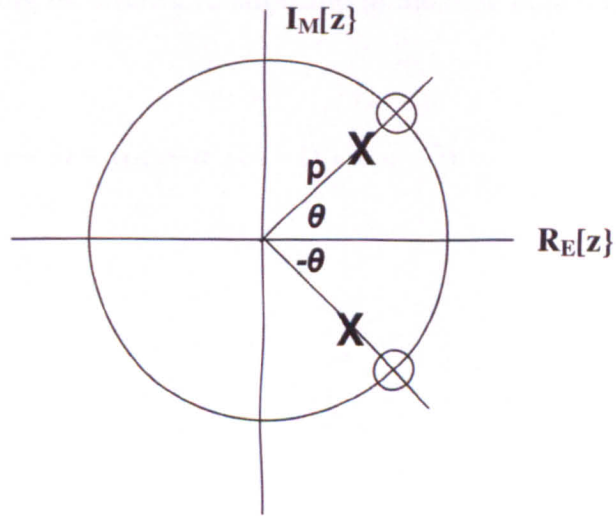

Figure 7.23 z-plane representation of the notch filter used to remove $S(\omega)$.

The angle from the real axis to the zero is defined as θ, the distance along this vector of the pole towards the zero from the origin is defined as p. By inspection, the z-transform is obtained.

$$H(z) = \frac{\left(z - e^{j\theta}\right)\left(z - e^{-j\theta}\right)}{\left(z - pe^{j\theta}\right)\left(z - pe^{-j\theta}\right)} \tag{7.16}$$

Which leads to the expression:

$$H(z) = \frac{1 - 2z^{-1}\cos\theta + z^{-2}}{1 - 2pz^{-1}\cos\theta + p^2 z^{-2}} = \frac{Y(z)}{X(z)} \tag{7.17}$$

Solving for $Y(z)$ gives:

$$Y(z) = 2pz^{-1}Y(z)\cos\theta - p^2 z^{-2}Y(z) + X(z) - 2z^{-1}X(z)\cos\theta + z^{-2}X(z) \tag{7.18}$$

This leads to the following recurrence relationship in the time domain:

$$y(n) = b_1 y(n-1) - b_2 y(n-2) + x(n) - a_1 x(n-1) + x(n-2) \tag{7.19}$$

Where,

$a_1 = 2\cos\theta$

$b_1 = 2p\cos\theta$

$b_2 = p^2$

By choosing appropriate values for ω_0 and p this filter may be used to remove a selected ply resonance peak. These filters can then be cascaded to remove subsequent ply resonance peaks. Theoretical frequency spectra for a 15 elemental structure system with and without the ply resonance component $S(\omega)$ removed via this method are shown in figure 7.24.

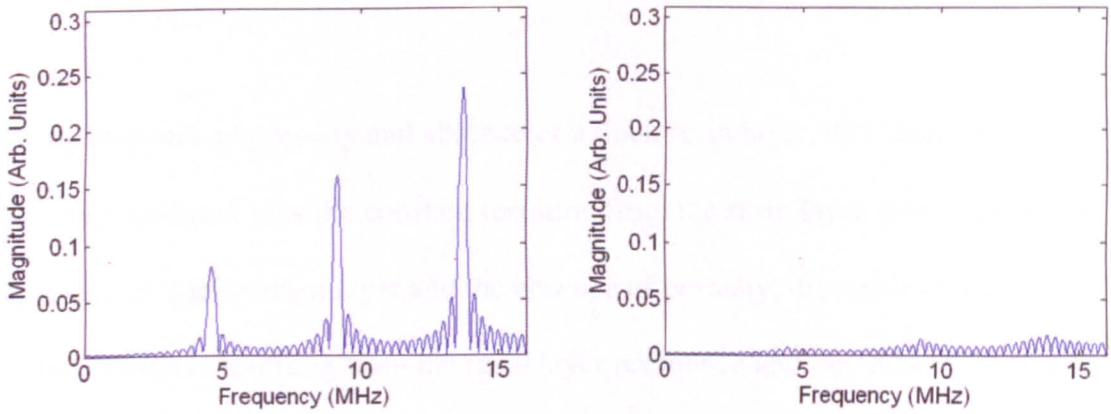

Figure 7.24 Frequency spectra for a 15 elemental structure system before filtering (left) and after the application of notch filtering (right).

Although a small component of $S(\omega)$ remains in the form of the "noise" between resonant peaks, the majority of the ply resonance has been removed and hence the remaining response is effectively:

$$F(\omega) = \left[R(\omega, t_{norm}) + C(\omega, t_{thick}) + P(\omega, t_{ply})\right] \qquad \textbf{(7.20)}$$

In the limit $kl << 1$ $R(\omega, t_{norm})$ is effectively $\Gamma \omega t_{norm}$ and $C(\omega, t_{thick})$ is $\gamma \omega t_{thick}$. This leads to

$$F(\omega) = \left[\Gamma \omega t_{norm} + \gamma \omega t_{thick} + P(\omega, t_{ply})\right] \tag{7.21}$$

The resin layer resonances can therefore be reduced to constant values by division of this function by ω.

$$F(\omega) = \left[\Gamma t_{norm} + \gamma t_{thick} + \frac{P(\omega, t_{ply})}{\omega}\right] \tag{7.22}$$

In the presence of porosity and absence of a thick resin layer, this should leave the porosity spectrum plus the constant resulting from the resin layer resonance. In the presence of a thick resin layer and the absence of porosity, the result should be the sum of the constants resulting from the resin layer resonance and the thick resin layer resonance. The results for normal composite, composite containing a thick resin layer and porous composite are shown in figure 7.25.

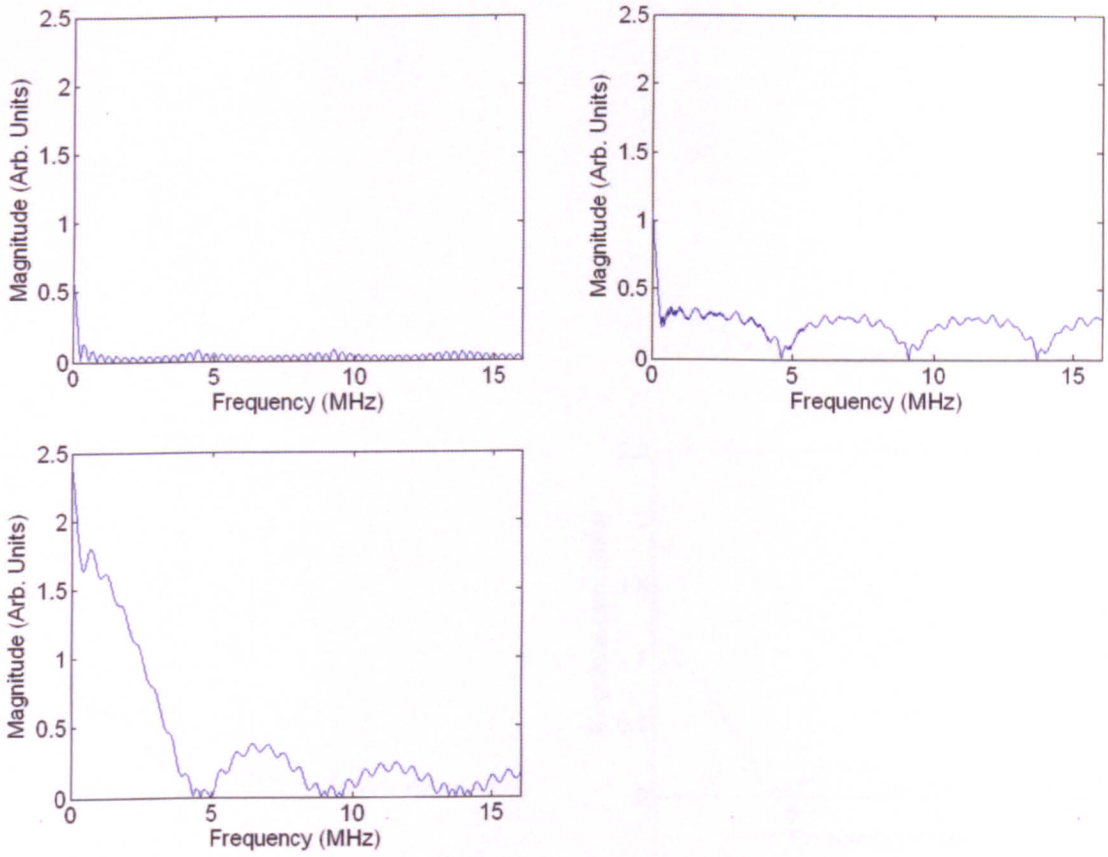

Figure 7.25 Frequency spectra for a 15 elemental structure system for normal composite (top left), composite containing a thick resin layer (top right) and for porous composite (bottom).

Figure 7.25 shows that although there is a constant level in the presence of a thick resin layer, this response has been modified by the process of the removal of the ply resonance $S(\omega)$, which has introduced minima to the spectrum. Although the spectrum for the porous case is similar to this case it is possible to determine differences. To help quantify these differences theoretical data was generated for a 15 elemental structure system containing either a layer of porosity of differing percentages or a thick resin layer of different thicknesses. For porosity, one layer of composite containing porosity was inserted into the system (at layer 7) with differing percentages of 0%, 2%, 4%, 6%, 8% and 10%. The resulting spectra are shown in figure 7.26.

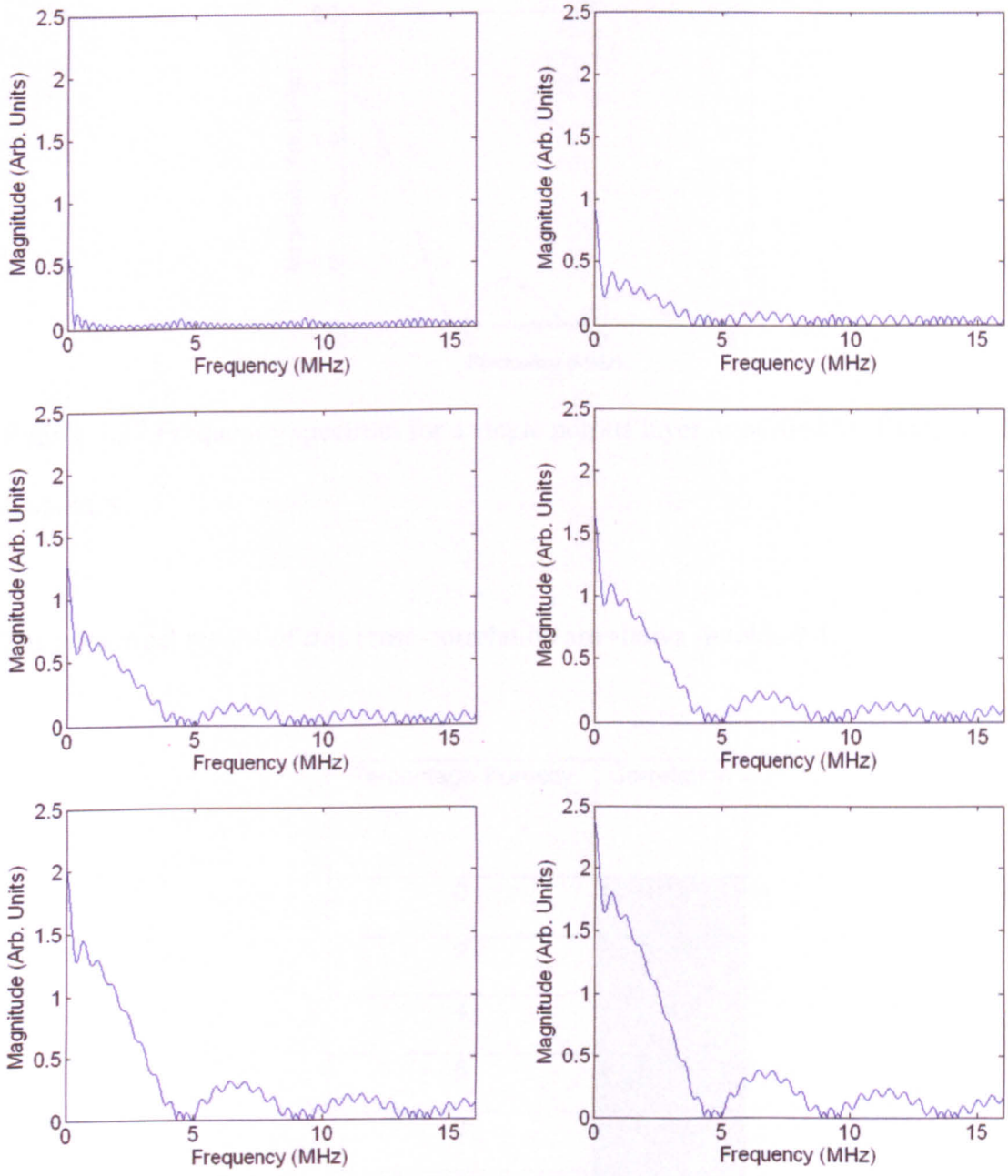

Figure 7.26 Frequency spectra for a modelled 15 elemental structure system with levels of porosity of 0% (top left), 2% (top right), 4% (middle left), 6% (middle right), 8% (bottom left) and 10% (bottom right).

The spectra shown in figure 7.26 were then processed as described previously. They were then cross-correlated with a modelled frequency spectrum for the resonance in a single layer containing porosity. This comparison spectrum was modified by dividing by frequency to leave only the porosity component, as shown in figure 7.27.

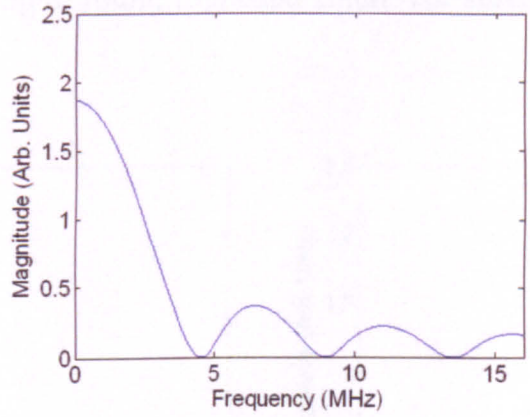

Figure 7.27 Frequency spectrum for a single porous layer, modified by dividing by frequency.

The numerical results of this cross-correlation are shown in table 7.1.

Percentage Porosity	Correlation
0	0.031
2	0.192
4	0.406
6	0.578
8	0.733
10	0.961

Table 7.1 Correlation between a resonance from a single porous layer and a 15 elemental structure system frequency spectra containing one layer of porosity.

To draw comparisons, further spectra were modelled in the same system, but with a thick resin layer present in layer 7 instead of porosity. The values of thick resin layer

used were 1μm, 2μm, 5μm, 10μm, 15μm and 20μm. The spectra produced are shown in figure 7.28.

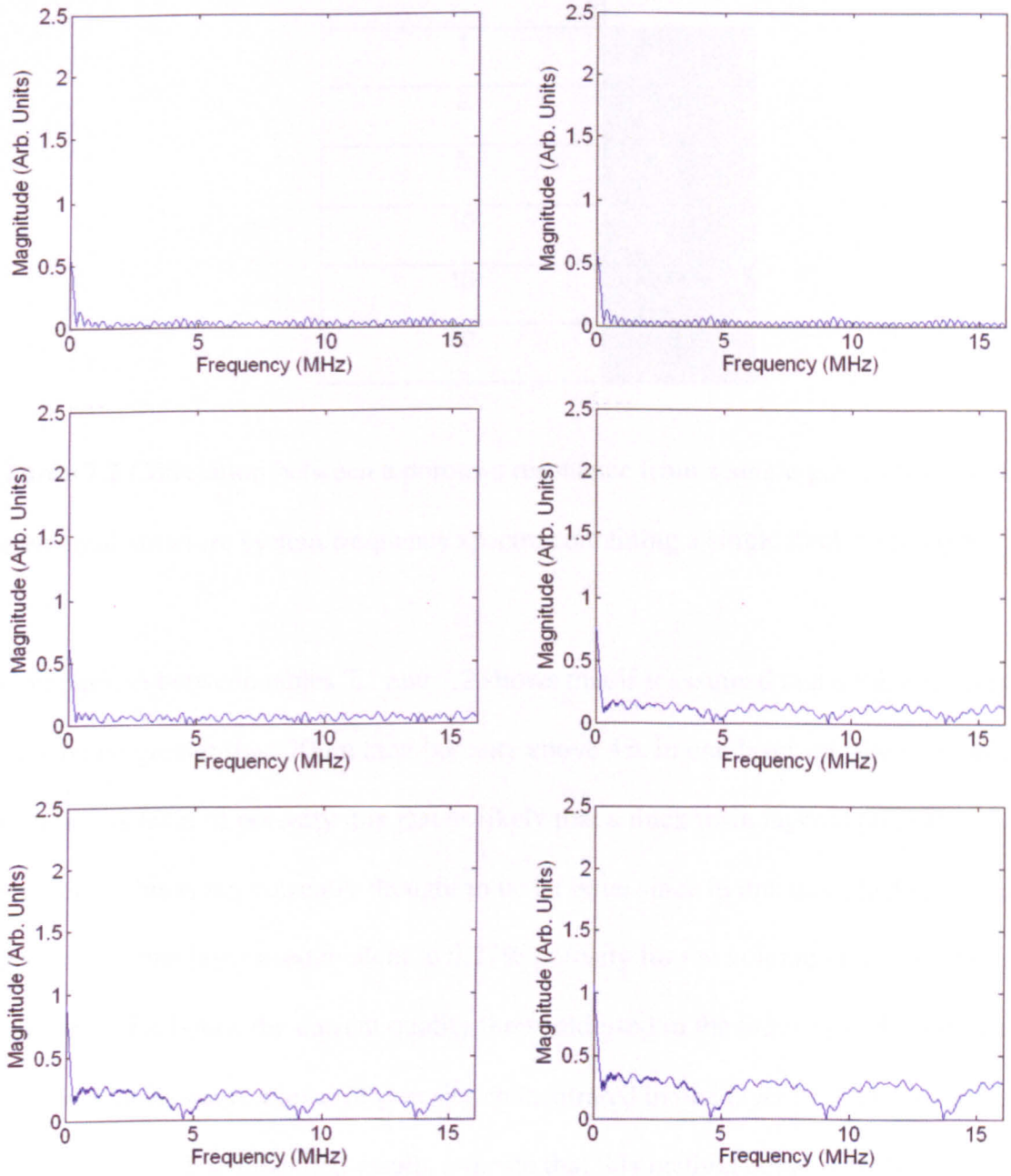

Figure 7.28 Modelled frequency spectra for a 15 elemental structure system containing one thick resin layer of thickness 1μm (top left), 2μm (top right), 5μm (middle left), 10μm (middle right), 15μm (bottom left) and 20μm (bottom right).

The spectra shown in figure 7.28 were cross-correlated with the spectrum shown in figure 7.27. The numerical results of this process are shown in table 7.2.

Resin Thickness (μm)	Correlation
1	0.057
2	0.073
5	0.132
10	0.185
15	0.266
20	0.339

Table 7.2 Correlation between a porous a resonance from a single porous layer and a 15 elemental structure system frequency spectra containing a single thick resin layer.

Comparison between tables 7.1 and 7.2 shows that if it assumed that a thick resin layer may be no greater than 20μm then porosity above 4% in one layer may be detected. Below this level of porosity it is just as likely that a thick resin layer is present. However, this is not currently thought to be an issue since in this modelled situation 4% porosity in one layer is equivalent to 0.27% porosity for the volume of the composite and this is far below the current quality threshold used in the industry (5%). To meet current requirements a level of porosity concentrated in one layer of 37.5% would need to be detected. The modelled results indicate that this method could meet this requirement.

Having considered isolated defects it is necessary to consider defects which may be spread across the CFRP. A defect of interest is porosity dispersed across the depth of the laminate; this was simulated by inserting porosity into each ply of percentage values 0%, 1%, 2%, 4% and 8%. The frequency spectra obtained were filtered using the notch

filters outlined previously and divided by frequency, the results obtained are shown in figure 7.29.

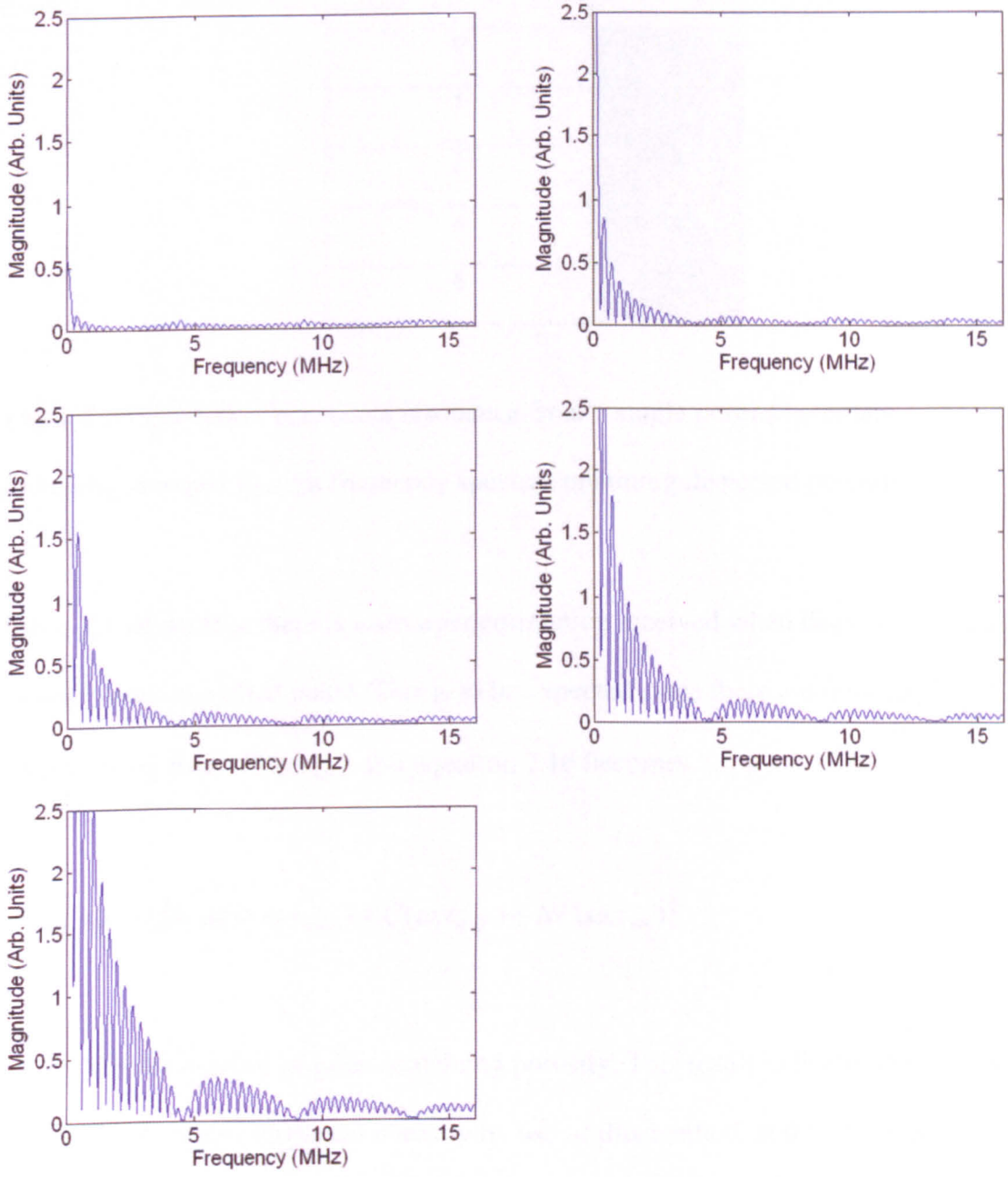

Figure 7.29 Modelled frequency spectra for a 15 elemental structure system with porosity dispersed evenly throughout the plies of percentage values 0% (top left), 1% (top right), 2% (middle left), 4% (middle right), 8% (bottom left).

The spectra shown in figure 7.29 were cross-correlated the spectrum shown in figure 7.27. The numerical results of this process are shown in table 7.3.

Percentage Porosity	Correlation
0	0.064
1	0.141
2	0.288
4	0.515
8	0.977

Table 7.3 Correlation between a resonance from a single porous layer and a 15 elemental structure system frequency spectra containing dispersed porosity.

Table 7.3 shows that there is a stronger correlation received when dispersed porosity is present in the modelled panel. This is to be expected since there are now 15 contributions from $P(\omega,t_{ply})$ and equation 7.16 becomes,

$$F(\omega) = T(\omega)\left[S(\omega)R(\omega,t_{norm}) + C(\omega,t_{thick}) + NP(\omega,t_{ply})\right] \quad \textbf{(7.24)}$$

where N is the number of plies containing porosity. This result indicates that it should be possible to detect dispersed porosity by use of this method, and to differentiate between dispersed porosity and a thick resin layer (typically between 5 μm and 20μm in thickness), providing the percentage value of dispersed porosity is greater than 4% and ignoring noise in the system. Comparison with the result of the envelope analysis method (chapter 5), this should allow all levels of dispersed porosity to be differentiated from the presence of a thick resin layer.

To determine the likely limits of this method under experimental conditions these results were repeated with spectra convolved with a transducer result, and with 50% randomness in the resin layers as specified in chapter 4, section 4.4.3. The resulting spectra obtained for porosity are shown in figure 7.30.

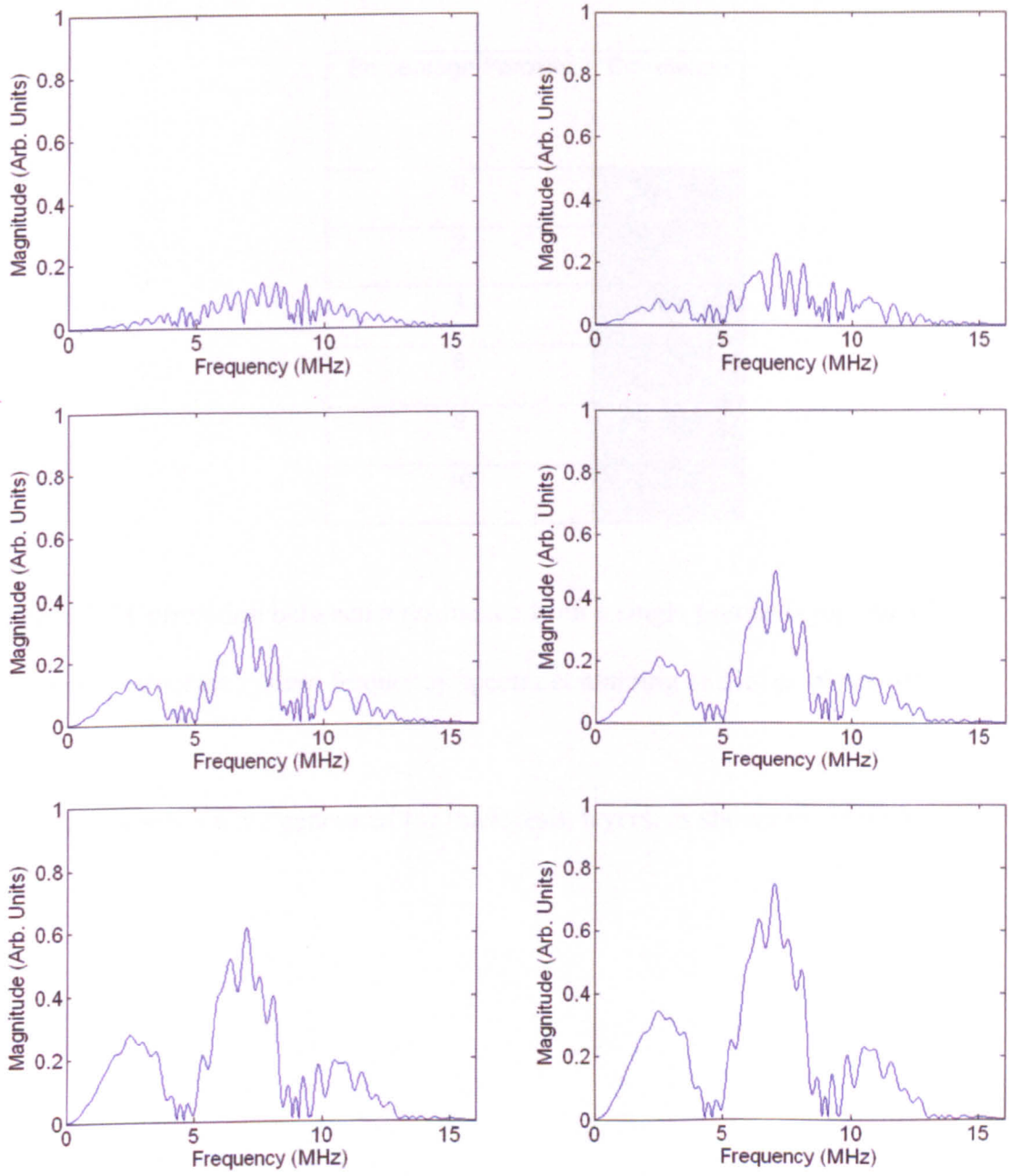

Figure 7.30 Frequency spectra for a modelled 15 elemental structure system with levels of porosity of 0% (top left), 2% (top right), 4% (middle left), 6% (middle right), 8% (bottom left) and 10% (bottom right).

The spectra shown in figure 7.30 were then processed as described previously and the results were then cross-correlated with a modelled frequency spectrum for a resonance in a single layer containing porosity. The numerical results of this cross-correlation are shown in table 7.4.

Percentage Porosity	Correlation
0	0.099
2	0.162
4	0.381
6	0.492
8	0.609
10	0.773

Table 7.4 Correlation between a resonance from a single porous layer and a 15 elemental structure system frequency spectra containing one layer of porosity.

Similarly spectra were generated for thick resin layers, as shown in figure 7.31.

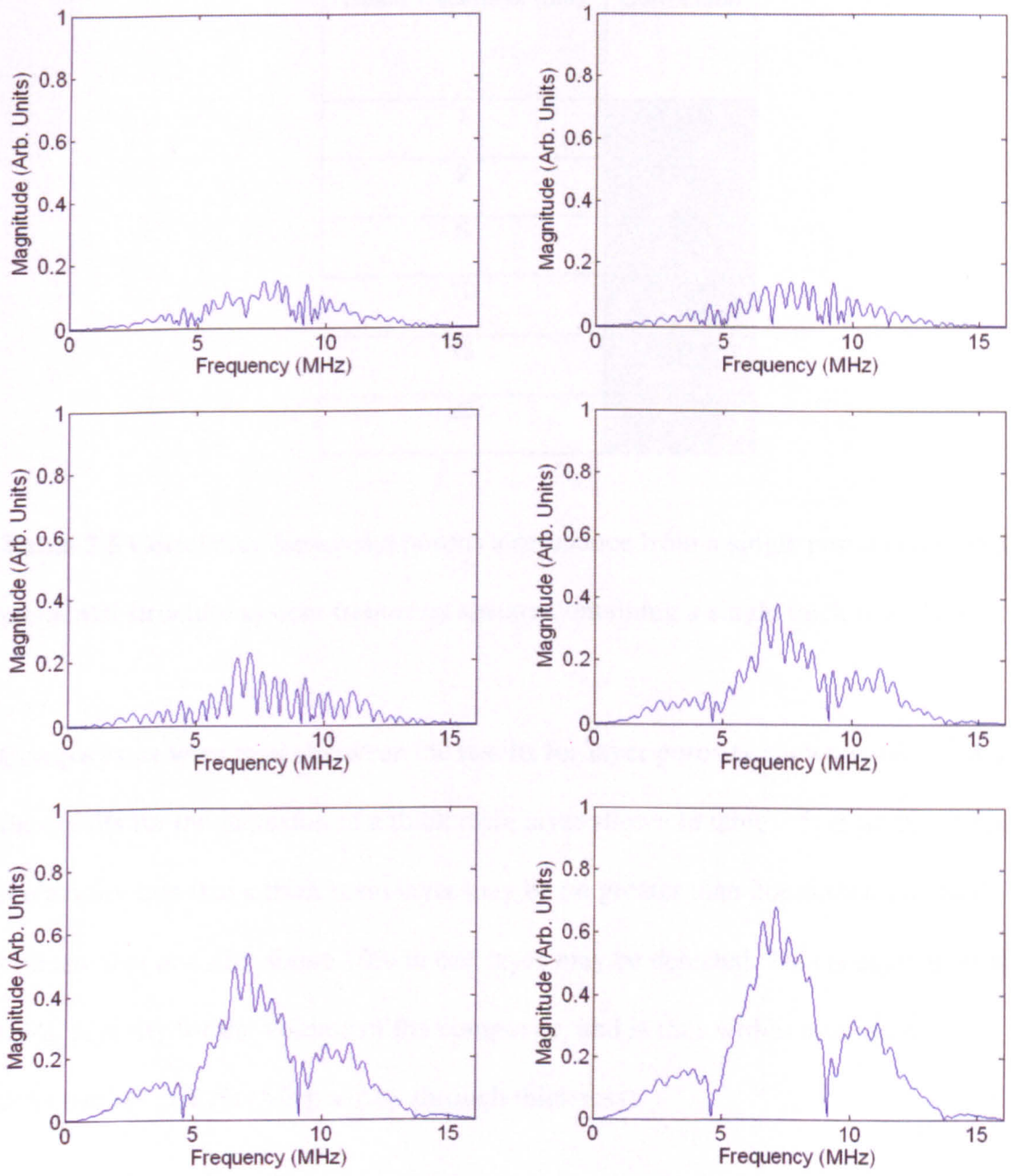

Figure 7.31 Modelled frequency spectra for a 15 elemental structure system containing one thick resin layer of thickness 1μm (top left), 2μm (top right), 5μm (middle left), 10μm (middle right), 15μm (bottom left) and 20μm (bottom right).

The spectra shown in figure 7.31 were cross-correlated with the spectrum shown in figure 7.27, the numerical results of this process are shown in table 7.5.

Resin Thickness (μm)	Correlation
1	0.179
2	0.135
5	0.180
10	0.355
15	0.531
20	0.727

Table 7.5 Correlation between a porous a resonance from a single porous layer and a 15 elemental structure system frequency spectra containing a single thick resin layer.

Comparisons were made between the results for layer porosity shown in table 7.4 and the results for the inclusion of a thick resin layer shown in table 7.5. If we again make the assumption that a thick resin layer may be no greater than 20μm then the results indicate that porosity above 10% in one layer may be detected. This is equivalent to 0.6% porosity for the volume of the composite, and is thus within minimum detectability criteria (5% porosity through thickness).

Simulations were conducted for porosity dispersed across the CFRP, and the spectra obtained are shown in figure 7.32.

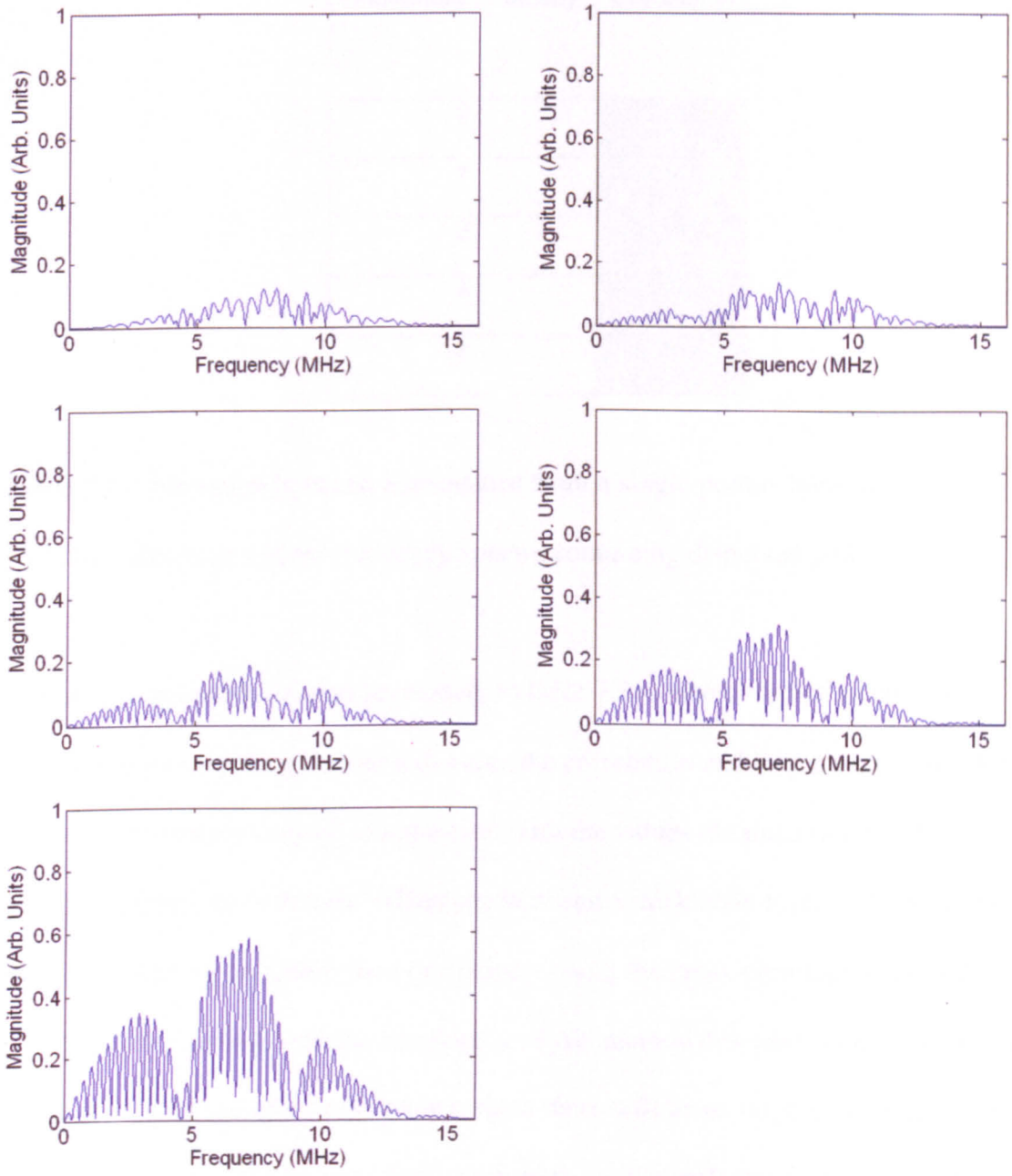

Figure 7.32 Modelled frequency spectra for a 15 elemental structure system with porosity dispersed evenly throughout the plies of percentage values 0% (top left), 1% (top right), 2% (middle left), 4% (middle right), 8% (bottom left).

Cross-correlating the spectra shown in figure 7.32 with the spectrum shown in figure 7.27 provides the following results (table 7.6).

Percentage Porosity	Correlation
0	0.104
1	0.116
2	0.189
4	0.249
8	0.604

Table 7.6 Correlation between a resonance from a single porous layer and a 15 elemental structure system frequency spectra containing dispersed porosity.

A level of correlation as seen previously in table 7.3 is also observed in table 7.6, however, the level of randomness disrupts the correlation and the numerical result is not as strong as seen previously. Comparison with the values obtained in table 7.5 for a thick resin layer show that the difference between a thick resin layer and dispersed porosity could not be determined exclusively using the cross-correlation method. However, comparison with the envelope analysis method described in chapter 5, should allow this difference to be determined, since there will be no large amplitude features in the waveform for dispersed porosity. However, such significant features would be expected when there is a thick resin layer present.

7.6 Examination of Effect of Defect Position on Broad Time Gate Response

To gain an insight into the factors affecting the response obtained in the frequency domain from a broad time gate of an ultrasonic signal received from flawed composite

simulations were again conducted using *MLM-Propmat.* These were done for gates covering 3, 5, 7, 9 and 11 plies, using a ply thickness of 125μm and 5μm resin layers; a fibre volume fraction 0.7 was assumed. A 32 ply stack was generated and the gate was centred on ply 16. A defect was added to the gate and the position of this defect varied, to simulate a gate moving over a defect in the A-scan. Simulations were done using a 20μm resin layer and a 10% 10μm porous layer as the defect. The normal spectrum obtained for unflawed composite for a 3 ply gate width is shown in figure 7.33.

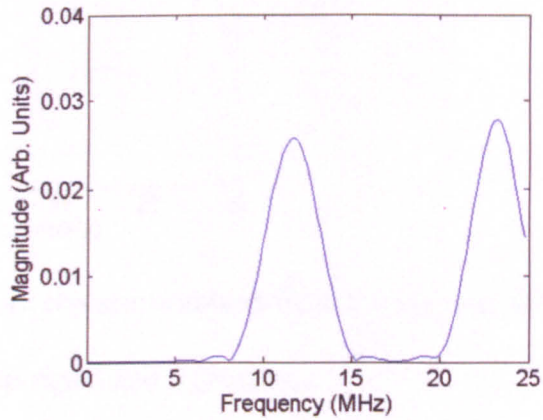

Figure 7.33 Frequency response obtained from a 3 ply gate for unflawed composite.

Porosity was added to the composite in fibre/resin layer 1, 2 and 3 the results which were obtained are shown in figure 7.34.

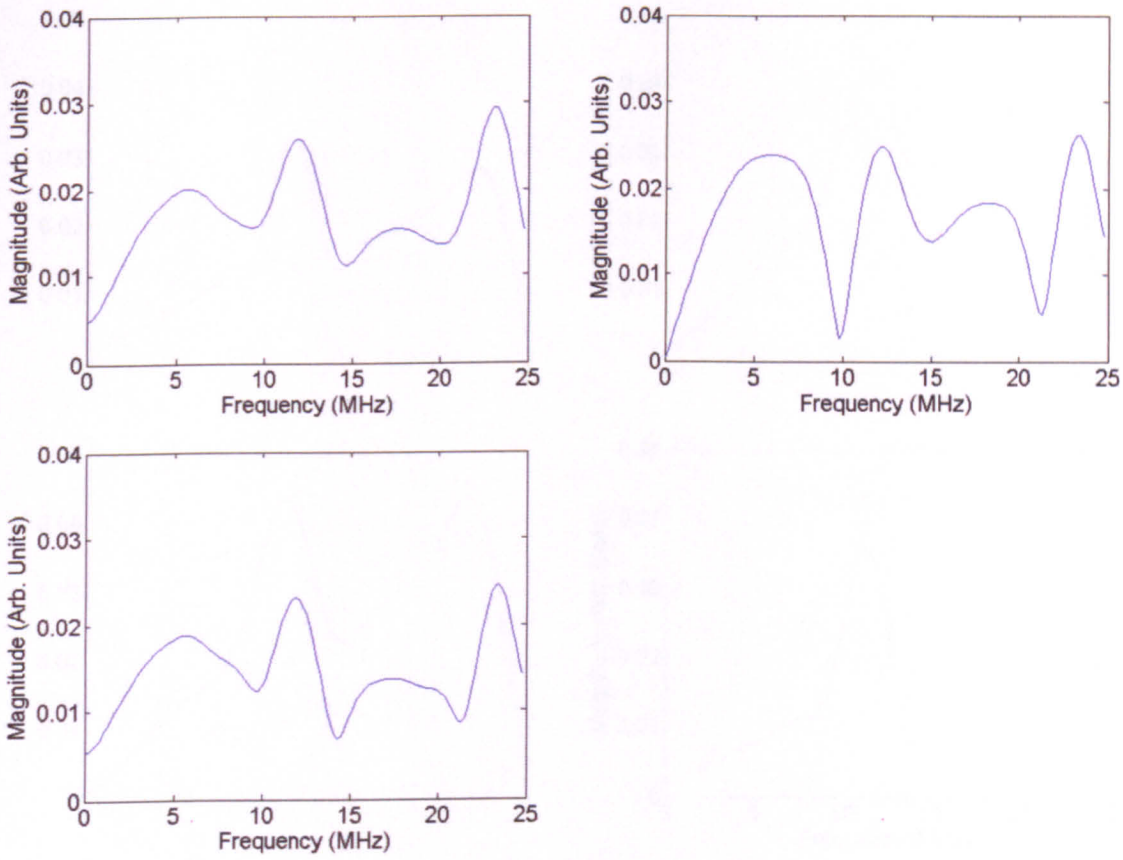

Figure 7.34 Frequency response obtained from a 3 ply gate with porosity in fibre/resin layer 1 (top left), 2 (top right) and 3 (bottom).

Figure 7.34 shows that the responses from the first and last ply are similar; however, the response from porosity in the central ply differs. The differences between the first and last ply are due to attenuation within the composite. The window function applied also appears to have an effect, resulting in the central ply response differing from the plies at the end of the gate. A thick resin layer was added before and after each of the fibre/resin layers, and the frequency spectra obtained are shown in figure 7.35.

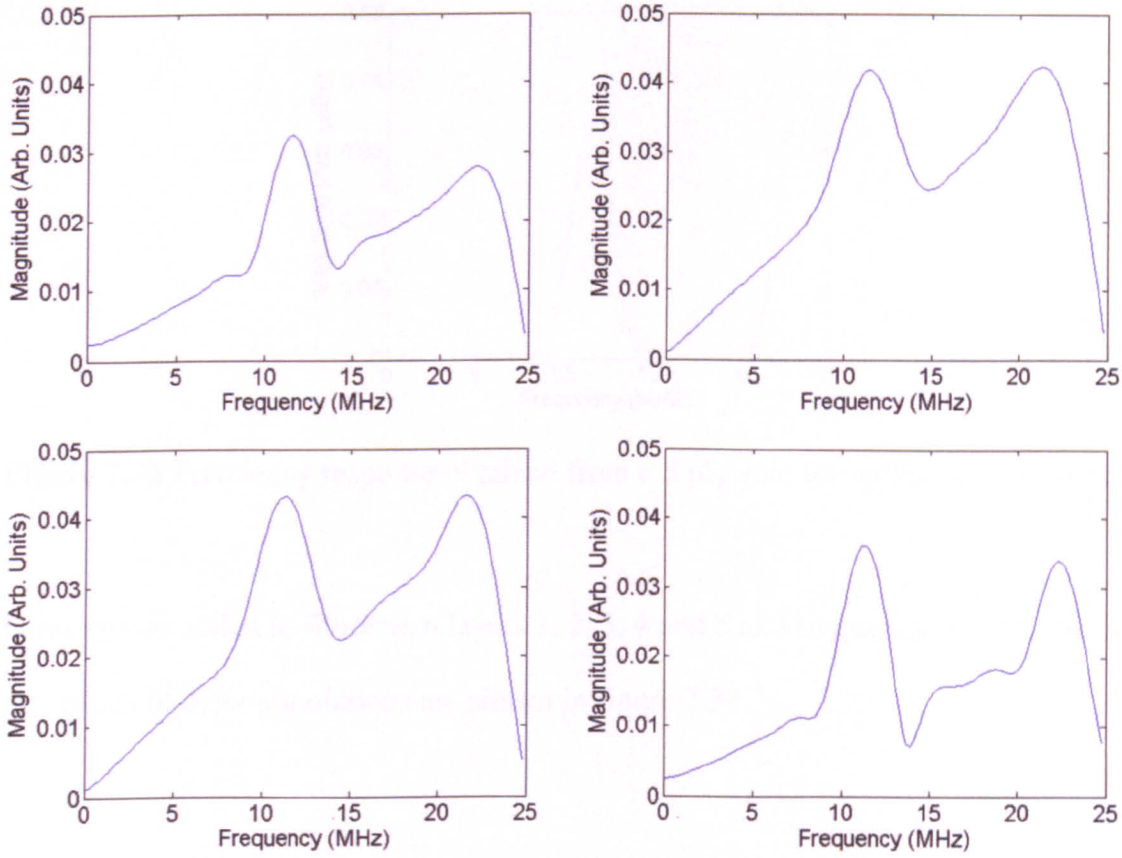

Figure 7.35 Frequency spectra obtained from a 3 ply gate with a thick resin layer before the first ply (top left), the second ply (top right), the third ply (bottom left) and after the third ply (bottom right).

Figure 7.35 shows that the frequency responses which are obtained from gates which are the same distance from the end of the gate, for example, the first and last resin layer, are similar. The frequency spectrum obtained for a 5 ply gate of unflawed composite is shown in figure 7.36.

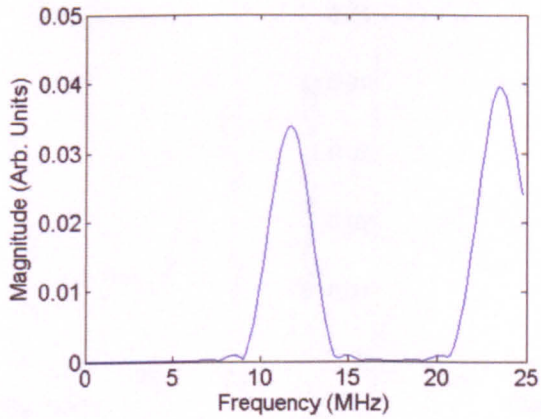

Figure 7.36 Frequency response obtained from a 5 ply gate for unflawed composite.

Porosity was added to fibre/resin layers 1, 2, 3, 4 and 5 and frequency spectra obtained, the results of these simulations are shown in figure 7.37.

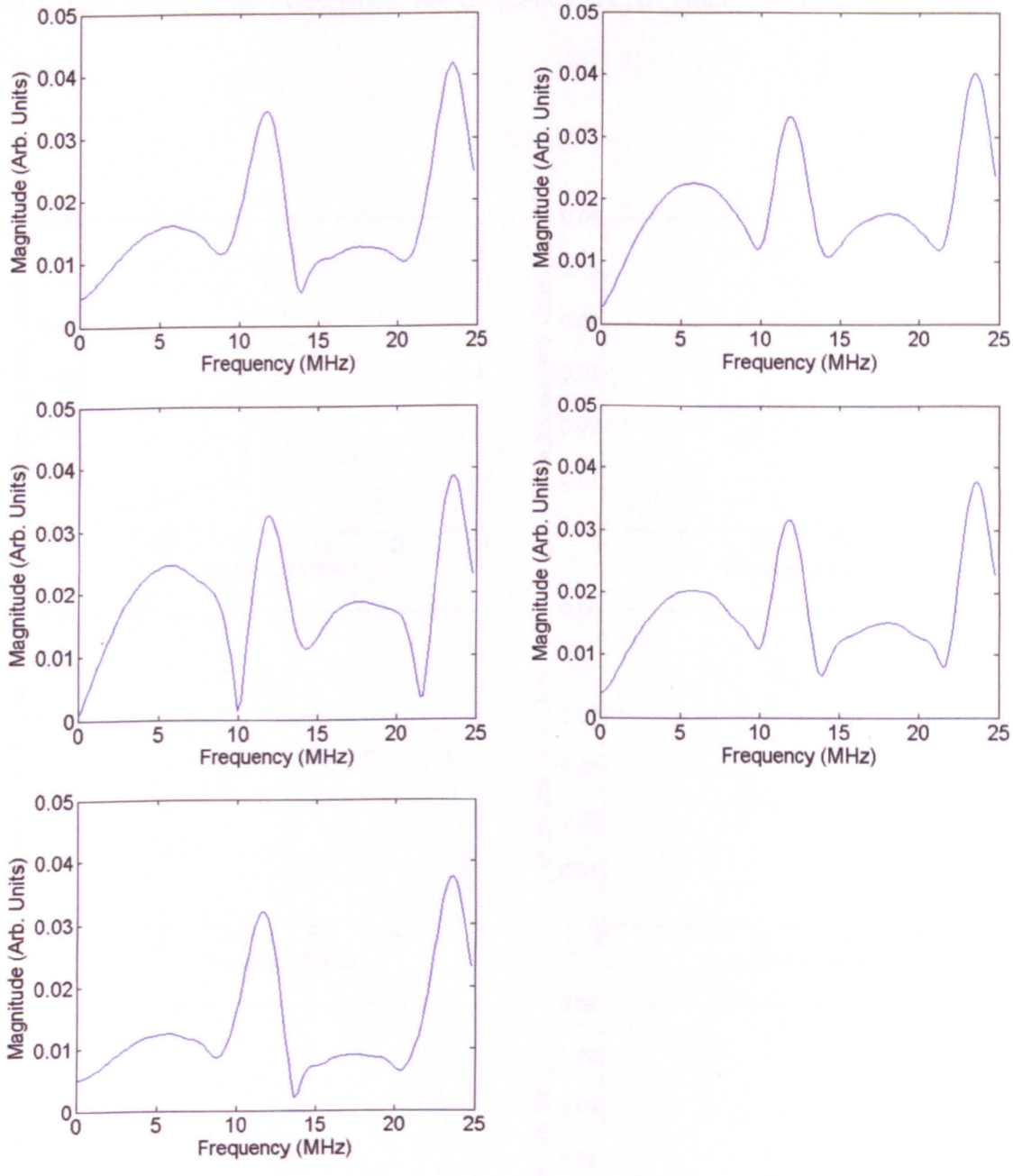

Figure 7.37 Frequency response obtained from a 5 ply gate with porosity in fibre/resin layer 1 (top left), 2 (top right), 3 (middle left), 4 (middle right) and 5 (bottom).

Figure 7.37 demonstrates the symmetry about the central ply in the frequency spectra. The differences in the spectra are attributed to additional resonances introduced between the porous layer, which is a strong reflector, and other features within the structure. The exact form of these resonances will differ with position of the defect within the gate but will be symmetrical about the centre of the gate. A thick resin layer was added to the

structure as previously described, the frequency spectra obtained are shown in figure 7.38.

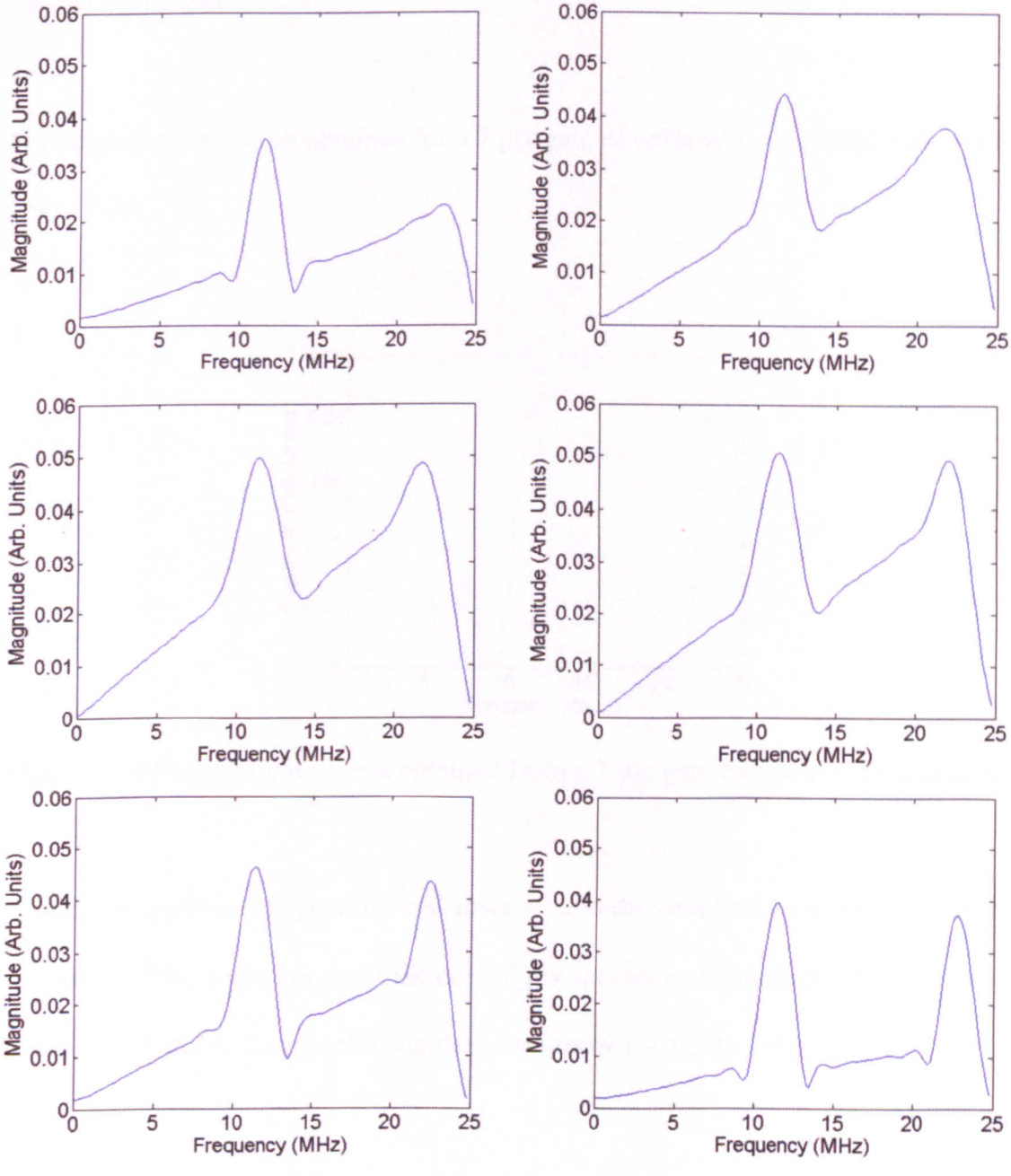

Figure 7.38 Frequency spectra obtained from a 5 ply gate with a thick resin layer before the first ply (top left), the second ply (top right), the third ply (middle left), the fourth ply (middle right), the fifth ply (bottom left) and after the fifth ply (bottom right).

Figure 7.38 shows that, again, there is symmetry of frequency spectra about the middle ply, the differences within these spectra are attributed to frequency dependent attenuation and windowing effects reducing amplitude of the response from the defect at the end of the gate.

The frequency spectrum obtained for a 7 ply gate of unflawed composite is shown in figure 7.39.

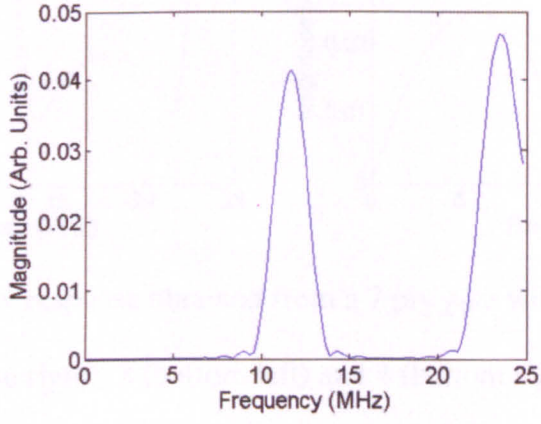

Figure 7.39 Frequency response obtained from a 7 ply gate for unflawed composite.

As described previously porosity was inserted into the structure, however, given the symmetry of these spectra about the central ply spectra were produced for fibre/resin layers 1, 2, 3 and 4. The spectra simulated are shown in figure 7.40.

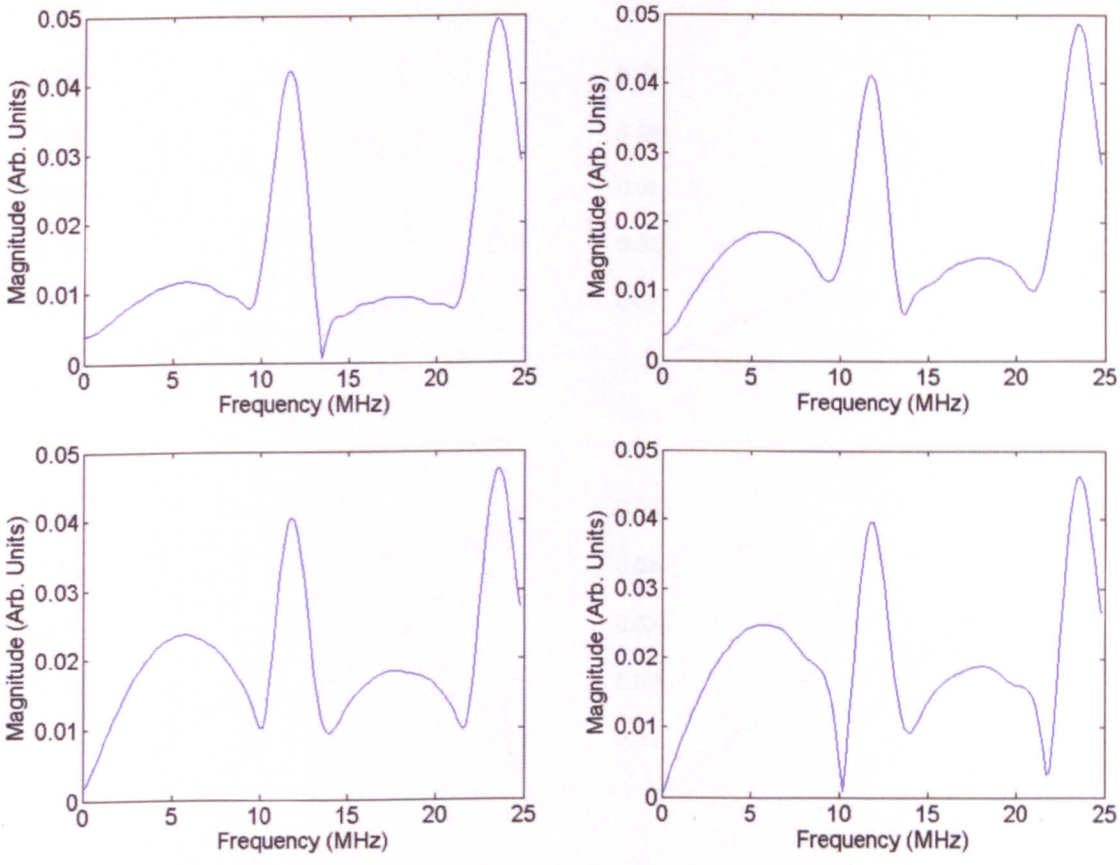

Figure 7.40 Frequency response obtained from a 7 ply gate with porosity in fibre/resin layer 1 (top left), 2 (top right), 3 (bottom left) and 4 (bottom right).

Figure 7.40 shows that the responses obtained are similar to those seen for previous defect types, the response most similar to that which would be expected is obtained when the defect is close to the centre of the gate. Similarly for a thick resin layer spectra were obtained before and after each ply, the results are shown in figure 7.41.

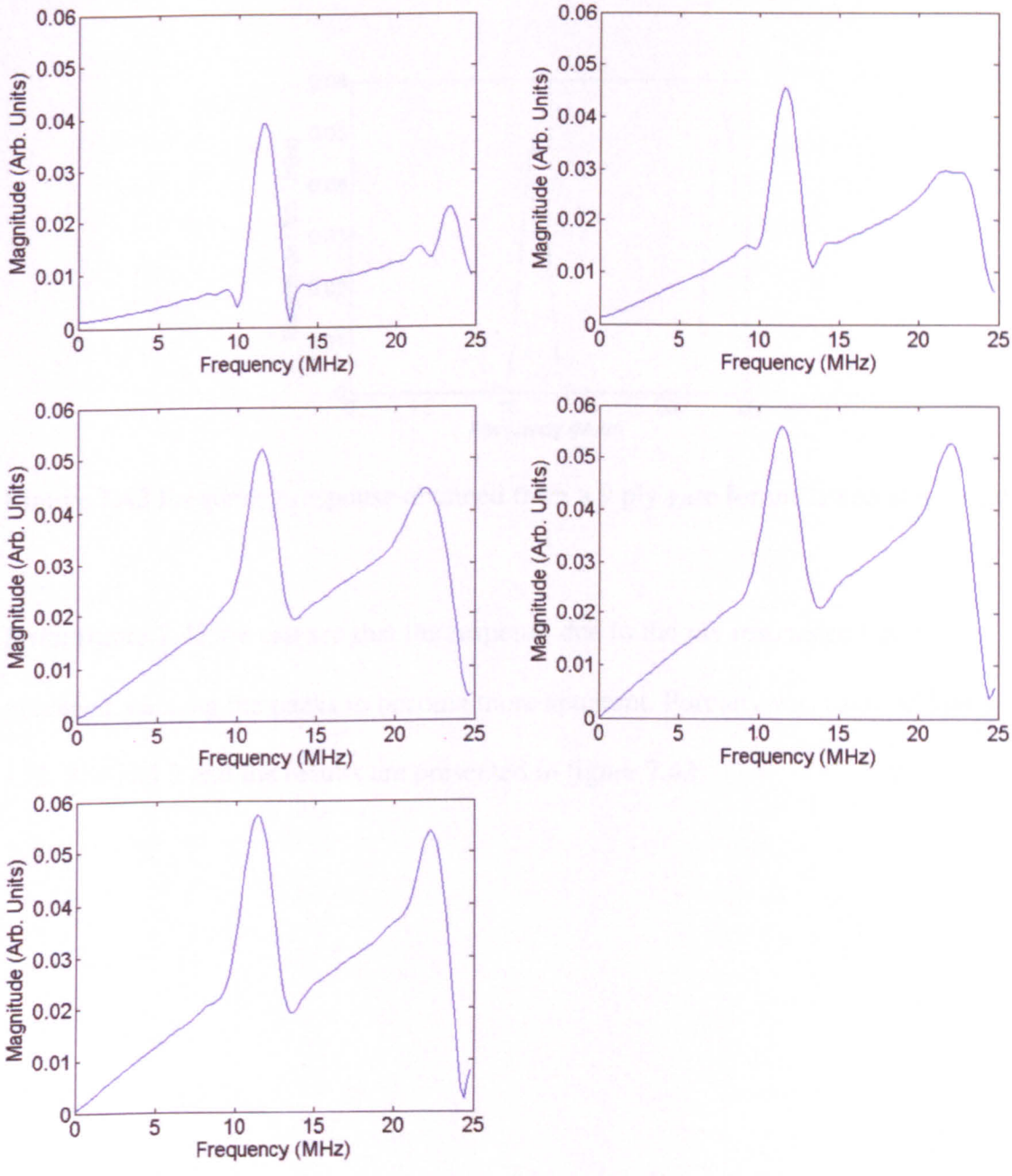

Figure 7.41 Frequency spectra obtained from a 7 ply gate with a thick resin layer before the first ply (top left), the second ply (top right), the third ply (middle left), the fourth ply (middle right) and after the fourth ply (bottom left).

Figure 7.41 shows that a response similar to that seen previously for a thick resin layer; there is a linear slope superimposed upon the spectrum; this is most noticeable when the defect is close to the centre of the gate. The frequency spectrum obtained for a 9 ply gate of unflawed composite is shown in figure 7.42.

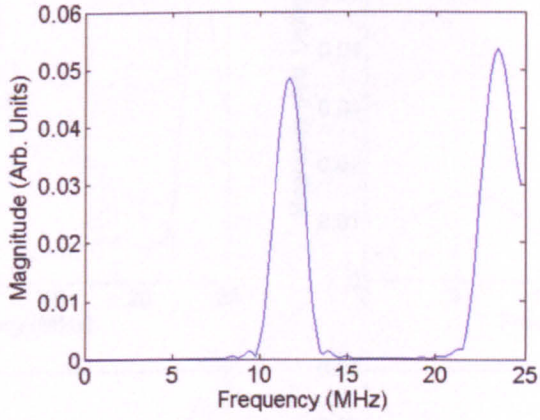

Figure 7.42 Frequency response obtained from a 9 ply gate for unflawed composite.

From figure 7.42 we can see that the response due to the ply resonance has been averaged, causing the peaks to become more apparent. Porosity was inserted into layer 1, 2, 3, 4 and 5 and the results are presented in figure 7.43.

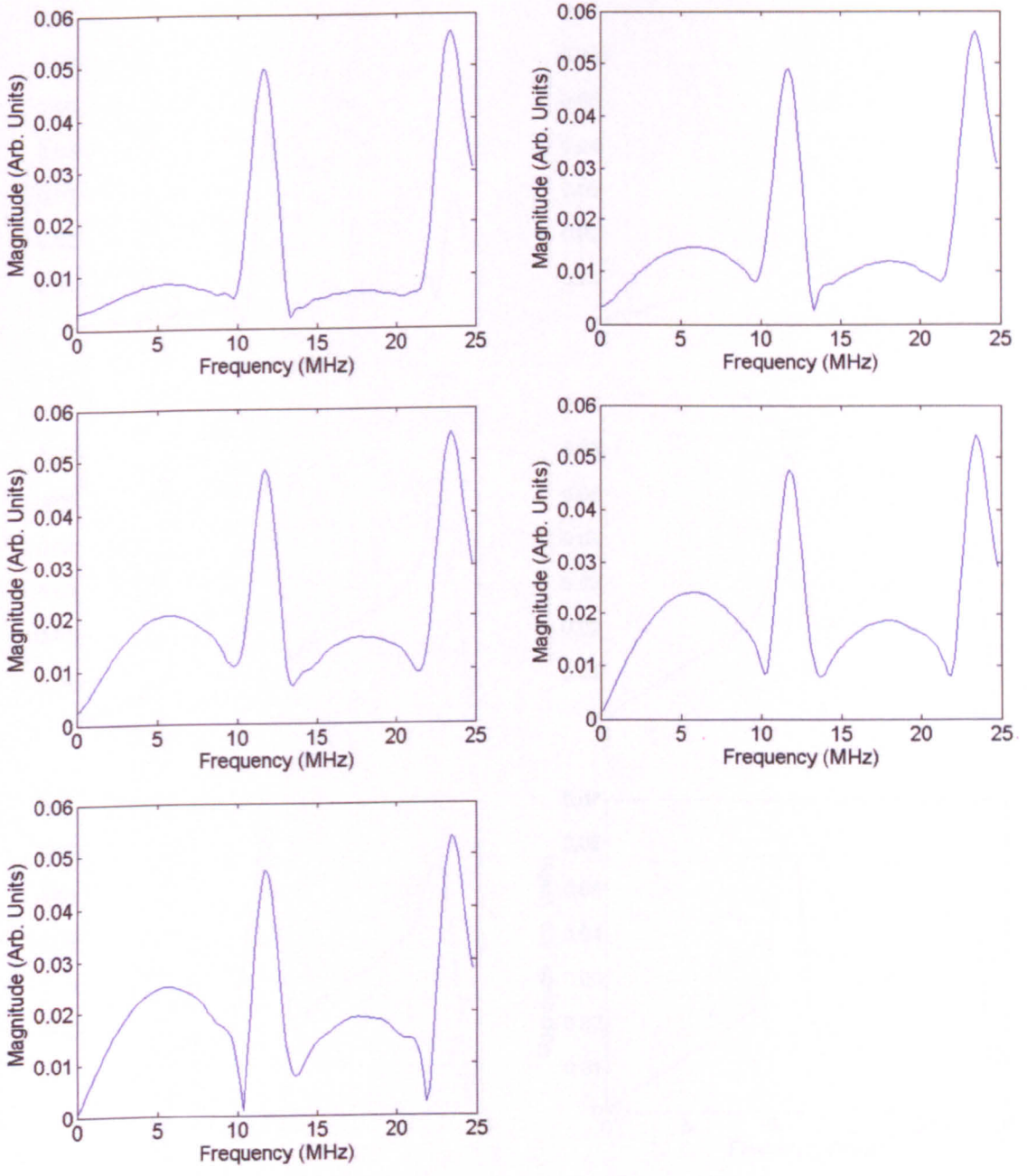

Figure 7.43 Frequency response obtained from a 9 ply gate with porosity in fibre/resin layer 1 (top left), 2 (top right), 3 (middle left), 4 (middle right) and 5 (bottom left).

Similarly for a thick resin layer spectra were obtained before and after each ply, the results are shown in figure 7.44.

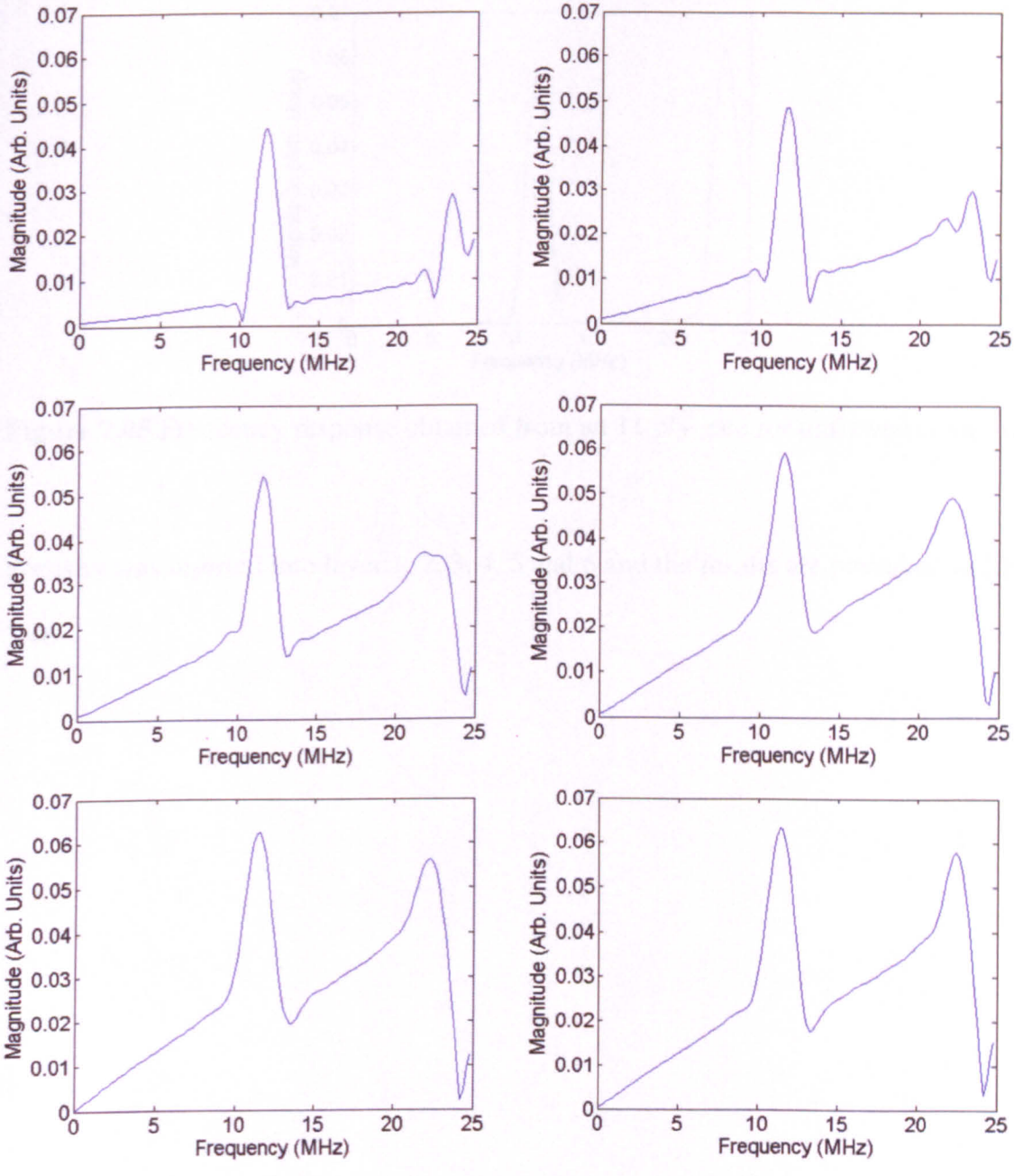

Figure 7.44 Frequency spectra obtained from a 9 ply gate with a thick resin layer before the first ply (top left), the second ply (top right), the third ply (middle left), the fourth ply (middle right), the fifth ply (bottom left) and after the fifth ply (bottom right).

The frequency spectrum obtained for an 11 ply gate of unflawed composite is shown in figure 7.45.

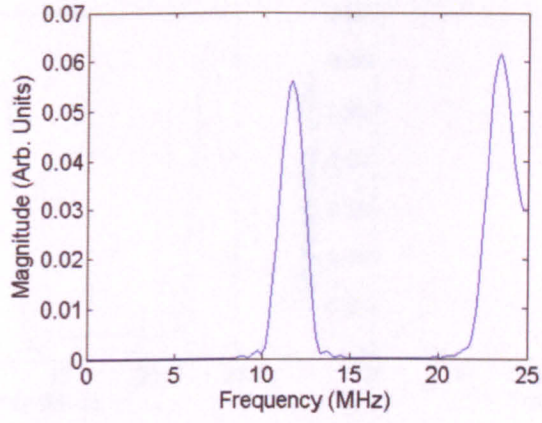

Figure 7.45 Frequency response obtained from an 11 ply gate for unflawed composite.

Porosity was inserted into layer 1, 2, 3, 4, 5 and 6 and the results are presented in figure 7.46.

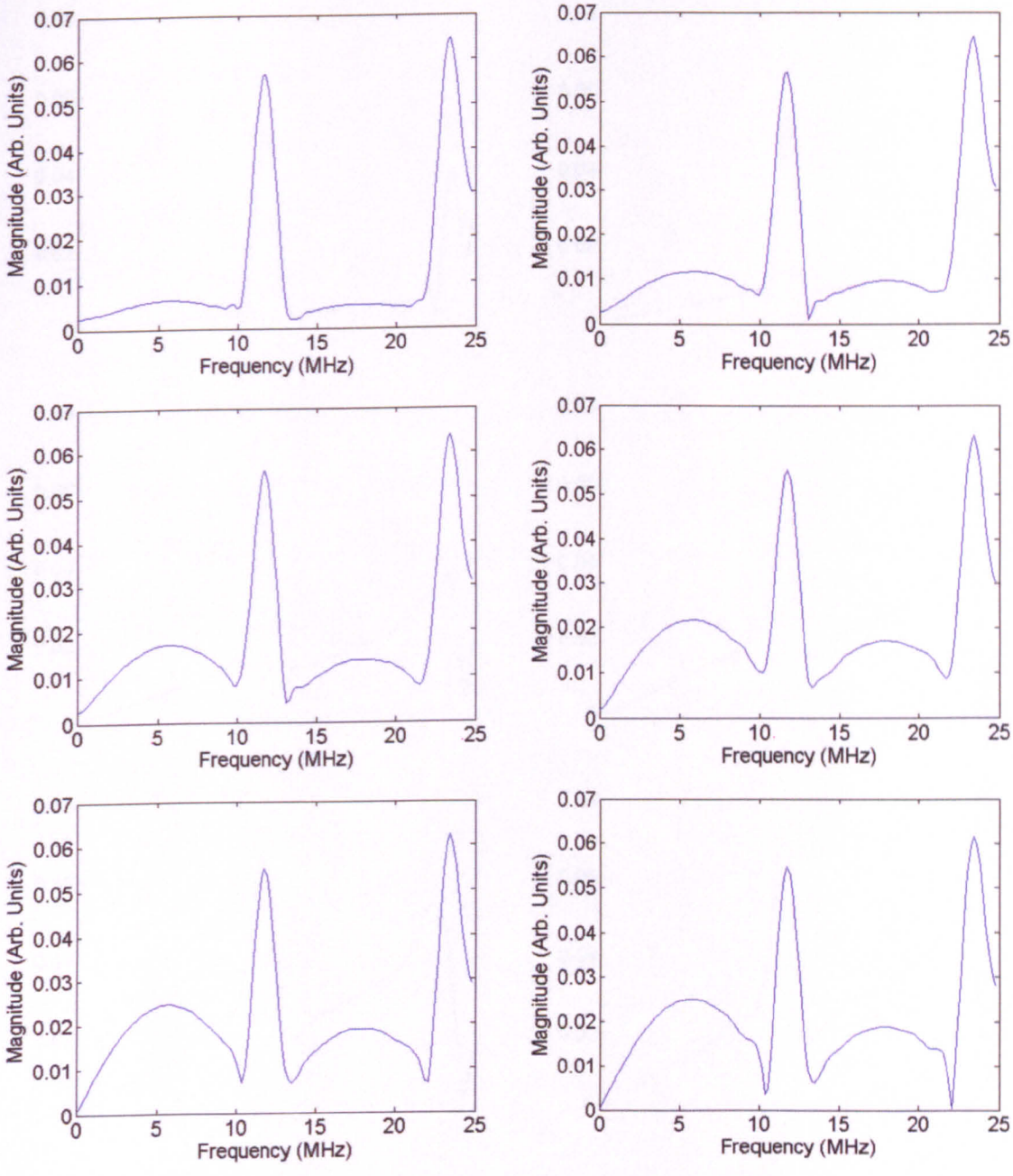

Figure 7.46 Frequency response obtained from an 11 ply gate with porosity in fibre/resin layer 1 (top left), 2 (top right), 3 (middle left), 4 (middle right), 5 (bottom left) and 6 (bottom right).

Similarly for a thick resin layer spectra were obtained before and after each ply, the results are shown in figure 7.47.

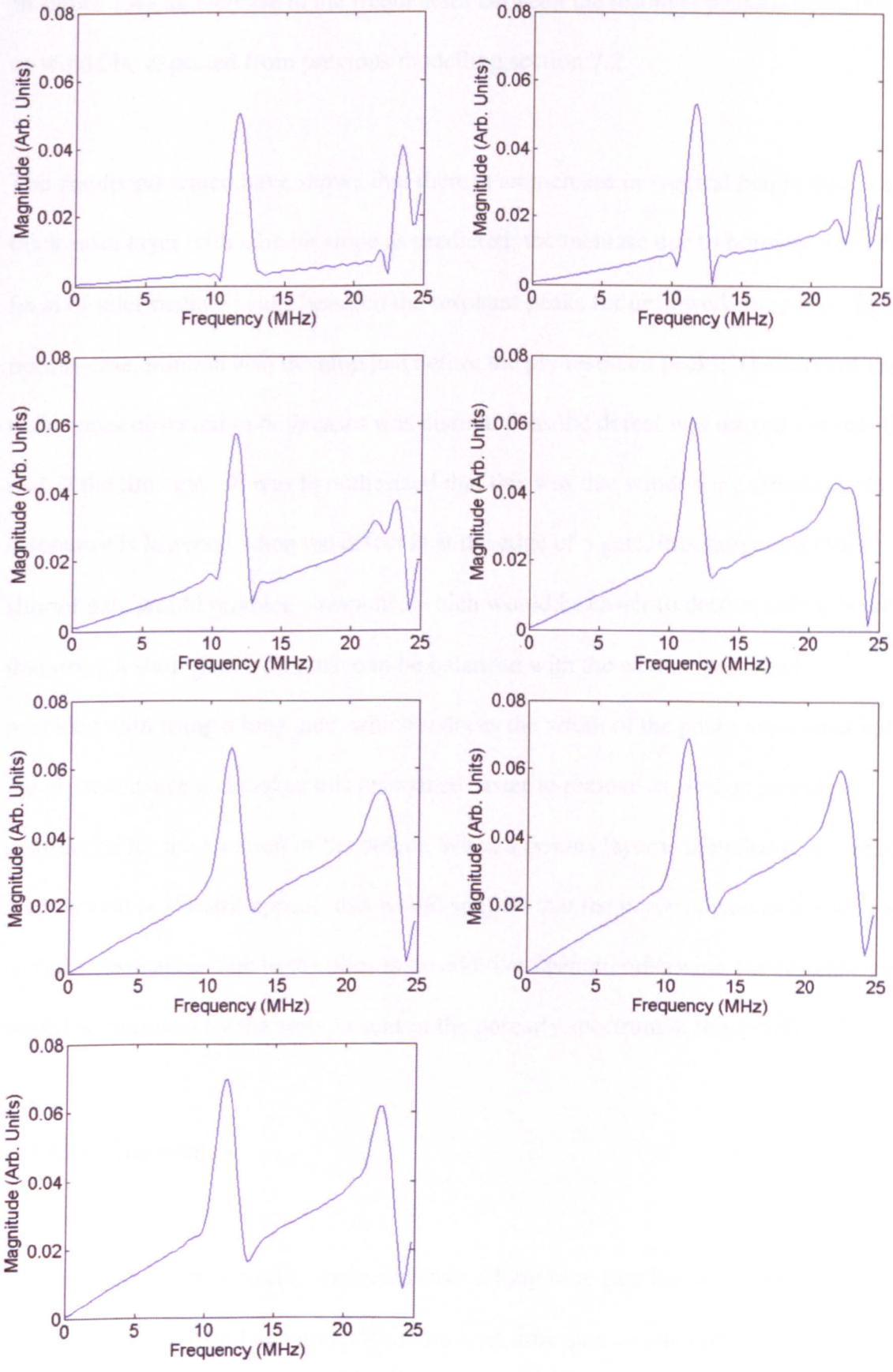

Figure 7.47 Frequency spectra obtained from a 11 ply gate with a thick resin layer before the first ply (first row left), the second ply (first row right), the third ply (second row left), the fourth ply (second row right), the fifth ply (third row left), the sixth ply (fourth row right) and after the sixth ply (bottom right).

In figure 7.47 an increase in the frequencies between the resonant peaks is seen, this is as would be expected from previous modelling section 7.2.

The results presented have shown that there is an increase in spectral height due to a thick resin layer with a linear slope as predicted; the increase due to porosity was of the form of intermediate peaks between the resonant peaks for unflawed composite. In the porous case, minima also develop just before the ply resonant peaks. The form of the resonances observed in both cases was disrupted, as the defect was moved towards the end of the time gate. It was hypothesized that this was due windowing effects. Since the resonance is lessened when the defect is at the edge of a gate, it is suggested that a shorter gate would produce a response which would be easier to decompose. It is noted that using a short gate would have to be balanced with the advantages which are provided with using a long gate, which reduces the width of the peaks associated with the ply resonance and makes this resonance easier to remove as well as providing confidence for the location of the defect. When a porous layer is included it is noted that the resonant peaks still appear; this would suggest that the porous resonance interacts with the resonances due to the plies in an additive fashion, otherwise, the resonant peaks would be removed by the zero present in the porosity spectrum at this point.

7.7 Conclusions

The response which would be expected from a long time gate has been investigated. By varying defect type and quantity within the long time gate an equation governing this system has been suggested. A method has been devised which minimises the contribution from the ply resonance and the resin layer resonance to leave a spectrum

which is sensitive to porosity. Further modelling has suggested that in practice this method would be sensitive to levels of porosity above 10% in one layer (0.6% by volume of the entire structure), allowing reliable detection. This method has difficulties however in determining between dispersed porosity and thick resin layers, where the numerical results of the process are similar. However, observation of the time domain signal with the envelope analysis method outlined in chapter 5 would allow differentiation between the two defect types. In the case of a thick resin layer we would expect a large localised response, and for dispersed porosity there would be no specific localised feature. Analysis of modelling based upon the position of the defect has shown that the frequency spectra which are obtained are sensitive to the position of the defect within the time gate; this is thought to be due to additional resonances between the defect and the ends of the gate and windowing effects.

The next chapter examines the potential for a method which uses the equation governing the frequency response in a gate which was determined in section 7.4, and decomposes the spectrum into a sum of contributing parts.

Chapter 8

Location of Porosity in Three Dimensions: Decomposition Method

8.1 Introduction

We saw in chapter 7, that there exists the potential for a decomposition method to decompose the spectrum into constituent parts (basis functions). If it were possible to obtain the basis functions in this fashion, accurate measures of porosity, ply spacing and thick resin layer presence could be obtained. This chapter will examine the design and derivation of a decomposition method, which aims to split the spectrum into parameters which will give an indication of the contribution to the spectrum from each of the basis functions. The derived method is then tested against modelled data to provide an indication of its limitations. Finally, the method is tested on experimental data and conclusions are drawn.

8.2 Derivation of Method

The A-scan signals from composites are formed of multiple resonances that result from the quasi-periodic structure of the materials. These are modified by the presence of flaws such as voids, inclusions and excessively thick resin layers. It is likely that the various phenomena that contribute to the overall signal are neither additive nor multiplicative. For example, if a particular local (in depth) resonance pattern can be associated with a given type of flaw then we would expect to see some evidence of this resonance in the A-scan response, but modified by the filtering effects of wave propagation between the flaw and the interrogating transducer. However, if these components could in some way be recognised in the received signal then flaw types can be identified – indeed, we have done this throughout this project. Hitherto, we have not made the assumption that the effects of the flaws are additive in the A-scan signal. This study investigates the possibility that significant components in the A-scan that represent flaws can be regarded as additive. This assumption enables an analytical procedure that seeks correlations between signal components of the form expected from known flaws and successive segments of the A-scan. The procedure effectively *decomposes* each A-scan segment (corresponding to a particular depth) into components that represent unflawed composite, porosity and excess resin. The following paragraphs outline the method.

We assume that the overall resonant behaviour of the composite can be expressed as the sum of a number of component sub-resonances, $F_n(f)$, each of which is assigned a weighting a_n. The observed echo spectrum becomes

$$y(f) = a_1 + a_2 F_2(f) + a_3 F_3(f) + a_4 F_4(f) \quad \textbf{(8.1)}$$

Here a_1 is a constant term to 'summarise' the inclusion of broad band noise or other 'flat' components in the spectrum. We now investigate possible forms for the functions F_n. First we denote $F_2(f)$ as the combined resonance behaviour of a normal ply with thin resin layers on either side. We have used *MLM-Propmat* to model this resonance, figure 8.1.

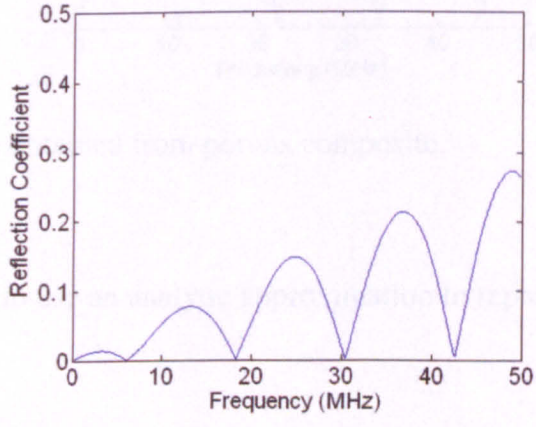

Figure 8.1 Normal resonance obtained from unflawed composite.

To build the function of equation 8.1 it is possible either to use the result of this computation or to use an analytic function as an approximation. The latter was chosen in order to reduce the computational load in the final analysis system. The function employed at present is

$$F_2(f) = \left|\sin\left(\frac{2\pi f}{\alpha}\right)\right| f \quad \textbf{(8.2)}$$

Here α is a coefficient that scales the frequency domain lobe width.

The function $F_3(f)$ represents the effect of porosity which modifies the half-wave resonance of figure 8.1 to the quarter-wave case shown in figure 8.2

.

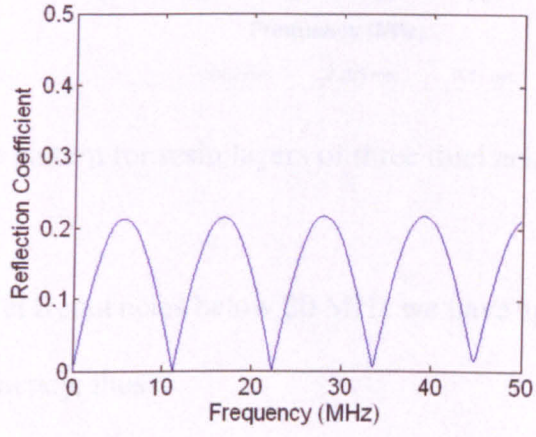

Figure 8.2 Resonance obtained from porous composite.

Again, we have opted to use an analytic approximation to represent this pattern, thus

$$F_3(f) = \left|\sin\frac{2\pi f}{\beta}\right| \tag{8.3}$$

where β is a scaling parameter. $F_4(f)$ represents resonant components due to the interstitial resin layers of excess thickness as shown in figure 8.3.

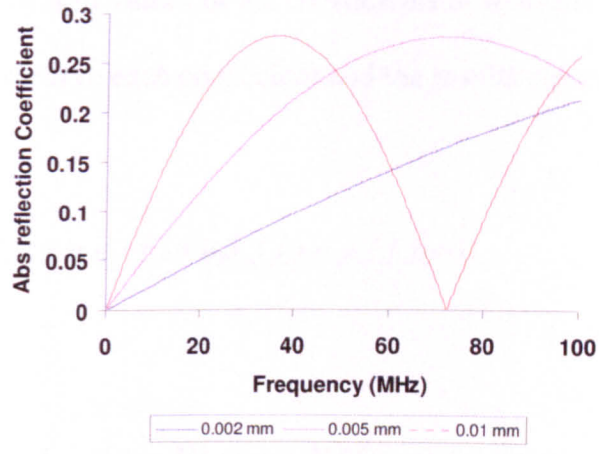

Figure 8.3 Resonance pattern for resin layers of three thicknesses.

Since we are working at frequencies below 20 MHz we have approximated this as a linear function of frequency, thus

$$F_4(f) = f \tag{8.4}$$

In order to determine the relative contributions of the three principal resonances we compare data modelled using equation 8.1 with measured data. This is done by calculating the sum-squared-error (*sse*) between the two, as follows

$$sse = \sum_{i=1}^{I} [y(f_i) - y_m(f_i)]^2 \tag{8.5}$$

hence,

$$sse = \sum_{i=1}^{I} 2[a_1 + a_2 F_2(f_i) + a_3 F_3(f_i) + a_4 F_4(f_i) - y_m(f_i)]^2 \tag{8.6}$$

In order to obtain the best fit values of the coefficients a_1 to a_4 the function is differentiated with respect to each coefficient and the results equated to zero:

$$\frac{\partial sse}{\partial a_1} = \sum_{i=1}^{I} 2[a_1 + a_2F_2(f_i) + a_3F_3(f_i) + a_4F_4(f_i) - y_m(f_i)] = 0$$

$$\frac{\partial sse}{\partial a_2} = \sum_{i=1}^{I} 2F_2(f_i)[a_1 + a_2F_2(f_i) + a_3F_3(f_i) + a_4F_4(f_i) - y_m(f_i)] = 0$$

(8.7)

$$\frac{\partial sse}{\partial a_3} = \sum_{i=1}^{I} 2F_3(f_i)[a_1 + a_2F_2(f_i) + a_3F_3(f_i) + a_4F_4(f_i) - y_m(f_i)] = 0$$

$$\frac{\partial sse}{\partial a_4} = \sum_{i=1}^{I} 2F_4(f_i)[a_1 + a_2F_2(f_i) + a_3F_3(f_i) + a_4F_4(f_i) - y_m(f_i)] = 0$$

These equations can be expressed in matrix form

$$\begin{bmatrix} \sum y_m \\ \sum F_2(f_i)y_m \\ \sum F_3(f_i)y_m \\ \sum F_4(f_i)y_m \end{bmatrix} = \begin{bmatrix} n & \sum F_2(f_i) & \sum F_3(f_i) & \sum F_4(f_i) \\ \sum F_2(f_i) & \sum F_2^2(f_i) & \sum F_2(f_i)F_3(f_i) & \sum F_2(f_i)F_4(f_i) \\ \sum F_3(f_i) & \sum F_2(f_i)F_3(f_i) & \sum F_3^2(f_i) & \sum F_3(f_i)F_4(f_i) \\ \sum F_4(f_i) & \sum F_2(f_i)F_4(f_i) & \sum F_3(f_i)F_4(f_i) & \sum F_4^2(f_i) \end{bmatrix} \begin{bmatrix} a_1 \\ a_2 \\ a_3 \\ a_4 \end{bmatrix}$$

(8.8)

or

$$[b] = [c][a] \qquad \textbf{(8.9)}$$

This equation is solved by inversion to get the required matrix $[a]$

$$[a] = [c]^{-1}[b] \tag{8.10}$$

The result is numerical values of the coefficients a_n which represent the contributions of the principal physical phenomena to the recorded signal segment. Specifically, we obtain numbers that represent the relative contributions of porosity and excess resin layer thickness.

8.3 Performance of Decomposition Method

To evaluate the performance of this method in arbitrary situations, a 32 ply composite was modelled, the ply thickness was 125 microns and the panel was immersed in water. The impulse response obtained was convolved with a 10MHz transducer response obtained from the transducer model described in chapter 4, section 4.3.2. Further analysis was applied to the A-scan signal, applying time-frequency analysis using a short time gate as described by chapter 6, section 6.3.1. The basis functions were also combined with this response. The result of this process was a spectrum which could be analysed using the method outlined previously. To verify the functionality of the method a layer of porosity was added to the 7th ply. The quantity of porosity used was varied from 0-95%, the size of the scatterers used was 10 microns. The value of the coefficients a_2, a_3 and a_4 was then calculated as described above and the results obtained are shown in figure 8.4.

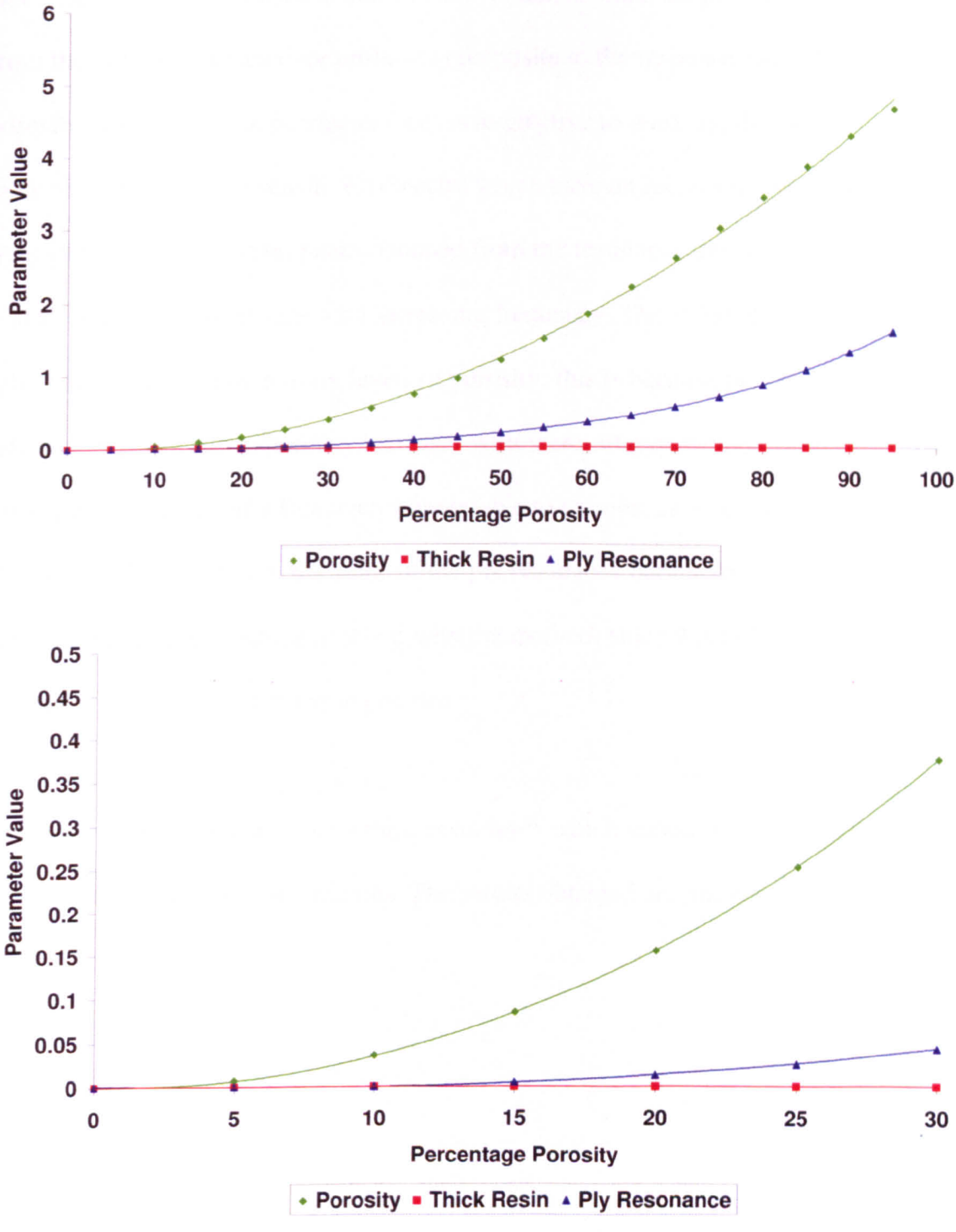

Figure 8.4 Variation of parameter values with increasing percentage porosity (top) and enhanced view for lower levels of porosity (bottom).

Figure 8.4 shows that the porosity parameter (green) rises steadily with increasing levels of porosity. The parameter is sensitive to porosity levels above 10%; this is expected

since the basis function used is that which is obtained when the porosity has moved from the normal resonance for unflawed composite to the response characteristic of porosity. The thick resin parameter (red) is insensitive to porosity; this is because the thick resin parameter is sensitive to spectra which have an increasing amplitude with frequency, but the resonant peaks obtained from the resonance due to porosity (figure 8.2) have constant amplitude with increasing frequency. The value of the ply resonance (blue) increases with increasing levels of porosity; this is because the amplitude of the subsequent peaks due to porosity increases with increasing percentage porosity. These subsequent peaks are of a frequency comparable to the normal resonance due to the plies (12 MHz) and hence, the value of the ply resonance parameter increases. This is not considered to represent a problem with the method, since it is unlikely that this parameter would be monitored in practice.

The process was repeated using a thick resin layer which varied from 2 microns (the nominal minimum) up to 40 microns. The results obtained are presented in figure 8.5.

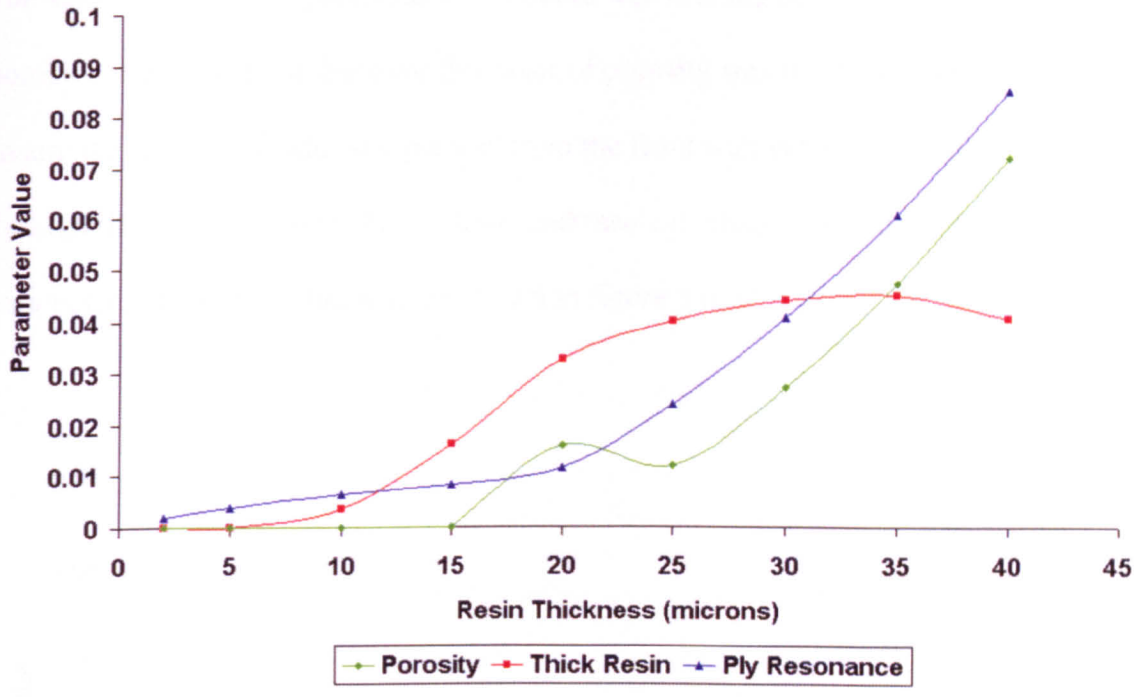

Figure 8.5 Variation of parameter values with increasing resin layer thickness.

From figure 8.5 we can see that the thick resin layer parameter (red) increases with increasing resin layer thickness until the resin thickness reaches 30 microns, then the value of the parameter begins to decrease. It is at this point that the approximation that the thick resin layer response is a straight line is no longer true, the resonant peak which is present due to the presence of the resin layer now moves into the bandwidth of the transducer. The porosity parameter (green) also increases with increasing resin layer thickness, although this is not thought to be significant for two reasons: First the numerical value of this increase is not of the same magnitude observed in the presence of porosity (0.07 at 40 micron resin thickness), and second, in the presence of porosity an increase in the thick resin layer parameter is not observed, making differentiation between the two defects trivial. Similarly the parameter which measures the ply resonance (blue) increases with increasing resin layer thickness.

The sensitivity to these parameters with depth was investigated by introducing a layer of porosity of 30% volume fraction; this layer of porosity was inserted at the 3rd ply (to ensure the response could be separated from the front wall echo) and then moved through the composite one ply at a time, and then calculating the value of the porosity parameter. The results obtained are shown in figure 8.6.

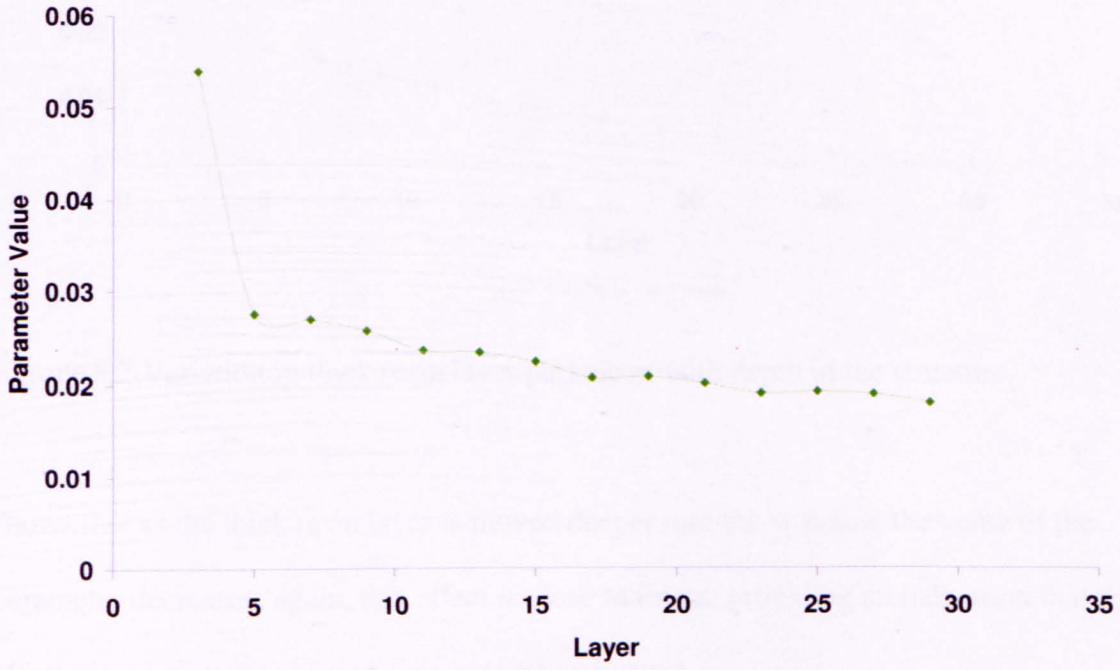

Figure 8.6 Variation in porosity parameter with depth in the structure.

Figure 8.6 shows that as the porosity is moved deeper into the structure the value of the parameter falls. The initial drop is due to interference with the front wall echo, which makes the porosity appear larger than it is. The fall in the value of the parameter after this point is approximately linear and provides an indication that this phenomenon may be corrected for. Similarly a thick resin layer of 20 microns was inserted into the structure and gradually moved through the depth. The value of the thick resin layer parameter was obtained and the results are shown in figure 8.7. The figure

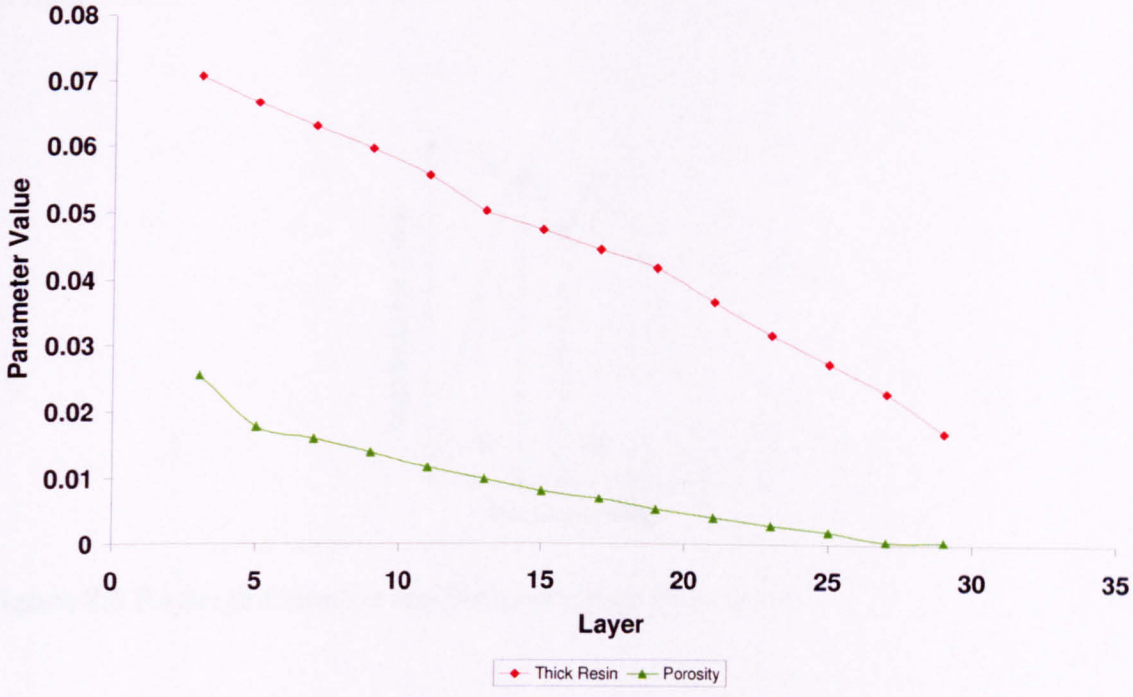

Figure 8.7 Variation in thick resin layer parameter with depth in the structure.

shows that as the thick resin layer is moved deeper into the structure the value of the parameter decreases; again, this effect is close to linear, providing an indication that this effect can be accounted for in a processing technique.

Another important factor which must be considered when examining the use of this technique is the depth resolution, that is to say the minimum distance in depth that defects must be separated by to be detectable. Combinations of defects were inserted into the modelled structure adjacent to one another; the distance between the defects was then increased and the Rayleigh Criterion applied to determine when the responses from the defects was significantly different to allow detection. The Rayleigh Criterion is based upon the assumption that two point sources are resolvable when the first diffraction minimum of one is at the maximum of another. In practice this is when the

ratio of the peak height to the trough height between the defects is 0.81, this is AB/CD in figure 8.8.

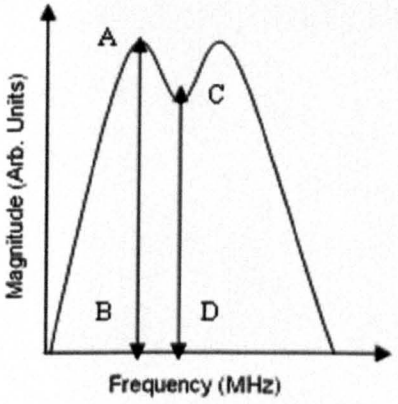

Figure 8.8 Rayleigh Criterion applied to an arbitrary function.

The defect combinations used were porosity-porosity, porosity-resin, resin-resin and resin porosity, and the defects used were 30% porosity and 20 micron thick resin layer. The minimum distances for detection obtained are shown in table 8.1.

Defect Combination	Minimum Distance (Plies)
Porosity-Porosity	1
Porosity-Resin	3
Resin-Resin	2
Resin-Porosity	3

Table 8.1 Minimum distance for detection for various defects.

Table 8.1 shows that by far the worst combination of defects is porosity followed by resin or vice versa. This is because there is a response obtained before and after the

porous layer from the thick resin parameter, and this interferes with the preceding or following thick resin layer. This is thought to be due to the "transition region" where the time gate is influenced by both the normal unflawed composite and the porous composite spectrum; this raises the amplitude of the porosity spectrum and may look like the response obtained from thick resin.

The defects were then separated by 5 plies and the percentage effect on the numerical value of the second parameter investigated. The results are presented in table 8.2.

Defect	Porosity Value	Thick Resin Value
Porosity-Porosity	-8%	N/A
Porosity-Resin	N/A	+10%
Resin-Resin	N/A	-5%
Resin-Porosity	+1%	N/A

Table 8.2 Variation of parameters with preceding defect.

Table 8.2 shows that the effect of a preceding defect is dependent both on the type of defect which occurs first in the depth as well as the nature of the defect which is greater in depth. Although the percentage difference that occurs in the value of the parameter if the preceding defect is porosity is relatively large it must be remembered that this is equivalent, for the defects used, to an error of -0.75% by volume porosity or + 2 microns resin layer thickness, which is numerically small and would be insignificant if the technique were to be used in the field.

To investigate the effect of multiple layers of defects and the response which would be obtained, multiple plies of porosity and multiple plies containing thick resin layers were simulated and the waveforms obtained examined. 1, 2, 3, 4, 5 and 6 plies of defects adjacent to each other were simulated using 30% porosity or alternatively 20 microns of thick resin. The results obtained for porosity are shown in figure 8.9.

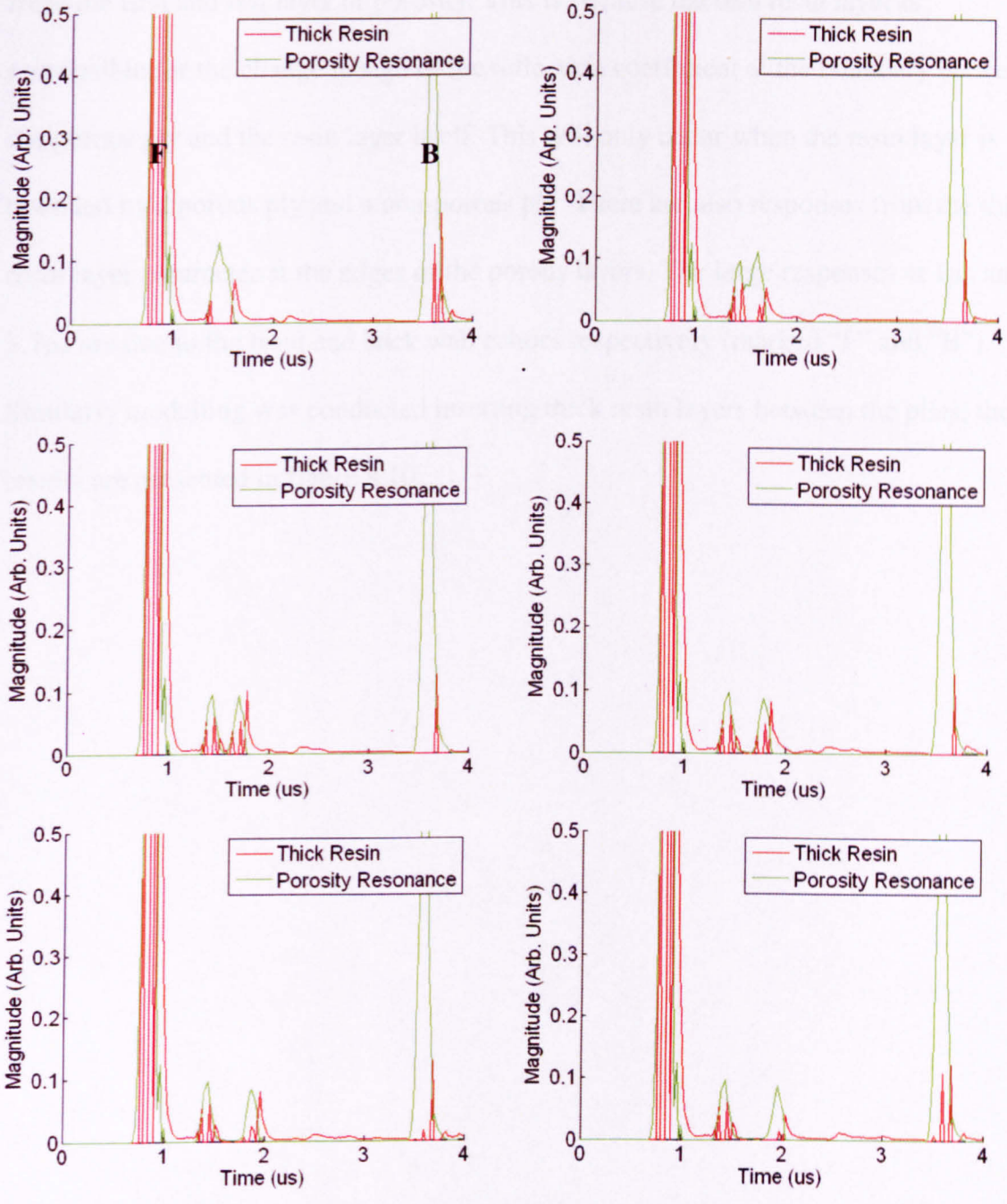

Figure 8.9 Parameter responses obtained for 1 layer of porosity (top left), 2 layers of porosity (top right), 3 layers of porosity (middle left), 4 layers of porosity (middle right), 5 layers of porosity (bottom left) and 6 layers of porosity (bottom right), showing front wall echo "F" and back wall echo "B".

Figure 8.9 shows that a response is obtained from the porosity parameter; initially this is one peak but as several layers of porosity are added this peak splits into two, one each

from the first and last layer of porosity. This is because the thin resin layer is responsible for the change in sign of the reflection coefficient at the boundary between the porous ply and the resin layer itself. This will only occur when the resin layer is bounded by a porous ply and a non-porous ply. There are also responses from the thick resin layer parameter at the edges of the porous layers. The large responses at 1μs and 3.7μs are due to the front and back wall echoes respectively (marked "F" and "B"). Similarly modelling was conducted inserting thick resin layers between the plies, the results are presented in figure 8.10.

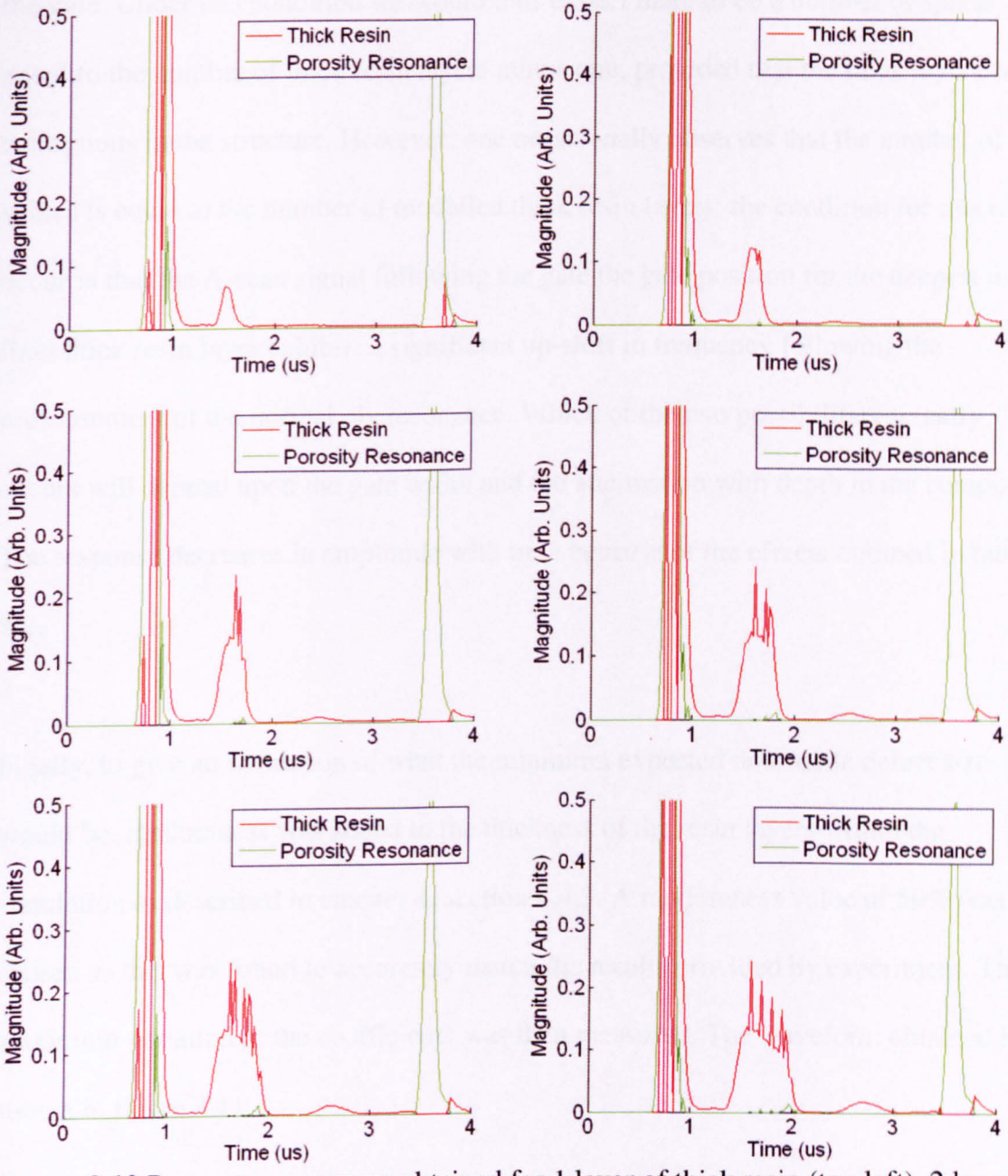

Figure 8.10 Parameter responses obtained for 1 layer of thick resin (top left), 2 layers of thick resin (top right), 3 layers of thick resin (middle left), 4 layers of thick resin (middle right), 5 layers of thick resin (bottom left) and 6 layers of thick resin (bottom right).

Figure 8.10 shows that as the number of thick resin layers increases so too does the width of the response. This is because each thick resin layer has a response which is detected by the time gate in turn. Superimposed on these broad peaks are "spike-like" features which occur when the gate covers the response from two resin layers; these occur due to constructive interference between reflections from the pair of layers within

the gate. Under this condition we would thus expect there to be a number of spikes equal to the number of thick resin layers minus one, provided that the thick layers were contiguous in the structure. However, one occasionally observes that the number of spikes is equal to the number of modelled thick resin layers; the condition for this to occur is that the A-scan signal following the gate the gate position for the deepest and final thick resin layer exhibits a significant up-shift in frequency following the reinstatement of the normal ply resonance. Which of the two possibilities actually occurs will depend upon the gate width and the attenuation with depth in the composite. The response decreases in amplitude with time because of the effects outlined in table 8.2.

Finally, to give an indication of what the minimum expected detectable defect size would be, randomness was added to the thickness of the resin layers within the simulation as described in chapter 4, section 4.4.3. A randomness value of 50% was chosen as this was found to accurately match the results provided by experiment. The maximum variation in the coefficients was then measured. The waveform obtained is shown in figure 8.11.

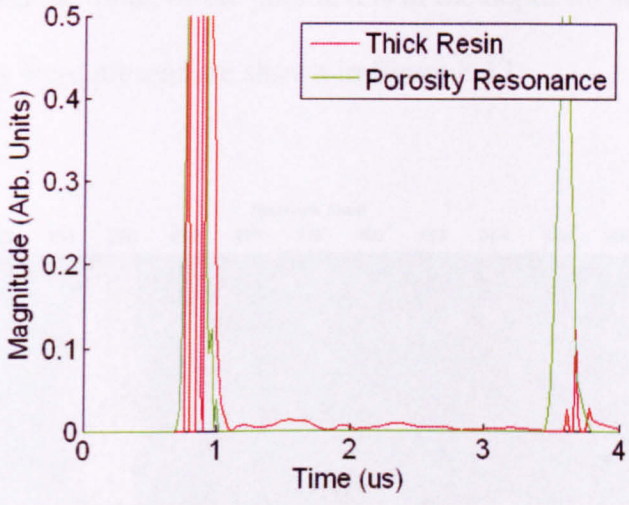

Figure 8.11 Parameter output for an unflawed composite, simulated with randomized layer thicknesses.

We can see from figure 8.11 that there is no variation in the porosity parameter, and as such we would expect the minimum detectable porosity volume fraction to be 10%. The peak value of the thick resin parameter is measured to be 0.013, which corresponds to a thick resin layer of 10 microns; above this level we could confidently say that the response is due to a resin layer which is thicker than the normal variation.

8.4 Performance using Experimental Data

To provide an indication of the performance of the method on data which better represents that which would be seen in reality, the method was applied to experimental data which had previously been analysed using the envelope analysis method (chapter 5, section 5.7). To provide comparisons, the output obtained from the thick resin layer parameter, or the porosity parameter, could be provided and then displayed in C-scan format. Sample 1 (Appendix E) was examined using the decomposition method and C-

scans which showed the value of the parameters at the depth for which the near surface glass microspheres were present are shown in figure 8.12.

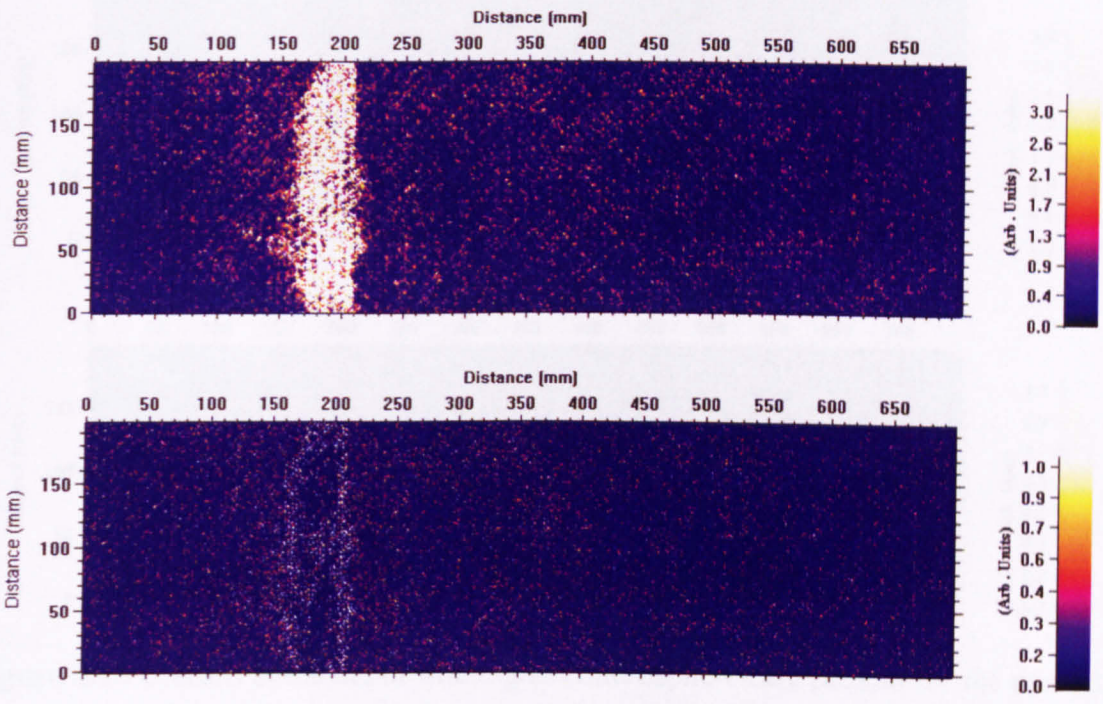

Figure 8.12 C-scans at the depth where glass microspheres are present for the porosity parameter (top) and the thick resin layer parameter (bottom) for Sample 1.

The figure shows a large response from the porosity parameter at the location of the glass microspheres, which run vertically across the panel between the points marked on the horizontal axis as 150 and 200mm. This response is highlighted by a light colour showing a strong response in the porosity parameter. The thick resin layer parameter at this point shows no response, however, around the edges of the region containing glass microspheres there is a response, highlighted in a light colour. This might be expected if the glass microspheres were larger than the nominal resin layer thickness and had introduced a thick resin layer at the edge of the region. Responses were obtained in a similar fashion for the region of glass microspheres which were deeper within the panel.

The results obtained from the porosity and the thick resin layer parameters are shown in figure 8.13.

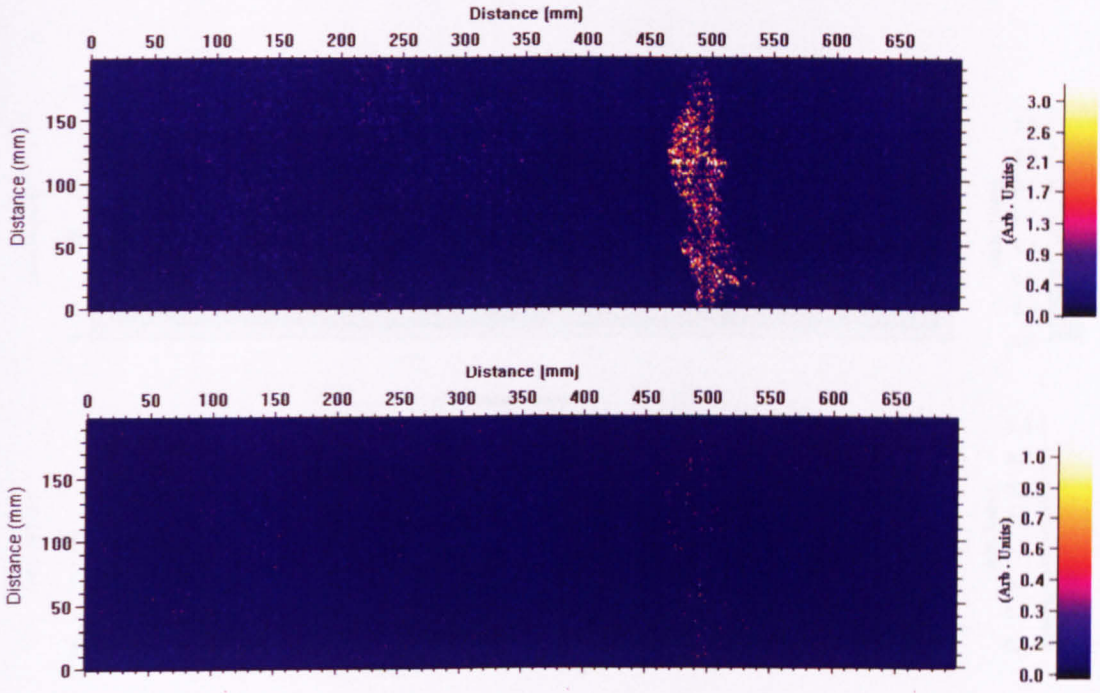

Figure 8.13 C-scans at the depth where glass microspheres are present for the porosity parameter (top) and the thick resin layer parameter (bottom) for Sample 1.

Figure 8.13 shows that again a strong response is obtained from the porosity parameter in the region where the glass microspheres are present; this is highlighted by lighter colours. The colours are not as bright as those observed in figure 8.11; this is due to the depth dependence of the porosity parameter and highlights the need for alterations to the method to remove this depth dependence. The thick resin layer response shows no significant changes in the parameter value at this depth, again highlighting the insensitivity of this parameter to the presence of porosity.

Sample 2 (Appendix E) was analysed in a similar fashion. The panel contained 8 plies per mm and was 4mm thick; there was a concentration of porosity and large voids at the right hand side of the panel. A depth was selected which contained various void defect

types. The C-scans obtained at this depth for the porosity parameter and the thick resin layer parameter are shown in figure 8.14.

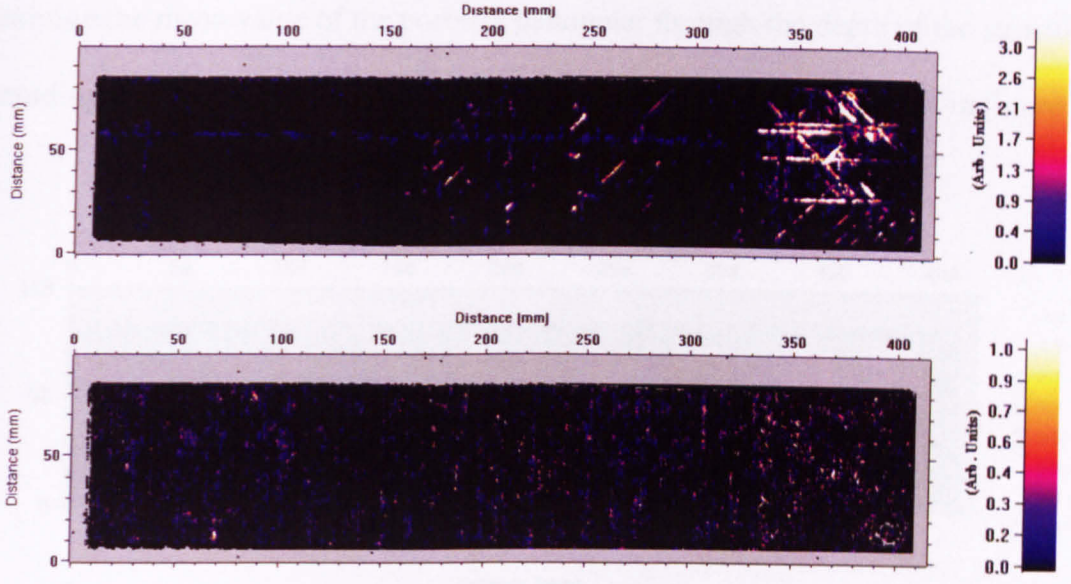

Figure 8.14 C-scans at the depth where porosity is present for the porosity parameter (top) and the thick resin layer parameter (bottom) for Sample 2.

Figure 8.14 shows that there is a strong response for the porosity parameter at this depth, the light colours represent the presence of porosity. It can be seen that there is a region of voids between 325 and 400mm on the horizontal axis. These voids run parallel to the direction of the fibres. There are also present regions of isolated porosity represented by a slight increase in the brightness of the colour. The thick resin layer parameter also shows responses running parallel to the direction of the fibres, and this would be expected since there is a small increase in the thick resin layer between fibres. This effect has been observed previously by Hsu et al (2002) and Smith et al (1994) and forms the basis of a method to determine fibre orientation. A comparison was made between the porosity parameter and the back wall echo, the purpose of which was to examine the effectiveness of the decomposition method for the detection of porosity.

We would expect the back wall echo to decrease in amplitude in the regions where porosity is present based upon the investigation conducted in chapter 5, section 5.9. To obtain a basis for comparison a projection was taken through the time gates, effectively obtaining the mean value of the porosity parameter through the depth of the structure, excluding the front and back wall echoes. The results obtained are shown in figure 8.15.

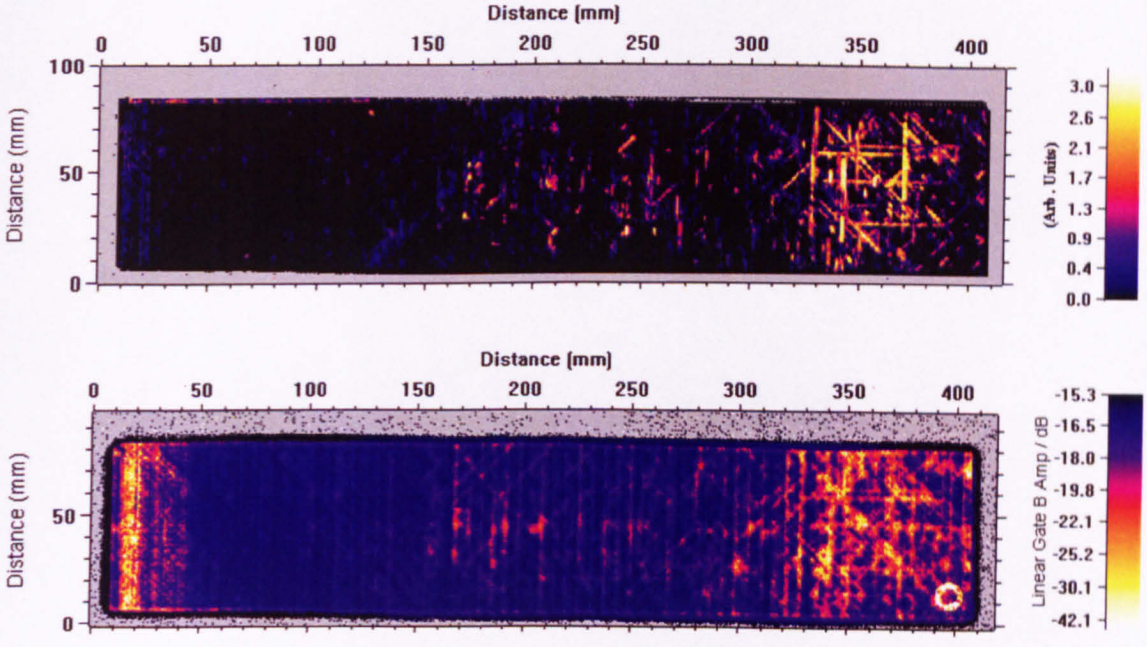

Figure 8.15 A comparison of C-scans between the mean value of the porosity parameter (top) and the back wall echo amplitude (bottom) for Sample 2.

From figure 8.15 we can see that there is good agreement between the results obtained from the porosity parameter and the back wall echo amplitude methods of detecting porosity. The regions of greatest density of defect (300-410mm on the horizontal axis) are both identified as having defects, the shape and structure of the response from these regions is in good agreement. The remaining defect regions are also similar in size and structure.

Finally, Sample 3, which contained thick resin layers as well as porosity was examined using the decomposition method. A depth which had been subject to previous investigations, and was of particular interest since there were present a variety of defect types, was examined using the method. The porosity parameter and the thick resin layer parameter responses were analysed and the results are shown in figure 8.16.

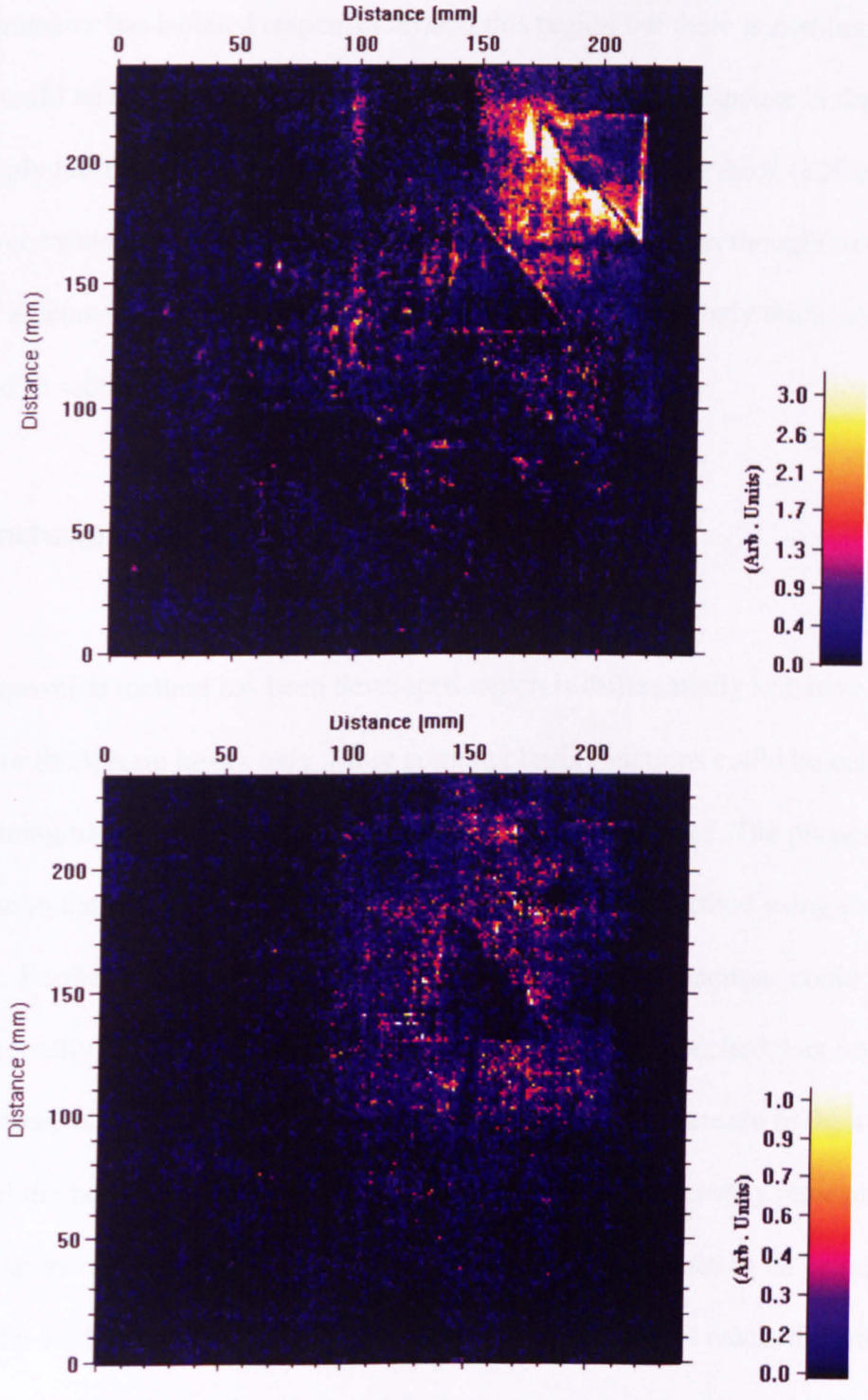

Figure 8.16 A comparison of C-scans between the mean value of the porosity parameter (top) and the thick resin parameter (bottom) for a panel containing thick resin layers and porosity for Sample 3.

Figure 8.16 shows that there is a strong response obtained from the porosity parameter on the edge of the area where a region of the ply has been removed. The thick resin

layer parameter has isolated responses around this region but there is nothing present which would be confused with porosity. However, there is no response in the region where a ply has been removed although it was known that a very thick (125 microns) resin layer existed there. The reason for this lack of response was thought to be the result of a decrease in thick resin parameter sensitivity for extremely thick layers, as discussed in section 8.2 and shown in figures 8.3 and 8.5.

8.5 Conclusions

A decomposition method has been developed which is differentially sensitive to porosity or thick resin layers only. More complex basis functions could be defined using real and imaginary parts or modelled data could be used if desired. The purpose of the discussion in the chapter is to illustrate the functioning of the method using simple functions. Further investigations of these more complex basis functions could improve the functionality of this method. Testing of this method with modelled data revealed that these parameters vary according to the type of the defect. An increase in the volume fraction of the porosity leads to an increase in the value of the porosity parameter, and similarly an increase in the thickness of the thick resin layer results in an increase in the value of the thick resin layer parameter until a maximum value is reached. Both of the parameters are sensitive to the depth within the structure and as such require development of a method to remove the depth dependence. There is a minimum distance which must be present between defects to allow successful detection, and this is thought to be a result of the choice of gate width; further investigations in this area should enable an optimum time gate width to be established. The presence of multiple defects leads to an over or underestimation of the size of the defect; however, modelling

has revealed whether the defect will be over or underestimated in size, as well as showing that the defect type can still be successfully identified. Examination of the performance of the method with experimental data has shown that the method performs as expected and is able to identify porosity and thick resin layers successfully. Further work is required to calibrate this method and remove the depth dependence.

Chapter 9

Discussion, Further Work and Conclusions

9.1 Discussion

This thesis began by reviewing earlier work which had been done to detect and quantify defects in composite structures. Two defects, porosity and fibre-resin effects, were identified, both of which have a critical impact on the structural integrity of the component. Historically, the detection of either or both of these has proven to be at best difficult and at worst impossible. The current industrial technique used to detect porosity is based on through-thickness attenuation measurements. Calibration curves produced from test samples of known porosity content have enabled the detected porosity to be quantified. The method does not enable the location of the porosity to be determined with respect to depth in the composite sample. With the advent of increased usage of composite structures in the aerospace industry there has been a drive to produce better methods to detect; characterize and locate porosity. The most recent work in this area has led to advances in the field aimed at producing three dimensional maps of porosity. Fibre resin effects, for example an increase in fibre volume fraction, have not received as much attention, probably due to difficulty in detection. The aim of this thesis was to advance these techniques by providing the means to detect both types of defect in three dimensions. It was important to be able to differentiate between the two types of defect.

In support of these aims the comprehensive modelling package, *MLM-Propmat* was developed. The package was necessary because of the cost and difficulty associated

with producing large numbers of experimental samples with known defects which were well characterised. A well-established scattering model was incorporated into a multi-layer wave propagation model to produce a package which could simulate the presence of a defect at an arbitrary position and with known properties (i.e. scatterer size and concentration). The package which was produced had significant advantages over similar modelling packages which are commercially available for example CIVA (CEDRAT, France). *MLM-Propmat* has the advantage of being a cheaper alternative to CIVA; it also requires less specialist knowledge to run, completes computations far faster and is able to compute the reflections from multiple layers and the resonance systems the presence of multiple layers introduces. An arbitrary number of layers could be simulated and since the complete propagation path was modelled, the resonances between plies in the composite structure could be analysed. This model was based on the use of simple mixture rules to determine material properties such as density and ultrasonic velocity. This was of significant benefit in the early stages of this work, allowing a large number of experimental situations to be analysed at great speed. Future work in this area could well further examine the use of more comprehensive mixture rules to model the local composite structure. Appendix B has been added to show the equivalences or otherwise between the simple mixture rules used for the body of this work and the more comprehensive formulations. Before this work, the scientific literature had concentrated on modelling the composite structure as one homogenous volume. The consequences of incorporating defects such as porosity or anomalous resin layers into a multiple layer formulation do not appear to have been addressed previously.

A toolset was developed which the allows detection and analysis of defects; it incorporated four main components:

- Envelope Analysis
- Short-Gate Time Frequency Analysis
- Long-Gate Time Frequency Analysis
- Decomposition Methods

With these methods, the means to detect and quantify the presence of porosity in three dimensions has been made available for the first time. Using the envelope analysis methods it is possible to detect the presence of anomalies within the envelope amplitude. This method is particularly useful for providing three dimensional images of large defects such as delaminations, but also allows the detection smaller defects such as porosity and a thickening of the resin layer between two adjacent plies. A significant disadvantage of the method is that it cannot differentiate between the two types of defect. Differentiation between large defects and small defects was easily achieved, and a system was developed which used a non-linear colour palette scale that readily identified this difference to an operator. As a result of the development of this method it was realised that porosity and thick resin layers, whilst having a similar response when viewed in an A-scan, had different responses in the frequency domain.

Analysis of the effect of the presence of porosity and thick resin layers was done using time-frequency analysis. It was found that for porosity there was an apparent decrease in the resonant frequency which would be measured by an algorithm, although modelling would show that this was due to the frequency response of the transducer and in fact an

increase in the frequency of the resonant peaks is observed. An increase in the bandwidth of the signal is observed when porosity is present, and this is due to transition regions, where the interrogating time gate is receiving a response from both flawed and unflawed composite. A slight decrease in the frequency of the resonant peaks is observed for the presence of a thick resin layer. These observations led to the development of three methods based upon time-frequency analysis of the A-scan signal using a short time gate:

- Resonant Frequency Analysis
- Bandwidth Analysis
- Frequency Magnitude Ratio

All three of these methods enabled the nature of a detected defect to be determined, be it a delamination, porosity or a thick resin layer. The methods showed that there is significant information contained within the frequency response from a short time gate of the A-scan response. Variation in the responses from these methods was observed, and was found to be due to inherent randomness in the structure of the ply and resin layers, the thickness of which was variable over a limited range.

A comprehensive study was conducted of the time-frequency response from a long time gate applied to from an A-scan signal. It was found that the form of the frequency response was dependent upon the nature of the defect which was present in the structure under investigation. Further analysis showed that the form of this spectrum is dependent upon the contribution from individual elements, namely:

- Natural Resonance due to Plies
- Natural Resonance due to Resin Layers
- Resonance Due to Porosity
- Resonance Due to Thick Resin Layers

It was found that the ply resonance could be removed using an appropriate filter, the resin layer resonance was found to be at high frequency and outside of the range of interest. The resonance due to porosity and the resonance due to a thick resin layer could be isolated, but location in three dimensions was not possible due to the length of the time gate. The observation that there are contributions to the spectrum due to many different sources and that these contributions can be regarded as interacting additively is significant.

A method based upon decomposing the spectrum into its constituent parts as identified by the long time gate analysis was proposed. To test this method, approximations were made to the form of these contributions to the spectrum. Testing of this method, using a short time gate to collect the data, showed that these approximations were sufficient to allow the detection and quantification of different types of defect, and differentiation between them. It is significant that the parameters remained independent, and reacted only to the defect type for which they were designed.

9.2 Suggestions for Further Work

The work presented in this thesis has generally been a first observation of phenomena which have previously been unknown or uncharacterised. Further work is therefore

necessary to confirm and develop many of the observations. The decomposition method has thus far shown most promise and work in this area is liable to lead to significant advances in the ability to detect and characterise defects in the field. In particular, further comparisons with experimental samples with known defects will help prove and advance this technology. Work is currently underway at QinetiQ (Farnborough, UK) to develop and test the decomposition methodology and parallel trials will soon be implemented at Airbus and their suppliers.

The technical equipment used to gather data suitable for processing by the methods developed in this thesis is already at a stage where the methods may be used in practice. Indeed, many systems in use in industry have the ability to gather full waveform data and conduct post-processing but many operators use their equipment with this functionality switched off!

The later observations on the validity of the simple mixture rule and more comprehensive formulations have led to questions about how the elastic properties of the composite structure is best modelled. It would make sense, therefore, to carry out a more comprehensive study of the many mixture rules that *could* be incorporated into wave propagation models. Some such work is on-going – R.A. Smith at QinetiQ is studying the formulation of elasticity *per se* and Challis and Pinfield (University of Nottingham) are considering how to incorporate diffraction effects into multi-layer formulations.

9.3 Conclusions

With the recent increase in usage of composite structures in the aerospace industries there has been an increased drive to better characterize defects in components. This thesis has provided a new insight into the structure of the A-scan which is obtained from ultrasonic interrogation of the structure. Namely, that defects which from first sight appear similar in an A-scan have radically differing frequency responses in pulse-echo. A comprehensive tool set has been developed which allows modelling of the ultrasonic response from a defect. This was used to determine how the frequency structure changes dependent on defect presence and nature. From this work, methods were developed which have allowed the location in three dimensions of defects and identification of defect type and morphology, at a scale thought previously to be impossible. Although further work is necessary to validate this system for use in industry, and have it applied to safety critical structures, these first observations of resonance phenomena provide a firm and sufficient basis for further development.

Appendix A

Matrices from Chapter 3

Equations from chapter 3.

Matrix from equation 3.8.

$$
[M]_{EC} \equiv
\begin{bmatrix}
a_c\, h_n'(a_c) & -n(n+1)\, h_n(a_s) & -a_c'\, j_n'(a_c') & n(n+1) j_n(a_s') & a_T\, h_n'(a_T) & -a_T' j_n'(a_T') \\
h_n(a_c) & -[h_n(a_s) + a_s\, h_n'(a_s)] & -j_n(a_c') & j_n(a_s') + a_s' j_n'(a_s') & h_n(a_T) & -j_n(a_T') \\
\eta[a_s^2 h_n(a_c) - & \eta 2n(n+1)[a_s\, h_n'(a_s) & -\eta'[a_s'^2 j_n(a_c') & -2\eta' n(n+1)[& \eta[M a_s^2 h_n(a_T) & -\eta'[M \\
2a_c^2 h_n''(a_c)] & -h_n(a_s)] & -2a_c'^2 j_n''(a_c')] & a_s' j_n'(a_s') - j_n(a_s')] & -2a_T^2 h_n''(a_T)] & a_s'^2 j_n(a_T') \\
 & & & & & -2a_T'^2 j_n''(a_T')] \\
\eta[a_c\, h_n'(a_c) & -\frac{\eta}{2}[a_s^2 h_n''(a_s) + & -\eta'[a_c' j_n'(a_c') & \frac{\eta'}{2}[a_s'^2 j_n''(a_s') + & \eta[a_T\, h_n'(a_T) & -\eta'[a_T' j_n'(a_T') \\
-h_n(a_c)] & (n^2+n-2)\, h_n(a_s)] & -j_n(a_c')] & (n^2+n-2) j_n(a_s')] & -h_n(a_T)] & -j_n(a_T')] \\
g\, h_n(a_c) & 0 & -g' j_n(a_c') & 0 & G h_n(a_T) & -G' j_n(a_T') \\
\kappa g a_c\, h_n'(a_c) & 0 & -\kappa' g' a_c' j_n'(a_c') & 0 & \kappa G a_T\, h_n'(a_T) & -\kappa' G' a_T' j_n'(a_T')
\end{bmatrix}
$$

Matrix from equation 3.11.

$$
[M]_{MT} \equiv
\begin{bmatrix}
a_c\, h_n'(a_c) & -n(n+1)\, h_n(a_s) & i\omega\, a_c j_n'(a_c') & -i\omega n(n+1) j_n(a_s') & a_T\, h_n'(a_T) & i\omega\, a_T j_n'(a_T') \\
h_n(a_c) & -[h_n(a_s) + a_s\, h_n'(a_s)] & i\omega j_n(a_c') & -i\omega[j_n(a_s') + a_s j_n'(a_s')] & h_n(a_T) & i\omega j_n(a_T') \\
\eta[(a_c^2 - 2a_c^2)\, h_n(a_c) & \eta 2n(n+1)[a_s\, h_n'(a_s) & -[(\omega^2 \rho' R^2 - 2\mu' a_c'^2) & -2\mu' n(n+1)[& \eta[(a_T^2 - 2a_T^2)\, h_n(a_T) & -[(\omega^2 \rho' R^2 - 2\mu' a_T'^2) \\
-2a_c^2\, h_n''(a_c)] & - h_n(a_s)] & j_n(a_c') - 2\mu' a_c'^2 j_n''(a_c')] & a_s' j_n'(a_s') - j_n(a_s')] & -2a_T^2 h_n''(a_T)] & j_n(a_T') - 2\mu' a_T'^2 j_n''(a_T')] \\
\eta[a_c\, h_n'(a_c) & -\frac{\eta}{2}[a_s^2\, h_n''(a_s) + & -\mu'[a_c' j_n'(a_c') & \frac{\mu'}{2}[a_s'^2\, j_n''(a_s') + & \eta[a_T\, h_n'(a_T) & -\mu'[a_T' j_n'(a_T') \\
- h_n(a_c)] & (n^2 + n - 2)\, h_n(a_s)] & - j_n(a_c')] & (n^2 + n - 2) j_n(a_s')] & - h_n(a_T)] & - j_n(a_T')] \\
b_c\, h_n(a_c) & 0 & i\omega\, b_c' j_n(a_c') & 0 & b_T\, h_n(a_T) & i\omega b_T' j_n(a_T') \\
\kappa b_c\, a_c\, h_n'(a_c) & 0 & i\omega\, \kappa' b_c'\, a_c' j_n'(a_c') & 0 & \kappa b_T\, a_T\, h_n'(a_T) & i\omega\, \kappa' b_T'\, a_T'\, j_n'(a_T')
\end{bmatrix}
$$

Matrix from equation 3.12.

$$
[M]_{XT} \equiv \begin{bmatrix}
a_c\, h_{n+1}(a_c) & n a_c\, h_{n+1}(a_c) & -a_c'\, j_{n+1}(a_c') & -n a_c'\, j_{n+1}(a_c') \\
h_n(a_c) & -[(n+1)h_n(a_c) - a_c\, h_{n+1}(a_c)] & -j_n(a_c') & (n+1)j_n(a_c') - a_c' j_{n+1}(a_c') \\
\mu[a_c^2\, h_n(a_c) - 2(n+2)\, a_c\, h_{n+1}(a_c)] & \mu\, n[a_c^2\, h_n(a_c) - 2(n+2)\, a_c\, h_{n+1}(a_c)] & -\mu'[a_c'^2\, j_n(a_c') - 2(n+2) a_c' j_{n+1}(a_c')] & -\mu' n[a_c'^2\, j_n(a_c') - 2(n+2) a_c'\, j_{n+1}(a_c')] \\
\mu[(n-1)h_n(a_c) - a_c\, h_{n+1}(a_c)] & -\mu[(n^2 - 1 - \frac{a_c^2}{2})h_n(a_c) + a_c\, h_{n+1}(a_c)] & -\mu'[(n-1)a_c' j_n'(a_c') - a_c' j_{n+1}(a_c')] & -\mu'[(n^2 - 1 - \frac{a_c'^2}{2}) j_n(a_c) + a_c'\, j_{n+1}(a_c')]
\end{bmatrix}
$$

Matrix $[\mathrm{M}]_{AH1}$.

$$
[M]_{AH1} \equiv
\begin{bmatrix}
a_c\, h_n(a_c) & -n\,(n+1)\, h_n(a_s) & i\omega\, a_c'\, j_n'(a_c') & -i\omega n(n+1) j_n(a_s') & a_T h_n(a_T) & i\omega\, a_T' j_n'(a_T') \\
h_n(a_c) & -\left[h_n(a_s) + a_s\, h_n'(a_s)\right] & i\omega j_n(a_c') & -i\omega\left[j_n(a_s') + a_s' j_n'(a_s')\right] & h_n(a_T) & i\omega j_n(a_T') \\
\eta\left[(a_s^2 - 2a_c^2)\, h_n(a_c)\right. & \eta 2n(n+1)\left[\right. & i\omega\eta'\left[(a_s'^2 - 2a_c'^2)\right. & i\omega 2\eta' n\,(n+1)\left[\right. & \eta\left[(a_s^2 - 2a_T^2) h_n(a_T)\right. & i\omega\eta'\left[(a_s'^2 - 2a_T'^2)\right. \\
-2a_c^2\, h_n''(a_c)\right] & a_s\, h_n'(a_s) - h_n(a_s)\right] & j_n(a_c') - 2a_c'^2 j_n''(a_c')\right] & a_s' j_n'(a_s') - j_n(a_s')\right] & -2a_T^2 h_n''(a_T)\right] & j_n(a_T') - 2a_T'^2 j_n''(a_T')\right] \\
\eta\left[a_c\, h_n'(a_c)\right. & -\frac{\eta}{2}\left[a_s^2\, h_n''(a_s) + \right. & i\omega\eta'\left[a_c'\, j_n'(a_c')\right. & -i\omega\frac{\eta'}{2}\left[a_s'^2\, j_n''(a_s') + \right. & \eta\left[a_T h_n'(a_T)\right. & i\omega\eta'\left[a_T' j_n'(a_T')\right. \\
-h_n(a_c)\right] & \left.(n^2 + n - 2)\, h_n(a_s)\right] & -j_n(a_c')\right] & \left.(n^2 + n - 2) j_n(a_s')\right] & -h_n(a_T)\right] & -j_n(a_T')\right] \\
b_c\, h_n(a_c) & 0 & i\omega b_c' j_n(a_c') & 0 & b_T h_n(a_T) & i\omega b_T' j_n(a_T') \\
\kappa\, b_c\, a_c\, h_n'(a_c) & 0 & i\omega\kappa' b_c'\, a_c' j_n'(a_c') & 0 & \kappa\, b_T\, a_T\, h_n'(a_T) & i\omega\kappa' b_T'\, a_T' j_n'(a_T')
\end{bmatrix}
$$

Matrix $[\mathrm{M}]_{AH2}$.

$$
[M]_{AH2} \equiv
\begin{bmatrix}
a_c\, h_n'(a_c) & -n\,(n+1)\, h_n(a_s) & i\omega\, a_c'\, j_n'(a_c') & -i\omega n\,(n+1) j_n(a_s') \\
h_n(a_c) & -\left[h_n(a_s) + a_s\, h_n'(a_s)\right] & i\omega j_n(a_c') & -i\omega j_n(a_s') + a_s' j_n'(a_s') \\
\mu\left[(a_s^2 - 2a_c^2)\, h_n(a_c) - 2a_c^2\, h_n''(a_c)\right] & \mu 2n(n+1)\left[a_s\, h_n'(a_s) - h_n(a_s)\right] & i\omega\mu'\left[(a_s'^2 - 2a_c'^2) j_n(a_c') - 2a_c'^2 j_n''(a_c')\right] & i\omega 2\mu' n\,(n+1)\left[a_s' j_n'(a_s') - j_n(a_s')\right] \\
\mu\left[a_c\, h_n'(a_c) - h_n(a_c)\right] & -\frac{\mu}{2}\left[a_s^2\, h_n''(a_s) + (n^2+n-2)\, h_n(a_s)\right] & i\omega\mu'\left[a_c'\, j_n'(a_c') - j_n(a_c')\right] & -i\omega\frac{\mu'}{2}\left[a_s'^2 j_n''(a_s') - (n^2+n-2) j_n(a_s')\right]
\end{bmatrix}
$$

Appendix B

Equivalent Media for Modelling - Perspectives

B.1 Introduction

We have seen in chapter 4 that simplified mixture rules were shown to provide realistic modelling results, but they were not justified in a formal sense. As the work of this thesis developed, more complex mixture rules came to light. It is the purpose of this Appendix to consider these more complex formulations and to compare the results obtained with the *MLM-Propmat* model using these for results obtained from the simple rules.

B.2 Equivalent Medium Model

We require a model which could have as its input the most basic elastic constants (Young's modulus, E, and Poisson's ratio υ) or alternatively if such data were available more comprehensive elastic constants C_{ij} for the constituent materials, in addition to their densities. The outputs of the model are to be wave speeds as functions of the concentrations of the constituent materials, including porosity where appropriate, or alternatively the effective elastic constants as functions of fibre volume fraction and porosity volume fraction.

Martin (1977) used mixture theory to derive the effective elastic moduli and the effective density of a composite containing both fibres and voids; the effects of

spherical void content in resin were incorporated using equations given by Hashin (1962), giving for low porosity volume fraction ($\phi_v \leq 0.1$) a bulk modulus defined by:

$$K = K_o\left[1-\frac{3(1-\upsilon_0)}{2(1-2\upsilon_o)}\phi_v\right] \tag{B.1}$$

where υ is Poisson's ratio and the zero subscripts indicate void-free values. For the shear modulus,

$$G = G_o\left[1-\frac{15(1-\upsilon_o)}{(7-5\upsilon_o)}\phi_v\right] \tag{B.2}$$

for a porosity volume fraction given by,

$$\phi_v = 1-\frac{\rho}{\rho_0} \tag{B.3}$$

where ρ_c is the effective density of the material and ρ_0 is the density of the void free composite. The effective elastic modulus of the mixture is then given by,

$$E = \frac{9KG}{3K+G} \tag{B.4}$$

and the Poisson's ratio is given by,

$$\nu_r = \frac{E - 2G}{2G} \tag{B.5}$$

The validity of this formulation when extended to larger void concentrations is examined further in section B.3.1. Martin then used earlier results from Smith (1972) concerning the mixture of anisotropic fibres to combine these results with the effect of fibres. The principal elastic constants of the resin containing voids are calculated from:

$$C_{11} = E\left(\frac{1-\nu_r}{(1+\nu_r)(1-2\nu_r)}\right) \tag{B.6}$$

$$C_{12} = E\left(\frac{\nu_r}{(1+\nu_r)(1+2\nu_r)}\right) \tag{B.7}$$

$$C_{13} = C_{12} \tag{B.8}$$

$$C_{44} = \frac{1}{2}(C_{11} - C_{12}) \tag{B.9}$$

Where the subscript 1 denotes the fibre direction and the subscript 2 is transverse with respect to direction of fibres and the subscript 3 is normal to the 2 direction. Expressions for composite elastic constants after the addition of fibres were provided for all axis directions. However, of interest here is the constant for C_{11}^c, that is, perpendicular to the direction of the fibres.

$$C_{11}^{c} = \frac{1}{2}\left[C_{11} + C_{12} + \left(C_{11}^{(f)} + C_{12}^{(f)} - C_{11} - C_{12}\right)\phi_f\right]$$

$$-\frac{1}{2}\left[\frac{\left(C_{11}^{(f)} + C_{12}^{(f)} - C_{11} - C_{12}\right)^2 \phi_f\left(1-\phi_f\right)}{\left(C_{11}^{(f)} + C_{12}^{(f)}\right)\left(1-\phi_f\right) + \left(C_{11} + C_{12}\right)\phi_f + 2C_{44}}\right] + C_{44}\left(\frac{1+\varepsilon\eta\phi_f}{1-\eta\phi_f}\right) \qquad \textbf{(B.10)}$$

$C^{(f)}$ are the principal elastic constants related to the fibre properties, ϕ_f is the volume fraction of fibres, ε is the "reinforcing factor" dependent on the matrix and η is given by:

$$\eta = \frac{C_{66}^{(f)} - C_{44}}{C_{66}^{(f)} + \varepsilon C_{44}} \qquad \textbf{(B.11)}$$

where,

$$C_{66}^{(f)} = \frac{1}{2}\left(C_{11}^{(f)} - C_{12}^{(f)}\right) \qquad \textbf{(B.12)}$$

From these results the elastic constants may be used to calculate the wave velocities, following Zimmer and Cost (1970), for compression waves normal to the fibres.

$$V_{L1} = \sqrt{\frac{C_{11}^{c}}{\rho_c}} \qquad \textbf{(B.13)}$$

The effective density ρ_c of the material was proposed to be,

$$\rho_c = \phi_f \rho_f + (1-\phi_f)\rho_r \qquad \textbf{(B.14)}$$

Martin made comparisons between results obtained for compression and shear wave velocities using this model and experimental data from the earlier results of Stone and Clarke (1975). It was found that the velocities of the waves increased with increasing fibre volume fraction; for an increase in fibre volume from 0.5 to 0.6 led to an increase in velocity of 1% which compared well with the results of Stone and Clarke.
The assumptions of this model are as follows: (i) that both constituent materials obey Hooke's law; (ii) the fibres are circular, uniform in shape and arranged in a pre described array; (iii) there are no voids or other irregularities; (iv) both materials are homogenous, isotropic and firmly bonded together.

In order to allow comparisons between the simple mixture rule provided in chapter 4, section 4.4.1 and this more comprehensive formulation, the results of Martin were incorporated into a computer program using Matlab®. The implementation allowed an arbitrary void volume fraction ϕ_v to be included into the resin and gave as an output the variation in velocity with increasing fibre volume fraction ϕ_f. By use of the material data provided by Martin the variation in compression wave velocity perpendicular to the fibres with increasing fibre volume fraction were computed, the results obtained from this implementation were consistent with those originally obtained by Martin.

B.3 Comparison between Simple Mixture Rule and Comprehensive Formulation

B.3.1 Definition of a Mixture Rule for an Arbitrary Void Volume Fraction

In order to compare the variation in compression wave velocity given by the comprehensive formulation provided by Martin with the simple mixture rule outlined in chapter 4, section 4.4.1, it was necessary to make modifications to allow for larger void volume fractions ($\phi_v \geq 0.1$). The limitation of the method outlined by Martin is the small concentration approximation provided by Hashin (1962). However, Hashin also provides a formulation for large concentrations. For large concentrations of voids the bulk modulus is given by:

$$K = K_p \left[1 - \frac{\left(1 - \frac{K_r}{K_p}\right)\left[2(1-2\upsilon_0) + (1+\upsilon_0)\frac{K_p}{K_r}\right]}{3(1-\upsilon_0)} \phi_p' \right] \qquad \textbf{(B.15)}$$

Where ϕ_p' is,

$$\phi_p' = 1 - \phi_p \qquad \textbf{(B.16)}$$

Similarly for the shear modulus,

$$G = G_p\left[1 - \frac{\left(1-\frac{G_r}{G_p}\right)\left[(7-5\upsilon_0)+2(4-5\upsilon_0)\frac{G_p}{G_r}\right]}{15(1-\upsilon_0)}\phi_p'\right] \quad \textbf{(B.17)}$$

The effective elastic modulus E and Poisson's ratio ν can then be calculated as shown in equations B.4 and B.5. The effective compression wave modulus M of the resin system with increasing void volume fractions can then be produced using the relation,

$$M = K^* + \frac{4}{3}G^* \quad \textbf{(B.18)}$$

as shown in figure B.1.

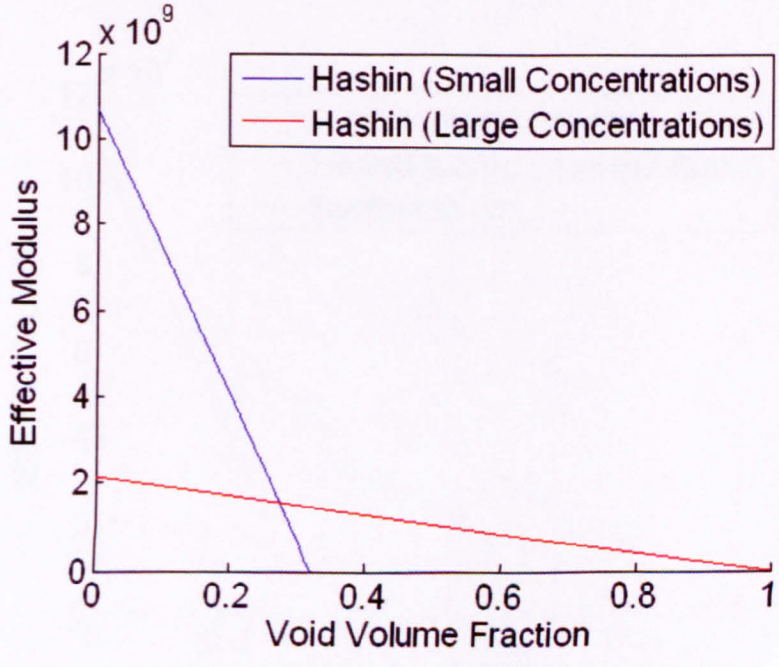

Figure B.1 Effective compression wave modulus defined by Hashin's approximations for small and large concentrations of voids.

The lines which are drawn for small and large concentrations are tangents to a curve which defines the variation of the modulus with void volume fraction. Having obtained these lines it is possible to define this curve as a quadratic Bézier curve. To produce a Bézier curve we define three points: P_0 is the value of the small concentration line at a void volume fraction of 0, P_1 is the intersection of the small and large concentration lines and finally P_2 the large concentration line at a void volume fraction of 1. The Bézier curve is then defined thus,

$$B(\phi_f) = (1-\phi_f)^2 P_0 + 2\phi_f (1-\phi_f) P_1 + \phi_f{}^2 P_2 \qquad \textbf{(B.19)}$$

Figure B.2 shows the Bézier curve produced when evaluating the small and large concentration results shown in figure B.1.

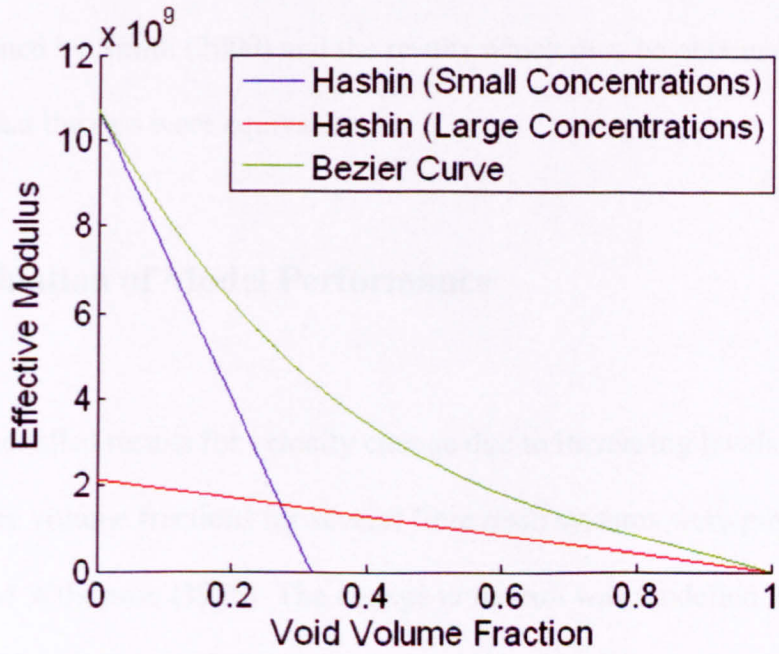

Figure B.2 Effective compression wave modulus defined by Hashin's approximations for small and large concentrations of voids and the Bézier curve produced highlighting the relationship between the two.

The modulus defined by the Bézier curve may be used as an input to the anisotropic mixture rules provided by Smith (1972) as implemented by Martin. For the purposes of comparison with the simple mixture rule defined in chapter 4, section 4.4.1 both the small concentration approximation defined by Hashin and the Bézier curve defining the behaviour of the modulus at all void volume fractions will be used. This is in order to allow analysis of the models to determine which best matches the response obtained from experimental data.

Hashin (1962) provided comprehensive expressions for the bulk and shear moduli covering the complete range of void volume fractions obtainable, however the author was unable to implement these successfully. It was later discovered that there was an algebraic error within Hashin (1962), the details of this error were discovered by Smith (2009) and led to an implementation of these formulations. Comparison between the results obtained by Smith (2009) and the results which may be obtained from a Bezier fit showed that the two were equivalent.

B.3.2 Evaluation of Model Performance

Extensive modelled results for velocity change due to increasing levels of porosity with differing fibre volume fractions for several fibre resin systems were presented by Reynolds and Wilkinson (1978). The change in moduli was modelled following the differential scheme outlined by Boucher (1975), for the addition of porosity to the resin the following relationships are used, for the bulk modulus,

$$\frac{K^* - K_1}{K_2 - K_1} = \Delta c \frac{K_1 + (4/3)G_1}{K_2 + (4/3)G_2} \quad \textbf{(B.20)}$$

and for the shear modulus,

$$\frac{G^* - G_1}{G_2 - G_1} = \Delta c \frac{G_1 + G_s}{G_2 + G_2} \quad \textbf{(B.21)}$$

Where the subscript 1 indicates the properties of the resin, the subscript 2 indicates the properties of the voids, Δc is a small concentration of voids and G_s is as follows,

$$G_s = \frac{G_1(9K_1 + 8G_1)}{6(K_1 + 2G_1)} \quad \textbf{(B.22)}$$

Stepwise numerical integration is then performed on the expressions shown in equations B.19 and B.20, with the concentration increased by a factor of $\Delta c/(1-c)$, where c is a finite concentration of voids. The values of K^* and G^* obtained are substituted into the next step of the equation as K_1 and G_1. Hashin (1965) provided results that were generalised by Reynolds and Wilkinson to allow the inclusion of fibres. Using the notation employed by Hashin, Reynolds and Wilkinson the bulk modulus k^* is calculated in terms of the material bulk (k_1 and k_2) and shear moduli (m_1) thus,

$$\frac{k^* - k_1}{k_2 - k_1} = \Delta c \frac{k_1 + m_1}{k_2 + m_1} \quad \textbf{(B.23)}$$

Using a subscript of 1 for the resin/void mixture and a subscript of 2 for the fibres. Similarly the shear modulus is shown to be,

$$\frac{m^* - m_1}{m_2 - m_1} = \Delta c \frac{2m_1(k_1 + m_1)}{(m_1 + m_2)k_1 + 2m_1 m_2} \tag{B.24}$$

Numerical integration is conducted as previously using a step size of $\Delta c/(1-c)$ and the velocity of the compression waves is shown by:

$$V_L = \sqrt{\frac{k^* + m^*}{\rho}} \tag{B.25}$$

Where ρ is the density of the composite. To allow the comparison between the simple mixture rule, the formulations provided by Hashin (1962) and this scheme, a constant fibre volume fraction of 0.6 was taken and the fractional volume of voids was varied. In the original work the percentage porosity in the resin phase before addition of fibres was provided and hence the same format is used here. Figures B.3-B.6 show the variation in velocity for differing resin void volume fractions for the simple mixture rule, the Hashin (1962) small concentration approximation and the extended Hashin formulation using Bézier curves for a composite structure using material parameters given in Reynolds and Wilkinson (1978).

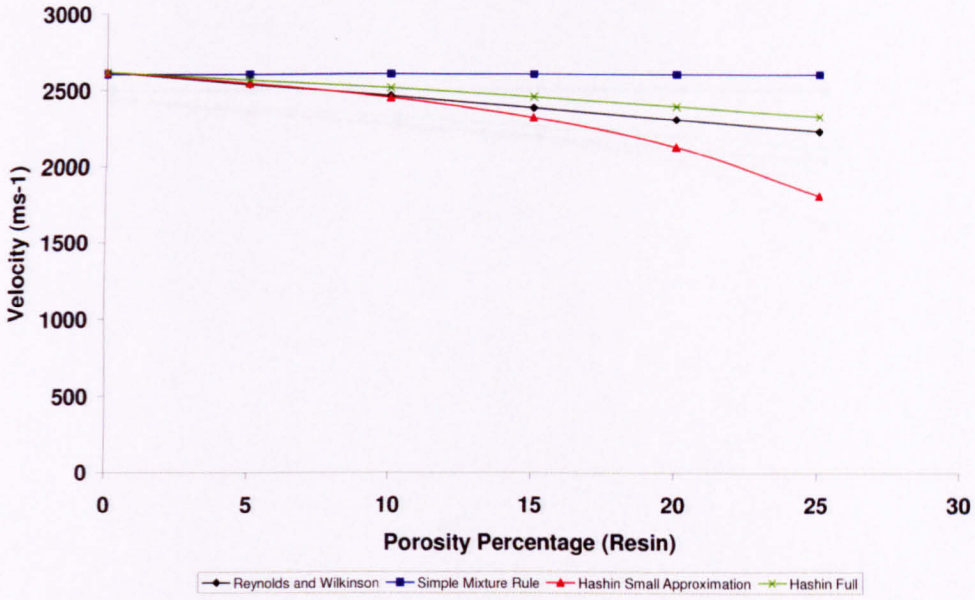

Figure B.3 Variation in longitudinal wave velocity for increasing void volume fraction, for Reynolds and Wilkinson (black), Hashin small concentration approximation (red), Bézier curve values (green) and simple mixture rule (blue).

Figure B.3 shows that a linear decrease in velocity is predicted by the method employed by Reynolds and Wilkinson, and this is matched closely by the Hashin formulation using Bézier curves. For small concentrations ($\phi_v \leq 0.1$) the small concentration approximation employed by Hashin (1962) closely follows the results of Reynolds and Wilkinson, thereafter the velocity decrease is larger than that observed by Reynolds and Wilkinson. The simple mixture rule shows no change in velocity. Similar results are obtained for the other fibre-resin mixtures given by Reynolds and Wilkinson (1978) as shown in figures B.4-B.6.

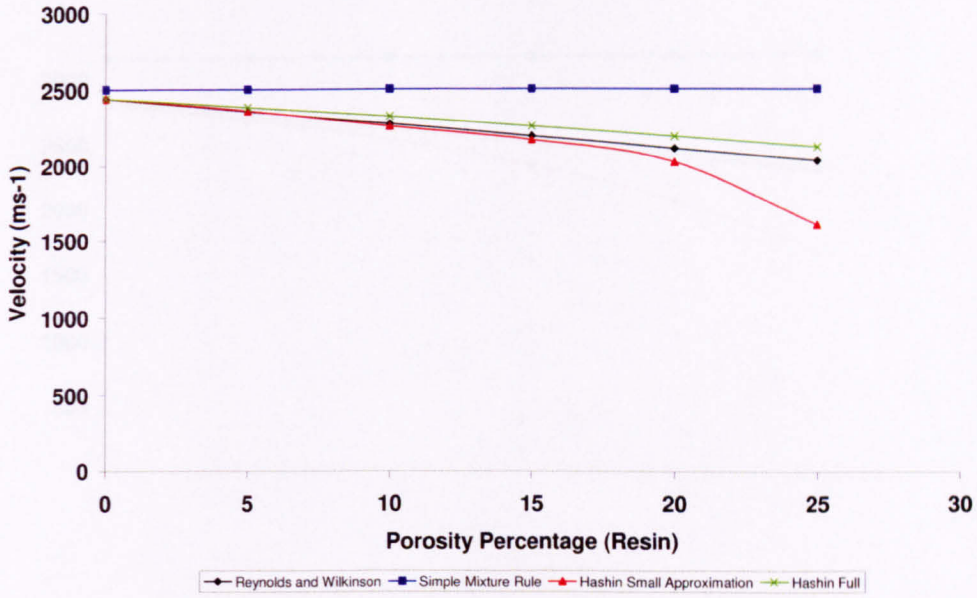

Figure B.4 Variation in longitudinal wave velocity for increasing void volume fraction, for Reynolds and Wilkinson (black), Hashin small concentration approximation (red), Bézier curve values (green) and simple mixture rule (blue).

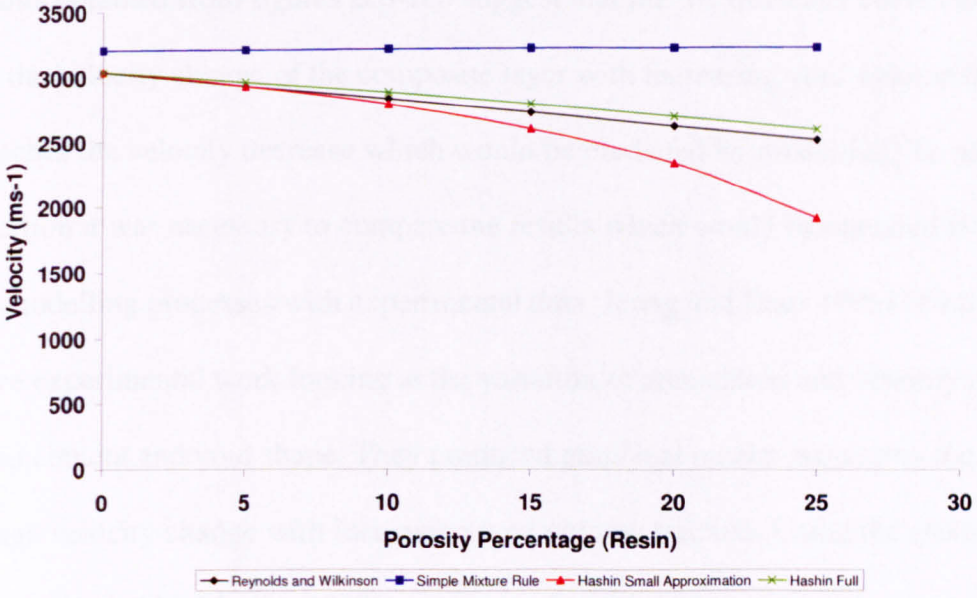

Figure B.5 Variation in longitudinal wave velocity for increasing void volume fraction, for Reynolds and Wilkinson (black), Hashin small concentration approximation (red), Bézier curve values (green) and simple mixture rule (blue).

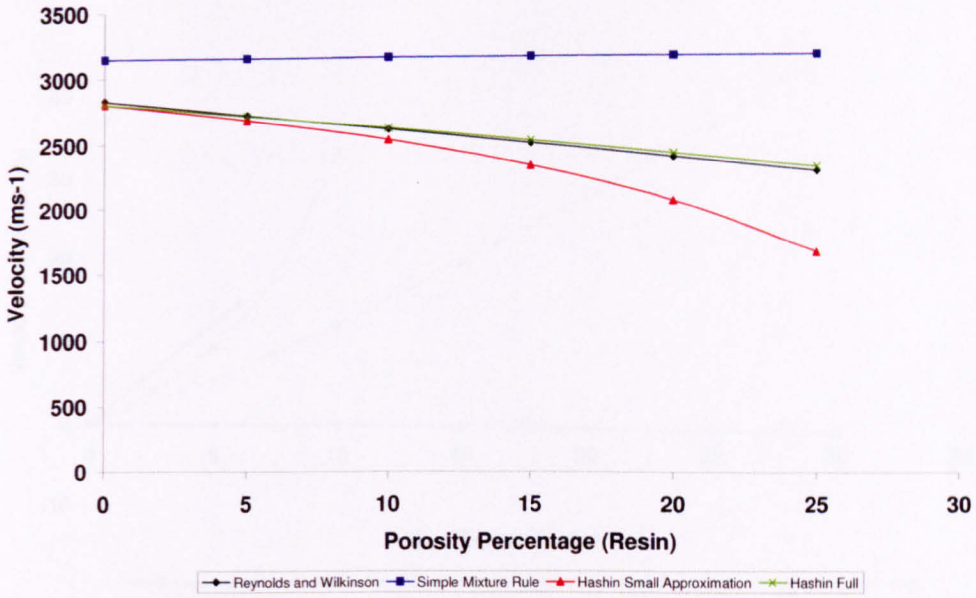

Figure B.6 Variation in longitudinal wave velocity for increasing void volume fraction, for Reynolds and Wilkinson (black), Hashin small concentration approximation (red), Bézier curve values (green) and simple mixture rule (blue).

The results obtained from figures B.3-B.6 suggest that the use of Bézier curves to analyse the velocity change of the composite layer with increasing void volume fraction best matches the velocity decrease which would be predicted by modelling. To support this assertion it was necessary to compare the results which would be obtained from the various modelling processes with experimental data. Jeong and Hsu (1995) conducted extensive experimental work looking at the variation of attenuation and velocity change with void content and void shape. They produced graphical results presenting the percentage velocity change with increasing void volume fraction. Using the elastic constants provided by Martin (1977), comparisons were made between the results obtained by Jeong and Hsu for uni-directional quasi-isotropic laminate and the mixture rules described previously. The velocity changes calculated are shown in figure B.7.

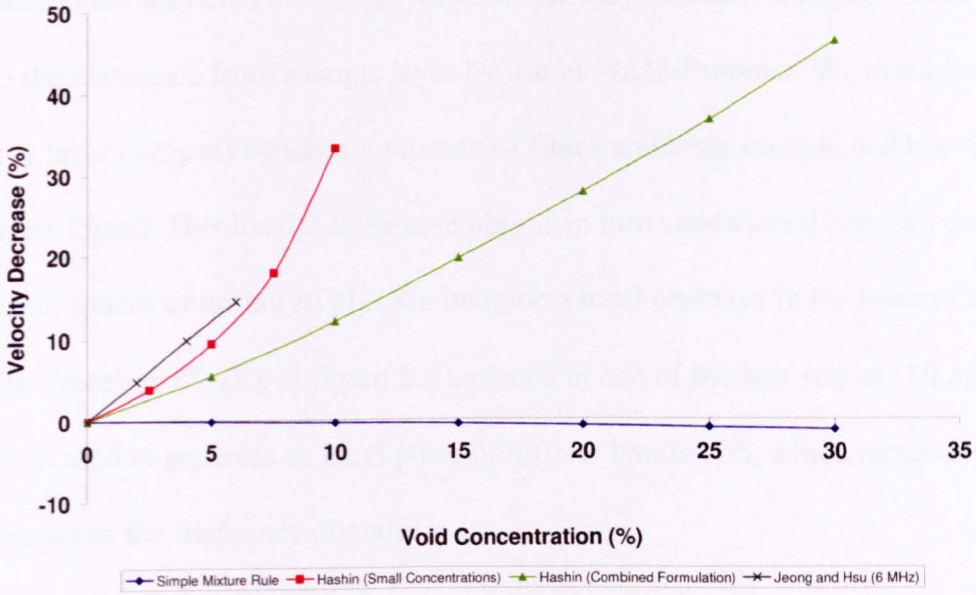

Figure B.7 Percentage velocity decrease for Jeong and Hsu (black), Hashin small concentrations (red), Bézier curve values (green) and simple mixture rule (blue).

Figure B.7 shows that numerically the Hashin small concentration method matches closest to the experimental results provided by Jeong and Hsu, but as the void concentration in the composite increases this model becomes less linear. The Bézier curve values, whilst not numerically similar to the results presented by Jeong and Hsu, are linear with void volume fraction and it is thought that if the elastic constants of the composite analysed by Jeong and Hsu were available then the results would be better numerically matched. The simple mixture rule shows a slight increase in velocity with increasing void volume fraction, which would indicate that for predicting the velocity of a combined medium the simple mixture rule cannot be employed. However, there are two effects which are present in carbon fibre composite due to the layered nature of the structure, which provides resonances in the fibre-resin mixture. When there are increasing levels of voids, there is a change in velocity; however, there is also present an impedance change through the change in density. Both of these effects will change the resonance, and it is necessary to determine which effect dominates. If the change in

impedance dominates then the simple mixture rule may be valid. It is possible to produce the resonance from a single layer by use of *MLM-Propmat.* We consider a single ply layer (125μm) which is a mixture of fibres and resin sandwiched between two resin layers (5μm). This local 3-layer assembly is in turn sandwiched between two semi-infinite half spaces of unflawed ply. We imagine a local observer in the form of a transmitter/receiver (Tx/Rx in figure B.8), placed in one of the half spaces. *MLM-Propmat* is used to generate an ideal pulse of infinite bandwidth, which receives the model output in the frequency domain.

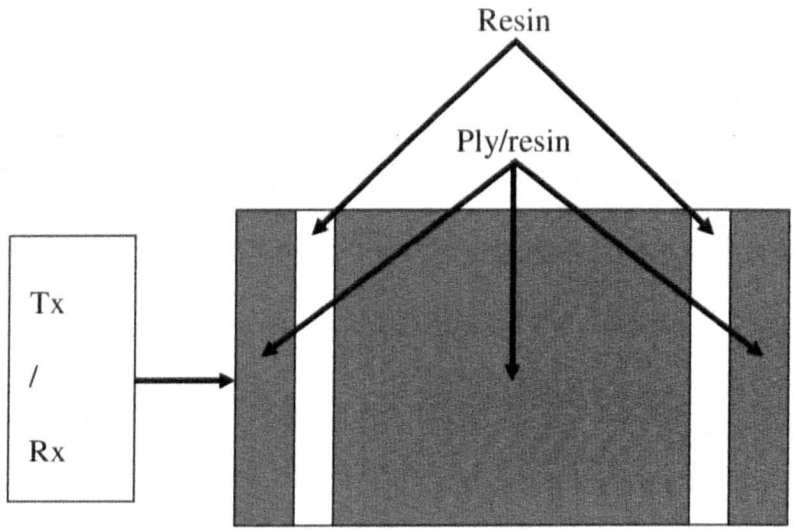

Figure B.8 Five Layer system analysed to determine local ply resonance.

The local resonance for flawed/unflawed composite could then be examined, the frequency response for unflawed composite is shown in figure B.9

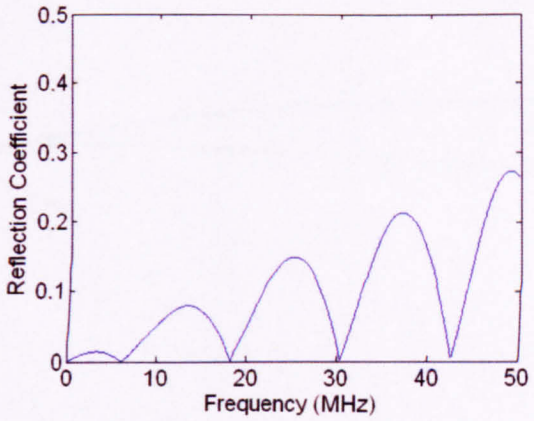

Figure B.9 Frequency response for unflawed composite calculated from the simple mixture rule.

Porosity can then be added to the central ply to examine its effect on the local resonance in the case of each of the mixture rules. To examine the differences between the mixture rule models the frequency and magnitude of the first resonant peak were calculated for differing void volume fractions. The results for variation in resonant frequency with increasing void content are shown in figure B.10, and for variation in magnitude in figure B.11.

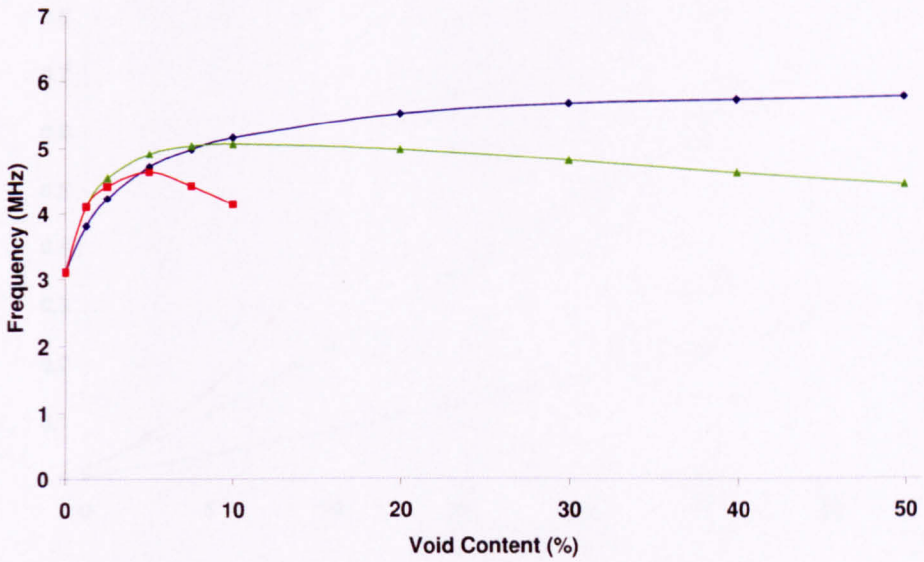

Figure B.10 Variation in resonant frequency with increasing void volume fraction for the simple mixture rule (blue), Hashin small concentrations (red) and Bézier curve values (green).

Figure B.10 shows that the simple mixture rule predicts an increase in resonant frequency. This is expected and is due to the impedance change which causes the sign of the reflection coefficient to change at the fibre/resin layer resin layer boundary, and the resonance to move from half wave to quarter wave. The Hashin small concentration approximation ends at limit given by Hashin of 10% void content and shows an increase in resonant frequency due to an impedance change similar to that observed via the simple mixture rule. There is then a decrease in resonant frequency due to the decreasing velocity. A similar effect is also observed for the Bézier curve values.

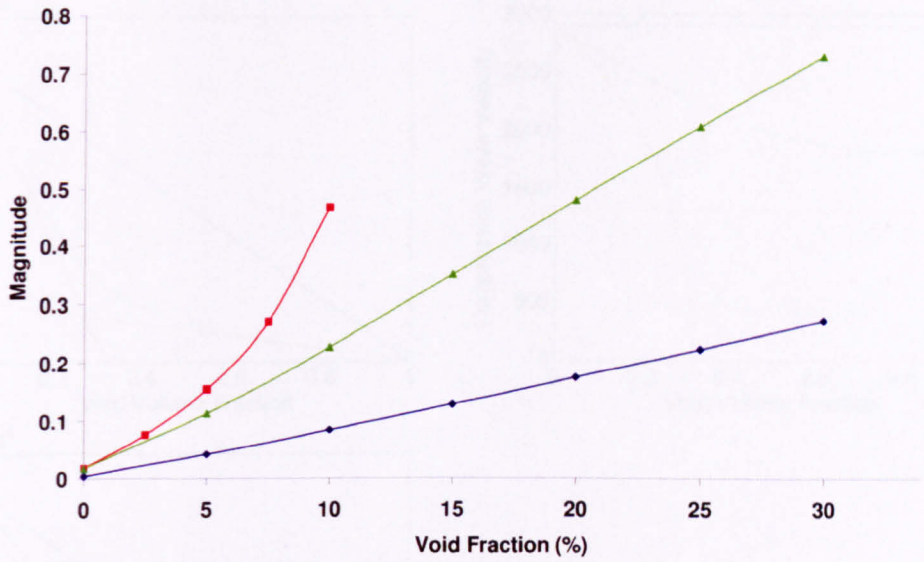

Figure B.11 Variation in resonant peak magnitude with increasing void volume fraction for the simple mixture rule (blue), Hashin small concentrations (red) and Bézier curve values (green).

From figure B.11 it is observed that both the simple mixture rule and the Bézier curve values show a linear increase in magnitude with increasing void volume fraction. The Bézier curve values increase at a greater rate than that for the simple mixture rule, this is due to the impedance change, which is greater in the case of the Bézier curve.

The principal reason for the similarities is best illustrated by observation of the variation of modulus, compression wave velocity and impedance for a composite structure with increasing concentrations of voids, as shown in figure B.12.

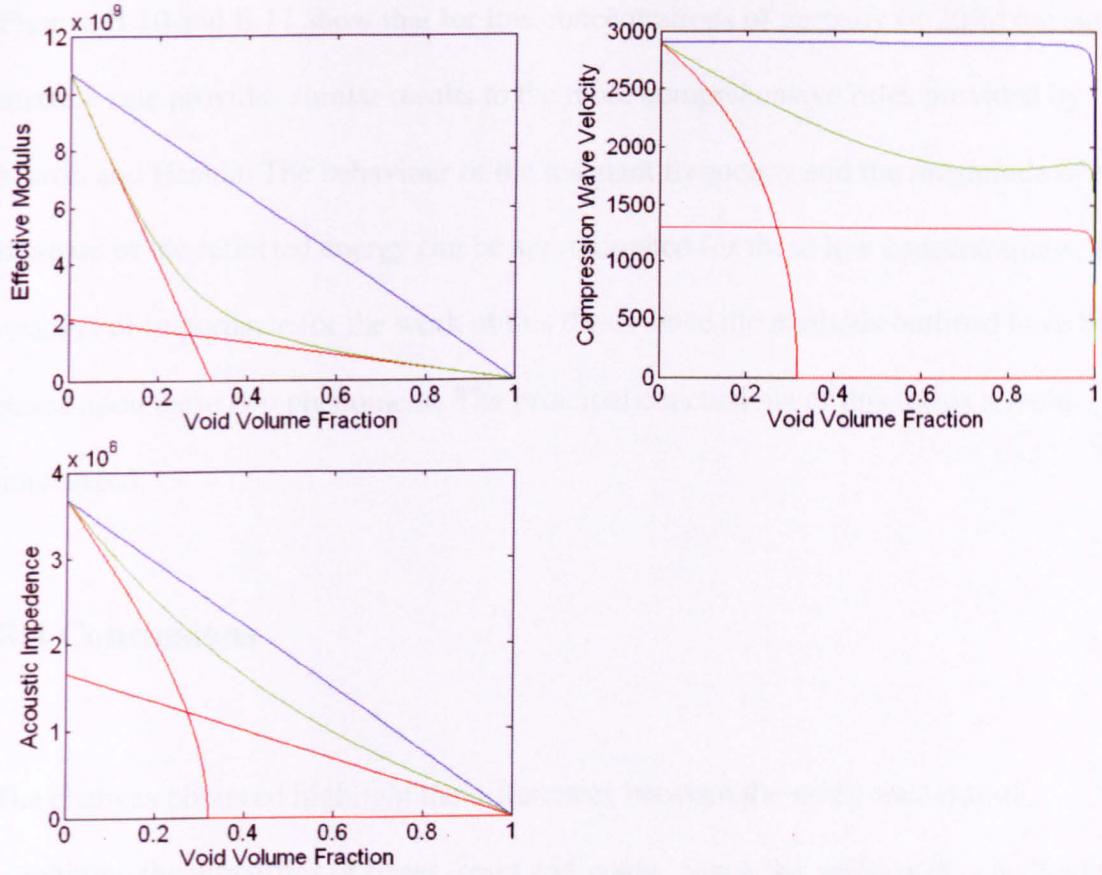

Figure B.12 Variation of effective compression modulus (top left), compression wave velocity (top right) and acoustic impedance (bottom left) with increasing void content for the simple mixture rule (blue line), Hashin small and large concentration rule (red lines) and Bezier fit (green line).

Figure B.12 shows that although there is a large difference between the modulus and velocity calculated on the basis of the different mixture rules, we see that for impedance the simple mixture rule is a reasonable approximation of the Bezier fit and matches it more closely. The impedance effect dominates and provides the initial change in resonant frequency. At higher concentrations of voids there is a further drop in frequency for the Bezier fit, again driven by the velocity change. Thus for concentrations below 20% this is an acceptable match.

Figures B.10 and B.11 show that for low concentrations of porosity (< 20%) the simple mixture rule provides similar results to the more comprehensive rules provided by Martin and Hashin. The behaviour of the resonant frequency and the magnitude of the increase of the reflected energy can be approximated for these low concentrations. This result is of importance for the work of this thesis since the methods outlined have been based upon these two phenomena. The principal conclusions of this thesis remain unchanged.

B.4 Conclusions

The changes observed highlight the differences between the many methods of combining the properties of fibres, resin and voids. Since the velocity change has an effect at large concentrations of voids it is considered that the neither the simple mixture rule nor the Hashin small concentration approximation adequately models the changes which are likely to be seen at varying void volume fractions. The Bézier curve method of creating a link between small and large concentrations of voids has been observed to match both modelled and experimental data for velocity change much more closely and hence it is considered that this method should be employed when calculating the longitudinal wave velocity and density of mixtures for use with *MLM-Propmat* in the future. However, the behaviour of the resonant frequency and the increase in reflected energy in the presence of porosity are adequately predicted by the simple mixture rules which have been employed in this project. The principal conclusions of this thesis remain unchanged, namely that the methods are valid and may be used to detect and quantify the presence of porosity in composite materials.

Appendix C

Material Properties for Modelling

C.1 Introduction

In order to accurately model a composite using *MLM-Propmat* it is necessary to define the effective velocity and density of a mixture of fibres and resin. In Chapter 4 a simple mixture rule was suggested which could give the required material properties provided that the velocity and density of the constituent layers were known. However, the composites used in practice and their material properties vary widely between manufacturer and application. It is thus necessary to choose with care the parameters for use as input to *MLM-Propmat*, which it is hoped will yield 'general case' representative simulations. This appendix documents the properties which have been used by previous authors in the field, and identifies the material properties that were used as input to *MLM-Propmat.*

C.2 Properties Documented in the Literature

Throughout the modelling papers examined in the literature review (Chapter 2) many and varied material properties were used by the authors. These varied dependent upon the particular samples under examination, and not every author provided the properties that had been used. A summary of the properties given in the principal publications for fibre and resin, density and velocity are shown in table C.1.

	Fibre Velocty (ms^{-1})	Fibre Density (kgm^{-3})	Resin Velocity (ms^{-1})	Resin Density (kgm^{-3})
Martin (1976)	3076	1690	2903	1270
Reynolds and Wilkinson (1978)	2524 / 3394	1770 / 1900	2449 / 2775	1100 / 1260
Dominguez (2006)	2340	1230	2960	1550

Table C.1 Material properties provided by various authors.

The material properties that result from these values when using the simple mixture rule to define a composite layer of fibre volume fraction 0.7 are shown in Table C.2.

	Composite Velocity (ms^{-1})	Composite Density (kgm^{-3})
Martin (1976)	3024	1564
Reynolds and Wilkinson (1978)	2502 / 3208	1569 / 1708
Dominguez (2006)	2526	1326

Table C.2 Material properties following from various authors.

From table C.2 we can see that there is a spread in the values of velocity and density which affects the compression modulus of the layer M as shown in Table C.3.

	Compression Modulus (GNm^{-2})
Martin (1976)	14.0
Reynolds and Wilkinson (1978)	9.8 / 17.4
Dominguez (2006)	8.4

Table C.3 Compression Modulus calculated on the basis of table C2.

From table C.3 we can see that the maximum value of compression modulus is $17.4GNm^{-2}$ and the minimum value is $8.4GNm^{-2}$. The value for compression modulus following from Martin (1976) is close to the average value ($12.4GNm^{-2}$) for the data set. It is concluded from this exercise that the values for compression velocity and density of fibre and resin provided by Martin are representative of the spread over which values may occur within composite structure. For this reason these values were used when developing methods for the detection of porosity and thick resin layer using *MLM-Propmat*. Within the main body of the thesis these values are used unless otherwise specified.

Appendix D

ANDSCAN® System Overview

D.1 Introduction

Extensive use was made of the software package Andscan® during the course of this work. This appendix aims to give an overview of the functionality and operation of the Andscan® system as used in this thesis.

D.2 System Overview

Andscan® has been developed over the course of many year by QinetiQ (Farnborough, UK), initially the system was designed to acquire ultrasonic data from automated scanning systems in the DOS environment. The software package has been upgraded and expanded over the years to acquire data from a number of sources (manual / automated scanning systems) and from a variety of NDE techniques (ultrasonic, eddy current, low frequency vibration). The package was converted to Windows in 1995, and at this time the ability to analyse captured wavé forms in a number of ways was added and has been significantly improved over the years.

Data display in Andscan® can be in one of four formats; initially the time-domain waveform for a single point is shown as an A-scan. Secondly this time-domain waveform can be gated to display the amplitude or the time of flight at a particular point within the data set; this data is plotted in two dimensions with a varying colour to

represent the parameter being measured (a C-scan). Thirdly the variation in amplitude or time of flight may be presented as a function of one spatial variable against time, this is known as a B-scan.

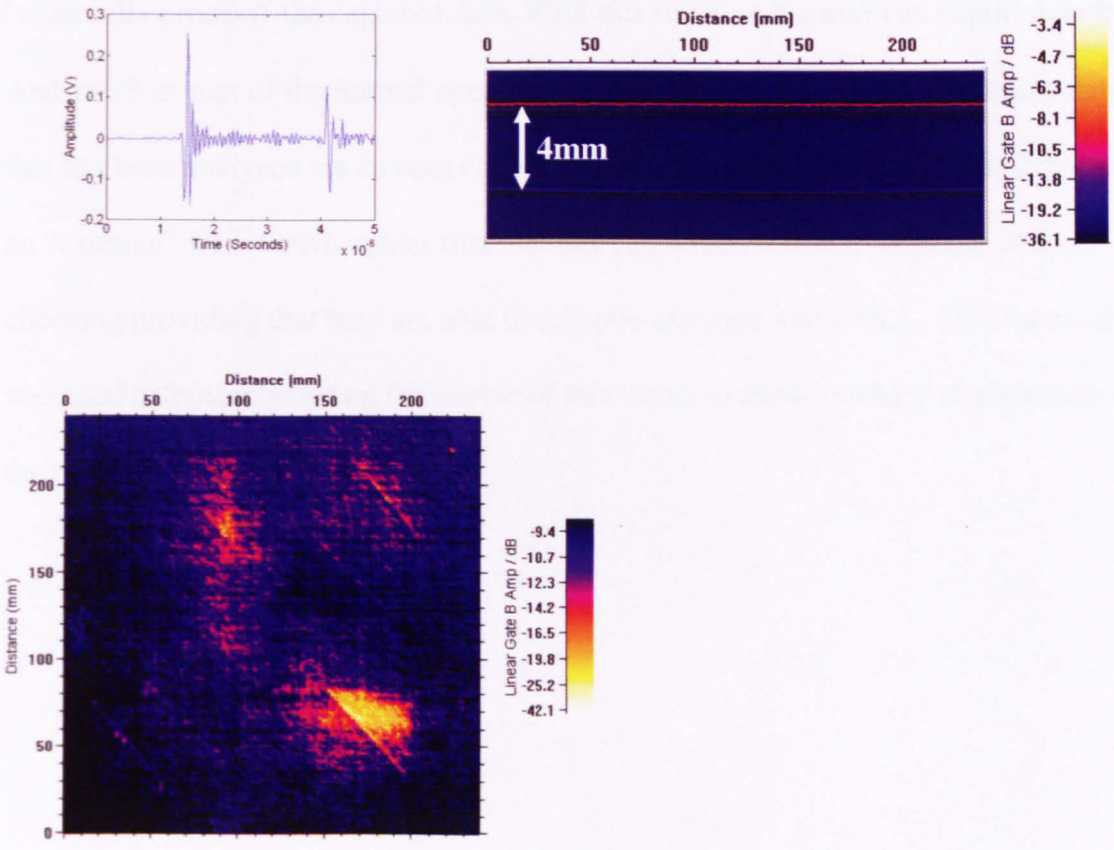

Figure D.1 A typical A-scan (top left), B-scan (top right) and C-scan (bottom) from Andscan®.

Finally, a 3-D profile may be generated by applying a small gate to the waveform and generating C-scans of the amplitude within the gate at each depth. This results in a set of C-scans for each depth from which B-scans are also generated giving cross sections both horizontally and vertically across the panel.

Data processing may be achieved via direct analysis of the A-scan or via global analysis of the C-scans of acquired data. Andscan® supports rectification, energy measurements,

RMS power, time of flight and integral of the A-scan. The package also supports spectral analysis, Fourier transforms of captured data and the application of filters. Although the in-built functionality provides a basis for comprehensive analysis of any data received via experiment; this thesis made use of the functionality provided to "externally process" the captured data. With this function the user can export data from Andscan® as part of the normal operation of the software and return for display data that has been analysed via custom code written by the user. This code is compiled into an "external" DLL which means that the user can write code in a language of their choosing providing that they are able to compile the code into a DLL. This functionality was used extensively during the course of this thesis to allow practical demonstration of the novel methods developed.

Appendix E

Definition of Test Samples

This appendix contains detailed descriptions of the test samples used to evaluate the methods developed during the course of this work.

Sample 1

The first sample was designed and constructed at Airbus; it contains two layers of glass micro spheres at different depths, to simulate layers of porosity. Although glass micro spheres provide a much larger reflection than would be expected from porosity, the sample does provide a useful opportunity to locate such a defect within a CFRP. The panel was constructed with 8 unidirectional plies per mm and is 2.7mm thick. A C-scan of back wall echo amplitude is shown in figure E.1.

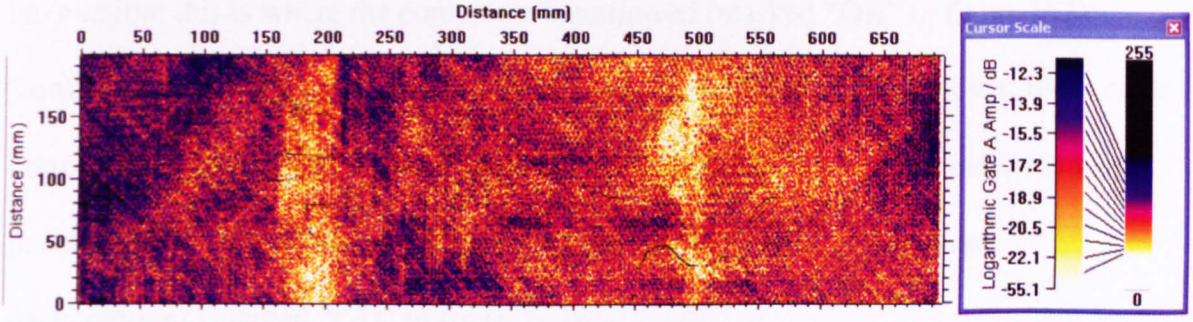

Figure E.1 C-scan of back wall amplitude for Sample 1.

Figure E.1 reveals that there are two areas of high attenuation, one at 200mm and the other at 500mm on the x-axis, both running vertically down the sample corresponding to the location of the layers of glass microspheres.

Sample 2

Sample 2 was produced by Airbus using standard production techniques (Airbus reference 5358), it was a panel 31 unidirectional plies thick at 8 plies per mm. The panel was cut from a larger test sample which had areas of gross porosity in the centre, small areas of voids outside of this and was classified as good at the edges. A C-scan of the back wall echo amplitude is shown in figure E.2.

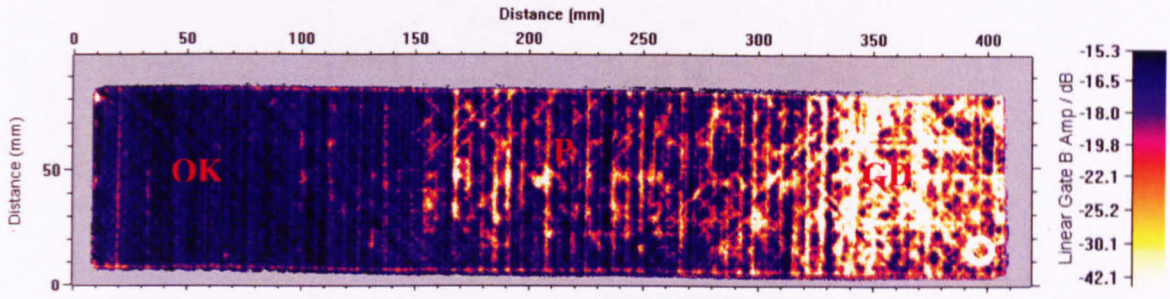

Figure E.2 C-Scan of back wall echo amplitude for Sample 2.

The darker colours on the right hand side correspond to areas of low back wall attenuation; this is where the composite is unflawed (marked "OK" in figure E.2). Towards the middle of the panel we see areas which contain lighter colours; these areas correspond to clusters of voids (marked "P" in figure E.2). The right hand side of the panel contains many areas of light colour corresponding to large voids and delaminations (marked "GD" in figure E.2).

Sample 3

Sample was designed and constructed by QinetiQ (Farnborough, UK); the panel reference was A0956; it contains variations in fibre volume fraction and porous areas. This was achieved by removing layers of fibres from some areas and adding them to other areas as shown in figure E.3.

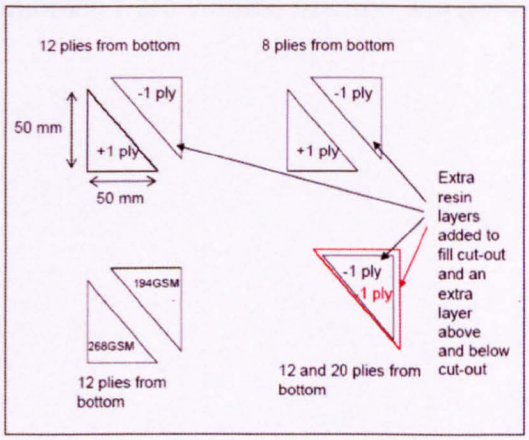

Figure E.3 Design of combined fibre volume fraction and porosity sample.

Flaws were embedded in Sample 3 as follows: (a, top left) A triangular ply section at a depth of 20 plies was removed and added to an adjacent area; the void left by the cup-out ply was filled with an extra resin layer. (b, top right) Similar to (a), but the flaw was set to a depth of 28 plies. (c, bottom left) Two triangular ply sections have been added at a depth of 20 plies; one of these was 192 gm^{-2} and matched the parent composite, and the other was thicker at 268 gm^{-2}. (d, bottom right) Two plies were removed, one at a depth of 12 plies and the other at a depth of 20 plies; extra resin filled the voids. A C-scan was plotted showing the variation in back wall echo amplitude across the sample, figure E.4.

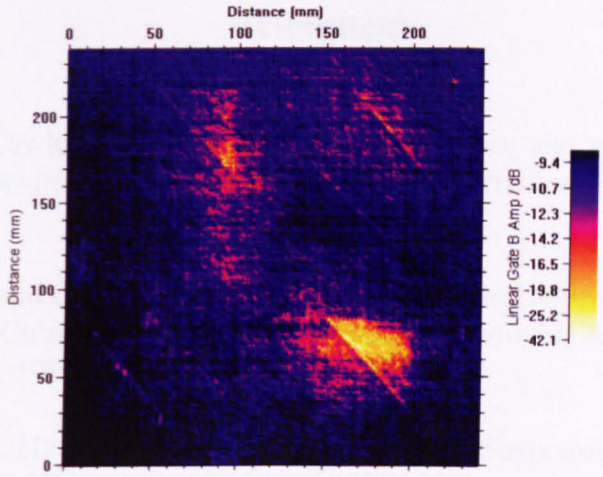

Figure E.4 C-scan of combined fibre volume fraction and porosity panel for Sample 3.

References

Adams, R.D. and Cawley, P., "A review of defect types and non-destructive testing techniques for composites and bonded joints", NDT International, Vol 21, pp. 208-222, 1988.

L. Adler, J.H. Rose and C. Mobley, "Ultrasonic Method to Determine Gas Porosity in Aluminum Alloy Castings: Theory and Experiment", Journal Applied Physics Vol. 59, pp 336-347, 1986.

J.R. Allegra and S.A. Hawley, "Attenuation of Sound in Suspensions and Emulsions, Theory and Experiments", Journal of the Acoustical Society of America Vol. 51 pp 1545-1564 1972.

S.F.M. de Almeida and Z.S.N. Neto, "Effect of void content on the strength of composite laminates", Composite Structures, Vol. 28., pp. 139-148, 1994.

Bose, S.K., Mal, A.K. "Longitudinal Shear Waves in a Fiber-Reinforced Composite", International Journal of Solids and Structures, 9, pp 1075-1085, 1973.

R.H. Bossi and G.E. Georgeson, "Composite structure development decisions using X-ray CT measurements," Materials Evaluation, pp. 1198-1203, Oct. 1995.

S. Boucher, "Effective moduli of quasi-homogenous composite materials", Revue M, 1975, 21, 3 and Revue M, 22, 1, 1976.

S. Boucher, "Effective moduli of quasi-homogeneous composite materials (I) Infinitesimal concentrations", Revue M, Vol. 21, 3, 1975, (II) Finite concentrations, Revue M, Vol. 22, 1, 1976.

P. Cervenka and P. Challande, "A new efficient algorithm to compute the exact reflection and transmission factors for plane waves in layered absorbing media (liquids and solids)", Journal of the Acoustical Society of America, Vol. 89, pp 1579-1589, 1991.

R.E. Challis, J.S. Tebbutt and A.K. Holmes, "Equivalence Between Three Scattering Formulations for Ultrasonic Wave Propagation in Particulate Mixtures", J. Phys. D : Appl. Phys. Vol. 31, pp 3481-3497, 1998.

R.E. Challis, F. Blarel, M.E. Unwin, J. Paul and X. Guo, "Models of Ultrasonic Wave Propogation in Epoxy Materials", IEEE Transactions on Ultrasonics, Ferroelectrics and Frequency Control, Vol. 56, No. 6, June 2009.

R.E. Challis, R.J. Freemantle, R.P. Cocker, D.L.Chadwick, D.J. Dare, C.M. Martin, A. Mendrasingham, and W. Fuller, Ultrasonic measurements related to the evolution of structure in curing epoxy resins, Plastics, Rubber and Composites, Vol 29, pp 109-118, 2000.

N. Choi and K. Takahashi, "Characteristics of acoustic emission wave attenuation in short fibre reinforced plastics", Journal of Composite Materials, Vol.24, pp 1012-1028, 1990.

K. Cotterell and R. Sharpe, "The use of carbon tetrachloride as a radiopaque penetrant," Journal of NDT, 20, pp. 234-235, 1962.

I.M. Daniel, S.C. Wooh and I. Komsky, "Quantitative porosity characterization of composite materials by means of ultrasonic attenuation measurements", Journal of Nondestructive evaluation, Vol. 11, No. 1, pp. 1-8, 1992.

O'Donnell M., Jaynes E.T. and Miller J.G., "General relationships between ultrasonic attenuation and dispersion", Journal of the Acoustical Society of America, Vol. 63, pp.1935-1937, 1978.

N. Dominguez, "Modélisation de la propagation ultrasonore en milieux complexes – application au contrôle non destructif et á la caractérisation de la porosité dans les matériaux composites stratifies", PhD Thesis, Universitie Toulouse III, 2006.

J. W. Dunkin, "Computation of modal solutions in layered elastic media at high frequencies", J. Bull. Seism. Soc. Am., Vol. 55, pp. 335-358, 1965.

P.S. Epstein, "On the absorption of Sound by Suspensions and Emulsions", Contributions to Applied Mechanics, Theodore Von Karman Anniversary Volume (Passadena: California Institute of Technology), pp 162-188, 1941.

P.S. Epstein and R.R. Carhart, "The Absorption of Sound in Suspensions and Emulsions I. Water Fog in Air", Journal of the Acoustical Society of America, Vol. 25 pp 553-565 1953.

A. G. Evans, B. R. Tittmann, L. Ahlberg, B. T. Khuri-Yakub and G. S. Kino, "Ultrasonic Attenuation in Ceramics", Journal of Applied Physics, Vol. 49(5), pp 2669, 1978.

R.H. Fassbender and D.J. Hagemair, "Low Kilovoltage Radiography of Composites", Materials Evaluation, 41, June 1983.

R.J. Freemantle, "Ultrasonic Compression Wave Evaluation of Adhered Metal Sheets and Thin Sheet Materials", PhD Thesis, University of Keele, UK, 1995.

R.J. Freemantle and R.E. Challis, "Combined compression and shear wave ultrasonic measurements on curing adhesive", MST Vol 9(8), 1291-1302, 1998.

B. Ghaffari, G. Mozurkewich, L.A. Godlewski and J.W. Zindel, "Ultrasonic Characterization of Shrinkage Microporosity in Aluminum Castings", Ultrasonics, Vol. 41, pp 699-707, 2004.

L.B. Greszczuk, "Interfiber Stresses in Filamentary Composites", AIAA Journal, 9, pp 1274-1284, 1971.

J. E. Gubernatis and E. Domany, "Effects of microstructure on the speed and attenuation of elastic waves in porous materials", Wave Motion, Vol. 6, 579, 1984.

N. Guo and P. Cawley, "The non-destructive assessment of porosity in composite repairs", Composites, Vol. 25(9), pp. 842-850, 1994.

C.C. Habeger, "The attenuation of ultrasound in dilute polymetric fiber suspensions", Journal of the Acoustical Society of America, Vol. 72(3), pp. 870-878, 1982.

D.J. Hagemaier and R.H. Fassbender, "NDT of advanced composites", Materials Evaluation, pp. 43 – 49, 1979.

J.M. Hale and J.N. Ashton, "Ultrasonic attenuation in voided fibre-reinforced plastics", NDT International, Vol. 21(5), pp. 321-326, 1988.

Z. Hashin, "The elastic moduli of heterogeneous materials", ASME Journal Applied Mechanics, 29, pp 143-150, 1962.

Z. Hashin, "On the elastic behaviour of fibre reinforced materials of arbitrary transverse phase geometry", Journal of the Mechanics and Physics of Solids, 13, pp 119, 1965.

N. A. Haskell, "The dispersion of surface waves on multilayered media", J. Bull. Seism. Soc. Am., Vol. 43, pp. 17-34, 1953.

D. Hsu, D. Fei and Z. Liu, "Ultrasonically mapping the ply layup of composite laminates", Materials Evaluation, Vol 60, No 9, pp 1099-1106, Sept 2002.

C.P. Hobbs, D. Kenway-Jackson, and M.D. Judd, "The application of transient thermography for the nondestructive testing and evaluation of aerospace materials", Proc Int Symp Advanced Materials for Lightweight Structures '94, Noordwijk, Netherlands, ESA WPP-070, pp645-653, 1994.

H. Jeong and D. Hsu, "Experimental analysis of porosity-induced ultrasonic attenuation and dispersion", Ultrasonics, Vol. 33, No. 3, pp. 195-203, 1995.

B.R. Jones and D.E.W. Stone, "Towards an ultrasonic attenuation technique to measure void content in carbon-fiber composites", Non-Destructive Testing, pp. 71-79, April 1976.

N.C.W. Judd and W.W. Wright, "Voids and their effects on the mechanical properties of composites – an appraisal", SAMPE Journal, pp.10-14, Jan/Feb, 1978.

V. K. Kinra et al, "Simultaneous measurement of the acoustical properties of a thin -layered medium: The inverse problem", Journal of the Acoustical Society of America, Vol. 95 (6), 3059-3074, 1994.

H.C. Kim, and J.M. Park, "Ultrasonic wave propagation in carbon fibre-reinforced plastics", Journal of Materials Science, Vol. 22, pp 4536-4540, 1987.

R. A. Kline, "Measurement of attenuation and dispersion using an ultrasonic spectroscopy technique", Journal of the Acoustical Society of America, Vol. 76(2), pp 496-504, 1984.

R. A. Kline, "The effect of microstructure on wave propagation in fiber reinforced composite materials", Ultrasonics Symposium, pp. 1119-1122, 1986.

R. A. Kline, "Quantitive NDE of advanced composites using ultrasonic velocity measurements", Journal of Engineering and Materials and Technology, Vol. 112, pp 218-221, 1990.

L. Knopoff, "A matrix method for elastic wave problems", J. Bull. Seism. Soc. Am., Vol. 54, pp. 431-438, 1964.

J.R. Kollgaard and S.G. LaRiviere, "NDE Challenges with future commercial aircraft – a Boeing perspective", Review of Progress in QNDE, Vol. 34A, pp. 23-28, 2007.

T.S. Lewis, D.W. Kraft, N. Hom, "Scattering of Elastic Waves by a Cylindrical Cavity in a Solid", Journal of Applied Physics, 47, pp 1795-1798, 1975.

M. J. S. Lowe, "Matrix Techniques for Modeling Ultrasonic Waves in Multilayered Media", IEEE Transactions on Ultrasonics, Vol. 42, No. 4, July 1995.

B. G. Martin, "Ultrasonic attenuation due to voids in fibre-reinforced plastics", NDT International, Vol. 9, pp. 242-246, 1976.

B.G. Martin, "Ultrasonic wave propagation in fiber-reinforced solids containing voids", Journal of Applied Physics, Vol. 48, No. 8, pp 3368-3373, 1977.

B. Mascaro, "Charactéisation ultrasonore de la porosité dans les composites Carbone/Epoxy stratifies", PhD Thesis, Universitie Toulouse III, 2006.

J.M. Milne and W.M. Reynolds, "Applications of thermal pulses and infrared thermal imagers for observing sub-surface structures in metals and composites", Proc SPIE vol 590, pp293-297, 1985.

A.P. Mouritz, "Ultrasonic and interlaminar properties of highly porous composites", Journal of Composite Materials, Vol. 34, No. 3, pp. 218-239, 2000.

S.M. Nair, D.K. Hsu, J.H. Rose, "Porosity Estimation Using the Frequency Dependence of the Ultrasonic Attenuation", Journal of Nondestructive Evaluation, Vol. 8, pp, 1989.

J.W. Newman, "Production and field inspection of composite aerospace structures with advanced shearography", Proc 22nd International SAMPE Tech Conf, Boston, Ma, pp. 1243-1249, 1990.

S. Pelletier, M. Fiset and R. Angers, "The use of ultrasonic velocities to characterize SiC_w/Al_2O_3 composites", Journal of the Canadian Ceramic Society, Vol. 62, No. 1, pp 58-62, 1993.

T. A. Pialucha, "The reflection coefficient from interface layers in NDT of adhesive joints", PhD thesis, Dept. Mech. Eng., Imperial College, London, UK, 1992.

A. P. Y. Phang, R. E. Challis, V. G. Ivchenko, A. N. Kalashnikov, "A field programmable gate array-based ultrasonic spectrometer", J. Meas. Sci. Tech., Vol. 19, Issue 4, pp. 045802, 2008.

W. Reynolds and S. Wilkinson, "The analysis of fibre-reinforced porous composite materials by the measurement of ultrasonic wave velocities", Ultrasonics, pp 159-163, July 1978.

S. I. Rokhlin, D.K. Lewis, K. F. Graff and L. Adler, "Real time study of frequency dependence of attenuation and velocity of ultrasonic waves during the cure reaction of epoxy resin", Journal of the Acoustical Society of America, Vol. 79(6), pp 1786-1793, 1986.

J.H. Rose, D.K. Hsu, L. Adler, "Ultrasonic characterization of porosity using the Kramers-Kronig relations", J. Phys (Paris) Colloq. 46 C10-787 - C10-790, 1985.

M. Seale, B. Smith, W. Prosser and J. Zalameda, "Lamb wave assessment of fiber volume fraction in composites", Journal of the Acoustic Society of America, 1998, 104(3), pp 1399-1403.

C.B. Scruby, "An Introduction to Acoustic Emission", Journal of Physics E: Scientific Instrumentation, 20, pp. 946, 1987.

H.M. Shang, F.S. Chau, C.J. Tay and S.L. Toh, "Estimating the depth and width of arbitrarily oriented disbonds in laminates using shearography", Journal of Nondestructive Evaluation, Vol 9, pp19-26, 1990.

B.T. Smith and A.M. Buoncristiani, "Digital signal processing methods for ultrasonic backscattered waves in composite materials", Ultrasonics Symposium, pp. 1041-1046, 1986.

B.T. Smith, "Ultrasonic characterization of porosity in composites", Review of Progress in QNDE, Vol. 9, pp. 1535-1540, 1990.

R.A. Smith and B. Clarke, "Ultrasonic C-scan Determination of Ply Stacking Sequence in Carbon-fibre Composites". Insight - Journal of the British Institute of NDT, Vol 36 (10) 741-747, October 1994.

R. A. Smith, Personal Communication, May 2008.

R. A. Smith, "Ultrasonic Interaction With Thin Layers", Personal Communication, September 2008.

R.A. Smith, Personal Communication, 20th April 2009.

R. E. Smith, "Ultrasonic elastic constants of carbon fibers and their composites", Journal of Applied Physics, Vol. 43 pp 2555, 1972.

P.W.A. Stijnman, "Determination of the elastic constants of some composites by using ultrasonic velocity measurements", Composites, Vol. 26, pp. 597-604, 1995.

D.E.W. Stone and B. Clarke, "Ultrasonic attenuation as a measure of void content in carbon fiber reinforced plastics", Non-Destructive Testing, pp. 137-145, June 1975.

W. T. Thompson," Transmission of elastic waves through a stratified solid medium", Journal of Applied Physics, Vol. 21, pp. 89-93, 1950.

H.J. Tiziani, "Physical properties of speckles in Speckle Metrology", RK Erf (ed), Academic Press, New York, pp5-9, 1978.

K.M. Uhl, B. Lucht, H. Jeong and D. Hsu, "Mechanical strength degradation of graphite fibre reinforced thermoset composites due to porosity", Review of Progress in QNDE, Vol. 7B, pp. 1075-1082, 1988.

J.H. Williams, H. Nayeb-Hashemi and S.S. Lee, "Ultrasonic attenuation and velocity in AS/3501-6 graphite fiber composite", Journal of Nondestructive Evaluation, Vol 1., No. 2, pp. 137-148, 1980.

C.F. Ying and R. Truell, "Scattering of a Plane Longitudinal Wave by a Spherical Obstacle in an Isotropically Elastic Solid", Journal of Applied Physics, Vol. 27, pp 1086-1097, 1956.

J. Zimmer, and J. Cost, "Determination of elastic constants of a uni-directional fiber composite using ultrasonic velocity measurements", The Journal of the Acoustical Society of America, 47, 3, pp 795, 1970.